

Alma Mater Studiorum – Università di Bologna

DOTTORATO DI RICERCA IN
INGEGNERIA CIVILE, CHIMICA, AMBIENTALE E DEI
MATERIALI

Ciclo XXIX

Settore Concorsuale di afferenza: 08/B2

Settore Scientifico disciplinare: ICAR/08

TITOLO TESI

Experimental Study of The Bond Behavior of Steel FRP-Concrete Joints
and Shear Behavior of Concrete Beams Reinforced With GFRP Bars

Presentata da: Imohamed Ali Omar Imohamed

Coordinatore Dottorato

Luca Vittuari

Relatore

Carlioni Christian

Esame finale anno 2017

For my beloved mother Azz Muftah and father Ali Omar,
and all people that help and supported me.
Also to my ever supporting supervisor Prof. Christian Carloni

ACKNOWLEDGEMENT

I would like to thank all the parties who have given the co-operation to me in writing this thesis. I am sincerely great full to my supervisor, Prof. Christian Carloni for his continuous support and guidance in this thesis. He has set a high standard for the conduct of this study and his valuable suggestions and guidance have provided me the motivation needed to complete this thesis.

I would like to extend my thanks to my colleague, Mattia Santandrea for his supportive friendship during my PhD study.

I would also like to thank the staffs and technicians of the laboratory LISG (Laboratory of Structural and Geotechnical Engineering) at University of Bologna are gratefully acknowledged. Kerakoll S.p.A. of Sassuolo, Italy, is gratefully acknowledged for providing the composite materials.

Finally, I thank my family and friends for their supports and encouragement. Their encouragement provided the often-needed motivation and inspirations for me to push through the hard times. I would also like to acknowledge the contributions of those who have helped either directly or indirectly in the completion of this thesis.

Thank You.

TABLE OF CONTENTS

TITLE.....	i
DEDICATION	ii
ACKNOWLEDGEMENT	iii
TABLE OF CONTENTS.....	iv
LIST OF TABLES	xi
TABLE OF FIGURES	xiii
TABLE OF APPENDICES	xxi
CHAPTER 1: INTRODUCTION.....	1
1.0 Background of the study	1
1.1 Fibre Reinforced Polymer (FRP)	3
1.1.1 Carbon Fibre Reinforced Polymer (CFRP)	5
1.1.2 Aramid Fibre Reinforced Polymer (AFRP)	5
1.1.3 Glass Reinforced Polymer (GFRP)	5
1.2 Steel Fibers	6
1.3 Objectives of dissertation	7
1.4 Scope of dissertation	8
1.5 Outline of dissertation	9
1.6 References	10
CHAPTER 2: SHEAR BEHAVIOUR IN CONCRETE BEAMS	
REINFORCED WITH FRP BARS	12
1.0 Introduction.....	12
2.0 Shear in RC beams	13

2.1 Shear in reinforced concrete beams without transverse reinforcement	13
2.1.1 Shear resistance mechanism.....	13
2.1.1.1 Shear resistance of uncracked concrete, V_{cz}	14
2.1.1.2 Interface shear transfer, V_a	15
2.1.1.3 Dowel action of longitudinal reinforcement, V_d	15
2.1.1.4 Arching action	15
2.1.1.5 Residual tensile stress across the inclined cracks, f_t	16
2.1.2 Modes of failure	16
2.1.3 Factors affecting the shear strength of concrete	18
2.2 Shear design equation in the codes and guideline's for FRP reinforced concrete members	18
2.2.1 American Concrete Institute (ACI)	19
2.2.2 Japan Society of Civil Engineers (JSCE).....	19
2.2.3 Canadian Standard Association (CSA)	20
2.2.4 ISIS M03-07 Design Manual	21
3.0 Experimental program.....	22
3.1 Introduction	22
3.2 Detail of test specimens	23
3.3 Materials.....	27
3.3.1 Concrete	27
3.3.2 Reinforcements	29
3.4 Fabrication and curing practices	33
3.4.1 Formwork and reinforcement layout	33
3.4.2 Casting and curing beam.....	33
3.5 Test Procedure.....	34
4.0 Experimental results and analysis	35

4.1 Introduction	35
4.2 General behaviour	36
4.2.1 Crack patterns	36
4.2.2 Cracking loads	42
4.2.3 Load deflection behaviour	43
4.2.4 Failure modes	44
4.3 Analysis of test data	50
4.3.1 Shear strength	50
4.3.2 Effect of main variables	51
4.3.2.1 Effect shear span-to-depth ratio, a/d	51
4.3.2.2 Effect of reinforcement ratio, ρ	51
4.3.2.3 Effect of Concrete Compressive Strength, f'_c	52
4.4 Comparison of experimental results with major design equations	54
4.4.1 Introduction	54
4.4.2 Comparison of the results	54
5.0 Conclusions	59
5.0 Recommendation.....	60
6.0 References	61

**CHAPTER 3: DEBONDING PHENOMENON, OF FRP COMPOSITES
APPLIED TO A CONCRETE SURFACE, A STATE-OF-THE
ART..... 64**

1.0 Introduction	64
2.0 Failure modes in FRP-concrete bond system	65
3.0 Test setups and methods	67
4.0 Bond stress-slip relationship	72
5.0 Current bond-slip models	73

5.1 Empirical models	75
5.1.1 De Lorenzis et al. (2001)	76
5.1.2 Chen and Teng (2001)	76
5.1.3 Dai et al. (2005)	77
5.2 Fracture mechanics based models	77
5.2.1 Täljsten (1996)	79
5.2.2 Neubauer and Rostásy (1999)	80
5.2.3 Brosens and Van Gemert (1999)	82
5.2.4 Brosens (2001).....	84
5.2.5 Nakabaet. al. (2001)	86
5.2.6 Savioa et al. (2003).....	88
5.2.7 Monti et al. (2003)	88
5.2.8 Dai and Ueda (2003)	89
5.3 Finite Element Models	90
5.4 Conclusions of bond–slip models	92
6.0 Previous research (experimental test programs and variability)	95
7.0 Parametric study of the bond strength	106
7.1 Concrete strength	106
7.2 Concrete surface preparation	106
7.3 Adhesive properties	107
7.4 Stiffness of FRP sheets	108
7.5 Effective bond length	108
7.6 Interfacial Fracture Energy	109
8.0 Conclusions based on previous research.....	110
9.0 References	111

CHAPTER 4: THE UNSOLVED ISSUES IN THE DESIGN PROCESS OF FRP STRENGTHENED RC MEMBERS.....	121
1.0 Introduction	121
2.0 Experimental investigation.....	121
2.1 Experimental details and test setup.....	121
2.2 Direct shear test results	123
3.0 Cohesive Material Law (CML).....	124
3.1 CML based on load responses	124
3.1.1 D’Ambrisi et al. (2012)	124
3.1.2 Dai et al. (2005)	125
3.2 Calibration method and construction of the analytical of the strain capacity (SC) response $\epsilon_{\max}(\ell)$	126
3.3 Construction of the analytical responses.....	126
3.4 Direct calibration of CML best on strain profile.....	130
3.4.1 Dai et al. (2006) function	133
3.4.2 Sine function.....	133
3.4.3 Polynomial function	135
3.4.4 Bilinear function	137
5.0 Beams	139
6.0 Results and discussion	140
6.1 Calibrated CML functions for load responses	140
6.2 Comparison	141
7.0 Conclusions	144
8.0 References	144

CHAPTER 5: BOND BEHAVIOR OF STEEL-FIBER (SRP) COMPOSITES APPLIED ONTO A CONCRETE SUBSTRATE	146
1.0 Introduction	146
2.0 Literature review	147
3.0 Experimental Program	151
3.1 Materials	151
3.1.1 Concrete	151
3.1.2 SRP Fiber	153
3.1.3 Adhesive	155
3.2 Test set-up's and Methods	155
3.2.1 Single-lap shear test set-up (Method I).....	156
3.2.2 TPB test set-up (Method II).....	159
4.0 Results	160
4.1 Failure modes	164
4.2 Strain analysis in direct-shear tests	166
4.3 Interfacial cohesive material law	169
5.0 Discussion	173
5.1 Fracture mechanics parameters	173
5.2 FRP-SFRP analogy	175
5.3 Influence of the bond set-up.....	176
6.0 Conclusions	176
7.0 References	177
CHAPTER 6: A STUDY OF THE COMPRESSIVE BEHAVIOR OF CONCRETE COLUMNS CONFINED WITH STEEL-FRP JACKETS USING DIGITAL IMAGE ANALYSIS	181
6.0 Introduction	181

6.1 Background	182
6.2 Experimental program.....	184
6.2.1 Materials	184
6.2.2 Methods.....	188
6.3 Results	192
6.3.1 Failure mode, Compressive strength, and Ultimate strain	192
6.3.2 Axial stress – Axial strain response	196
6.3.3 Steel-FRP jacket strains	199
6.4 Discussion	203
6.4.1 Influence of test variables	203
6.4.2 Ductility	205
6.4.3 Fracture Surface of Cross-Section	206
6.5 Conclusions	209
6.6 References	210

LIST OF TABLES

CHAPTER 1	1
1.1 Mechanical properties for steel fibers (Kerakoll 2016)	6
CHAPTER 2	12
2.1 Modes of failure due to shear	17
2.2 Detail of beam and test variables	25
2.3 Concrete mix design computation.....	28
2.4 Result of cube test	29
2.5 Geometrical characteristics of the GFRP test samples	31
2.6 Mechanical properties for GFRP bar	32
2.7 Mechanical properties for Mild Steel bar.....	32
2.8 Experimental results.....	44
2.9 Axial stiffness of the reinforcing bars in different beams.....	45
2.10 Comparison of the experimental results with different design methods.....	56
CHAPTER 3	64
3.1 Factors affecting the bond behaviour	64
3.2 Bond stress-slip relationship	93
CHAPTER 4	121
4.1 Details about the specimen geometry and the test configuration considered for the calibration of the CML's (Subramaniam et al. 2007)	122
4.2 Main parameters characterizing the CMLs	143

CHAPTER 5	146
5.1 Material properties of SRP (Matana et. al, 2005)	148
5.2 Test results (SRP, 1-23 cords/in density) (Matana et. al, 2005)	148
5.3 Specimen data and key results from bond tests Mitolidis et al. (2008)	151
5.4 Properties of steel fibers provided by manufacturer (Kerakoll 2016).....	154
5.5 Mechanical properties of matrix by provided by manufacturer (Kerakoll 2016).....	155
5.6 Test specimen characteristics (Direct-shear single lap test set-up).....	158
5.7 Test Specimen Characteristics (TPB test set-up).....	160
5.8 Test results (Direct-shear single lap test set-up)	162
5.9 Test results (TPB test set-up)	163
5.10 Fracture mechanics parameters	171
5.10 (cont.) Fracture mechanics parameters	172
 CHAPTER 6	 181
6.1 Properties of steel fibers provided by manufacturer (Kerakoll S.p.A.)	187
6.2 Mechanical properties of matrix by provided by manufacturer (Kerakoll S.p.A.)	187
6.3 Test specimen characteristics	191
6.4 Summary of test results.....	195

TABLE OF FIGURES

CHAPTER 1	1
1.1 Comparison among fiber, resin and composite tensile properties	3
1.2 (a) FRP rebars and (b) FRP sheets/laminates.....	4
1.3 Steel fiber sheets	6
1.4 Stress-strain characteristics of steel, FRP, SRP materials	7
CHAPTER 2	12
2.1 Internal forces in a cracked beam without stirrups	14
2.2 Arch action in a beam (MacGregor and Bartlett 2000)	16
2.3 Summary of test parameters.....	23
2.4 The nomenclature of test specimen.....	24
2.5 Specimen geometry.....	26
2.6 Relationship between the specimens.....	27
2.7 Concrete cube tests.....	28
2.8 Different types of reinforcement used in this study.....	29
2.9 The experimental setup for GFRP bar testing.....	30
2.10 Typical GFRP bar tensile test specimen with end anchors	31
2.11 Stress-strain relationship of GFRP bar	32
2.12 Typical formwork and reinforcement layout	33
2.13 Curing process and removing the beams from the formworks	34
2.14 Schematic diagram of the test setup for the beam.....	35
2.15 Test setup and cracks mapping	35
2.16 Typical formation of cracks in a beam during a test.....	37
2.17 Crack patterns for beams with different shear span-to-depth ratios	38

2.18 Crack patterns for normal strength concrete beams with different depths.....	39
2.19 Crack patterns for beams with height equal to 150 mm	40
2.20 Crack patterns for beams with different concrete strengths and reinforcement ratio ($\rho_f = 0.52\%$)	41
2.21 Crack patterns for beams with different concrete strengths and reinforcement ratio ($\rho_f = 0.93\%$)	42
2.22 Typical load versus deflection curves (Beam BGG-A2-01)	45
2.23 Load-deflection behaviour of 150 mm thick beams in Group A1	46
2.24 Load-deflection profile of beams in Group A2: (a) $a/d = 2.5$, and (b) $a/d = 3.0$	47
2.25 Load-deflection behaviour of 250 mm thick beams with different concrete strengths and same reinforcement types and ratios in Group 4: (a) $\rho_f = 0.52\%$ (b) $\rho_f = 0.93\%$	47
2.25 (cont.) Load-deflection behaviour of 250 mm thick beams with different concrete strengths and same reinforcement types and ratios in Group 4: (c) $\rho_s = 0.52\%$ and (d) $\rho_s = 0.93\%$	48
2.26 Bond/anchorage failure of beam BGN-A2-02	49
2.27 Failure pattern of beam BGN-A1-01	49
2.28 Failure pattern of beam BGL-A3-02.....	49
2.29 Effect a/d of experimental shear strength of beams in Group A2.....	51
2.30 Effect of reinforcement ratio for 350 mm thick beams: (a) experimental shear strength, (b) normalized shear strength	52
2.31 Variation of normalized shear strength with respect to the cubic root of the axial stiffness	52
2.32 Effect of concrete compressive strength, experimental shear strength for 250 mm beams height with reinforcement ratios; (a) $\rho = 52\%$ and (b) $\rho = 93\%$	53
2.33 Normalized shear strength for 250 mm beams height with reinforcement ratios; (a) $\rho = 52\%$ and (b) $\rho = 93\%$	53

2.34 Comparison of the experimental results with ISIS M03-07 predictions.....	57
2.35 Comparison of the experimental results with ACI 440.1R-06 predictions.....	57
2.36 Comparison of the experimental results with CSA S806-02 predictions	58
2.37 Comparison of the experimental results with JSCE (1997) predictions	58
CHAPTER 3	64
3.1 Possible debonding locations	67
3.2 Illustrates the possible failure modes for strengthened flexural RC member	67
3.3 Double shear test (a) plan, (b) double shear push test, and (c) double shear pull test	69
3.4 Single shear test (a) plan, (b) Single shear push test, and (c) Single shear pull test	70
3.5 Beam Test.....	71
3.6 Bond stress-slip relationship	72
3.6 (cont.) Bond stress-slip relationship.....	73
3.7 Local bond-slip curves reported in literature (a) Mazzotti et al. (2008) and (b) Liu and Wu (2012)	75
3.8 Bond-slip models for plate to concrete bonded joints, Yuan and Wu (1999).....	79
3.9 Bond displacement curve of an adhesive joint based on nonlinear fracture mechanics, Täljsten (1996).....	80
3.10 Idealized local bond law of Holzenkämpfer (1994)	81
3.11 Representative schematics of configurations of different layers used for the computation of bond slip (Brosens and Van Gemert 1999)	82
3.12 Representative schematics of configurations of different layers used for the computation of bond slip (Brosens 2001).....	84
3.13 Mohr-coulomb failure criterion (Brosens 2001).....	84
3.14 (a) Bi-linear Stress-Slip Relationship between Concrete and FRP and (b) Popvic's Expression Based Stress-Slip Relationship Concrete and FRP.....	87

3.15 Bond-slip curve for FRP-concrete interface obtained from CFJT-Plate experimental data	88
3.16 Bond slip models suggested by Lu et al. (2005)	90
3.17 Bond-slip curves from existing bond-slip models (Lu et al. 2005).....	91
3.18 Single-lap shear bond test setup (Chajes et al. 1996).....	96
3.19 Sketch of the test equipment used in the tensile test series (Täljsten et al. 1997).....	97
3.20 Shear test specimen (Brosens and Van Gemert 1997).....	98
3.21 (a) Specimens, (b) Arrangement of strain gages (Maeda et al. 1997).....	98
3.22 Schematic of strain distribution in CFS	99
3.23 Finite element mesh	99
3.24 (a) Specimen configuration, (b) Test Rig, Side and front view (Bizindavyi and Neale 1999)	100
3.25 Test specimen. (Note: 1 in. = 25.4 mm.) (De Lorenzis et al. 2001)	101
3.26 (a) Test specimen, (b) Data acquisition sketch (Nakaba et al. 2001)	102
3.27 Shear-slip model for bonded concrete joints, Chen and Teng (2001).....	103
3.28 Single and double shear tests: (a) Single shear test; (b) Double shear test and (c) Plan	103
3.29 Pullout test setup (Dai et al. 2005).....	104
3.30 Test specimen (Yao et al. 2005).....	105
3.31 Effects of the concrete Strength on interfacial fracture energy of the bond (Dai et al. 2005)	106
3.32 Effects of the adhesive properties on interfacial fracture energy of the bond (Dai et al. 2005)	107
3.33 Effects of FRP stiffness on interfacial fracture energy of the bond (Dai et al. 2005)	108

CHAPTER 4	121
4.1 Specimen dimensions and loading arrangement (Subramaniam et al. 2007)	122
4.2 Typical load versus global slip response of the FRP bonded to concrete for test W_4 in Subramaniam et al. (2007).....	123
4.3 Typical CML (D' Ambrisi et al. 2012)	125
4.4 Typical CML (Dai et al. 2005).....	125
4.5 (a) Typical CML for an FRCM composite. (b) Strain profiles consequent to the typical CML. (c) Load response corresponding to the typical CML. (d) Joint and slip capacity responses corresponding to the typical CML.....	127
4.6 Typical CML (Bilinear function).....	139
4.7 Interfacial crack in beam.....	139
4.8 The best fitting curve of the load responses of specimen W_4.....	140
4.9 Bond stress-slip relationship between CFRP and concrete substrate: (a) all tested specimens Eq.(2) and (b) all tested specimens Eq.(3).....	141
4.10 Cohesive material law τ -s for specimen W_4 obtained using six different functions to fit experimental data.	141
4.11 S-shape ϵ_{yy} profile for specimen W_4 using four different functions to fit experimental data	142
 CHAPTER 5	 146
5.1 Direct shear test setup (Matana et. al, 2005).....	148
5.2 a) Scheme of shear test; b) photograph of test set sample (Figeys et al. 2005) ..	149
5.3 The SRP used in the experiments (Figeys et al. 2005)	149
5.4 Experimental set-up and configurations of representative specimens (Mitolidis et al. 2008)	150
5.5 Strength development of cubic and cylindrical specimens over time.....	152
5.6 a) and b) Experimental set-up for fracture mechanics tests for 150 mm width specimens.....	153

5.7 a) P/b – δ response for 70 mm width specimens. b) P/b – δ response for 150 mm width specimens.....	153
5.8 SRP Fiber (Kerakoll S.p.A.)	154
5.9 The SRP used in this work (Kerakoll S.p.A.)	154
5.10 The epoxy resin used in this work (Kerakoll S.p.A.).....	155
5.11 Direct-shear single lap test set-up	158
5.12 TPB test set-up	159
5.13 a) Typical load-global slip response for SFRP. b) Load response for specimen DS_300_50_MD_ND_B_2. c) Load response for specimen DS_300_50_HD_D_S_5. d) Load response for specimen DS_300_50_HD_ND_B_1. e) Load response for specimen DS_300_50_UHD_ND_S_3. f) Load response for specimen DS_300_50_UHD_D_B_5.	161
5.14 Failure mode for specimen DS_300_50_UHD_D_B_3.	162
5.15 a) Load response for MD notched specimens tested in TPB. b) Load response for HD notched specimens tested in TPB.	163
5.16 a) Failure mode for specimen TPB_400_50_MD_B_1. b) Failure mode for specimen TPB_400_50_HD_B_1.....	164
5.17 a) SFRP strip after debonding for specimen DS_300_50_MD_ND_B_3. b) SFRP strip after debonding for specimen DS_300_50_UHD_ND_S_2.	165
5.18 Failure mode for specimen TPB_400_50_MD_B_3	166
5.19 a) Load response for specimen DS_300_50_UHD_D_B_5. b) S-shape ϵ_{yy} profile for specimen DS_300_50_UHD_D_B_5.....	168
5.20 S-shape ϵ_{yy} profile for specimen DS_300_50_UHD_D_B_5 using three different functions to fit experimental data.....	169
5.21 Cohesive material law τ -s for specimen DS_300_50_UHD_D_B_5 obtained using three different functions to fit experimental data.	170
5.22 Typical variation of strain as a function of x, for different locations along the bond length for specimen DS_300_50_UHD_D_B_5.....	173

CHAPTER 6	181
6.1 Concrete strength gain: (a) compressive strength; (b) tensile strength	184
6.2 Experimental set-up for fracture mechanics tests for 150 mm width prisms: (photograph)	185
6.2 (cont.) Experimental set-up for fracture mechanics tests for 150 mm width prisms (Sketch)	186
6.3 150 mm width prisms: (a) P/b – CMOD response; (b) P/b – δ response	186
6.4 70 mm width prisms: (a) P/b – CMOD response; (b) P/b – δ response	186
6.5 Specimen preparation: (a) application of matrix to concrete surface; (b) application of steel fiber sheet around the prism; (c) application of external layer of matrix; (d) finished specimen	189
6.6 (a) Photo of specimen; (b) test setup	190
6.7 Failure mode of steel-FRP confined specimen (specimen SQ-450-HD-CE-UT- S-1L-1 shown): (a) front face; (b) right face; (c) back face; (d) left face; (e) cut section	192
6.8 Axial stress - axial strain response determined by each LVDT for representative specimens: (a) SQ-450-MD-CE-T-S-1L-2; (b) SQ-450-HD-CE-UT-S-1L-3	196
6.9 Axial stress – axial strain response for specimens in: a) Groups 1 and 2; b) Groups 1 and 3; c) Groups 3 and 4; d) Groups 4 and 5; e) Groups 5 and 6; f) Groups 5 and 7	198
6.10 Comparison of axial stress – axial strain response determined by LVDTs and DIC (specimen SQ-450-HD-CE-T-R-1L-1)	200
6.11 Representation of the eight squares used to calculate the values of the strain using DIC technique: (a) axial strain; (b) hoop strain	200
6.12 Axial stress – strain response determined by DIC for confined specimens: (a) Group 1; (b) Group 2; (c) Group 3; (d) Group 4; (e) Group 5; (f) Group 6; (g) Group 7.	202
6.13 Average A_{total}/A_{peak} for each group	206

6.14 Photos of cut cross-sections after failure: (a) SQ-450-HD-CE-UT-S-1L-1; (b) SQ-450-HD-CE-UT-R-1L-3.....	207
6.15 Variation of the ratio: a) $\overline{f'_{cc}} / \overline{f'_{co}}$; and b) $\overline{f'_{cc}} / \overline{f'_{cc,S}}$ with respect to corner radius ratio $2r/b$	208

TABLE OF APPENDICES

APPENDIX	TITLE.....	PAGE
I	Photographs of the failure mode of all beams	213
II	Photographs of the experimental program of debonding investigation in chapter 5	216

CHAPTER 1

INTRODUCTION

1.0 Background of Study

Corrosion of the reinforcement is the main reason for deterioration of reinforced concrete (RC) structures with conventional steel. Corrosion is generally associated with the reduction of the effective area of the reinforcement causing a decrease of the strength and stiffness of the reinforcement and, consequently, of the RC element. In order to restore existing buildings that suffer deterioration problems, in the last few decades new strengthening materials, known as fiber reinforced polymer (FRP) composites, gained a wide diffusion all over the world. FRP composite materials are employed in all those applications related to strengthening and rehabilitation of existing concrete structures. FRPs have several advantages if compared to traditional strengthening materials that can be summarized as follow: high strength to weight ratio, corrosion resistance, ease of handling and installation, and design and construction flexibility. The application of FRP materials in civil engineering is worldwide recognized. Various organizations in countries such as United States, Canada, Great Britain, Japan, and Italy released design guidelines, recommendations, and standards related to FRP composites.

FRP composites consist of high strength fibers embedded in an organic matrix. Different types of fibers are available, such as carbon (CFRP), aramid (AFRP), glass (GFRP), and steel (SRP). Fibers are commercially available in the form of plates/sheets or bundles (used as external reinforcement) and bars (used as internal reinforcement).

The use FRP plates/sheets externally bonded to existing concrete elements has steadily emerged, over last three decades, as an efficient technique for structural rehabilitation, repair and strengthening of deteriorated and deficient concrete

components and systems, as highlighted from Karbhari et al. (2006), and Meier (1995). FRP composites have successfully been used for strengthening of reinforced concrete (RC) structures as pointed out from Teng et al. (2002).

The use of internally FRP reinforcement bars as an alternative to steel reinforcement bars in concrete structures has been accepted in construction industry mainly due to their excellent electrochemical corrosion resistance and high mechanical performances. FRP reinforcement bars can be used as longitudinal and shear reinforcement. However, some properties of FRP reinforcement, such as its brittleness, could have adverse effects on its performance as reinforcement for concrete members. Since GFRP is more economical balance of cost and strength properties than other available FRP (CFRP and AFRP), it is more attractive for infrastructure application and has been used as reinforcement in concrete beams, bridges and slabs for more than twenty years (Benmokrane et al. 2006). GFRP has more resistance to corrosion and higher tensile resistance compared to steel (Newhook et al. 2002). Therefore, the present study discusses mainly in chapter 2 on the behaviour of beams reinforced internally with GFRP reinforcement bars.

A steel reinforced polymer (SRP) system was also tested as part of this research in chapter 4 and 5. SRPs are made with high-strength twisted steel wires embedded in an epoxy matrix. SRPs have several benefits over traditional FRP materials including lower cost, better fire resistance, and compatibility with anchorage systems.

Since GFRP and SRP are newly developed strengthening materials, a better understanding of the mechanical behaviour of these composite systems is needed. The current research is mainly focused on the following aspects: the use of GFRP bars as internal reinforcement for simply supported concrete beams as reported in Chapter 2 and the use of SRP system externally for debonding and confinement investigation as reported in chapter 5 and 6.

1.1 Fibre Reinforced Polymer (FRP)

Fiber reinforced polymers (FRP) are a particular typology of composite materials, made of high resistance fibers impregnated with polymeric resins. The mixing result is a material with properties between fiber and resin Figure 1.1.

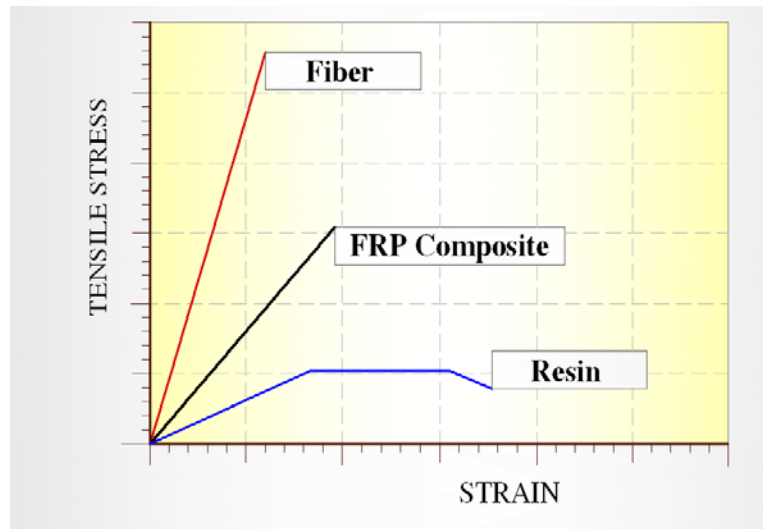


Figure 1.1: Comparison among fiber, resin and composite tensile properties

FRP materials are characterized by excellent tensile strength in the direction of the fibers and by negligible strength in the direction transverse to the fibers; this illustrates the anisotropic nature of these materials. FRP composites do not exhibit yielding, but instead are elastic up to failure and they are also characterized by relatively low modulus of elasticity in tension and low compressive properties.

Their function usually consists in adsorbing tensile stress due to shear and flexural actions. Often, among the several advantages, it can be listed also the increase of the overall stiffness and ductility.

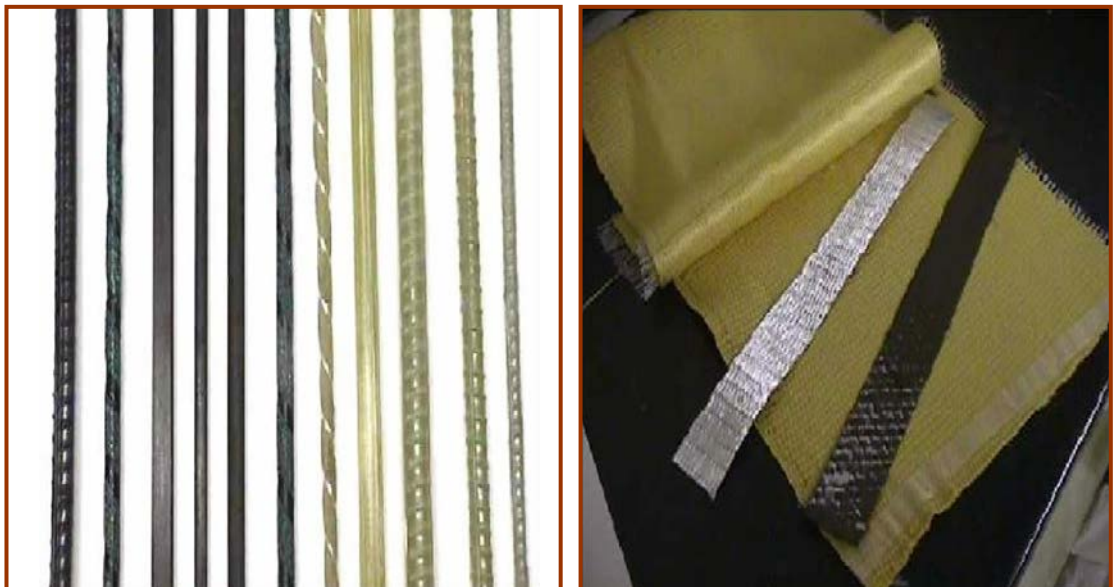
FRP properties make these materials particularly suitable for structural applications, especially in support or substitution of steel. The general advantages of FRP reinforcement compared to steel are:

- Durability in aggressive environments
- High strength-to-density ratio
- Magnetic and electric neutrality
- Low specific weight
- Low axial coefficient of thermal expansion

Without underlining the importance of a lower installation cost, the use of FRP composites possesses some advantages compared to traditional retrofitting methods; as an example, the disturbance of both occupants and facilities are minimal and there is no loss of valuable space. In addition, from the structural point of view, the dynamic properties of the structure remain unchanged because there is no addition of weight that would lead to increase the seismic forces.

FRP products are commercialized in different shapes: rods, tendons, laminates and three-dimensional components.

FRP reinforcement comes in the shape of rods of circular cross-sections, strips of rectangular cross-sections, strands, and laminates, which enable different types of applications, as shown in Figure 1.2.



(a) (b)
Figure 1.2: (a) FRP rebars and (b) FRP sheets/laminates

Generally, FRP can be classified into three types which are Glass Fiber Reinforced Polymer (GFRP), Carbon Fiber Reinforced Polymer (CFRP) and Aramid Fiber Reinforced Polymer (AFRP).

1.1.1 Carbon Fiber Reinforced Polymer (CFRP)

CFRP is a composite material which consists of carbon fibre and resins. CFRP is more expensive composite material, compared to GFRP and AFRP, but have some advantages, such as high strength, stiffness and most durable.

Although CFRP have many advantages compared to steel, such as lighter in weight and corrosion resistant materials, but cost of CFRP still remain as the issue of replace steel as reinforcement materials. Beside this, the brittle behaviour of CFRP is also one of the problem that been concerned.

1.1.2 Aramid Fiber Reinforced Polymer (AFRP)

AFRP is highly oriented organic fiber derived from polyamide incorporating into aromatic ring structure.

AFRP offers excellent impact resistance, good electric and temperature insulating properties and they are also resistant to organic solvents, fuels and lubricants. AFRP have a medium modulus and a very low density as compared to GFRP and CFRP. It is available in tows, yarns and various woven cloth products.

1.1.3 Glass Fiber Reinforced Polymer (GFRP)

Fiber drawn from an inorganic product of fusion that has cooled without crystallizing. GFRP produces a common, low cost reinforcing fiber, but they weight more than CFRP or AFRP and the lower modulus requires special design treatment where stiffness is critical. Glass has been the predominant fiber for many civil engineering applications because of an economical balance of cost and specific strength properties.

The two types of glass fibres most commonly used are E-glass and S-glass. E-glass has the lowest cost of all commercially available reinforcing fibres, and is used for general purposes where strength, electrical resistance, acid resistance, and low cost are important. S-glass has higher strength, stiffness and ultimate strain than E-glass, but is more expensive, and more susceptible to degradation in alkaline environments than E-glass (Benmokrane et.al, 1995).

1.2 Steel Fibers

High strength steel fibers have recently been introduced as an alternative to FRPs such as carbon fiber reinforced polymer (CFRP) (Prota et al., 2006).

It made of high strength twisted steel wires impregnated with epoxy resin, in the case of steel reinforced polymer (SRP), or with cementitious, in the case of steel reinforced grout (SRG) systems.

The advantages of using these materials over FRPs, among them, the material cost is relatively, and SRP have some inherent ductility (Casadei et al., 2005). However, the application method for FRPs and SRP/SRG composite sheets for strengthening concrete/masonry structures are same.



Figure 1.3: Steel fiber sheets

Table 1.1. Mechanical properties for steel fibers (Kerakoll 2016).

Density of steel fibers	weight [g/m ²]	n ^o cords/mm	Break Deformation [%]	Tensile Strength [MPa]	Modulus [GPa]	Equivalt thickness t* [mm]
Medium density (MD)	1200	0.314	> 2	> 3000	> 190	0.168
High density (HD)	2000	0.472	> 2	> 3000	> 190	0.254
Ultra-High Density (UHD)	3300	0.709	> 2	> 3000	> 190	0.381

The stress versus strain behavior of some typical FRP and SRP materials are presented in Figure 1.4. Also shown in the figure are the traditional building materials used in tension: mild steel reinforcing and high strength steel used in prestressing strands.

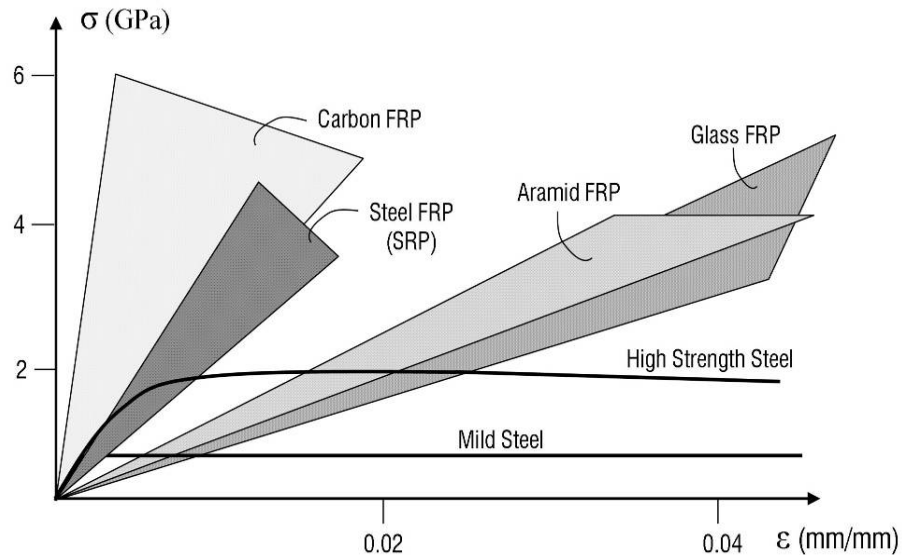


Figure 1.4 Stress-strain characteristics of steel, FRP, SRP materials

1.3 Objectives of dissertation

The objective of this research program is to investigate a number of issues related to glass fiber reinforced polymer (GFRP) bars, and steel reinforced polymer (SRP) composite strips.

1. To investigate the shear strength of concrete beams reinforced with glass fiber reinforced polymer GFRP bars.
2. To investigate the debonding mechanism between steel reinforced polymer (SRP) composites strips and the concrete surface, using two different set-up; concrete specimens were tested using the single-lap shear test set-up and specimens were tested using a three-point bending set-up, and compare the results obtained based on two different test set-ups.
3. To investigate the behavior of short concrete prisms with a square cross-section confined by steel reinforced polymer (SRP) composite strips.

1.4 Scope of dissertation

A total of 96 concrete (beams, prisms) were tested in the course of this research;

14 as part of a shear strength of concrete beam reinforced with GFRP bar Study, 7 as part of the Debonding Phenomenon Study, 19 as part of the Bond Study, 31 as part of the Fracture Mechanics Study and 25 as part of the Confinement Study.

The Shear Strength Study, whose experimental program is described in Chapter 2 of this dissertation, examined the shear behavior of simply supported concrete beams reinforced with longitudinally GFRP bars. The variables examined in the experimental program included the GFRP longitudinal reinforcement ratio and the concrete strength.

The Bond Study, A state-of-the art was compiled and an indirect calibration of the Mode-II cohesive law for CFRP sheets bonded to concrete surface, described in Chapter 3 of this dissertation.

The Bond Study, deals with the debonding phenomenon, a better understanding of FRP-concrete bond behavior assessing some of the common cohesive material law (CML) relationship on the basis of the results of an experimental program conducted by Subramaniam et al. (2007), described in Chapter 4.

The Bond Study (SRP) using the single-lap shear test set-up, whose experimental program is described in Chapter 5 of this dissertation, the bond behaviour of SRP composite strips externally bonded to a concrete substrate was investigated, 99 specimens were tested. The variables examined included the bonded length, bonded widths, loading rate and density of SRP composite.

The Bond Study (SRP) using the three-point bending set-up, whose experimental program is described in Chapter 5 as well, of this dissertation, 6 specimens were tested to analyze the debonding mechanism between SRP composite strips and the concrete surface. The variable examined was density of SRP composite.

The Confinement Study, whose experimental program is described in Chapter 6, examined the effectiveness of concrete compressive members confined by SRP composites in terms of load-bearing capacity and ultimate strain with respect to unconfined prisms. The variables examined included the density of steel fibers, concrete corner condition, concrete surface treatment, FRP jacket height, and number

of confinement layers. Digital image correlation (DIC) is used to qualitatively and quantitatively study the displacement and strain fields on the composite surface.

The Fracture Mechanics Study, using the three-point bending set-up, whose experimental program is described in Chapter 5 also of this dissertation, 31 specimens with different sizes cast from the same concrete used for confined specimens were tested to evaluate the fracture energy of concrete. All concrete prisms had a central notch with a V-shaped tip.

1.5 Outline of dissertation

This dissertation is divided into six chapters. The following is a brief description of each chapter's content:

Chapter One of the dissertation, presented an introduction, including an overview on FRP and SRP composites, the main characteristics and various applications of both composite. The objectives, scope and outline of the research project are also included in this chapter.

Chapter Two of the dissertation, deals with the experimental campaign to study the shear strength of GFRP longitudinally reinforced concrete beams without shear reinforcement. All beams were simply supported and subjected to two point loads and known as four point bending test. It was analyzed the behavior of beams, such as failure load, failure mode, cracking load, crack patterns, deflections. Moreover, experimental results are compared using the different analytical equations provided by the available design codes for FRP reinforcement.

Chapter Three of the dissertation, deals with the debonding phenomenon, of fiber reinforced polymer (FRP) composites applied to a concrete surface. A state-of-the art was compiled and a indirect calibration of the Mode-II cohesive law was attempted.

Chapter Four of the dissertation, deals with the debonding phenomenon, a better understanding of FRP-concrete bond behavior assessing some of the common CML or bond-slip (τ -s) relationship on the basis of the results of an experimental program conducted by Subramaniam et al. (2007).

Chapter Five of the dissertation, divided into two parts, and both part related to the debonding studies but with different methods. The first part, deals with an experimental

study using single-lap shear test set-up. The second part comprises, deals with an experimental study using three-point bending set-up and the test specimens had a central notch. Both methods performed to analyze the debonding mechanism of SRP composite strips applied onto a concrete substrate. For each test campaign describes the test set-up, test details and materials used. Furthermore, the results were reported and then compared.

Chapter Six of the dissertation, presents an experimental study was carried out to understand the behavior of short concrete prisms with a square cross-section confined by SRP composite sheets embedded in an epoxy matrix subjected to a monotonic concentric compressive load. In addition, concrete prisms casted from the same concrete used for confined specimens were tested using a three point bending set-up to evaluate the fracture energy of concrete. All concrete prisms had a central notch with a V-shaped tip.

Each chapter consists of background information, literature review, details of the experimental program, design of the specimens test and a conclusion of the results obtained from the experiments and analyses with respect to the issues and observations discussed throughout the thesis, finally, references in each chapter separately.

1.6 References

Benmokrane B., Chaallal O. & Masmoudi R. (1995). "Glass fibre reinforced plastic (GFRP) rebars for concrete structures," *Constr. and Bldg. Mat.*, 9(6), pp 353–364

Benmokrane B, El-Salakawy E, El-Ragaby A, Lackey T. (2006). "Designing and testing of concrete bridge decks reinforced with glass FRP bars. *J Bridge Eng* 2006;11(2):217–29.

Casadei, P., Nanni, A., & Alkhrdaji, T. (2005). "Steel-reinforced polymer: An innovative and promising material for strengthening infrastructures." *Concrete Engineering International*, 9(1), 54-56.

Karbhari, V. M., Niu, H., and Sikorsky, C., (2006). "Review and Comparison of Fracture Mechanics-Based Bond Strength Models For FRP-Strengthened Structures, *Journal of Reinforced Plastics and Composites*, Vol. 25, No. 17, 1757-1738.

Kerakoll S.p.A. - web site: <www.kerakoll.com> (accessed Jan 2016).

Meier u. (1995). "Strengthening of structures using carbon fibre/epoxy composites", *Construction and Building Materials*, Vol. 9, No. 6, pp 341–351.

Newhook J., Ghali, A, and Tadros, G. (2002), "Concrete Flexural Members Reinforced Concrete with Fibre Reinforced Polymer: Design for Cracking and Defonnability," *Canadian Journal of Civil Engineering*, 29, pp. 125-134.

Prota, A., Tan, K. Y., Nanni, A., Pecce, M., & Manfredi, G. (2006). "Performance of shallow reinforced concrete beams with externally bonded steel-reinforced polymer. *ACI structural journal*, 103(2), 163.

Teng, J. G., Chen, J. F., Smith, S. T.and Lam, L. (2002). "FRP Strengthened RC Structures." England: John Wiley& Sons, Ltd.

CHAPTER 2

SHEAR BEHAVIOUR IN CONCRETE BEAMS REINFORCED WITH FRP BARS

1.0 Introduction

The use of fibre reinforced polymer (FRP) bars, as an alternative to steel reinforcement for reinforced concrete structures, is gaining acceptance among the structural engineers. These bars have some favorable properties than conventional steel bars; such as; corrosion resistance, high strength to weight ratio. longer durability and magnetic neutrality.

The behavior of reinforced concrete beams at failure in shear is distinctly different from their behavior in flexure (Nawy, E.D. 2003). A failure due to shear is sudden as compared to a failure due to flexure. This type of failure should be avoided in design of reinforced concrete structures. Due to the fact that FRP bars behave brittle type of rupture and low modulus of elasticity, and the shear strength of beams reinforced with GFRP bars have not been adequately studied (MacGregor, J. and Wright, J. K. 2005). The behavior of reinforced concrete beams reinforced with FRP bars failed in shear will become remarkable topics to investigate. In addition, although some equations for shear design have been provided in the most of the codes but not all of the behaviors of concrete beam reinforced with FRP bars have been covered especially on diagonal shear cracking load (Thamrin, R. et al. 2002).

There has been extensive research on the flexural behavior of FRP reinforced concrete members, and it has been well established that the flexural capacity of concrete members reinforced with FRP bars can be predicted by traditional beam theory (Faza and Gangarao 1993, Nanni 1993, ISIS 2001). In contrast, the shear behaviour of FRP reinforced concrete members is different from that of steel-reinforced concrete members due to their different properties; including the modulus of elasticity, E , surface characteristics, and bond characteristics. Several

studies on the shear capacity of FRP reinforced concrete members without shear reinforcement has indicated that the shear strength is influenced by the stiffness of the tensile reinforcement (Sonobe et al. 1997, Michaluk et al. 1998, Tureyen and Frosch 2002). In addition, the behaviour of FRPs is elastic-brittle with no yielding or ductility at failure and its modulus of elasticity is lower than that of steel. These characteristics make the shear behaviour of FRP reinforced concrete beams more complex. Therefore, it has been recognized that the shear behaviour of FRP reinforced concrete beams should be further investigated independently to reflect these specific material characteristics.

The focus of this research is to investigate the size effect of concrete beams reinforced with GFRP bars on its shear behaviour. A total of eighteen beams reinforced with longitudinal reinforcement. The main variables in this investigation were shear span-to-depth ratio (a/d), longitudinal reinforcement ratio (ρ), concrete compressive strength (f'_c) and reinforcement type.

2.0 Shear in RC beams

2.1 Shear in reinforced concrete beams without transverse reinforcement

The shear strength of reinforced concrete beams without transverse reinforcement has generated a lot of research since the beginning of the last century. However, a clear understanding of shear behaviour of those beams is still limited. This is referred to the complexity of the affecting parameters that govern the shear strength of concrete beams without shear reinforcement. Many structural concrete members are constructed without transverse reinforcement such as slabs, footings, joists, and lightly stressed members.

2.1.1 Shear resistance mechanism

Shear transfer mechanisms in concrete beams are complex and difficult to identify clearly due to the complex stress redistributions that occur after cracking. Shear is transmitted between two planes in various ways in reinforced concrete members.

According to the ACI-ASCE committee 445 (1998) reported that after the formation of diagonal cracks in members without stirrups, shear is carried by concrete as a combination of five structural mechanisms as shown in Figure 2.1:

- (i) Shear resistance of uncracked concrete, V_{cz}
- (ii) Interface shear transfer, V_a
- (iii) Dowel action of longitudinal reinforcement, V_d
- (iv) Arching action
- (v) Residual tensile stress across the inclined cracks, f_t

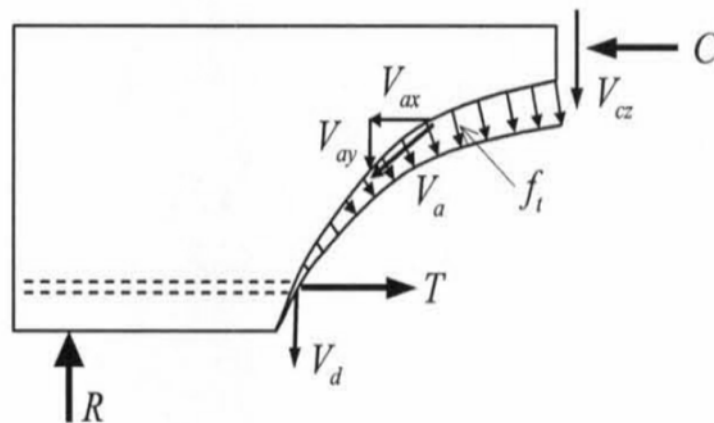


Figure 2.1: Internal forces in a cracked beam without stirrups

2.1.1.1 Shear resistance of uncracked concrete, V_{cz}

This shear transfer mechanism occurs in uncracked members or in the uncracked portions of structural members. In an uncracked concrete member, the shear force is transferred by inclined principal tensile and compressive stresses.

Failure may occur by inclined cracking or crushing of the concrete depending on whether the tensile or compressive stresses reach the corresponding strength of concrete.

The shear force can be calculated by the integration of the shear stresses over the depth of the compression zone. Many researchers quantified the contribution of this shear mechanism is between 20% and 40% of the total shear force (ASCE-ACI 1973).

2.1.1.2 Interface shear transfer, V_a

This shear transfer mechanism is based on the friction along the inclined crack interface, which develops due to the relative slip between the two surfaces of the crack. The crack passes through the aggregate or instead of around the aggregates, depending on the concrete strength and type. In normal strength concrete as the aggregates protruding from the crack surface provide resistance against slip, which is termed as aggregate interlock. In lightweight and high strength concrete, the cracks go through the aggregate rather than around the aggregate, it still has the ability to transfer shear, in this case the shear is transferred by friction or interface shear.

However, the term Friction or Interface Shear is more appropriate than aggregate interlock to describe this mechanism of shear transfer. Tests conducted to quantify the contribution of this mechanism indicated that between 33% and 50% of the total shear force on a beam may be carried by interface shear transfer (ASCE-ACI 1973).

2.1.1.3 Dowel action of longitudinal reinforcement, V_d

If the reinforcing bars cross a crack, shearing displacements along the crack will be resisted, in part, by a dowelling force in the bar. Dowel contribution is strongly dependent on the transverse rigidity and strength of the longitudinal bar.

Normally, dowel action is not very significant in beams without transverse reinforcement, the reason behind that is the maximum shear in a dowel is limited by the tensile strength of the concrete cover supporting the dowel. Dowel action may be significant in beams with large amounts of longitudinal reinforcement. Particularly when the longitudinal reinforcement is distributed in more than one layer (ASCE-ACI 1998). Many studies on dowel action indicated that the dowel shear force to the total shear force by about 15-25% (ASCE-ACI 1973).

2.1.1.4 Arching action

The arching action occurs in deep beams, or beams with shear span-to-depth ratio (a/d) having less than 2.5 (Razaqpur et al. 2004). For such members, a significant redistribution of internal forces can be expected after cracking, and the shear force can be transferred directly to the supports Figure 2.2. For arch action to develop, a horizontal reaction component is required at the base of the arch. In beams this is usually provided by the tie action of the longitudinal bars.

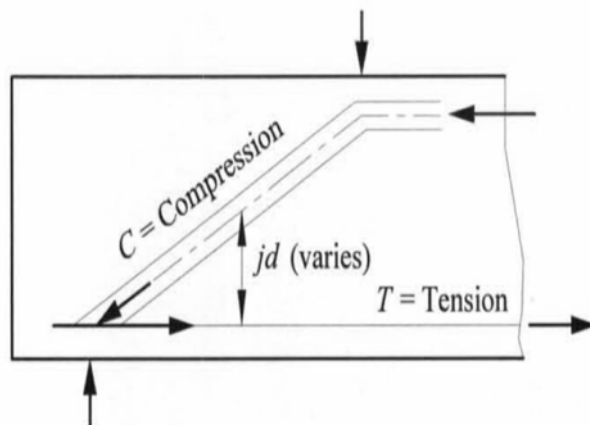


Figure 2.2: Arch action in a beam (MacGregor and Bartlett 2000)

2.1.1.5 Residual tensile stress across the inclined cracks, f_t

When concrete is loaded in direct tension, there is an important descendent (softening) branch has been known when the peak tensile stress is reached for some time Gopalaratnam and Shah (1985). This softening branch is attributed to the residual tensile stress across the crack. Hence, small parts of concrete bridge the crack and continue to transmit a tensile force up to crack widths in the range of 0.05 to 0.15 mm (ASCE-ACI 1998).

Reineck (1991) has found that the shear stresses across inclined cracks can be related to the residual tensile stresses which provide a important portion of the shear resistance of very shallow members with depths less than about 100 mm, where the crack widths are small.

2.1.2 Modes of failure

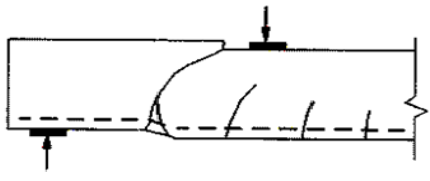
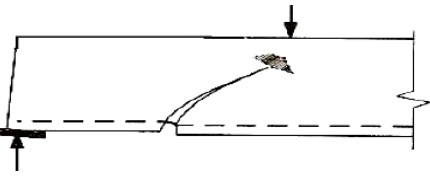
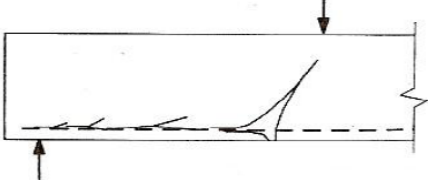
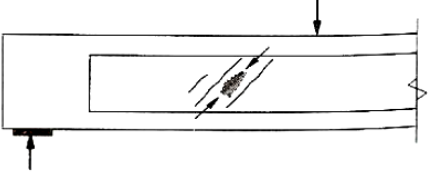
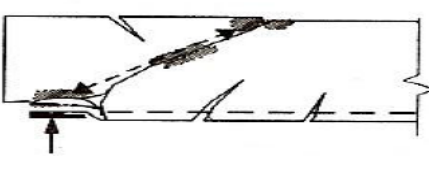
For beams with low span-to-depth ratio or inadequate shear reinforcement, the failure can be due to shear. A failure due to shear is sudden as compared to a failure due to flexure.

The following five modes of failure due to shear are identified.

- 1) Diagonal tension failure
- 2) Shear compression failure
- 3) Shear tension failure
- 4) Web crushing failure
- 5) Arch rib failure

The occurrence of a mode of failure depends on the span-to-depth ratio, loading, cross-section of the beam, amount and anchorage of reinforcement. The following five modes of failure due to shear are identified and presented in Table 2.1.

Table 2.1: Modes of failure due to shear

Type	Failure mode
<p>Diagonal tension failure</p> <p>In this mode, an inclined crack propagates rapidly due to inadequate shear reinforcement.</p>	 <p>The diagram shows a cross-section of a beam under a downward point load. A single, sharp, diagonal crack has formed, extending from the bottom edge towards the top edge. The crack is perpendicular to the principal stress direction. The beam is supported by a pin support on the left and a roller support on the right.</p>
<p>Shear compression failure</p> <p>There is crushing of the concrete near the compression flange above the tip of the inclined crack.</p>	 <p>The diagram shows a cross-section of a beam under a downward point load. An inclined crack is present, and above its upper end, there is a shaded region representing the crushing of concrete. The beam is supported by a pin support on the left and a roller support on the right.</p>
<p>Shear tension failure</p> <p>Due to inadequate anchorage of the longitudinal bars, the diagonal cracks propagate horizontally along the bars.</p>	 <p>The diagram shows a cross-section of a beam under a downward point load. Diagonal cracks are shown propagating horizontally along the length of the longitudinal reinforcement bars. The beam is supported by a pin support on the left and a roller support on the right.</p>
<p>Web crushing failure</p> <p>The concrete in the web crushes due to inadequate web thickness.</p>	 <p>The diagram shows a cross-section of a beam under a downward point load. The central web of the beam is shaded with diagonal lines, indicating crushing of the concrete. The beam is supported by a pin support on the left and a roller support on the right.</p>
<p>Arch rib failure</p> <p>For deep beams, the web may buckle and subsequently crush. There can be anchorage failure or failure of the bearing.</p>	 <p>The diagram shows a cross-section of a beam under a downward point load. The web of the beam is shown buckling and crushing, forming an arch-like shape. The beam is supported by a pin support on the left and a roller support on the right.</p>

2.1.3 Factors affecting the shear strength of concrete

Several analytical and experimental studies have revealed that the concrete contribution to the shear resistance (V_c) of beams without shear reinforcement is affected by some dominant parameters, Among them ASCE-ACI Committee 445 (1998):

1. Shear span-to-depth Ratio, a/d
2. Tensile strength of concrete, f'_c
3. Longitudinal reinforcement ratio, ρ
4. Effective depth, d , (Size of beam)
5. Axial force

However, the significance of each parameter to the shear resistance (V_c) of beams without shear reinforcement is still under debate.

2.2 Shear design equation in the codes and guideline's for FRP reinforced concrete members

Shear design recommendations for FRP-reinforced concrete beams in current design codes adopt a similar approach as conventional steel reinforced concrete design methods. The nominal shear capacity (V_n) of reinforced concrete beams is computed by:

$$V_n = V_c + V_s \quad (2.1)$$

where V_c is the shear strength of concrete beams and V_s is the shear resistance offered by shear reinforcement.

This section summarizes the design equations used to compute V_c as recommended by the American Concrete Institute (ACI) standard ACI 440.1R-06 (ACI 2006); Canadian Standards Association (CSA) standards CSA S806-02 (CSA 2002); the Japan Society of Civil Engineering (JSCE) standard (JSCE 1997) and Intelligent Sensing for Innovative Structures, Canadian Network of Excellence (ISIS 2007).

2.2.1 American Concrete Institute (ACI)

According to American Concrete Institute (ACI) committee 440, the shear design of FRP reinforced concrete is similar to that of steel reinforced concrete as given in ACI 318-08. However, the mechanical properties of FRP affect the shear strength with the main factors being the low FRP modulus of elasticity and low transverse shear strength of FRP. Using a model developed by Tureyen and Frosch (2003), the concrete shear capacity V_c , for flexural members with FRP as main reinforcement can be evaluated as follows:

$$V_c = \frac{2}{5} \sqrt{f'_c} b_w c \quad (2.2)$$

where c is the cracked transformed section neutral axis depth, for singly reinforced, rectangular cross sections is given as:

$$c = k d$$

The computation of the neutral axis depth k dependent on the flexural FRP reinforcement ratio and the ratio of the modulus of elasticity of the FRP reinforcement to the concrete, k is calculated as;

$$k = \sqrt{2\rho_f n + (\rho_f n)^2} - \rho_f n$$

where ρ_f being the flexural FRP reinforcement ratio, and $n = E_f/E_c$, where E_f and E_c are the modulus of elasticity of FRP reinforcement and concrete, respectively; f'_c is the specified compressive strength of concrete; b_w is the web width; and d is the distance from the compression fiber to the centroid of the main tensile reinforcement.

2.2.2 Japan Society of Civil Engineers (JSCE)

The Japan Society of Civil Engineers (JSCE 1997) recommended the following expression for shear strength (V_c) of FRP reinforced concrete members:

$$V_c = \beta_d \beta_p \beta_n f_{vcd} b_w / \gamma_b \quad (2.3)$$

where,

$$\beta_d = (1000/d)^{1/4} \leq 1.5$$

$$\beta_p = (100\rho_f E_f/E_s)^{1/3} \leq 1.5$$

$$\beta_n = 1 + M_o/M_d \leq 2 \quad \text{For } (N'_d \geq 0)$$

$$\beta_n = 1 + 2M_o/M_d \geq 0 \quad \text{For } (N'_d < 0)$$

$$f_{vcd} = 0.2(f'_{cd})^{1/3} \leq 0.72$$

where f'_c represents concrete strength, b_w reflects effective web width, d reflects effective depth, E_f is modulus of elasticity of flexural FRP reinforcement and E_s is modulus of elasticity of steel, γ_b is strength reduction factor, generally equal to 1.3, M_a is decompression moment, M_d is design bending moment, N'_d is design axial compressive force, and β_n equal to 1.0 for sections without axial force resultant. According to this code, the concrete contribution to the shear strength has a limiting value. Similar to the ACI (2006), this method does not include the effect of shear span-to-depth ratio (a/d), and if a section has no longitudinal reinforcement, the equation will give zero shear strength.

2.2.3 Canadian Standard Association (CSA)

According to the Canadian Standard Association (CSA-S806-02) Code. The shear strength of members having either at least the minimum amount of transverse reinforcement as specified by the CSA standard or an effective depth not exceeding 300 mm, the shear strength calculated as:

$$V_c = 0.035\lambda\phi_c \left(f'_c \rho_f E_f \frac{V_f}{M_f} d \right)^{1/3} b_w d \quad (2.4)$$

$$0.1\lambda\phi_c\sqrt{f'_c}b_w d \leq V_c \leq 0.2\lambda\phi_c\sqrt{f'_c}b_w d$$

where λ reflects the concrete density factor, ϕ_c represents the concrete material resistance factor, f'_c represents concrete strength, b_w reflects effective web width and d reflects effective depth. The quantity $(V_f/M_f)d$, is not to be taken as greater than 1.0. $(V_f/M_f)d$, is the value of the factored shear, V_f , divided by the factored

moment, M_f , at the section under consideration and is the inverse of the a/d ratio for a simply supported member. This equation considers the effect of axial stiffness ($E_f\rho_f$), shear span-to-depth ratio (a/d), and concrete compressive strength f'_c for calculating the shear strength.

To account for the size effect for members having an effective depth exceeding 300 mm and with no transverse shear reinforcement or less transverse reinforcement than the minimum given by CSA standard, the value of V_c is calculated using:

$$V_c = \left(\frac{130}{1000 + d} \right) \lambda \phi_c \sqrt{f'_c} b_w d \geq 0.08 \lambda \phi_c \sqrt{f'_c} b_w d \quad (2.5)$$

This equation gives the concrete contribution to the shear strength of FRP reinforced concrete members regardless of the FRP reinforcement ratio or the FRP type, which is anomalous to the findings that the shear strength increases with an increase in the reinforcement ratio. Thus, the equation gives more conservative results for the beams with high axial stiffness ($E_f\rho_f$) of the longitudinal FRP bar (EI-Sayed et al. 2006). In addition, the equation neglects the shear transfer by arch action and it is quite conservative for beams with a/d less than 2.5 (Razaqpur and Isgor 2006).

2.2.4 ISIS M03-07 Design Manual

Intelligent Sensing for Innovative Structures (ISIS) published a series of design manuals that address the production, testing, and use of FRP. Design Manual 03 (ISIS 2007) provides guidance for design of concrete structures internally reinforced with FRP. The shear design method for FRP reinforced members is based on the simplified method of CSA A23.3-94 code.

According to this method. The shear capacity of FRP reinforced concrete members containing no transverse web reinforcement and having an effective depth less than 300 mm is calculated as:

$$V_c = 0.2 \lambda \phi \sqrt{f'_c} b_w d \sqrt{\frac{E_f}{E_s}} \quad (2.6)$$

where λ reflects the concrete density factor, ϕ_c represents the concrete material resistance factor, f'_c represents concrete strength, b_w reflects effective web width, d reflects effective depth, E_f is modulus of elasticity of flexural FRP reinforcement and E_s is modulus of elasticity of steel. For beams which have an effective depth greater than 300 mm, V_c , is taken as:

$$V_c = \left(\frac{260}{1000 + d} \right) \lambda \phi_c \sqrt{f'_c} b_w d \sqrt{\frac{E_f}{E_s}} \quad (2.7)$$

The Equation 2.6 and Equation 2.7, the reduction in V_c , compared to the steel reinforced concrete is based on the ratio of the modulus of elasticity. However, this method does not consider the effect of shear span-to-depth ratio and longitudinal reinforcement ratio, which are believed to affect the shear strength.

3.0 Experimental program

3.1 Introduction

This research program a systematic experimental investigation was carried out to examine the effect of some of the parameters, discussed in Section 2.2.3, on the shear strength of Glass Fiber Reinforced Polymer (GFRP) reinforced concrete beams without transverse reinforcement. Besides, steel reinforced concrete beams are fabricated as the control beam to investigate the effect of the type of reinforcements. A summary of the test parameters investigated is shown in Figure 2 .3.

In this chapter, the details of the test specimens, materials and procedure used in the preparation of specimens, instrumentation of the test specimens, testing procedure and test set-up are discussed.

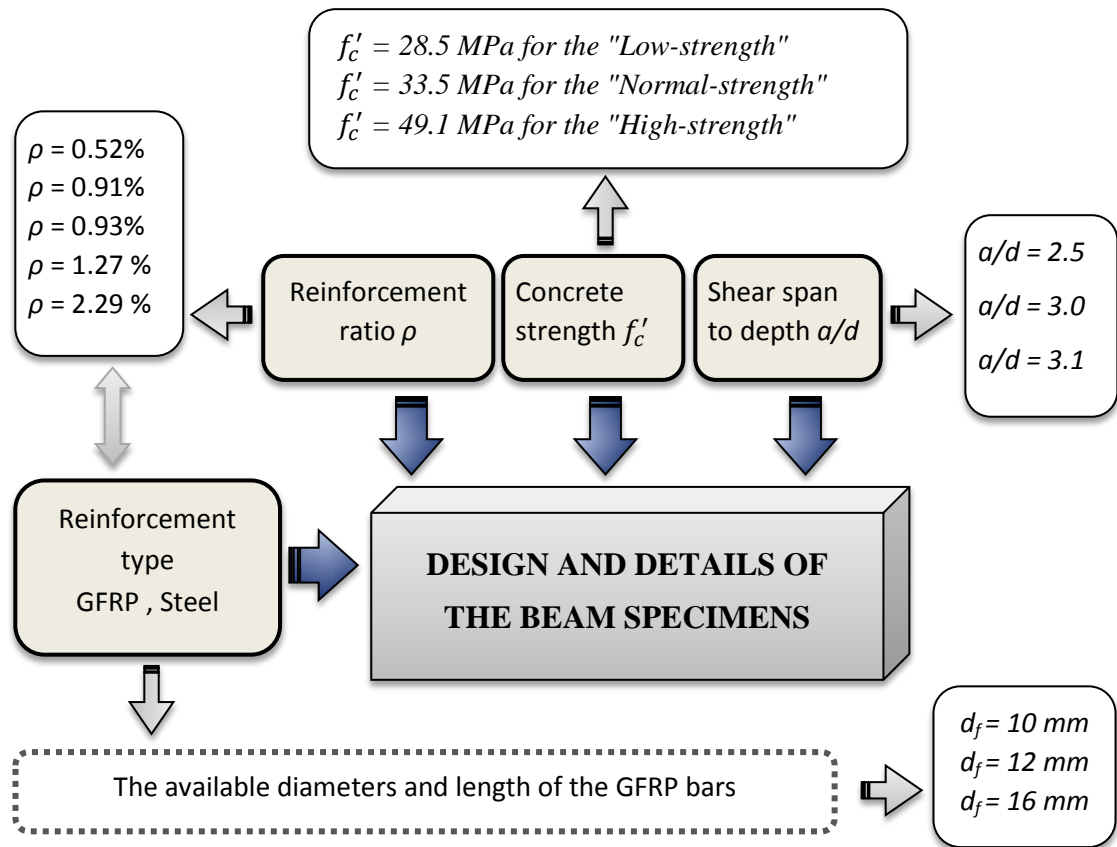


Figure 2.3: Summary of test parameters

3.2 Detail of test specimens

There are several structural members, such as retaining walls, foundation, upper and lower slabs of cut-and-cover tunnel and bridge deck, where shear reinforcement is not used. The specimens in the current research represent those members as well as beams and girders without transverse shear reinforcement. The main objective of the current research is to determine the concrete contribution to the shear strength. Eight concrete beams reinforced with GFRP bars and six control concrete beams reinforced with steel bars, were tested until failure. In order to realize the occurrence of shear failure, all tested beams were reinforced with longitudinal reinforcement only, its means, without shear reinforcement. All beams were simply supported and subjected to two point loads and known as four point bending test in laboratory. Based on the parameters investigated (Figure 2.3). The specimens were divided into three groups for GFRP reinforced beams. While, the steel reinforced concrete specimens were divided into two groups, since the effect of reinforcement ratio was not investigated for this type of reinforcement. Figure 2.6 shows the relationship between the specimens.

The beams in Group A1 were designed to investigate the effect of the longitudinal reinforcement ratio. two sets of beams with 150 mm width, 150 mm height and 1000 mm length were reinforced only with GFRP reinforcements, the reinforcement ratio for this investigation were 1.27% and 2.29%.

To investigate a/d of normal strength concrete beams, four sets of beams were selected in Group A2. Two beams reinforced with GFRP reinforcement sized with same width of 130 mm and same high of 230 mm, but different lengths, which are 1500 mm and 1800 mm, it's means, different a/d ratios, which are 2.5 and 3.0. Similarly, for other two beams reinforced with steel reinforcement.

The effect of concrete strength was investigated using the beams in Group A3. Eight sets of beams with 200 mm width, 250 mm height and 2000 mm length, four for beams reinforced with GFRP and four for beams reinforced with steel reinforcements, the concrete strengths for this investigation were, low strength concrete 28.5 MPa and high strength concrete 49.1 MPa.

The specimen identifications (IDs) as shown in Figure 2.4 were defined in the following manner. The first letter of the specimen ID was (B), all specimens started with this letter, which is first letter of (Beam). The second letter was for the type of reinforcement used (“G” for GFRP and “S” for Steel). This was followed by character for concrete compressive strength “L” for Low concrete strength, “N” for Normal concrete strength and “H” for High concrete strength, where the concrete compressive strength was followed by group numbers “A1” for group 1, “A2” for group 2 and “A3” for group 3. The last number was for the numbers followed in each group. The details of beams and test parameters that were used for the identifications of a specimen are highlighted in Table 2.2, and cross sections of specimens are shown in Figure 2.5.

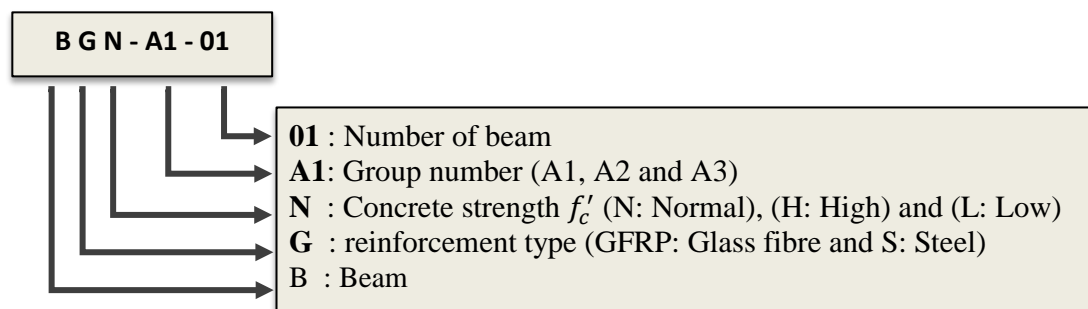
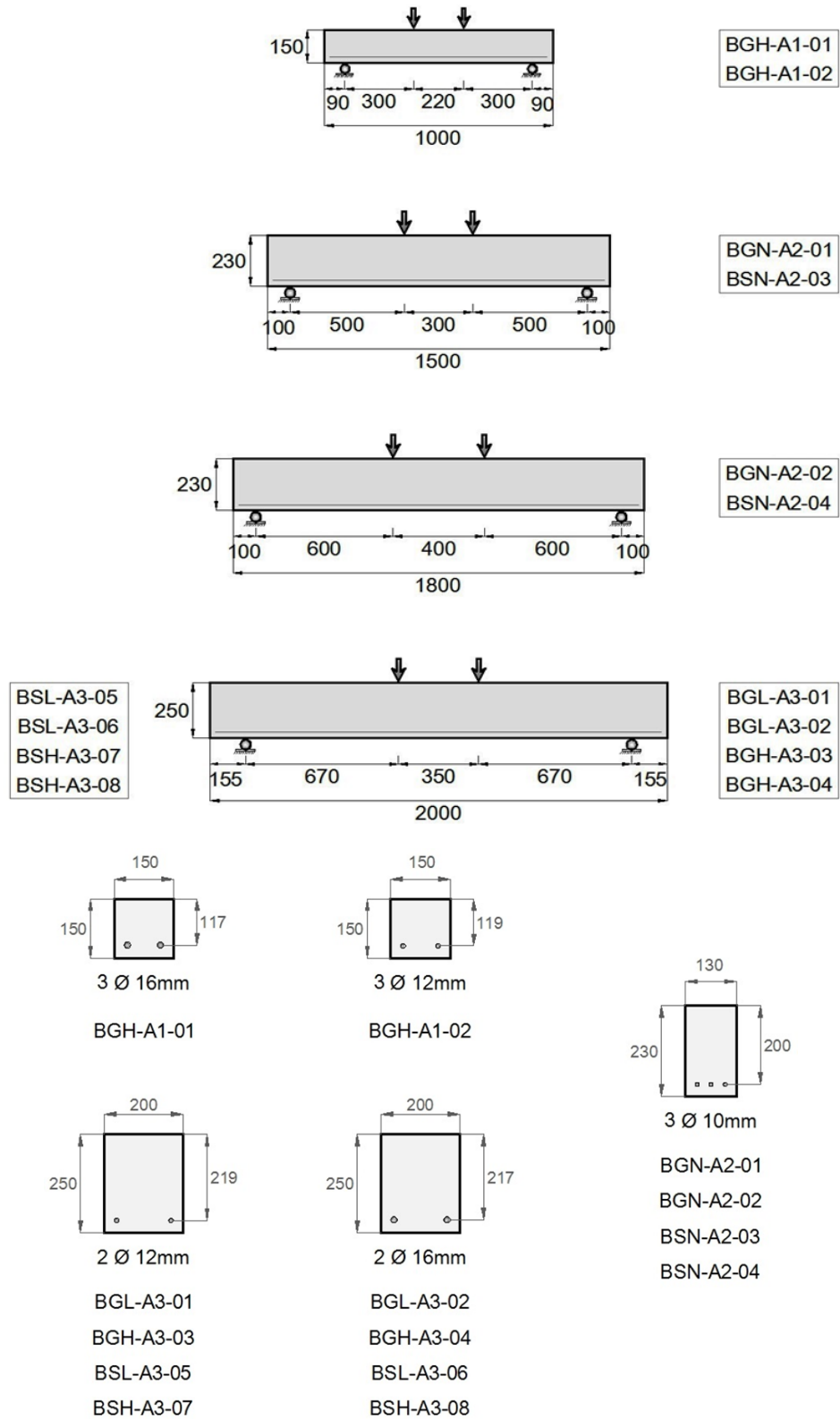


Figure 2.4. The nomenclature of test specimen

Table 2.2: Detail of beam and test variables

Group	Bar Type	Specimens ID	f_c' (MPa)	b_w (mm)	h (mm)	d (mm)	a (mm)	a/d	m (mm)	L (mm)	Lh (mm)	$L Total$ (mm)	Longitudinal Reinforcement				Axial stiffness $A_f E_f$ (N $\times 10^6$)	Parameters investigated
													Bar No.	d_b (mm)	A_f (mm 2)	ρ (%)		
A1	GFRP	BGN-A1-01	33.5	150	150	119	300	2.50	220	820	90	1000	2	12	226.2	1.27	11.83	ρ
		BGN-A1-02	33.5	150	150	117	300	2.50	220	820	90	1000	2	16	402.1	2.29	22.81	ρ
A2	GFRP	BGN-A2-01	33.5	130	230	200	500	2.50	300	1300	100	1500	3	10	235.6	0.91	12.23	a/d
		BGN-A2-02	33.5	130	230	200	600	3.00	400	1600	100	1800	3	10	235.6	0.91	12.23	a/d
	Steel	BSN-A2-03	33.5	130	230	200	500	2.50	300	1300	100	1500	3	10	235.6	0.91	49.43	a/d
		BSN-A2-04	33.5	130	230	200	600	3.00	400	1600	100	1800	3	10	235.6	0.91	49.43	a/d
A3	GFRP	BGL-A3-01	28.5	200	250	219	670	3.10	350	1690	155	2000	2	12	226.2	0.52	11.83	ρ, f_c'
		BGL-A3-02	28.5	200	250	217	670	3.10	350	1690	155	2000	2	16	402.1	0.93	22.81	ρ, f_c'
		BGH-A3-03	49.1	200	250	219	670	3.10	350	1690	155	2000	2	12	226.2	0.52	11.83	f_c'
		BGH-A3-04	49.1	200	250	217	670	3.10	350	1690	155	2000	2	16	402.1	0.93	22.81	f_c'
	Steel	BSL-A3-05	28.5	200	250	219	670	3.10	350	1690	155	2000	2	12	226.2	0.52	47.46	ρ, f_c'
		BSL-A3-06	28.5	200	250	217	670	3.10	350	1690	155	2000	2	16	402.1	0.93	84.37	ρ, f_c'
		BSH-A3-07	49.1	200	250	219	670	3.10	350	1690	155	2000	2	12	226.2	0.52	47.46	f_c'
		BSH-A3-08	49.1	200	250	217	670	3.10	350	1690	155	2000	2	16	402.1	0.93	84.37	f_c'



Note: All dimensions in mm

25 mm clear cover and 25 mm clear spacing between layers of reinforcement.

Figure 2.5: Specimen geometry.

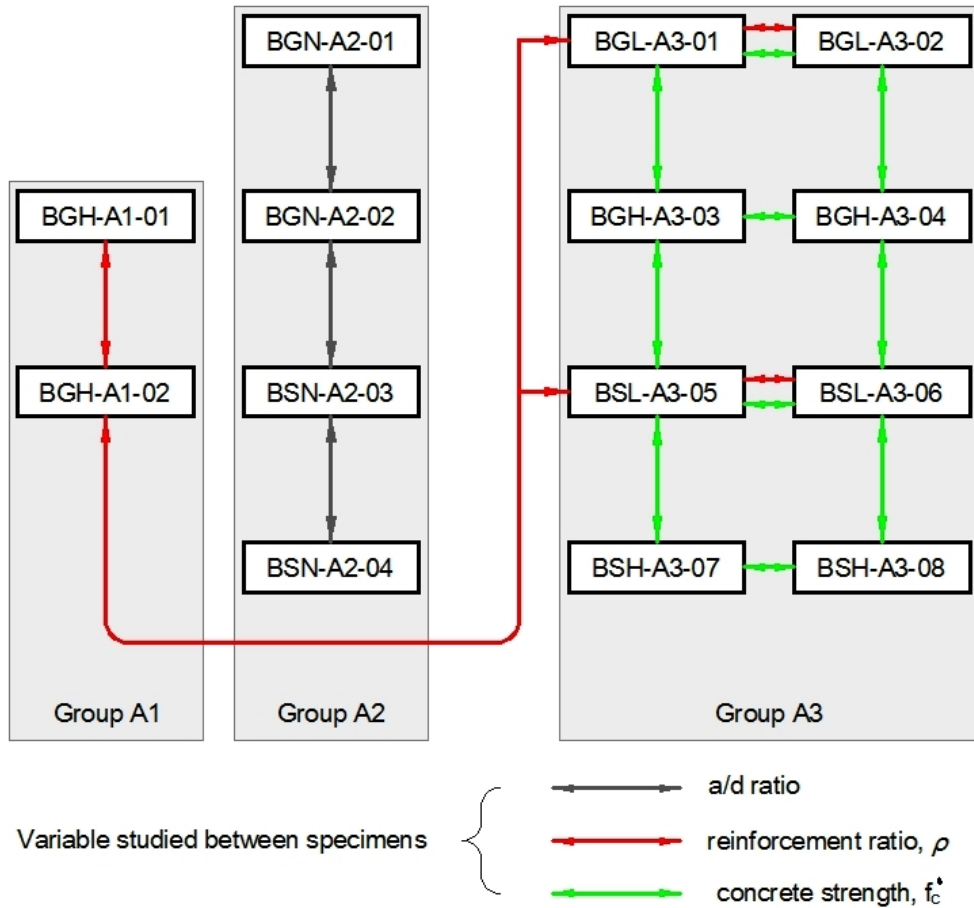


Figure 2.6: Relationship between the specimens.

3.3 Materials

In addition to the structural tests, material tests were carried out to determine the mechanical properties of the concrete and bars that were used in the beams. These tests and their results are presented next.

3.3.1 Concrete

The beams were cast using ready mix concrete (Table 2.3) that was delivered from a local batch plant. Three different type of concrete compressive strength were used in this study. A low strength concrete with specified nominal strength of 28.5 MPa at 28 days, a normal strength concrete with specified nominal strength of 33.5 MPa at 28 days and a high strength concrete with specified nominal strength of 49.1 MPa at 28 days, with 20 mm maximum aggregate size were used for all mixes concrete.

Nine control (150 x 150 x 150 mm) cubes were cast from each concrete batch and cured under the same conditions as the beams; the cubes were used to determine the compressive strength of the concrete. Three tests were carried out at 7, 14 and 28 days, for purposes of quality and curing control. Figure 2.7 shows the concrete cube. The compressive strength was taken as the average of the three cubes. The concrete test results are detailed in Table 2.4.

Table 2.3: Concrete mix design computation

Properties		Specified 49.1 MPa	Specified 33.5 MPa	Specified 28.5 MPa
Cement Content		460 kg/m ³	433 kg/m ³	378 kg/m ³
Free W/C Ratio Specified		0.35	0.39	0.46
Maximum Aggregate Size		20 mm	20 mm	20 mm
Coarse Aggregate	4.75≈12.5mm	560	587 kg/m ³	670 kg/m ³
	12.5≈20.0mm	560	533 kg/m ³	450 kg/m ³
Fine Aggregate Content		682 kg/m ³	686 kg/m ³	700 kg/m ³
Water Content		163 kg/m ³	168 kg/m ³	174 kg/m ³
Concrete Density (kg/m ³)		2425	2407	2372



Figure 2.7: Concrete cube tests.

Table 2.4: Result of cube test

No. of samples	Low strength (N/mm ²)			Normal strength (N/mm ²)			High strength (N/mm ²)		
	7 days	14 days	28 days	7 days	14 days	28 days	7 days	14 days	28 days
1	22.24	24.32	29.60	25.80	24.67	34.52	41.95	48.77	49.72
2	21.56	26.12	26.67	29.22	30.12	32.86	45.66	46.86	51.89
3	22.08	27.92	29.27	28.15	33.80	33.23	44.82	44.13	45.55
Average	21.96	26.12	28.51	27.72	29.53	33.54	44.14	46.59	49.05

3.3.2 Reinforcements

The reinforcing materials used in this investigation were glass FRP bars and conventional steel bars, as shown in Figure 2.8. One type of GFRP bars was used as longitudinal reinforcement: E-Glass FRP. The bars were sand coated to enhance the bond between the bars and the concrete. The GFRP reinforcement bars used in this study are manufactured by FIDIA global service.

The glass FRP bars were used in three sizes: No. 3 ($d_b = 9.53$ mm), No. 4 ($d_b = 12.70$ mm) and No. 5 ($d_b = 15.88$ mm). the deformed steel bars had also two different sizes: ($d_b = 9.8$ mm), ($d_b = 11.93$ mm) and ($d_b = 15.96$ mm) were used in reinforcing the control beams.

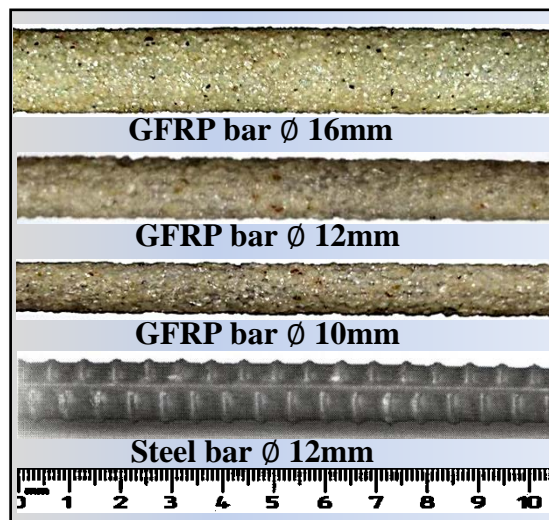


Figure 2.8: Different types of reinforcement used in this study

The GFRP samples have been tested under axial tensile load using a universal testing machine (UTM) having a load capacity of 500 kN. Figure 2.9 shows the experimental setup for the GFRP tensile specimens.

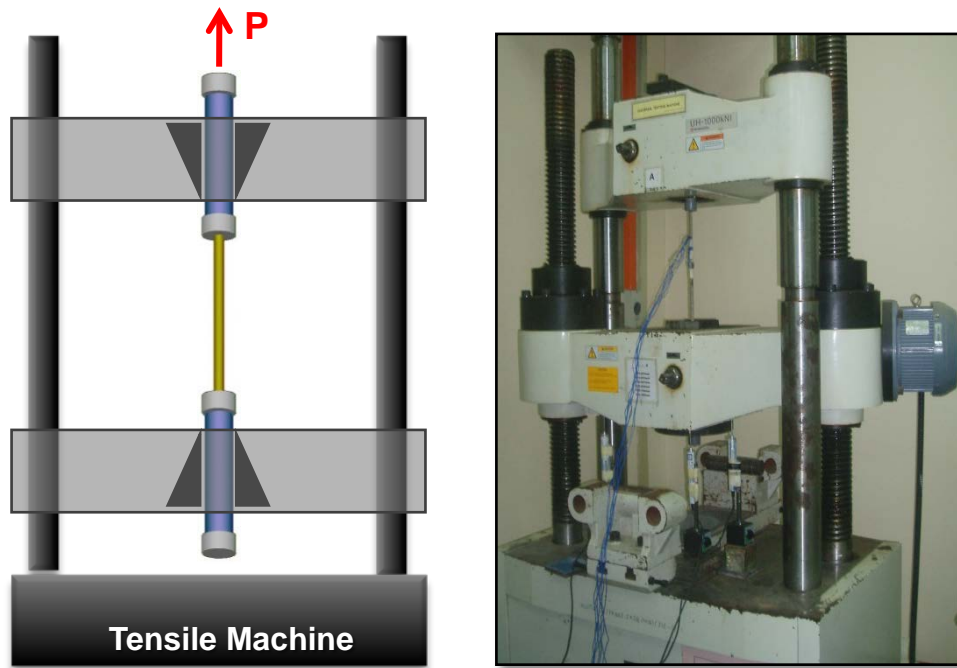


Figure 2.9: The experimental setup for GFRP bar testing

The tensile test specimens were prepared in conformance with the guidelines of the ACI 440.3R-04 (ACI 2004), which specifies specimen dimensions and requirements of the testing procedure itself, Figure 2.10 shows a schematic sample of GFRP reinforced wrapped epoxy at both end, and geometrical characteristics of the GFRP test samples shown in Table 2.5.

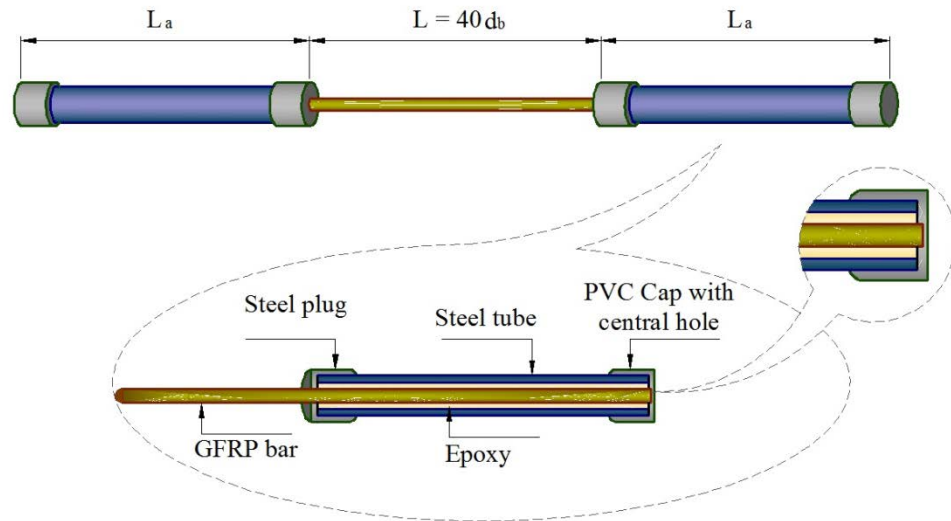


Figure 2.10: Typical GFRP bar tensile test specimen with end anchors

Table 2.5: Geometrical characteristics of the GFRP test samples

Diameter of the GFRP bar, d_b (mm)	Outside diameter of the steel tube (mm)	Nominal wall thickness of the steel tube (mm)	length of the steel tube, L_a (mm)	The free length $L = 40d_b$ (mm)
10	35	4.8	300	400
12	42	4.8	380	480
16	42	4.8	380	640

The mechanical properties of the reinforcing bars were determined by performing tensile tests on representative specimens; 12 GFRP specimens and 12 Steel specimens. The characteristics of the glass FRP and steel reinforcement used in this study are summarized in Table 2.6 and Table 2.7. It can be seen that the modulus of elasticity of GFRP reinforcement is significantly lower than the modulus of elasticity of steel reinforcement. GFRP bars in tension exhibit a linear elastic stress-strain response up to failure as seen in Figure 2.11. Unlike steel, no plastic behaviour such as yielding occurs in GFRP bars and failure is sudden and brittle with a large release of energy.

Table 2.6: Mechanical properties for GFRP bar

Properties	Ø 10	Ø 12	Ø 16
Nominal Diameter, \varnothing (mm)	9.53	12.70	15.88
Area, (mm ²)	71.3	126.7	198
Modulus of Elasticity, E_f (GPa)	51.91	52.32	56.72
Tensile Strength, f_{fu} (MPa)	769	719	690
Ultimate Strain, ε_f (%)	1.52	1.43	1.34

Table 2.7: Mechanical properties for Mild Steel bar

Properties	Ø 10	Ø 12	Ø 16
Nominal Diameter, \varnothing (mm)	9.80	11.93	15.96
Area, (mm ²)	75.4	111.8	200
Modulus of Elasticity, E_s (GPa)	209	209	209
Yield Strength, f_y (MPa)	480	480	480
Ultimate Strain, ε_y (%)	0.23	0.23	0.23

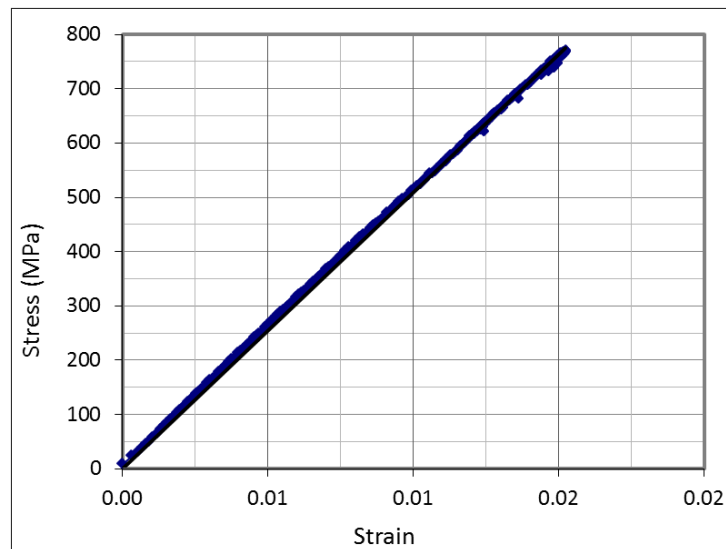


Figure 2.11: Stress-strain relationship of GFRP bar

3.4 Fabrication and curing practices

3.4.1 Formwork and reinforcement layout

The formwork was designed and constructed using 20 mm thick plywood sheets. The sides of the form work were cut according to the height off each beam. Figure 2 .12 shows a typical formwork and reinforcement layout. The beams contained longitudinal reinforcement only that was placed at the bottom of each beam. The bars were placed on plastic chairs to maintain clear cover. The surface of the form work was oiled a day before casting process of the beam.



Figure 2.12: Typical formwork and reinforcement layout

3.4.2 Casting and curing beam

Specimens that used in this study were cast from each batch of concrete as shown in Table 2.3. Fresh concrete is placed into the formwork. The distance of placement was as low as possible to avoid segregation. Finally, at the end of the pour, the top surface of each beam was leveled with a steel trowel to produce a smoother surface.

After the final set of the concrete, the cast specimens were curing used wet gunny were watered 2 times a day for 7 days. After the curing process was finished for 28 days, the beams were removed from the formwork and stored in the laboratory until the day of testing. Before testing, the beams were painted using white colour paint to facilitate the observation of the crack propagation. Figure 2.13 shown curing process and removing the beams from the formworks.



Figure 2.13: Curing process and removing the beams from the formworks

3.5 Test procedure

All beams were simply supported and subjected to two point loads and known as four point bending test in laboratory Figure 2.14. The specimens were tested in a MTS testing frame having a load capacity of 500 kN in compression, in displacement control. A spreader beam was used to divide the load into two points. The load was applied and increased continuously at a rate within the range 1 KN/mint. At each load increment, the beam was inspected and the cracks were monitored and mapped until failure load was reached as shown in Figure 2.15.

Linear Variable Differential Transducer (LVDT) was used to measure the deflection of the beam when the load was applied. Figure 2.14 shows the location of LVDTs which were placed to the behind at bottom part of the beam. A total of three LVDTs were used, one was placed at the center of the beam while the other two at the middle of shear span.

A data logger was recorded and stored the test data for each load increment at a frequency of one reading per second. All components including the applied load and deflections were connected to data logger in order to collect the experimental data.

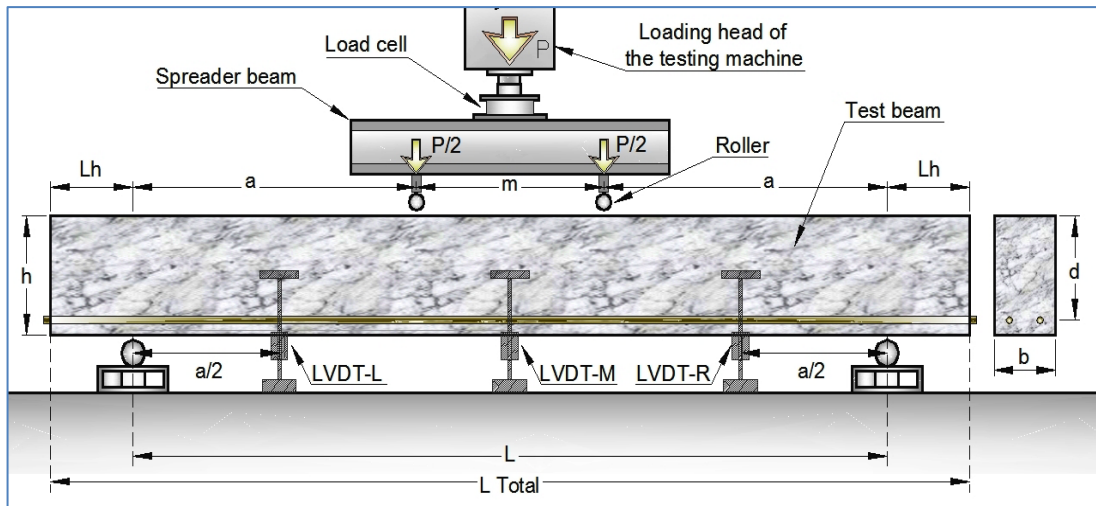


Figure 2.14: Schematic diagram of the test setup for the beam



Figure 2.15: Test setup and cracks mapping

4.0 Experimental results and analysis

4.1 Introduction

The experimental results of the current investigation are presented in this section. As mentioned earlier, a total of fourteen beams reinforced with GFRP and steel were tested. The experimental program was undertaken to investigate the influence of four parameters on the behaviour and shear strength of concrete beams. The parameters were the shear span-to-depth ratio (a/d), longitudinal reinforcement ratio (ρ), concrete compressive strength (f'_c), and reinforcement type.

The results are presented in terms of crack patterns, load-deflection behavior and failure modes. The test results are analyzed to show the effect of the different parameters on the behaviour and capacity of the test beams. Finally, the test results are compared with the theoretical prediction of some of the proposed shear design expressions and cods predictions that are available in the literature.

4.2 General behaviour

4.2.1 Crack patterns

During the test and at the end of a load increment, the growth of cracks was marked on each beam. This was carried out to identify the direction of crack propagation and to determine the differences in crack patterns of the beams. Figure 2.16 shows the typical gradual formation of cracks in a test beam (BGN-A2-02). The thick lines in the figure are used to identify the cracks that were formed at failure. The slope of the inclined crack at failure is shown on the figures of the crack patterns. The cracks were drawn to scale as in the actual tests. The extent t of a crack at the end of a load increment was marked by a short horizontal line. The loads shown at each crack tip corresponds to the actuator load in kilo-newton (KN). This load was twice the value of the load at each loading point. For all beams, the first flexural cracks initiated at the bottom of the beam in the constant moment region, where the flexural tension stress was the highest and the shear stress was zero. The observed flexural cracks propagated vertically upward to the level of the neutral axis, which reflected the absence of shear stress. As the load was increased, additional flexural cracks were developed within the shear span. Due to the presence of shear stresses, these flexural cracks became progressively more inclined and propagated towards the load points. These types of cracks are known as flexural-shear cracks. These cracks extended rapidly through the beam leading to the so-called diagonal-tension failure. The duration between the formation of an inclined crack and failure of a beam was small. ASCE-ACI Committee 426 (1973) reported that for beams with shear span-to-depth ratio between 2.5 and 6.0, the inclined flexural cracks extend to form a diagonal tension crack. This behavior was observed for most of the beams in the current study. Photographs of the crack patterns for all beams at failure are shown in Appendix I.

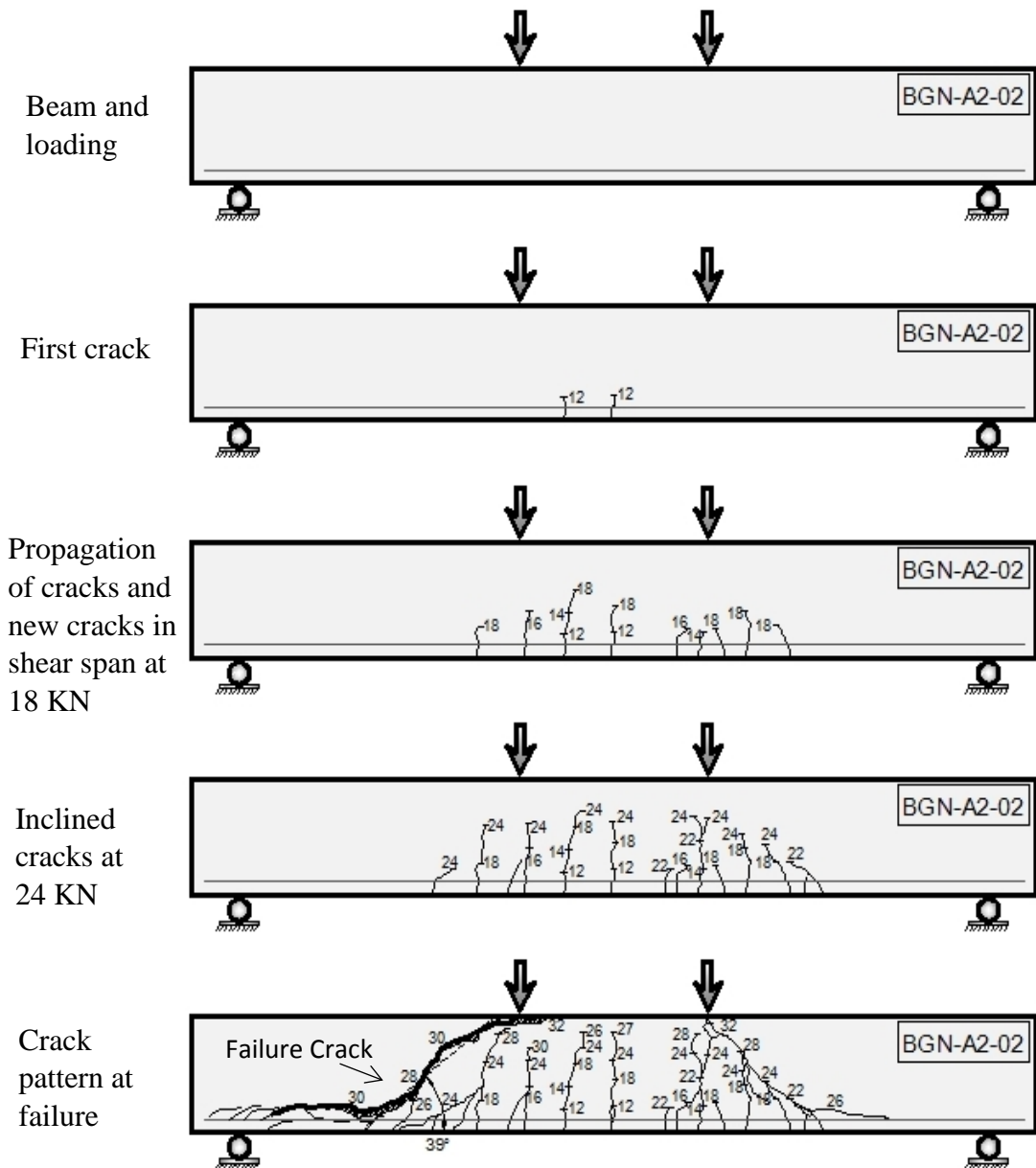


Figure 2.16: Typical formation of cracks in a beam during a test

Figure 2.17 shows the crack patterns for the beams in Group A2 with variable shear span-to-depth ratio (a/d). In general, the slope of the inclined crack decreased as the a/d ratio of the beam increased for all reinforcement types. This is because; at certain shear load, the moment as well as flexural stress increases as the shear span to depth ratio of a beam increases. Higher flexural stress could lead to the reduction in the inclination of shear cracks. Hence, the horizontal projection of the inclined cracks increased with an increase in the shear span-to-depth ratio, for beams with the same depth.

It can be seen from Figure 2.17 that for the same shear span-to-depth ratio, the slope of the inclined shear crack was almost the same for both types of reinforcements. At a certain load level, and prior to the formation of inclined cracks, the flexural cracks penetrated deeper into the beam for GFRP reinforced beams than in steel reinforced beams. This could be due to the higher axial stiffness of the steel reinforcement.

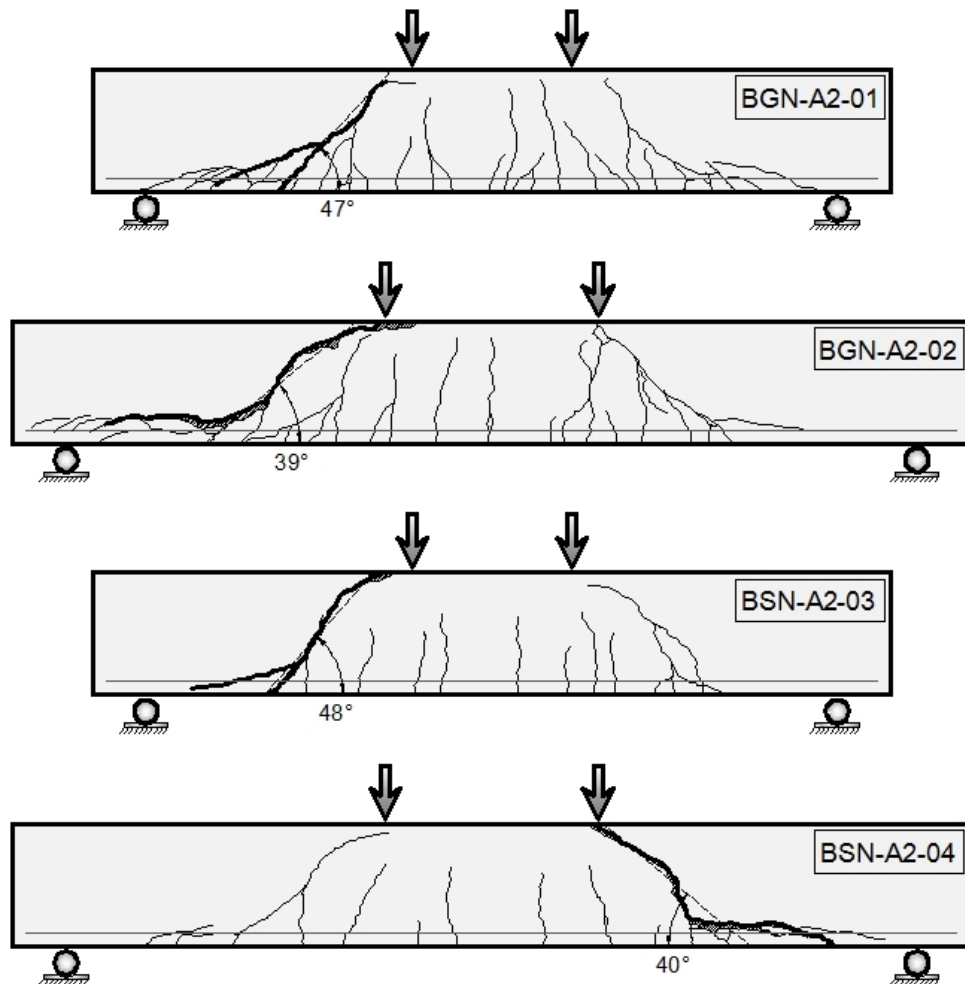


Figure 2 .17: Crack patterns for beams with different shear span-to-depth ratios

Crack patterns for normal strength concrete beams with different depths and different reinforcement types are shown in Figure 2.18. The beams had a constant shear span-to-depth ratio. It was noted that the slope of the inclined crack at failure for all beams was close to the 47° . This result revealed that, as the shear span-to-depth ratio of the beams remains constant, the horizontal projection of the inclined crack at failure was almost same irrespective of the reinforcement type and depth. The number of cracks in the shear span zone during failure was found to be approximately the same

for all reinforcement types and depths. At a certain load level, the flexural cracks penetrated deeper into the beam as the axial stiffness of the reinforcing bars decreased.

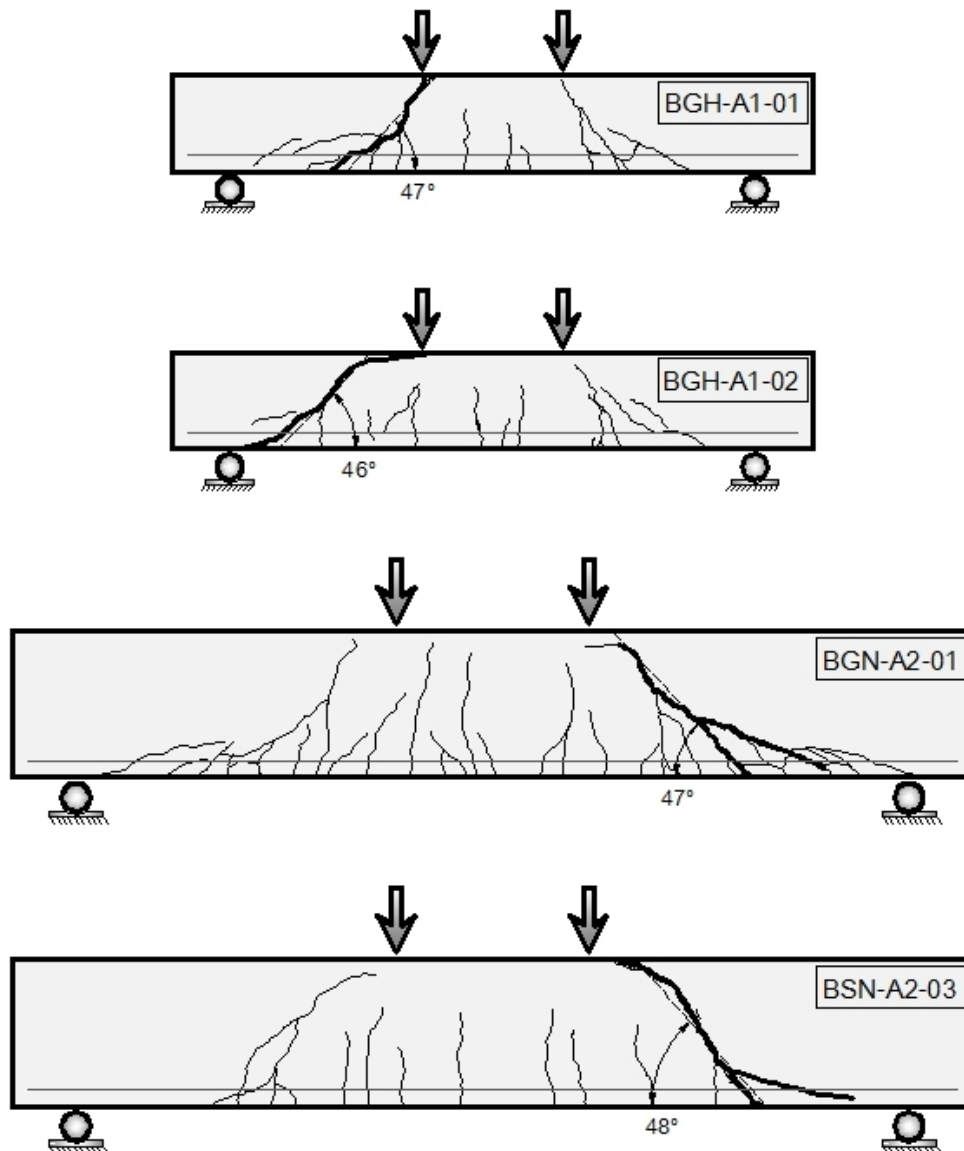


Figure 2.18: Crack patterns for normal strength concrete beams with different depths

The effect of reinforcement ratio on the crack patterns of Group A1 beams with height equal to 150 mm is shown in Figure 2.19. The beams in this set had the same shear span-to-depth ratio. It was noted that the slope of the inclined crack at failure for the two beams was almost same. Moreover, the number of cracks was found to be approximately the same. It can be seen from Figure 2.19 that the horizontal projection of the cracks for beams was less than the effective depth (d).

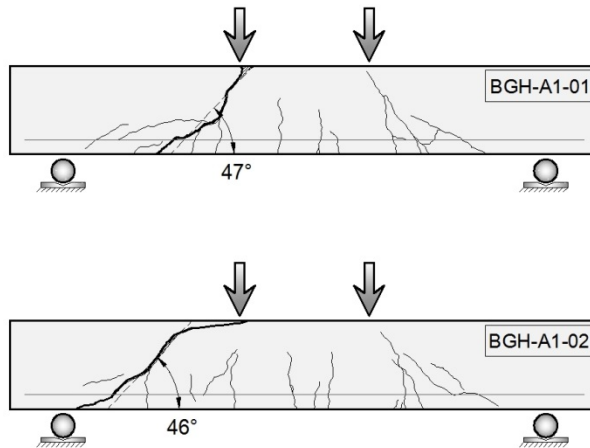


Figure 2.19: Crack patterns for beams with height equal to 150 mm

The crack patterns of Group A3 beams with different compressive strengths and different reinforcement ratios are shown in Figure 2.20 and Figure 2.21. The concrete strengths and reinforcement ratios of the beams were (28.5 MPa and 49.1 MPa), and (0.52% and 0.93%), respectively.

As a result, in the case of BGL-A3-01 and BGH-A3-03 with $\rho_f = 0.52\%$, a number of random cracks was also detected in the concrete around the longitudinal tension reinforcement for both sides. One of the vertical cracks in the shear span became critical and extended towards the load point at the ultimate stage. The failure of these beams was observed to be mainly due to the low modulus of elasticity of the GFRP bars. For beam BSL-A3-05 and BSH-A3-07 with $\rho_s = 0.52\%$, the initial shear cracking in the specimen behaves similarly as the previous specimens. The secondary crack also propagates for both sides as shown in Figure 2.20.

The failure of the beams with $\rho = 0.93\%$, the diagonal crack started first and when force was increased development of secondary cracks propagated on one side of the beam. Although vertical cracks and inclined cracks were the main cracks that developed during the loading stage in all the beams tested, some steel reinforced beams and GFRP reinforced beams exhibited horizontal cracks along the reinforcement. The crack width in the shear span in the beams with GFRP bar was observed to be more when compared to that in the corresponding beams with steel bar as shown in Figure 2.21.

In general, the beams in this group with same reinforcement ratio and different concrete strength had the same crack patterns. This result is in good agreement with the other test results of FRP reinforced concrete beams without web reinforcements (Tureyen and Frosch 2002, EI-Sayed et al.2006).

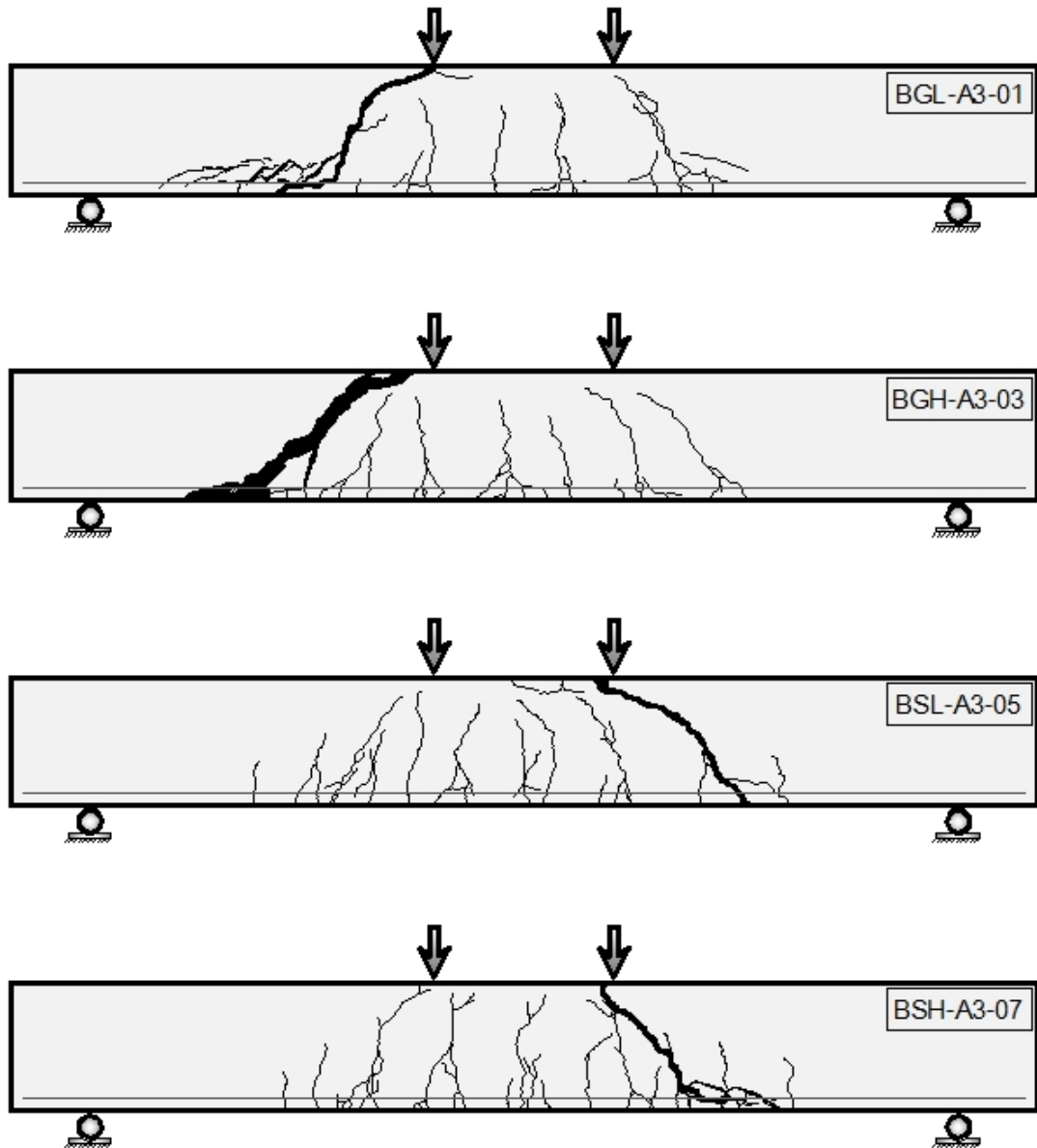


Figure 2.20: Crack patterns for beams with different concrete strengths and reinforcement ratio ($\rho_f = 0.52\%$)

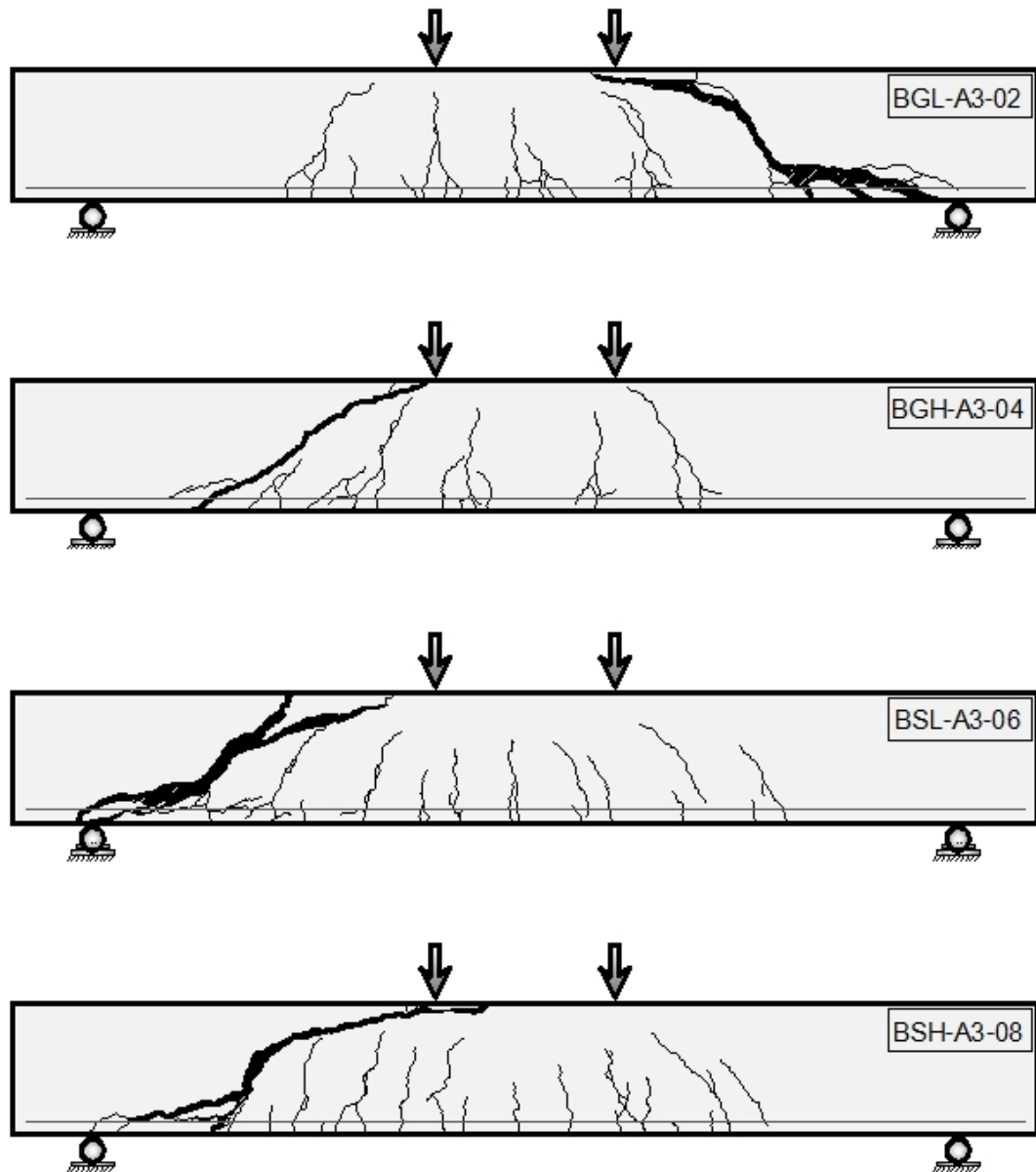


Figure 2.21: Crack patterns for beams with different concrete strengths and reinforcement ratio ($\rho_f = 0.93\%$)

4.2.2 Cracking loads

The load at first flexural cracking was recorded for all beams. The first flexural crack occurred when the moment at a section of the beam reached the cracking moment. Therefore, the shear load, which created first cracking at midspan, V_{cr-obs} , will vary according to the loading position and the shear span of the beams. Hence, for beams with identical cross section, V_{cr-obs} may not be the same. The observed cracking loads V_{cr-obs} , ultimate shear loads (V_{exp}), and failure modes are tabulated in Table 2.8.

In general, and for all reinforcement types, the cracking load decreased as the shear span-to-depth ratio was increased, and the cracking loads increased with an increase in the reinforcement ratio, height of beam, and concrete strength. These results were expected according to the theoretical predictions of the cracking loads of these beams.

4.2.3 Load deflection behaviour

The deflections of all beams were measured using linear variable differential transducer (LVDT) and were recorded using a high-speed data acquisition system as mentioned in section 3.5. Typical load versus deflection curves obtained from the three LVDTs are shown in Figure 2.22 (Beam BGH-A2-01). The deflections of all beams at mid-span are tabulated in Table 2.8. The reactions at the supports are equal to the applied load, which are one half of the actuator load. The shear force in a beam is equal to the applied load. Hence, in the discussion of the results, the term shear load is used instead of the applied load. The load versus deflection diagram that is shown in the figures contains three stages behaviour: before cracking, transition from un-cracked to cracked stage, and after cracking. Since the beams in this investigation failed shortly after the formation of diagonal cracks, the shear crack induced deformation was small and this was neglected.

Table 2.8: Experimental results

Group	Bar Type	Specimens ID	Beam properties							Experimental observations				
			f'_c	b	h	d	a/d	L Total	ρ	V_{cr-ops}	P_{exp}	V_{exp}	$Def.$	Failure Modes
			(MPa)	(mm)	(mm)	(mm)		(mm)	(%)	(KN)	(KN)	(KN)	(mm)	
A1	GFRP	BGN-A1-01	33.50	150	150	119	2.5	1000	1.27	6.92	34.32	17.16	10.54	BF
		BGN-A1-02	33.50	150	150	117	2.5	1000	2.29	7.32	41.22	20.61	6.48	SC
A2	GFRP	BGN-A2-01	33.50	130	230	200	2.5	1500	0.91	7.12	40.62	20.31	13.22	DT
		BGN-A2-02	33.50	130	230	200	3.0	1800	0.91	6.05	32.36	16.18	13.12	DT
	Steel	BSN-A2-03	33.50	130	230	200	2.5	1500	0.91	7.63	53.86	26.93	7.02	Y-DT
		BSN-A2-04	33.50	130	230	200	3.0	1800	0.91	6.90	43.90	21.95	11.09	Y-DT
A3	GFRP	BGL-A3-01	28.50	200	250	219	3.1	2000	0.52	8.90	51.80	25.90	13.35	ST
		BGL-A3-02	28.50	200	250	217	3.1	2000	0.93	9.10	71.20	35.60	9.84	SC
		BGH-A3-03	49.10	200	250	219	3.1	2000	0.52	10.45	59.52	29.76	14.12	ST
		BGH-A3-04	49.10	200	250	217	3.1	2000	0.93	12.50	74.20	37.10	10.71	ST
	Steel	BSL-A3-05	28.50	200	250	219	3.1	2000	0.52	10.30	62.50	31.25	6.08	ST
		BSL-A3-06	28.50	200	250	217	3.1	2000	0.93	14.80	85.60	42.80	6.88	SC
		BSH-A3-07	49.10	200	250	219	3.1	2000	0.52	11.80	71.36	35.68	5.74	ST
		BSH-A3-08	49.10	200	250	217	3.1	2000	0.93	16.95	89.60	44.80	6.12	SC

SC = Shear-compression failure

ST = Shear-tension failure

DT = Diagonal tension failure

Y-DT = Diagonal tension failure after yielding (steel reinforcement)

BF = Bond failure

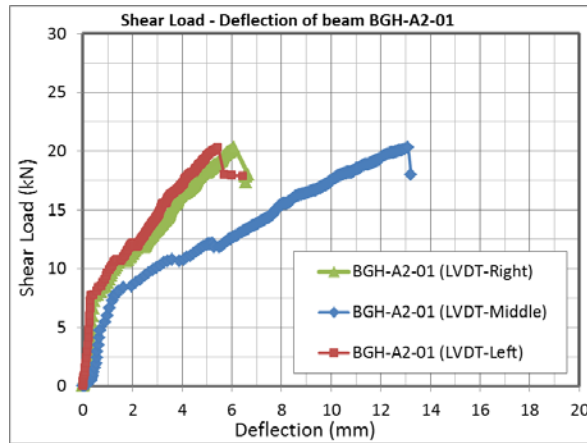


Figure 2.22: Typical load versus deflection curves (Beam BGH-A2-01)

The load-deflection behaviour of 150 mm thick beams in Group A1 for different reinforcement ratios. In general, the load-deflection behaviour of the beams can be defined by three stages: before cracking, transition from un-cracked to cracked stage, and after cracking, as shown in Figure 2.23. It can be seen that all beams behaved linear elastic at the beginning. However, the load-deflection behaviour in the second stage, which is the transition zone from the uncracked to the cracked stage, where the existing cracks grow and new flexural cracks developed in the constant moment zone.

The behaviour of the beams after the second stage; for the same load level, and as expected, the deflection of the beam decreased as the axial stiffness of GFRP bars increased. Table 2.9 shows the axial stiffness of GFRP bars. This result is in good agreement with the other test results of FRP reinforced concrete beams without web reinforcements (Tureyen and Frosch 2002, EI-Sayed et al.2006a).

Table 2.9: Axial stiffness of the reinforcing bars in different beams

Group	Bar Type	Beam ID	E_f (GPa)	ρ_f	Axial stiffness (GPa)
A1	GFRP	BGH-A1-01	52.32	1.27	0.66
		BGH-A1-02	56.72	2.29	1.30

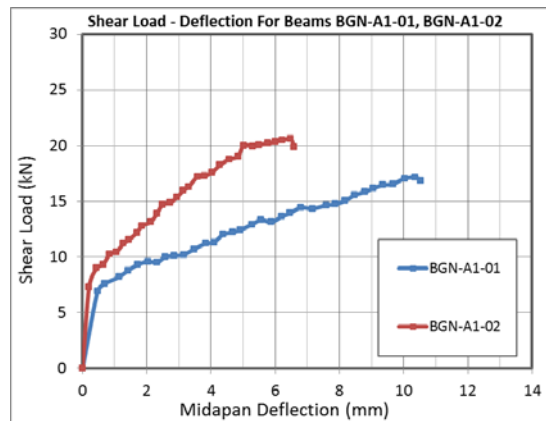
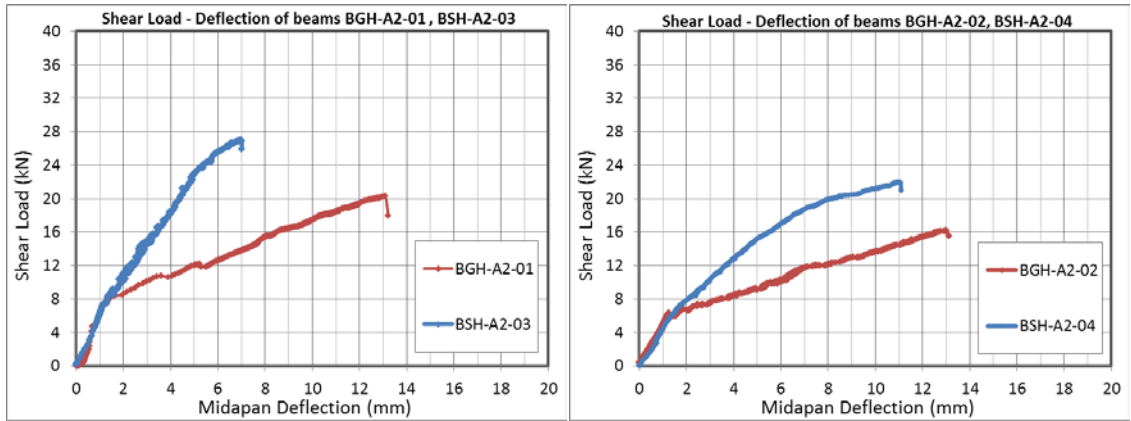


Figure 2.23: Load-deflection behaviour of 150 mm thick beams in Group A1

Figure 2.24 shows the applied shear load versus mid-span deflections for all of the beams in Group A2 with different shear span-to-depth ratio (a/d). Before flexural cracking occurred, the load-deflection behaviour was approximately linear. In this stage, the stiffness of the beams with the same shear span to depth ratio was approximately the same for different reinforcement types. This indicated that the deflections before cracking were not affected by the reinforcement type. The beam progressively changed from an un-cracked to fully cracked state, where the existing cracks grow and new flexural cracks developed in the constant moment zone. At the end of this stage, the behaviour of the beams became shortly linear, this linear behaviour continued until failure.

For the same shear span-to-depth ratio, and at a certain load level, the deflections of the GFRP reinforced beams were higher than those reinforced with steel. This could be attributed to the low axial stiffness of GFRP reinforcement. Nonetheless, it should be noted that GFRP reinforced members have greater tension stiffening than steel reinforced members (Bischoff and Paixao 2004).

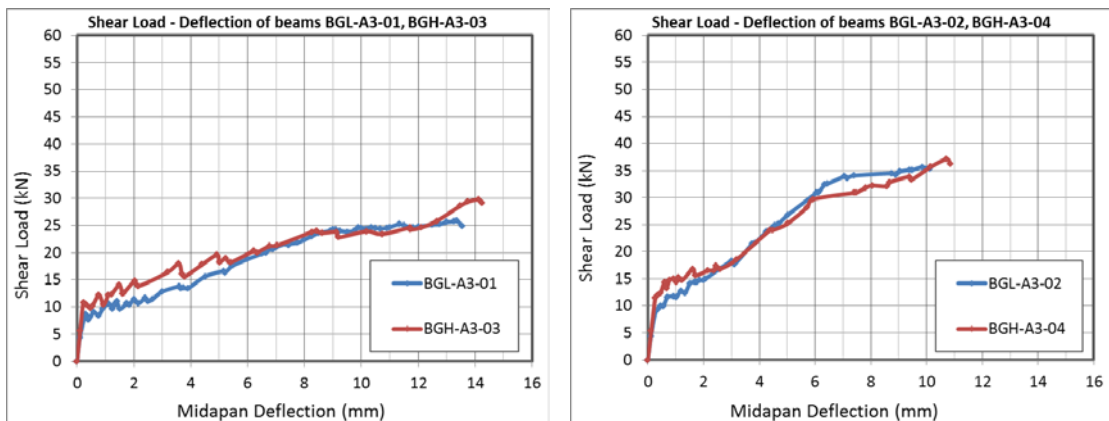


(a)

(b)

Figure 2.24: Load-deflection profile of beams in Group A2: (a) $a/d = 2.5$, and (b) $a/d = 3.0$

The concrete strength did not have a significant effect on the shape of the load-deflection behaviour for 250 mm thick beams. All beams in Group A3 showed similar load-deflection characteristics as shown in Figure 2.25. It can be seen that all beams behaved linear elastic at the beginning, and as the load increases, the beam starts to behave non-linear due to the development of cracks until failure occurred. However, beams reinforced with steel bar had higher load compared to GFRP bar reinforced concrete beams. This could be attributed to their low modulus of elasticity of GFRP bar.

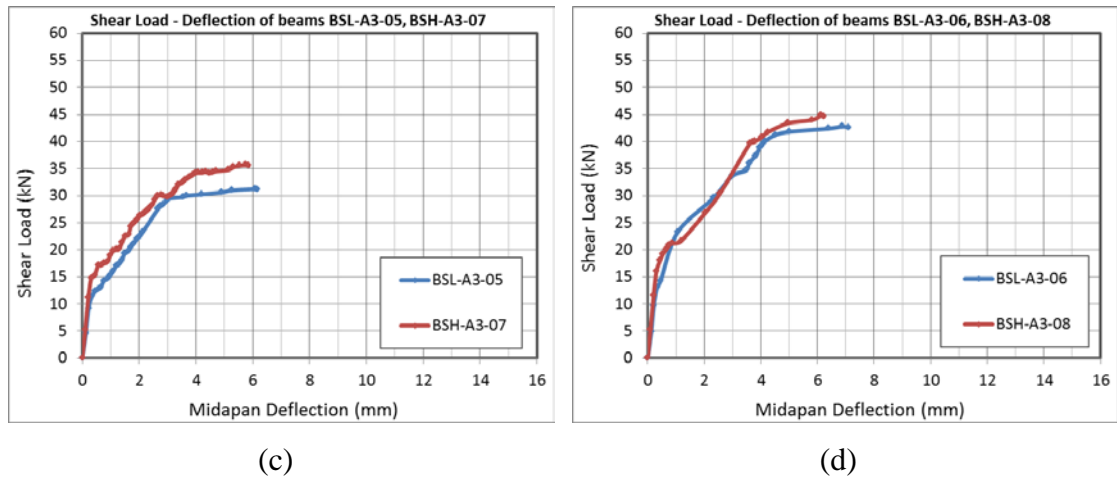


(a)

(b)

Figure 2.25: Load-deflection behaviour of 250 mm thick beams with different concrete strengths and same reinforcement types and ratios in Group 4:

(a) $\rho_f = 0.52\%$ (b) $\rho_f = 0.93\%$



(cont.) Figure 2.25: Load-deflection behaviour of 250 mm thick beams with different concrete strengths and same reinforcement types and ratios in Group 4:

(c) $\rho_s = 0.52\%$ and (d) $\rho_s = 0.93\%$

4.2.4 Failure modes

The observed failure modes for the beams tested in this investigation were reported in Table 2.8. Photographs of the failure mode of all beams are shown in Appendix I. Some of the failure modes are discussed in this section. In general, the failure modes of the beams were either by shear-tension, or shear-compression, or diagonal tension. For some beams, a secondary bond/anchorage failure was observed within the shear span as shown in Figure 2.26. When shear failure was imminent, new type of cracks developed from the existing flexural shear cracks and propagated along the longitudinal reinforcement towards the support leading to a bond or splitting failure. This can be attributed to the fact that when aggregate interlock was lost due to the opening of the inclined crack, the redistribution of the internal forces took place. As the aggregate interlock was lost, the dowel action in the longitudinal reinforcement would increase to maintain equilibrium. The sudden increase in the dowel action increased the vertical tensile stresses in the concrete surrounding the bars. This stress in combination with the existing spitting stress, due to the flexural bond, leads to the final spitting failure along the plane of the reinforcement. (Figure 2.26) shown, splitting along the reinforcement stopped before the support and did not cause any splitting past the support, which occurred simultaneously with the diagonal tension crack propagating towards the concentrated load.



Figure 2.26: Bond/anchorage failure of beam BGN-A2-02

Typical shear-compression failure mode was observed for normal strength concrete beams in Group 1. However, beam BGN-A1-01, for which the compressive strength was 33.5 MPa and reinforced with GFRP bars, failed by bond failure between the bars and the sand coating. One of the cracks near the loading point became excessively wide as the bars pulled off. The failure of this beam was sudden and associated with the spalling of concrete around the bars as shown in Figure 2.27.

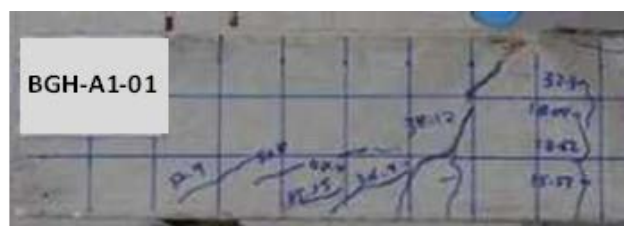


Figure 2.27: Failure pattern of beam BGN-A1-01

Although beam BGL-A3-02 failed by shear-compression near the loading point, this beam continued to carry load after the initial failure as shown in Figure 2.28.



Figure 2.28: Failure pattern of beam BGL-A3-02

In general, the failure modes were found to be more brittle, when the depth and the reinforcement ratio of the beams were increased for each type of reinforcing bars. Steel reinforced beams had the highest axial stiffness of the longitudinal bars and these beams showed more brittle behavior than the GFRP reinforced beams. This means, that the ductility of the beams that failed in shear decreased as the axial stiffness of the beams increased, which is evident from the test results of the beams in these groups.

4.3 Analysis of test data

4.3.1 Shear strength

Bažant and Kazemi (1991) considered the first peak load as the shear strength of a beam as this load agreed reasonably well with the overall trend of the size effect that the authors proposed. The authors also mentioned that it is unreasonable to design a beam for the second main peak load, regardless of which main peak is higher.

Tureyen and Frosch (2002) identified the shear strength of the flexural members by the formation of an inclined crack and the subsequent sudden drop in load carrying capacity. The differences between the formation of inclined cracking loads and the ultimate loads were within 15% of each other.

According to Rebeiz (1999), the shear strength at ultimate failure is a more defined and reliable measure than the cracking shear strength. It should be noted that for some beams more than one peak might appear in the load-deflection curve. This would occur due to the formation of an inclined crack at one end of the beam that is arrested and eventually the beam fails due to the inclined crack at the other end of the beam.

In this investigation, the maximum load at which there was either a complete and abrupt failure, as shown in Figure 2.22 (Beam BGH-A2-01). For a few beams, the inclined cracking load was considered as the failure shear strength. This failure shear strength, which is the concrete contribution, V_c , is identified as V_{exp} in this chapter and is reported in Table 2.8.

4.3.2 Effect of main variables

4.3.2.1 Effect shear span-to-depth ratio, a/d

The effect of shear span-to-depth ratio on concrete shear strength of the test beams in Group A2 is shown in Figure 2.29. In general, the shear strength decreased with an increase in the shear span-to-depth ratio.

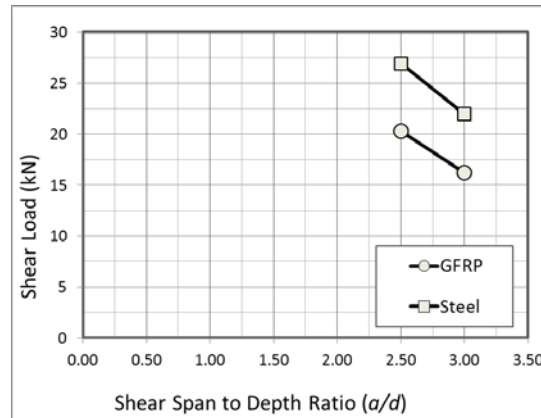


Figure 2.29: Effect shear span-to-depth ratios of experimental shear strength of beams in Group A2

4.3.2.2 Effect of Reinforcement Ratio, ρ

The test results for different reinforcement ratios and different reinforcement types are illustrated in Figure 4.20 for some beams in Group A3 with height equal to 350 mm and $f'_c = 28.5$ MPa, the reinforcement ratios were 0.52% and 0.93% for GFRP and steel reinforced beams. It can be seen (Figure 2.30 a) that the shear strength increased with an increase in the longitudinal reinforcement ratio. This was more prominent in Figure 2.30 (b) when the shear strengths were normalized by $\sqrt{f'_c} b_w d$. Gross et al. (2003) also observed a slight increase in the shear strength of GFRP reinforced beams with an increase in the longitudinal reinforcement ratio. It can be shown here (Figure 2.31) that the increase in shear strength is related to approximately the cubic root of the axial stiffness of the reinforcing bars.

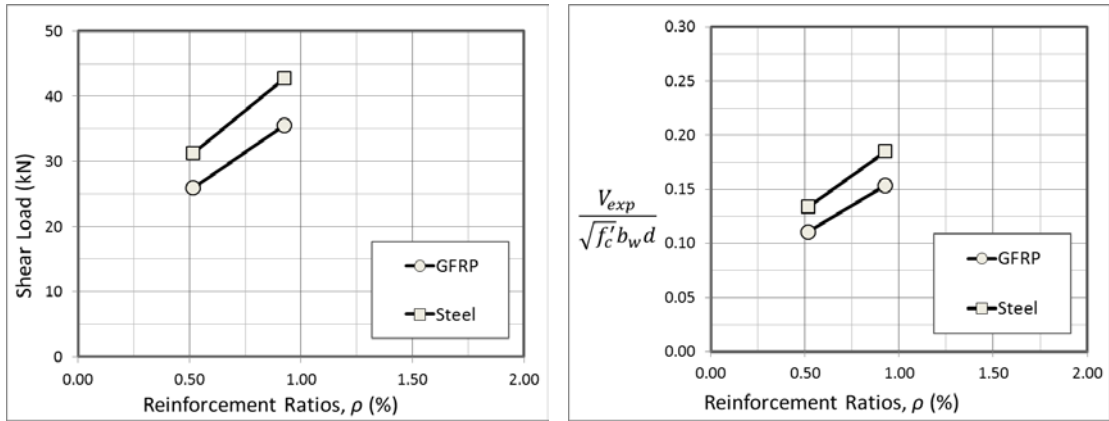


Figure 2.30: Effect of reinforcement ratio for 350 mm thick beams: (a) experimental shear strength, (b) normalized shear strength

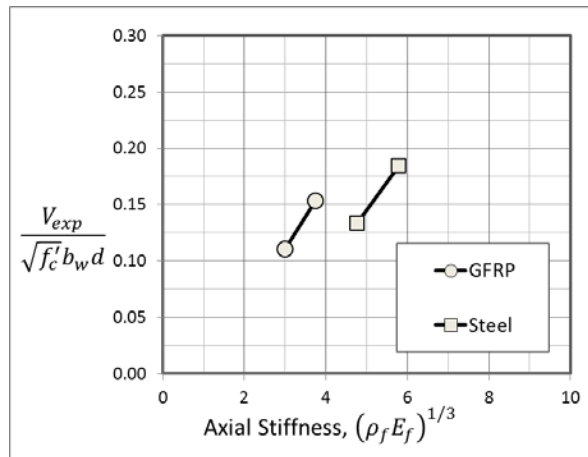
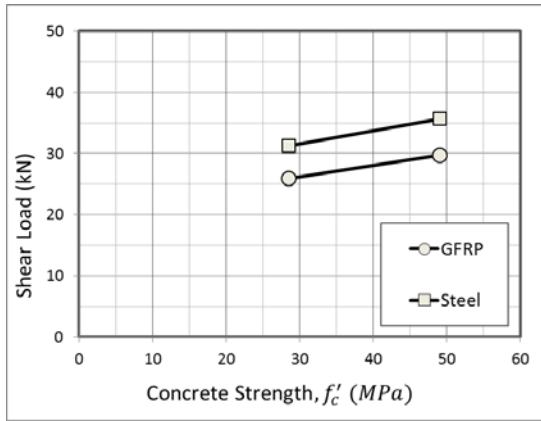


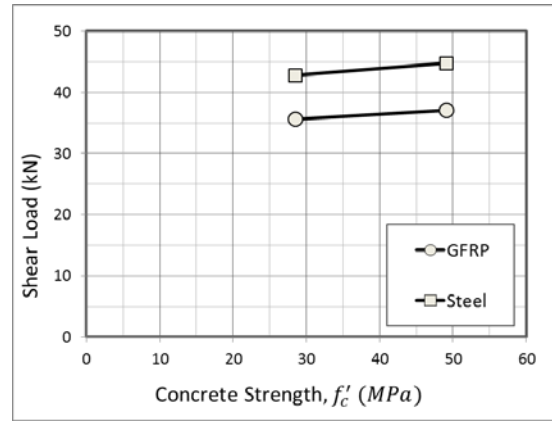
Figure 2.31: Variation of normalized shear strength with respect to the cubic root of the axial stiffness

4.3.2.3 Effect of Concrete Compressive Strength, f'_c

The effect of concrete strength was investigated best of reinforcement ratio (ρ) 52 % and 93%. The results of the beams in Group A3 with height equal to 250 mm and compressive strengths (f'_c) of 28.5 and 49.1 MPa are shown in Figure 2.32. For these beams, a slight increase in shear strength was observed for an increase in the concrete strength. Similar behaviour was observed for FRP reinforced slender beams by EI-Sayed et al. (2006).



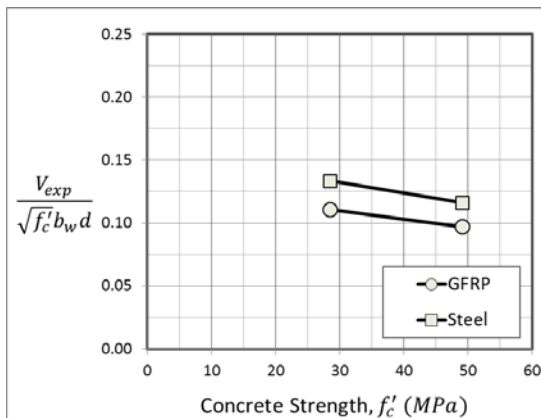
(a)



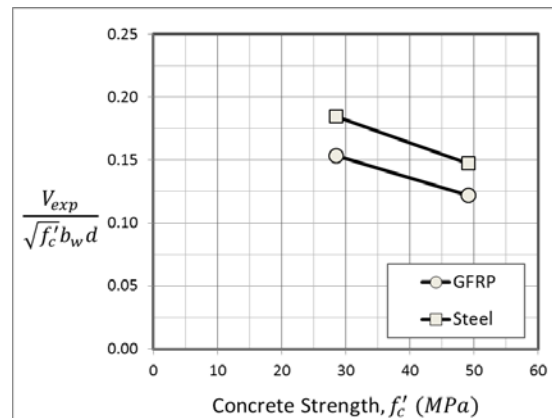
(b)

Figure 2.32: Effect of concrete compressive strength, experimental shear strength for 250 mm beams height with reinforcement ratios; (a) $\rho = 52\%$ and (b) $\rho = 93\%$.

However, the normalized shear strength ($V_{exp}/\sqrt{f'_c}b_wd$) shows a decreasing trend with an increase in the concrete strength (Figure 2.33). The decrease in normalized shear strength with an increase in the concrete strength can be explained by the decrease in shear resistance by the aggregate interlock. For high strength concrete, the crack passes through the aggregate reducing the aggregate interlock forces EI-Sayed et al. (2006).



(a)



(b)

Figure 2.33: Normalized shear strength for 250 mm beams height with reinforcement ratios; (a) $\rho = 52\%$ and (b) $\rho = 93\%$.

4.4 Comparison of experimental results with major design equations

4.4.1 Introduction

The shear strengths of the beams were predicted using the theoretical prediction methods of the design codes and guidelines for FRP reinforced concrete members, which include the American Concrete Institute (ACI) standard ACI 440.1R-06 (ACI 2006); Canadian Standards Association (CSA) standards CSA S806-02 (CSA 2002); the Japan Society of Civil Engineering (JSCE) standard (JSCE 1997); and Intelligent Sensing for Innovative Structures, Canadian Network of Excellence (ISIS 2007). All of these methods were discussed in Section 2.2. The predicted results were compared with the experimental results. The predicted shear strengths from different methods are presented and discussed in the following section.

4.4.2 Comparison of the results

The experimental shear strength of the testing data (V_{exp}) compared with shear strength (V_{theor}) for different shear design methods are shown in Table 2.10. For clarity, the results of major design methods (CSA, ACI, JSCE, and ISIS) are plotted as a bar chart in Figures 2.34 to 2.37 and these will be discussed. For consistency with different design methods, only the results of GFRP reinforced beams are shown. It should be noted that the material resistance factor (ϕ_c) and the concrete density factor (λ) in CSA S806-02 method were considered equal to 1.0, and member safety factor (γ_b) in JSCE (1997) design methods was considered equal to 1.3, while β_n was considered equal to 1.0 for sections without axial force resultant. It can be seen from Table 2.10 that the average ratios of the shear strengths between the experimental and the predicted values are conservative for all design methods. Notice that the JSCE (1997) and ISIS-M03-07 the methods predicted shear strengths are better than the other methods for all beams.

The statistical results from Table 2.10 show that the average and the standard deviation of V_{exp}/V_{theor} are greater than one for all four design methods. The ISIS method shows more consistent results than all other methods (Figure 2.34). This can be attributed to the fact that this method considers most of the shear strength parameters, which are believed to affect the shear strength. The average ratio predicted using this method is very close to 1.0, However, This method shows more

conservative results for beams BGN-A1-01, BGN-A1-02 and BGL-A3-02. On the other hand, the average and the standard deviation of V_{exp}/V_{theor} for ACI method are higher than the other methods. One of the possible reasons could be the fact that this method considers the shear strength for uncracked compression zone only and neglects any interface shear transfer. Another possible reason is that this method does not consider the shear span-to-depth ratio and size effect in shear, as shown in Figure 2.35. Although, the average ratio predicted using the CSA is high as shown in Figure 2.36, the standard deviation of the results are the second highest followed by ACI and the number of unconservative results is the highest for this method. The consistency in the ratios of the experimental to the predicted values in the JSCE method (Figure 2.37) is less than the CSA method.

Table 2.10: Comparison of the experimental results with different design methods

Group	Specimens ID	Exp.	ISIS M03-07	ACI 440.1R-06	CSA S806-02	JSCE (1997)	ISIS M03-07	ACI 440.1R-06	CSA S806-02	JSCE (1997)
		V_{exp}	V_{theor}	V_{theor}	V_{theor}	V_{theor}				
		(KN)	(kN)	(kN)	(kN)	(kN)	V_{exp}/V_{theor}	V_{exp}/V_{theor}	V_{exp}/V_{theor}	V_{exp}/V_{theor}
A1	BGN-A1-01	17.16	10.32	8.17	8.15	9.0	1.66	2.10	2.11	1.90
	BGN-A1-02	20.61	10.56	10.77	10.03	11.1	1.95	1.91	2.05	1.85
A2	BGN-A2-01	20.31	14.97	10.20	10.59	11.7	1.36	1.99	1.92	1.73
	BGN-A2-02	16.18	14.97	10.20	10.59	11.7	1.08	1.59	1.53	1.38
A3	BGL-A3-01	25.90	23.35	12.76	14.05	15.2	1.11	2.03	1.84	1.70
	BGL-A3-02	35.60	24.09	17.13	17.38	18.8	1.48	2.08	2.05	1.89
	BGH-A3-03	29.76	30.65	14.75	16.84	17.9	0.97	2.02	1.77	1.66
	BGH-A3-04	37.10	31.62	19.88	20.83	22.2	1.17	1.87	1.78	1.67
Mean =							1.08	1.56	1.50	1.38

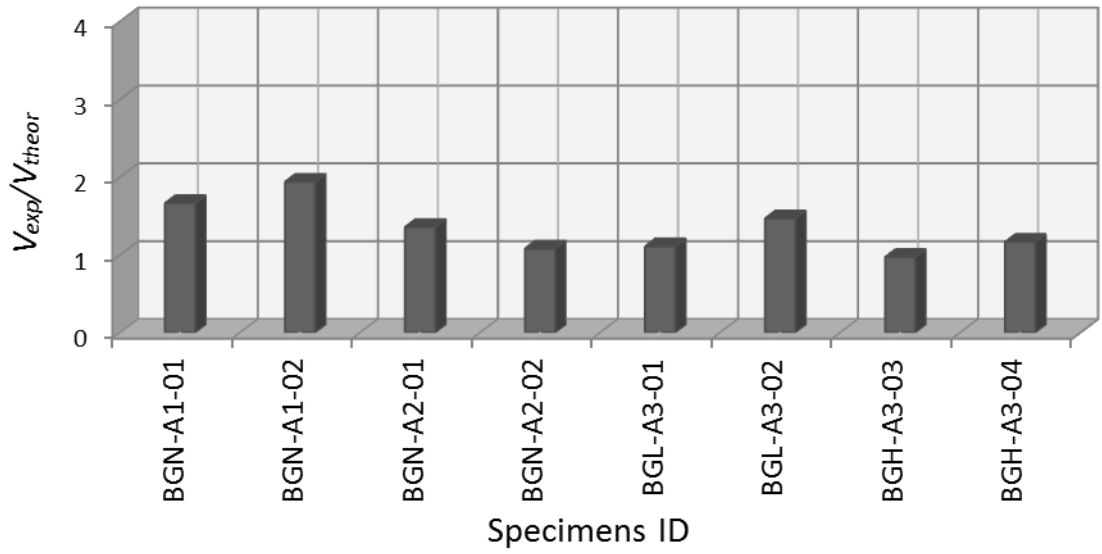


Figure 2.34: Comparison of the experimental results with ISIS M03-07 predictions

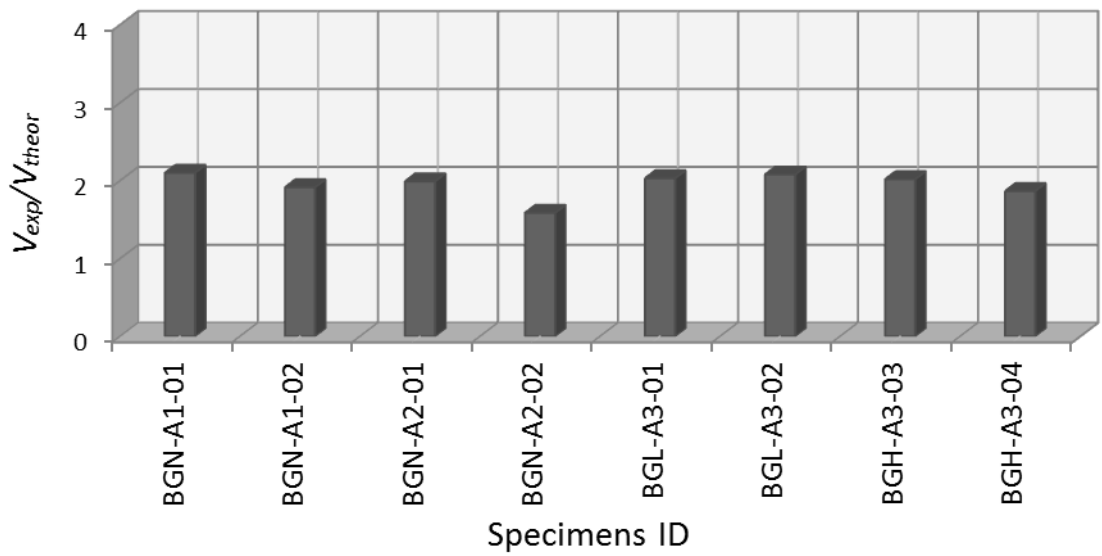


Figure 2.35: Comparison of the experimental results with ACI 440.1R-06 predictions

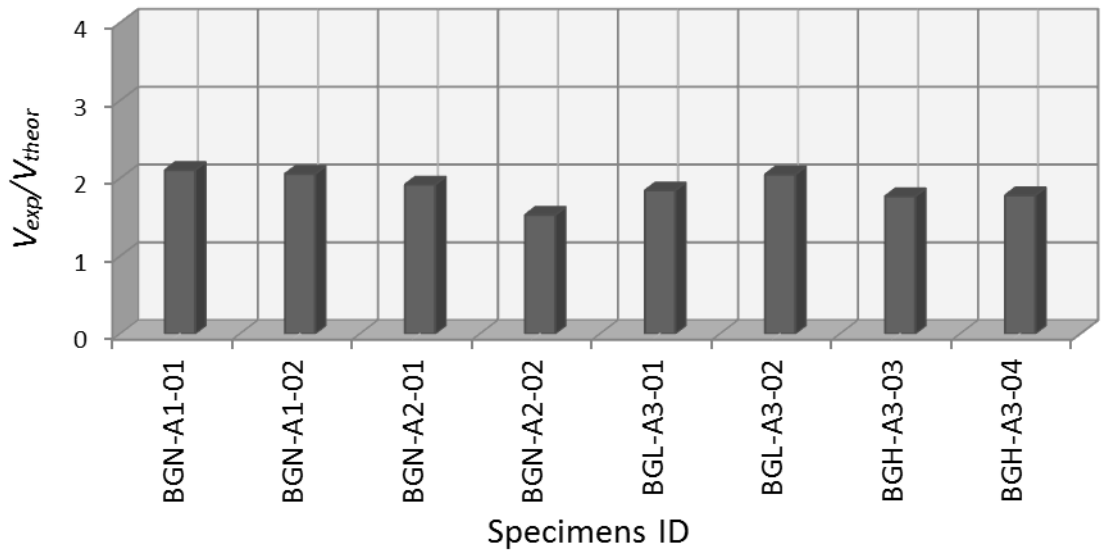


Figure 2.36: Comparison of the experimental results with CSA S806-02 predictions

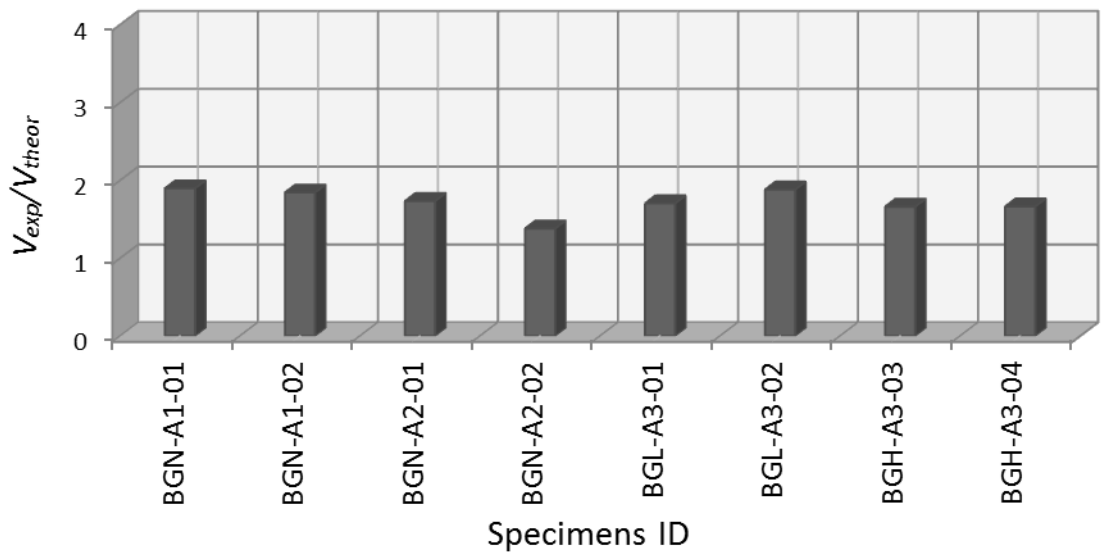


Figure 2.37: Comparison of the experimental results with JSCE (1997) predictions

5.0 Conclusion

Eight concrete beams reinforced with GFRP bars and six control concrete beams reinforced with steel bars were tested until failure. In order to realize the occurrence of shear failure, all tested beams were designed reinforced with longitudinal reinforcement only and without shear reinforcement. The beams were simply supported and subjected to two point loads and known as four point bending test in laboratory. Based on the Experiment results, Theoretical values and Analytical Results, analysis purposes are to investigate the influence of four parameters on the behaviour and shear strength of concrete beams. The parameters were the shear span-to-depth ratio (a/d), longitudinal reinforcement ratio (ρ), concrete compressive strength (f'_c), and reinforcement type. The following Conclusions can be drawn from the experimental investigation:

1. Beams reinforced with GFRP bars showed similar shear behaviour compare to that of beams reinforced with steel. However the shear strength of beams reinforced with GFRP bars lower than that beams reinforced with steel bars. This fact is due to the low elastic modulus of GFRP bars.
2. The load-deflection behaviour of the beams before cracking was governed by the gross section properties of the beams, and the behaviour after cracking was approximately directly proportional with the axial stiffness of the reinforcing bars. The beams reinforced with GFRP reinforcement exhibited much greater deflections than those with steel reinforcement. In addition, shear crack widths, measured at the same load levels, were also generally larger for the GFRP RC beams than those observed in the equivalent steel RC beams
3. The ratio of longitudinal reinforcement, ρ is directly proportional with the capacity of beam. The distance of beam consisting GFRP bars and control beam also influence with ρ , when the ρ is increasing the distance of cracking increasing also. The value of angle shear cracking also reduces when the ratio of longitudinal reinforcement ρ is increasing.
4. An inclined crack was formed for almost all of the beams before failure. The angle of the inclined crack, at failure, decreased with an increase in a/d . For

beams with the same a/d , the angle of inclined cracks at failure was almost the same for different reinforcement types and concrete strengths.

5. Most of the beams in this investigation failed in shear. The observed failure modes were shear-tension, shear-compression, or diagonal-tension. For one beam, a bond/anchorage failure was observed.
6. Comparisons between shear capacity calculated from four different methods recently developed in the literature and that measured in the current study show inconsistent agreement as shown in Table 2.10.

6.0 Recommendation

There are some recommendations that can be suggested to improve the usage of GFRP bars as reinforce in concrete.

1. All tested beams in this Research were reinforced with longitudinal reinforcement only and without shear reinforcement. Do more research on concrete beams reinforced with GFRP bars with consist shear reinforcement.
2. Research can be done on performance of other structural members with GFRP bars such as columns, shear wall and slabs.
3. Considerations on the elastic modulus and proper design method are important when GFRP bars are to be used as reinforcement for concrete beam.
4. Further experimental and analytical studies should be conducted to investigate the shear behaviour of concrete beams reinforced with GFRP bars with a wider range of reinforcement ratios and for both normal and high strength concrete.
5. Since the current experimental work was carried out using only GFRP reinforcement, similar experiments should be conducted on concrete beams reinforced with CFRP or AFRP to be able to formulate general design rules for shear behaviour of concrete beams reinforced with FRP bars.

6. A series of continuous FRP reinforced concrete beams should be tested under different loading configurations in order to compare the experimental shear strength with theoretical values. For instance, in a two span continuous beam under symmetrical point loads, the load may be applied at various distances from the middle support.

7.0 References

ACI Committee 318 (1995), "Building Code Requirements for Reinforced Concrete (ACI 318M-95) and Commentary (ACI 318RM-95)," Detroit, Michigan.

ASCE-ACI Committee 426 (1973), "The Shear Strength of Reinforced Concrete Members," Journal of Structural Division, ASCE, Vol. 99, No. ST6.

ASCE-ACI Committee 445 on Shear and Torsion (1998), "Recent Approaches to Shear Design of Structural Concrete, Journal of Structural Division, ASCE. Vol. 124. No 12.

ACI Committee 440 (2006). "Guide for the Design and Construction of Structural Concrete Reinforced with FRP Bar(ACII 440.1R-06)," Farmington Hills. Mich.

Bažant, Z. P. and Kazemi, M. T. (1991), "Size effect on Diagonal Shear Failure of Beams without Stirrups." ACI Structural Journal, Vol. 88. No. 3.

Bischoff, P. H. and Paixao, R. (2004), "Tension Stiffening and Cracking of Concrete Reinforced with Glass Fibre Reinforced Polymer (GFRP) Bars," Canadian Journal of Civil Engineering, Val. 31.

Canadian Standard Association (2002). "Design and Construction of Building Components with Fibre Reinforced Polymers." CSA 5806-02, Rexdale, Ontario. Canada

EI-Sayed, A. K.; EI-Salakawy, E. F, and Benmokranc, B. (2006), "Shear Strength of FRP-Reinforced Concrete Beams without Transverse Reinforcement," ACI Structural Journal, V. 103, No.2.

Faza, S. S. and Gangarao, H. V. S. (1993). "Theoretical and Experimental Correlation of Behaviour of Concrete Beams Reinforced with Fibre Reinforced Plastic Rebars," fibre-Reinforced-Plastic Reinforcement for Concrete Structures-International Symposium, SP-138, A. Nanni and C. W. Dolan, eds., American Concrete Institute, Farmington Hills, Mich.

Gopalaratnam, V.S. and Shah, S. P. (1985), "Softening Response of Plain Concrete in Direct Tension," ACI Journal, Vol. 82. No. 3.

ISIS-M03-07 (2007), "Reinforcing Concrete Structures with Fibre Reinforced Polymers," The Canadian Network of Centers of Excellence on Intelligent Sensing for Innovative Structures, ISIS Canada, University of Winnipeg, Manitoba.

Japan Society of Civil Engineers (JSCE) (1997), "Recommendation for Design and Construction of Concrete Structures using Continuous Fiber Reinforcing Materials," Research Committee on Continuous Fibre Reinforced Materials, A. Mochida, ed. Tokyo, Japan.

MacGregor, J. G. and Bartlett, F. M. (2000), "Reinforced Concrete: Mechanics and Design," First Canadian Edition.

MacGregor, J. and Wright, J. K. (2005). "Reinforced Concrete Mechanics and Design." 4th. ed. New Jersey: Pearson Prentice Hall. 209 – 216.

Michaluk, C. R.; Rizkalla, S. H.; Tadros, G.; and Benmokrane, B. (1998). "Flexural Behaviour of One-way Slabs Reinforced by Fibre Reinforced Plastic Reinforcement," ACI Structural Journal Vol. 95, No. 3.

Nanni, A. (1993), "Flexural Behaviour and Design of Reinforced Concrete Using FRP Rods," Journal of Structural Engineering, ASCE, Vol. 119. No 11.

Nawy, E.D. (2003). "Reinforced Concrete: A Fundamental Approach." Prentice Hall. Fifth Edition, New Jersey: Pearson Education, Inc. 149 – 156

Razaqpur, A. G.; Isgor, B. O.; Greenway, S.; and Selley, A. (2004), "Concrete Contribution to the Shear Resistance of Fibre Reinforced Polymer Reinforced Concrete Members," Journal of Composites for Constructions, ASCE, Vol. 8, No.5.

Razaqpur, A. G.; Isgor, B. O. (2006), "Proposed Shear Design Method for FRP-Reinforced Concrete Members without Stirrups," ACI Structural Journal, Vol. 103, No. 1.

Rebciz, K. S. (1999), "Shear Strength Prediction for Concrete Members," Journal of Structural Engineering, ASCE, Vol. 125, No. 3.

Reineck, K. H. (1991), "Ultimate Shear Force of Structural Concrete Members without Transverse Reinforcement Derived from a Mechanical Model," ACI Structural Journal, Vol. 85, No. 5.

Sonobe, Y. (1997). "Design Guidelines of FRP Reinforced Concrete Building Structures," Journal of Composite for Construction, ASCE, Vol. 1, No.3.

Thamrin, R., Abdul Aziz Abdul Samad, Noor Azlina Abdul Hamid (2009). "Evaluation On Shear Capacity And Tension Force Of Longitudinal Reinforcement Of RC Beams With FRP Bars." Proceedings Of APSEC 2009 & EACEF 2009. 2. 424-430.

Tureyen, A. K. and Frosch, R. J. (2002), "Shear Test of FRP-Reinforced Concrete Beams without Stirrups," ACI structural Journal, Vol. 99, No. 4.

Tureyen, A. K. and Frosch, R. J. (2003), "Concrete Shear Strength: Another Perspective," ACI Structural Journal, Vol. 100, No. 5.

CHAPTER 3

DEBONDING PHENOMENON, OF FRP COMPOSITES APPLIED TO A CONCRETE SURFACE, A STATE-OF- THE ART

1.0 Introduction

Fibre reinforced polymer (FRP) composites materials have experienced a continuous increase of use in structural strengthening and repair applications over the past decades. Thus such, the flexural strength of reinforced concrete (RC) beams can be increased significantly by externally bonded FRP sheets. Several issues related to the structural performance of FRP strengthened RC elements have been studied. Among them, the interfacial debonding mechanism between FRP composites and concrete substrate may be the most fundamental one, as debonding is brittle and often occurs in a thin layer of concrete close to the FRP composite.

Bond behavior is influenced by the physical and mechanical properties of the FRP composite, concrete dimensions and properties, adhesive properties and loading conditions as shown in Table 3.1; the influencing factors are:

Table 3.1. Factors affecting the bond behavior

Elements	Influencing Factors
Concrete	Modulus of elasticity, strength, thickness, surface condition
FRP Composite	Modulus of elasticity, strength, thickness, type, surface condition, stiffness, width effect, length effect
Adhesive	Modulus of elasticity, strength, number of plies, thickness, type, glass transition temperature, spread
Loading Condition	Load speed, Bending, shearing, punching, cyclic

2.0 Failure modes in FRP-concrete bond system

Many experimental investigations have been concerned with failure modes of reinforced concrete beams and slabs strengthened with FRP laminates Ritchie et al. (1991), Saadatmanesh and Ehsani (1991), Chajes et al. (1994), Shahawy et al. (1996), Arduini and Nanni (1997), Maalej and Bian (2001), Smith and Teng (2001), Sayed-Ahmed et al. (2009), Oehlers (2005), and Lu et al. (2005). It is worth noting that the terminology used to describe the various failure modes varies within the literature. The failure modes of concrete beams and slabs strengthened by plate bonding can be classified into two categories based on the duration of composite action between the materials *fib* Bulletin (2001). i) Flexural or Classical Failure Modes (Full Composite Action): When composite action is maintained until the ultimate load is reached, failure can occur in one of three modes depending on the reinforcement ratio and the shear strength of the beam:

- Concrete crushing prior to or following yielding of the steel reinforcement.
 - Tensile rupture of the FRP.
 - Shear failure of the concrete beam.
1. Concrete crushing: Concrete crushes in the compression zone before or after the yielding of the inner reinforcing steel, while the FRP composite is intact. This mode of failure will be brittle and undesirable particularly if the concrete crushes before steel yielding.
 2. FRP rupture: For relatively low ratios of both internal and external reinforcements, failure may occur through tensile fracture of the FRP strip.
 3. Shear failure: The reinforced concrete beam may reach its shear limit prior to any kind of flexural failure if it is not properly reinforced in shear.

Generally, Failure can take place by concrete crushing in compression, steel yielding followed by concrete crushing, steel yielding followed by FRP rupturing, and FRP debonding Buyukozturk et al. (2004)

However, when composite action is not maintained until the ultimate load is reached, premature failure results from debonding of the FRP laminates, termed: ii) Debonding Failure Modes (Loss of Composite Action): when a reinforced concrete beam is subjected to the external forces, high tensile and shear forces develop

through the beam. These stresses contribute to debonding of the FRP plate from the substrate.

Debonding failures occur before the full strength of the FRP sheet has been reached and the majority of research has scrutinized the debonding failure mode for several reasons.

One reason is that debonding is the most common mode of failure observed in flexural strengthened with FRP Buyukozturk et al. (2004). Second, when debonding occurs, the full FRP capacity is lost with loss of composite action Teng and Chen (2007), so require increased attention by structural engineers. For these reasons, it is important to understand and be able to accurately predict the behavior of bonded FRP sheets.

Debonding failure may occur at one of the following different interfaces as shown in Figure 3.2 through Smith and Teng (2002), Teng et al. (2002), Lu et al. (2005), Oehler et al. (2003), Teng et al. (2004), Teng and Chen (2007).

Debonding failures can be further grouped into two categories;

- Plate-end interfacial debonding Figure 3.2. (d) and (e).
- Intermediate (flexure or flexure shear) crack- induced interfacial debonding Figure 3.2. (f) and (g)

1. Intermediate crack induced debonding (IC Debonding): where it initiates at flexural or flexural-shear crack in the high moment region. The debonding crack then grows towards one of the laminate ends.
2. Plate end interfacial debonding (End plate debonding, EPD): where it initiates at the termination of the FRP sheet, and then propagates toward the mid-span of a concrete beam. The failure can either travel up to the tensile reinforcement and then along the reinforcement, so that the concrete cover debonds, which is termed concrete cover separation, or it can propagate at the FRP-concrete interface, which is termed plate end interfacial debonding. This debonding failure is depends on properties of the materials as well as the interface between FRP and the substrate (Gunes et al. 2013).

Probable debonding scenarios are illustrated in Figure 3.1. Whereas, Figure 3.2. illustrates the possible failure modes for strengthened flexural RC member.

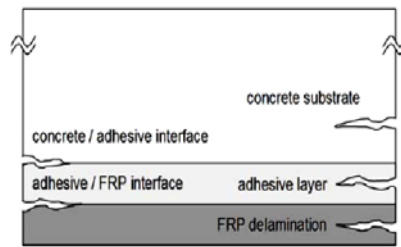


Figure 3.1. Possible debonding locations

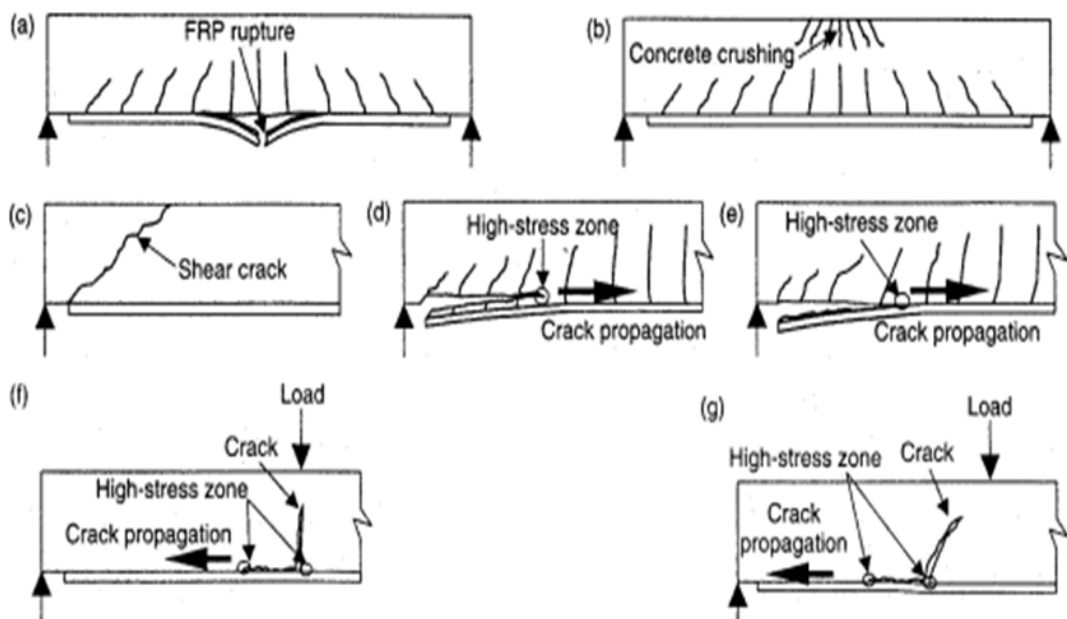


Figure 3.2. Illustrates the possible failure modes for strengthened flexural RC member

3.0 Test setups and methods

Many test setups have been used in the past to determine FRP-to-concrete bond behavior and strength. An accurate bond strength model is necessary to accurately predict failures of FRP shear and flexurally strengthened RC beams, since failure is very often due to debonding. Chen et al. (2001) grouped existing experimental test setups into five types: (a) double-shear pull (Double Pull) test; (b) double-shear push (Double Push) test; (c) single-shear pull (Single Pull) test; (d) single-shear push (Single Push) test; and (e) beam (or bending) test (Beam Test). Yao et al. (2005) renamed these test setups (a) far end supported (FES) double-shear test; (b) near end

supported (NES) double-shear test; (c) far end supported (FES) single-shear test; and (d) near end supported (NES) single-shear test, These definitions are based on the loading condition in the concrete block and on the symmetry of the specimens, which are shown in Figures 3.3 to 3.5.

In single shear pull/push tests and double shear pull/push tests setups the FRP is directly pulled from the concrete block by tensile force. For better clarity, all these four tests may be referred to as pull tests, as the FRP is always directly pulled by a tensile force.

The double shear pull test and the single shear pull test are the most popular test setups among researchers because of their simplicity Van Gemert et al. (1999), Chen et al. (2001), Ueda and Dai (2005), Yao et al. (2005) and Nakaba et al. (2001). The results of both numerical and experimental studies have been conducted the use of different test setups can lead to significantly different test results Chen et al. (2001) and Yao et al. (2005). Little difference can be expected between the double and single shear push tests and between the double and single shear pull tests Chen et al. (2001). it has also been reported that small variations in test setups within each test method such as the height of the support block may also have significant effects based on a recent stress analysis. Therefore, significant difference may exist between these two methods Chen et al. (2001).

A considerable number of studies based on Single Pull test setup have been published of which some of them are reported here Chajes et al. (1996), Taljsten (1997), Bizindavyi and Neale (1999), Dai et al. (2005), Xia and Teng (2005), Yao et al. (2005), Pan and Leung (2007), Subramaniam et al. 2007, Mazzotti et al. (2008), Bilotta et al. (2009) and Woo and Lee (2010). some researches that applied double shear pull test setup are Nakaba et al. (2001), Xiao et al. (2004), Yang et al. (2007), Zhao et al. (2007) and Cao et al. (2007).

The single shear push test can offer savings in both materials and labour because only one plate coupon is bonded to the concrete Chen et al. (2001). The double pull tests are more suitable for standard universal testing machines, which enable the application of different loading procedures at different loading speeds, including cycling loading and fatigue tests. This is one reason why they are used more commonly among researchers Van Gemert (1980), Kobatake et al. (1993), Yoshizawa et al, (1996), Brosens and van Gemert (1997), Hiroyuki and Wu (1997),

Maeda et al. (1997), Horiguchi and Saeki (1997), Ueda et al. (1999) and Casareto et al (2003).

The Single Push tests are the second most popular tests after the Double Pull tests. It was used by Täljsten (1994, 1997), Chajes et al (1995, 1996), Bizindavyi and Neale (1997, 1999), Yoshizawa et al (1996), Oehlers and Seracino (2004), McSweeney and Lopez (2005) and Yao et al (2005).

In double push test Figure 3.3(b), the pushing force acting on concrete prism is usually applied through a supporting wedge Swamy et al. (1986) and Neubauer and Rostásy (1997). In this setup the stresses generated are applied through compressive forces in the concrete prism, instead of tensile forces applied on FRP, as in the case of double pull test. This difference may lead to discrepancies among test results Chen et al. (2001), as well as the mechanism of fracture.

The Single Pull test, shown in Figure 3.4(c), although no studies appear to have used such test setup in the past Chen et al. (2001). In this case only one FRP sheet is bonded on one side of the concrete block. This leads to loss of symmetry, unlike the Double Pull tests Chen et al. (2001).

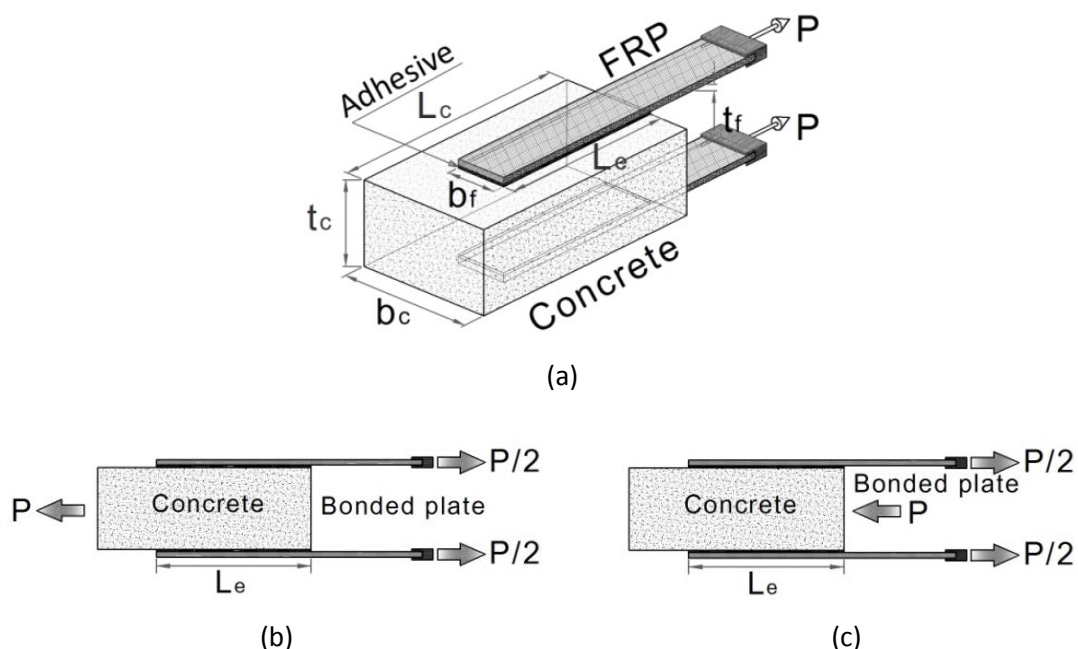


Figure 3.3. Double shear test (a) plan, (b) double shear push test, and (c) double shear pull test

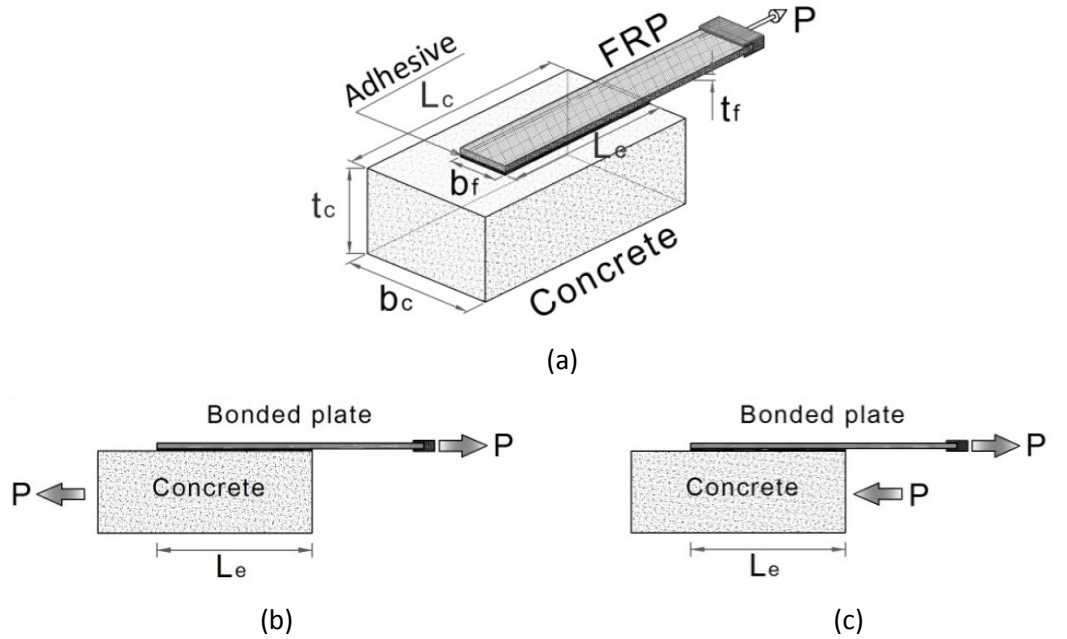
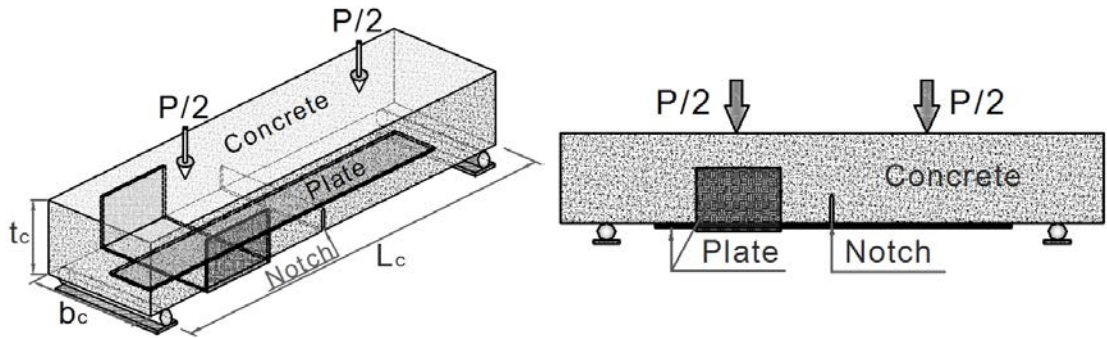


Figure 3.4. Single shear test (a) plan, (b) Single shear push test, and (c) Single shear pull test

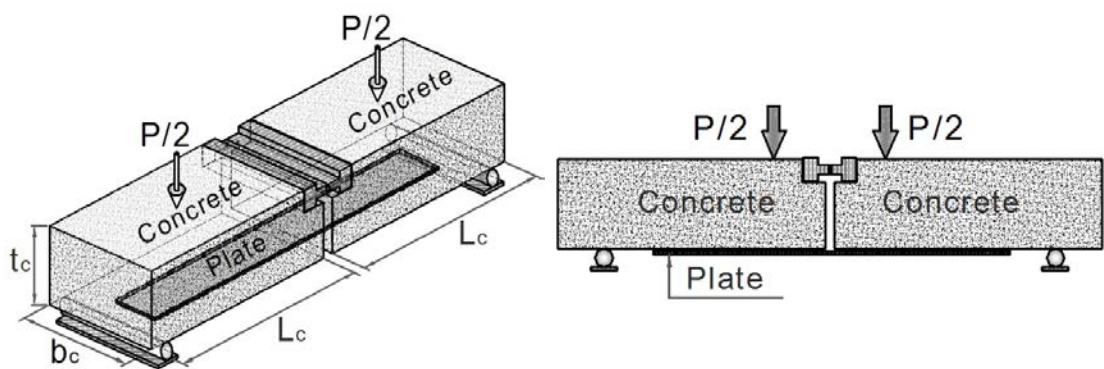
As well as the unidirectional tests mentioned above, Figure 3.5. shows Beam Tests, conducted for the purpose of investigating the mechanism of bond in flexural members. One form of a beam test setups, shown in Figure 3.5(a) may consist of a concrete beam with a saw cut (notch) in the middle when the beam is under the load, the crack grows from the notch to the top joint. Therefore, the crack location is predetermined before the test. Figure 3.5(b) shown that two pieces of concrete blocks joined by a steel hinge on the top forming a simply supported beam, subjected to point loading, this set-up can simulate the effects of moment variation and shear force along the length of the concrete block. Similar test setups were adopted by van Gemert (1980) to investigate the bond behavior of surface bonded steel plates on concrete beams. Ziraba et ai. (1995) also used a similar setup to investigate the effect of concrete compressive strength on steel-concrete bond strength. In this case, the researchers used a solid beam, cut a certain depth to create a weak section, with a steel sheet surface bonded over the cut as shown in Figure 3.5(c).

Ziraba et ai. (1995) found no dependence of the failure of the joint to concrete strength and concluded that the concrete-glue-plate interface behavior was rather a surface phenomenon. However, this contradicted with other experimental observations Chajes et al (1996), Horiguchi and Saeki (1997), De Lorenzis et al.

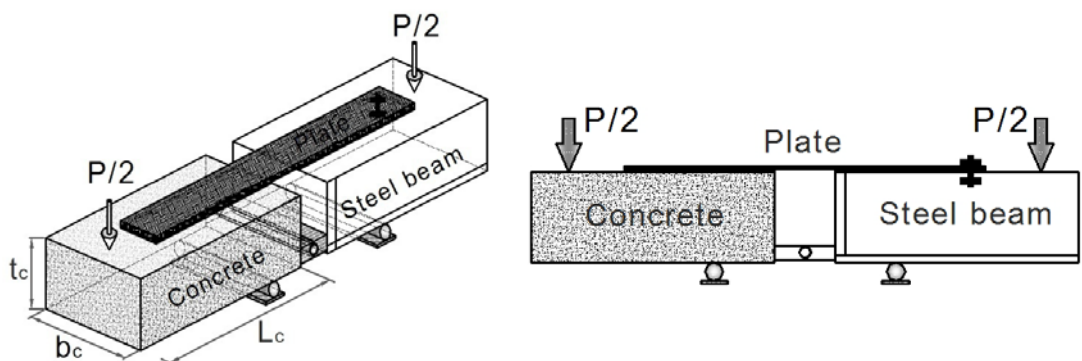
(2001) and Dai et al (2005). Some recent studies in which beam test set-up have been used to investigate the bond behavior are De Lorenzis et al. (2001), Perera et al. (2004), Xiao et al. (2004), Guo et al. (2005) and López et al. (2012).



(a) Beam test



(b) Beam test, Van Gemert (1980)



(c) Modified beam test, Ziraba et al. (1995)

Figure 3.5. Beam Test

4.0 Bond stress-slip relationship

Among the interface parameters have been proposed for bond strength, effective bond length (L_e), and bond stress (τ)-slip (s) (interface shear stress vs. relative slip between FRP and concrete) relationship. In order to evaluate the interfacial debonding mechanism between FRP composites and concrete substrate the τ - s relationship is of fundamental importance. A number of τ - s relationships have been developed by different researchers Focacci et al. (2000), Nakaba et al. (2001), Yuan et al. (2004) and Lu et al. (2005), which differ to each other because of different shapes used in each of the study including: (a) Cutoff type, (b) Elasto-plastic type, (c) Bi-linear type and (d) Popovics type, Sato et al. (1997), De Lorenzis et al. (2001), Nakaba et al. (2001), Sato et al. (2001) and Yoshizawa et al. (2000).

When using the cutoff type or elasto-plastic type model, it is necessary to be careful because these models are unrealistic. The bilinear type model Brosens and Van Gemert (1997) and Brosens (2001) is divided into an elastic ascending part and plastic descending part based on experimental data. The maximum bond stress in the elastic part is defined as τ_{max} , with s_0 the relative slip corresponding to τ_{max} . The end of the plastic part, which corresponds to zero bond stress, has a relative slip s_f . The Popovics type model Nakaba et. al. (2001) originated from Popovics numerical approach for a complete concrete stress-strain relationship Popovics (1973). The surface area underneath the bond stress-slip relationships expresses the fracture energy (G_f) of the bond system.

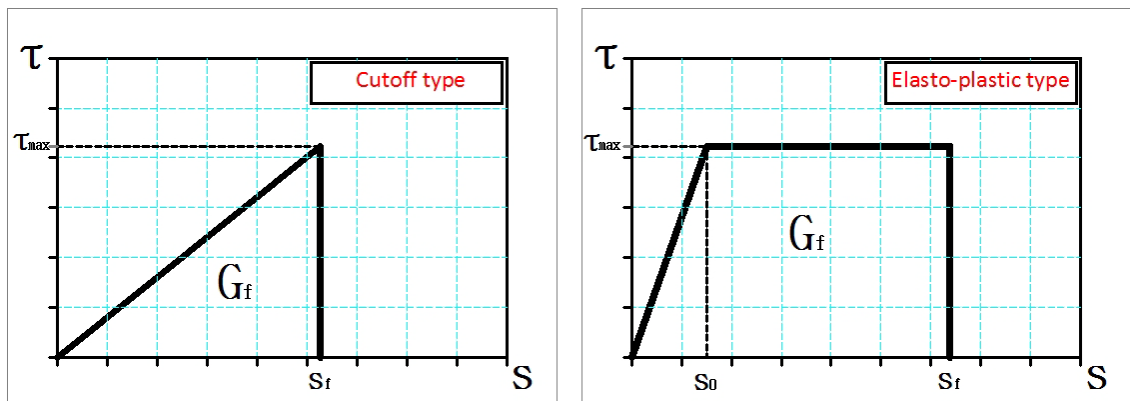


Figure 3.6. Bond stress-slip relationship

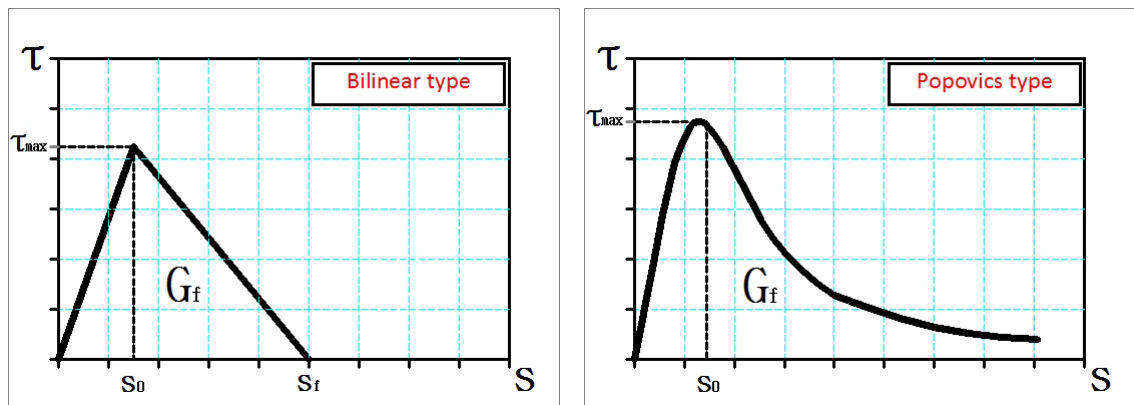


Figure 3.6 (cont.). Bond stress-slip relationship

Those differences may be due to different interfacial material properties (e.g., concrete strength, FRP stiffness) or the bonding skills (the deviations of concrete surface conditions or the adhesive's thickness) applied in different researches. In addition, the large scattering among the experimentally observed bond stress-slip relationships in different interfacial locations may be another factor, which effects on the shapes of the τ - s relationships and the calibration of the needed empirical parameters. However, even though a number of models of interfacial bond between FRP sheets and concrete have been proposed regarding the bond stress-slip relationship proper bond stress-slip model has yet to be generally accepted due to its complexity and many parameters.

5.0 Current bond-slip models

Local bond-slip (τ - s) model for FRP-concrete interface is of fundamental significance towards accurate modelling and therefore deeply understanding of failures due to debonding of the external reinforcement, as well as to estimate interfacial fracture energy G_f as the area under curve. Many of different τ - s models available in the existing literature (Brosens and Van Gemert 1999; Neubauer and Rostasy 1999; Brosens 2001; Nakabaet. al. 2001; De Lorenzis et al. 2001; Monti et al. 2003; Ueda et al. 2003; Savioa et al. 2003; Dai and Ueda 2003; Dai et al. 2005

and Lu et al. 2005). They have been compared with each other based on various types of models; they are characterized by the following fundamental parameters:

- The maximum local bond stress τ_{max}
- The slip s_0 when the bond stress reaches τ_{max}
- The local slip when the local bond stress reduces to zero (maximum slip) s_f

In order to make an equitable comparison, all models studied have been sorted based on parameters related to FRP, parameters related to adhesives, and parameters related to concrete substrate. Those models include:

- The bond -slip relationships $\tau - s$
- The maximum local bond stress τ_{max}
- The slip s_0 when the bond stress reaches τ_{max}
- The local slip when the local bond stress reduces to zero (maximum slip) s_f
- The width ratio factor β_w
- The interfacial fracture energy G_f

The summary of the equations defining the models is given here, while complete details are given in the original references, where τ (MPa) is the local bond stress, s (mm) is the local slip, τ_{max} (MPa) is the maximum local bond stress, s_0 (mm) is the slip when the bond stress reaches τ_{max} ((some of references using: s_{peak} or s_τ)), s_f (mm) is the local slip when the local bond stress reduces to zero (maximum slip) ((some of references using: s_{ult} or s_{max})), s_e (mm) is the elastic component of local slip, G_f (N/mm) is the interfacial fracture energy, β_w is the width ratio factor ((some of references using k_b)), f_c (MPa) is the concrete compressive cylinder strength, f_t (MPa) is the concrete tensile strength, E_c (MPa) is the elastic modulus of concrete, b_c (mm) is the width of concrete prism, t_c (mm) is the effective thickness of concrete contributing to shear deformation, b_f (mm) is the width of FRP, t_f (mm) is the thickness of FRP, E_f (MPa) is the elastic modulus of FRP, t_{ref} is various with the maximum size of aggregate, t_a (mm) is the thickness of adhesive layer, E_a (MPa) is the elastic modulus of adhesive, t_m (mm) is the thickness of epoxy mortar layer, E_m (MPa) is the elastic modulus of epoxy mortar layer, G_a is the elastic shear modulus of adhesive, G_c is the elastic shear modulus of concrete, K_a the shear stiffness of the adhesive layer $K_a=G_a/t_a$, and K_c is the shear stiffness of concrete.

Chen and Teng (2001) many of different τ - s models have been advanced in the last few years. They may be classified into three categories: empirical models based directly on the regression of test data, fracture mechanics models, finite element analysis.

5.1 Empirical models

Empirical-based models are mainly determined by regression of the interface parameters based on experimental data. The formulation of these models is quite simple and the results of these models show that high variation. This is because of the fact that the bond parameters are derived for specific experimental conditions such as, test set-up and type instrumentation, materials (concrete, adhesive or FRP plate), and loading regime, these conditions may change from one experiment to the other.

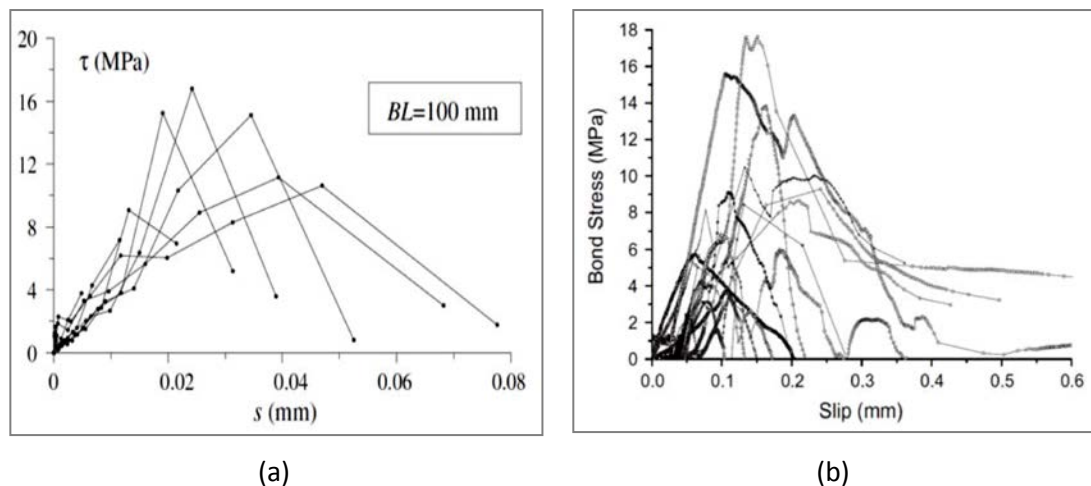


Figure 3.7. Local bond-slip curves reported in literature (a) Mazzotti et al. (2008) and (b) Liu and Wu (2012).

In the majority of the researches, the interface behavior is may characterizes by the bond strength and more importantly the local shear stress-slip profiles which is called the local interface law. Figure 3.7 shows the bond-slip relationships derived from the experiments. The local slip at any location can be derived from the strain values by integration of the strain profile along the bond length to that position while shear stress is obtained from the production of FRP stiffness and the gradient of the axial strain of the FRP strip.

5.1.1 De Lorenzis et al. (2001)

De Lorenzis et al. (2001) followed Täljsten's (1996) analytical model but proposed an elastoplastic bond slip model based on their experimental data. The maximum shear stress, measured in MPa, can be expressed by

$$\tau_{max} = 0.0182\sqrt{nE_f t_f} \quad (1)$$

5.1.2 Chen and Teng (2001)

Based on the work of Chen and Teng (2001) and Yuan et al. (2001) concluded that typical values of slip corresponding to the maximum shear and local failure for surface bonded FRP on concrete were 0.02mm and 0.2mm, respectively. Through the regression analysis of experimental test data, it was shown that the analytical values matched well with the experimental data for bond strength and effective bond length, it also was stated that the bond strength was strongly consideration of significant effect of width ratio. Chen and Teng (2001) proposed that ultimate bond strength given as.

$$P_u = 0,427\beta_p\beta_l\sqrt{f'_c}b_pL_e \quad (1)$$

where

$$\beta_p = \sqrt{\frac{2 - b_p/b_c}{1 + b_p/b_c}} \quad (2)$$

b_p is the width of the bonded plate and b_c is the width of the concrete member in mm.

$$\beta_l = \begin{cases} 1 & L \geq L_e \\ \sin\left(\frac{\pi L}{2L_e}\right) & L < L_e \end{cases} \quad (3)$$

L is the bond length, L_e is the effective bond length in mm and

$$L_e = \sqrt{E_p t_p \sqrt{f'_c}} \quad (4)$$

in which t_p (mm) and E_p (MPa) is the thickness and Young's modulus of the bonded FRP plate, respectively. f'_c is the cylinder concrete compressive strength in MPa.

5.1.3 Dai et al. (2005)

Dai et al.'s model using regression analysis of experimental data, proposed a new single curve bond-slip model, accounting for the effect of the adhesive through its shear modulus G_a and thickness t_a , Bond stress development as a function of slip was expressed as:

$$\tau = 2BG_f(\exp(-Bs) - \exp(-2Bs)) \quad (1)$$

$$s_0 = 0.693/B \quad (2)$$

where

$$B = 6.846(E_f t_f)^{0.108} (G_a/t_a)^{0.833} \quad (3)$$

The fracture energy is given by Equation:

$$G_f = 0.446(E_f t_f)^{0.023} (G_a/t_a)^{-0.352} (f_c)^{0.236} \quad (4)$$

In the above equations, G_a and t_a are the modulus and the thickness of the adhesive, respectively. In this case, the thickness was measured microscopically after the test specimens failed. The maximum bond stress can be expressed as:

$$\tau_{max} = 0.5BG_f \quad (5)$$

5.2 Fracture mechanics based models

The use of a fracture mechanics-based approach is extremely attractive since, in principle, it can potentially capture the critical aspects related to interfacial mechanics and failure initiation and propagation. In spite of the powerful analytical tools that fracture mechanics offer, most existing theoretical models have been developed on the basis of simple bond tests (single-lap or double-lap shear tests of FRP-bonded concrete prism, or idealized flexural test). That is why they cannot replicate complicated stress conditions as affected by cracks that can be seen in actual structural systems. Experimentally obtained models also tend to involve too

many parameters to be considered of practical use. In some cases these models were modified through the use of parameters that represent physical/mechanistic conditions, but derived empirically by curve fitting (Karbhari et al. 2006).

Vilnay (1988) was among the first researchers who adopted a theoretical approach to describe the bond behavior of surface bonded FRP. Vilnay developed an analytical model and applied it to a composite beam with externally bonded steel plate. Vilnay obtained an expression for the maximum bond stress from the moment-deflection differential equation.

Several researchers presented analytical models using the principles of fracture mechanics. Among them are; Holzenkämpfer (1994), Täljsten (1994), Brosens and van Gemert (1998), Yuan and Wu (1999), Yuan et al. (2001) and Wu et al. (2002). The fracture-mechanics based models are based on experimentally observed bond-slip relationships. Various empirical bond-slip relationships pertaining to the FRP-concrete interface were proposed based on specific sets of experimental observations. Figure 3.8 shows some bond-slip models in the literature. A number of analytical relationships were also developed based on mechanics. The variety of shapes used in describing the bond-slip phenomenon demonstrates the difficulty in defining reliable and comprehensive relationship based on simplistic tests, short bond transfer length, and local geometric and material variations. It is noted that the use of fracture mechanics implicitly leads to a very simple generic expression for the determination of bond capacity, related only to the FRP stiffness and interfacial fracture energy (defined as the area beneath the bond stress-slip curve), no matter what type of interfacial constitutive law is adopted Täljsten (1996), Yuan et al. (2001) and Wu et al. (2002).

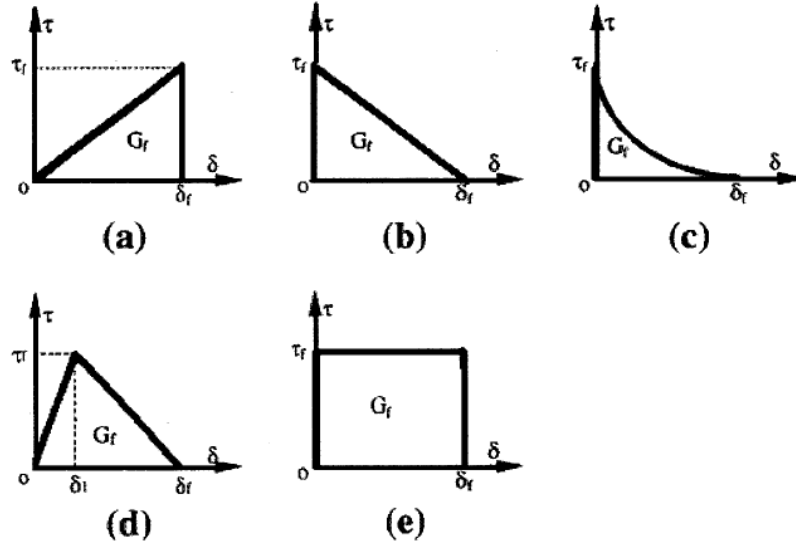


Figure 3.8. Bond-slip models for plate to concrete bonded joints,
Yuan and Wu (1999)

5.2.1 Täljsten (1996)

Täljsten (1996) and Holzenkämpfer (1994) used a nonlinear fracture mechanics bond slip model which is shown in Figure 3.9. Täljsten simplified this model by assuming linear segments and used interfacial fracture energy to determine the maximum transferable load or bond capacity, P_{max} , in terms of interfacial fracture energy, G_f , and steel/FRP plate reinforcing stiffness, $E_p t_p$, Täljsten (1994).

$$P_{max} = b_p \sqrt{\frac{2E_p t_p G_f}{1 + \alpha_T}} \quad (1)$$

Where,

$$\alpha_T = \frac{E_p t_p}{E_c t_c} \quad (2)$$

Where E_c (MPa) is the elastic modulus of concrete, t_c (mm) is the effective thickness of concrete contributing to shear deformation, b_p (mm) is the width of the plate, t_p (mm) is the thickness of the plate, E_p (MPa) is the elastic modulus of the plate

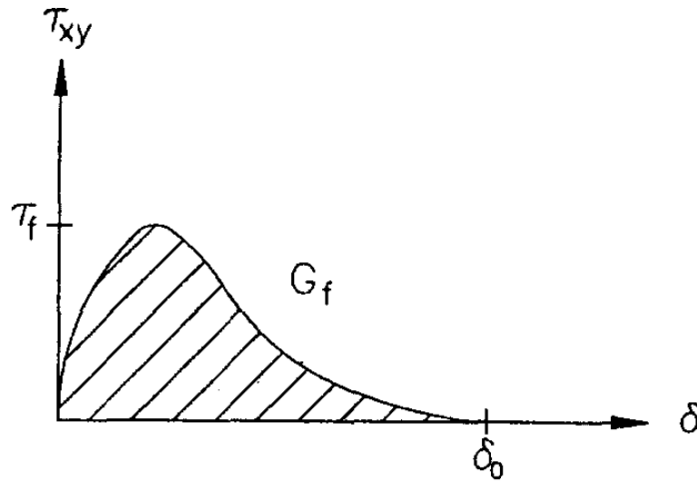


Figure 3.9. Bond displacement curve of an adhesive joint based on nonlinear fracture mechanics, Täljsten (1996)

Täljsten (1996) also presented the maximum bond stress τ_{max} as shown below Täljsten (1994, 1997):

$$\tau_{max} = 0.0184\sqrt{E_p t_p} \quad (3)$$

5.2.2 Neubauer and Rostásy (1999)

Neubauer and Rostásy (1999) first confirmed that the bond strength model initially developed to describe the relationship between the steel plates and the concrete substrates can be valid in the application of CFRP bonded on the concrete substrates.

$$\tau = \tau_{max}(s/s_0) \quad \text{if } s \leq s_0 \quad (1)$$

$$\tau = \tau_{max} \frac{s_f - s}{s_f - s_0} \quad \text{if } s > s_0 \quad (2)$$

where

$$s_0 = 0.202k_b \quad (3)$$

The maximum bond stress τ_{max} was expressed in terms of the tensile strength of concrete f_t as expressed below:

$$\tau_{max} = 1.8k_b f_t \quad (4)$$

Neubauer and Rostásy (1999) concluded that, for both concrete fracture failures and FRP delamination failures, the bond-slip relationship may be represented by the bi-linear (triangular) model as shown in Figure 3.10. The fracture energy, G_f , can then be calculated using:

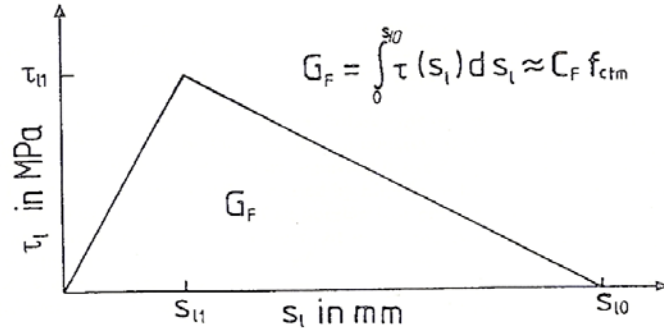


Figure 3.10. Idealized local bond law of Holzenkämpfer (1994)

$$G_f = C_f \cdot f_t \quad (5)$$

Where C_f is a coefficient reported to be equal to a mean value of 0.202mm for the 72 specimens investigated and f_t is the tensile strength of concrete measured following the CEB-FIP Model Code (1993) given below:

$$f_t = 1.4 \left(\frac{f_c - 8}{10} \right)^{2/3} \quad (6)$$

and k_b is a geometric factor related to the width of bonded plate b_p and the width of concrete prism b_c .

$$k_b = \sqrt{1.125 \frac{2 - (b_p/b_c)}{1 + (b_p/400)}} \quad (7)$$

they proposed that bond strength was dependent on the fracture energy.

$$P_{max} = 0.64 k_b b_f \sqrt{E_f t_f f_{ct}} \quad \text{when } L \geq L_0 \quad (8)$$

$$P_{max} = 0.64 k_b b_f \sqrt{E_f t_f f_{ct}} \frac{L}{L_e} \left(2 - \frac{L}{L_e} \right) \quad \text{when } L < L_0 \quad (9)$$

where

$$L_0 = \sqrt{\frac{E_p t_p}{2f_{ct}}} \quad (10)$$

5.2.3 Brosens and Van Gemert (1999)

Brosens and Van Gemert (1999) modified the models of Niedermeier (1996) included the adhesive thickness in their formulation. Furthermore, they also incorporated the thickness of concrete substrate near the surface which is considered to be effective in developing bond. This is illustrated in Figure 3.11.

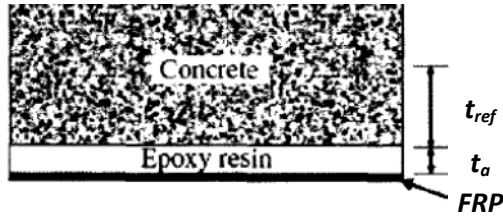


Figure 3.11. Representative schematics of configurations of different layers used for the computation of bond slip, Brosens and Van Gemert (1999)

This layer, which essentially serves as an additional interface, can significantly affect both the bond transfer length and the level of bond strength.

Brosens and Van Gernert (1999) derived expressions for the maximum shear stress and interfacial fracture energy. They modified Neubauer and Rostásy (1997) Equations to account for the effects of FRP width. The resulting expressions for maximum bond stress τ_{max} and interfacial fracture energy G_f are shown below:

$$\tau = \tau_{max}(s/s_0) \quad \text{if } s \leq s_0 \quad (1)$$

$$\tau = \tau_{max} \frac{s_f - s}{s_f - s_0} \quad \text{if } s > s_0 \quad (2)$$

$$\tau_{max} = 1.8k_b f_t \quad (3)$$

The slip s_o corresponding to the maximum bond stress is determined as the sum of the slip in the adhesive and the slip in concrete shown in Figure 3.11.

$$s_0 = \tau_{max} \left(\frac{t_a}{G_a} + \frac{t_{ref}}{G_c} \right) \quad (4)$$

where t_a is the thickness of the adhesive was estimated about 0.2 mm, G_a is the shear modulus of the adhesive and is expressed as $G_a = E_a/2(1 + \nu_a)$ where Poisson's ratio ν_a estimated to be 0.3 for ordinary adhesive, E_a is the young's modulus of the adhesive, t_{ref} is the reference distance in the concrete where the concrete is influenced by direct shear load, the reference thickness t_{ref} in concrete that shown in Fig.(above) is the reference distance in concrete over which stresses are influenced by FRP, this thickness can be taken as 2.5 - 3 times the maximum aggregate size and usually resulting in a depth of 40-50 mm, E_c is the young's modulus of the concrete which is determined by the CEB FIP Model Code (1993) as $E_c = 2.15 \times 10^4 \left(\frac{f'_c}{10}\right)^{1/3}$, and the G_c is the shear modulus of the concrete and it is expressed as $G_c = E_c/2(1 + \nu_c)$ where the Poisson's ratio ν_c was estimated to be 0.16 in their study.

The ultimate slip s_f corresponding to local bond failure was computed as shown below based on the bilinear bond-slip model.

$$s_f = \frac{2G_f}{\tau_{max}} \quad (5)$$

$$k_b = \sqrt{\frac{1.5(2-(b_p/b_c))}{1+(b_p/100)}} \quad (6)$$

$$G_f = k_b^2 C_f f_t \quad (7)$$

The constant C_f above was found to be 0.3 from test data. The maximum transferable FRP force was determined as;

$$P_u = b_b \sqrt{2G_f E_p t_p} \quad (8)$$

5.2.4 Brosens (2001)

Based on a microscopic study, Brosens proposed model that considers the effect of the adhesive layers between FRP composite materials.

Based on microscopic study of the interfacial region, Brosens (2001) concluded that it was critical not only to consider size effects which could cause significant effect on bond level mechanisms through local irregularities, but also the effect of additional interfaces between layers of FRP as shown in Figure 3.12.

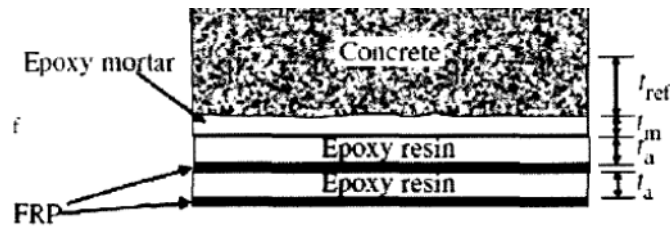


Figure 3.12. Representative schematics of configurations of different layers used for the computation of bond slip (Brosens 2001)

In addition, through a re-evaluation of the bond stress model used by Holzenkämpfer (1994), it was hypothesized that a state of pure shear was responsible for maximum bond-stress leading to modification of the Mohr-Coulomb envelope as shown in Figure 3.13.

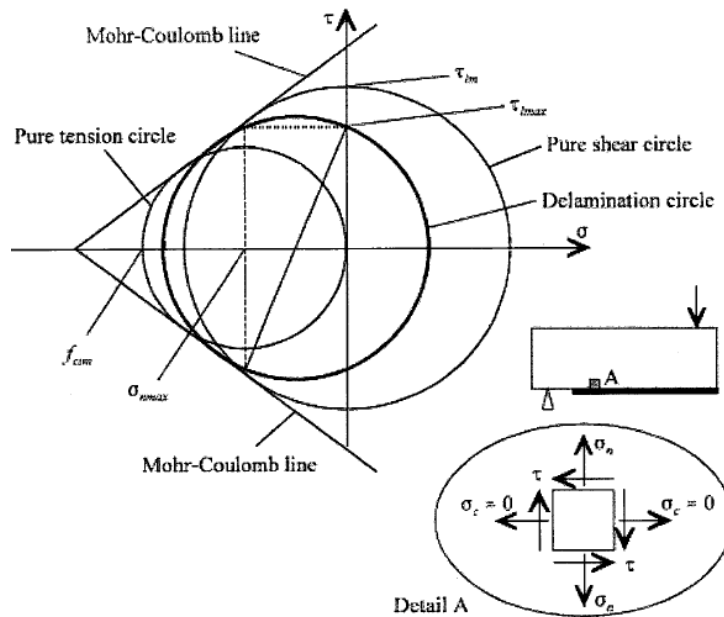


Figure 3.13. Mohr-coulomb failure criterion (Brosens 2001)

Brosens (2001) modified the formulation as indicated below to introduce the size effect and local irregularities.

$$\tau = \tau_{max}(s/s_0) \quad \text{if } s \leq s_0 \quad (1)$$

$$\tau = \tau_{max} \frac{s_f - s}{s_f - s_0} \quad \text{if } s > s_0 \quad (2)$$

$$\tau_{max} = k_b k_c \frac{f'_c f_t}{f'_c + f_t} \quad (3)$$

Where k_b is a factor related to width ratio of FRP over concrete member

$$k_b = \sqrt{\frac{k(2-(b_p/b_c))}{1+(b_p/b_0)}} \quad (4)$$

and k_c is factor representing the concrete surface preparation which was dependent on the environment and workmanship, and it is various from 0.65 to 1.00, k is a constant which is empirically derived from experiments to be 1.47 and b_0 is a function in terms of reference concrete thickness.

$$b_0 = \frac{t_{ref}}{k-1} \quad (5)$$

leading to

$$\tau_{max} = \sqrt{\frac{1.47(2-(b_p/b_c))}{1+(b_p/85)}} \cdot \frac{f'_c f_t}{f'_c + f_t} \quad (6)$$

Brosens (2001) concluded the slip of concrete and adhesive the slip, include the slip in epoxy mortar between FRP layers:

$$s_0 = \tau_{max} \left(n \frac{t_a}{E_a} + 2.4 \frac{t_{ref}}{E_c} + 2.5 \frac{t_m}{E_m} \right) \quad (7)$$

where n is the number of layers of FRP used, E_m is the modulus of elasticity of epoxy mortar and t_m is the thickness of epoxy mortar which was noted to vary between 2mm and 5mm depending on the size of irregularities on concrete surface.

The maximum slip and fracture energy are given by Equations:

$$s_f = \frac{2G_f}{\tau_{max}} \quad (8)$$

$$G_f = k_b^2 k_c^2 C_f f_t \quad (9)$$

Where, the value of C_f was 0.40 mm determined through calibration with experimental results, leading to

$$G_f = \frac{0.588(2-(b_f/b_c))}{1+(b_f/85)} f_t \quad (10)$$

The maximum transferable FRP force was determined as;

$$P_u = b_b \sqrt{2G_f E_p t_p} \quad (11)$$

5.2.5 Nakaba et al. (2001)

Nakaba et al. (2001) proposed a bond-slip relationship using series of double-lap shear tests with different properties of concrete and FRP and using curve-fit of experimental data, their shear-slip curve follows Popovics' equation and shown in is different from the bilinear that suggested earlier by Holzenkämpfer (1994) and Neubauer and Rostásy (1997) the bond-slip relationship as shown in Figure 3.14(a)

According to Nakaba et al.'s study, the shear-slip response relationship Figure 3.14(b) can be expressed by the following power law:

$$\tau = \tau_{max} \left[\frac{s}{s_{max}} \frac{n}{(n-1)+(s/s_{max})^n} \right] \quad (1)$$

where s and s_{max} both measured in mm are values of slip corresponding to local bond stress and the maximum bond stress, respectively, and n is empirical parameter related to the compressive strength, for the range of concrete compressive strengths of 24-58 MPa, n was determined to be 3 mm. This results in the following expression:

$$\tau = \tau_{max} \left[\frac{s}{s_{max}} \frac{3}{2+(s/s_{max})^3} \right] \quad (2)$$

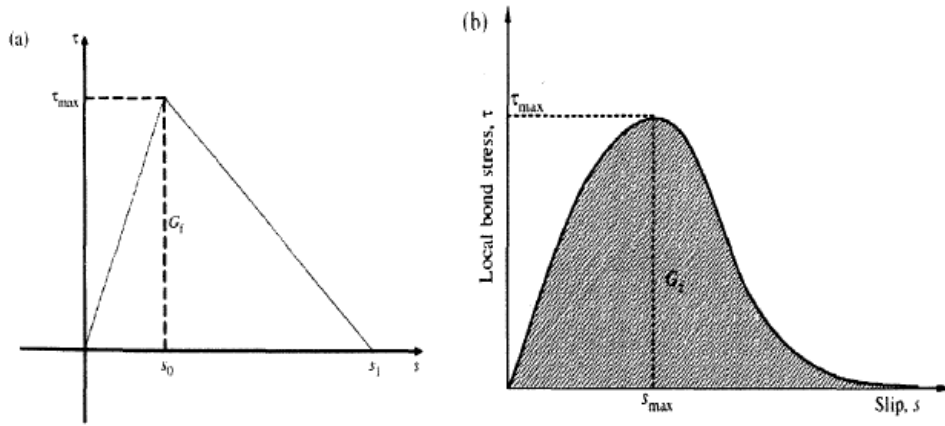


Figure 3.14. (a) Bi-linear Stress-Slip Relationship between Concrete and FRP and (b) Popvic's Expression Based Stress-Slip Relationship Concrete and FRP

The maximum bond stress τ_{max} measured in MPa as expressed below.

$$\tau_{max} = 3.5f_c'^{0.19} \quad (3)$$

where s_{max} is the slip corresponding to the maximum shear stress.

$$s_{max} = 0.065 \quad (4)$$

The interfacial fracture energy G_f , defined as the area below the bond stress-slip curve, can then be obtained as

$$G_f = \int_0^{\infty} \tau ds = \int_0^{\infty} \tau_{max} \left[\frac{s}{s_{max}} \frac{3}{2+(s/s_{max})^3} \right] ds \approx 0.184\tau_{max} \approx 0.644f_c'^{0.19} \quad (5)$$

5.2.6 Savioa et al. (2003)

Savioa et al. (2003) suggested the use of the bond slip curve suggested by Popovics with the empirical parameter n redefined as 2.86.

$$\tau = \tau_{max} \frac{s}{\bar{s}} \frac{2.860}{1.860 + (s/\bar{s})^{2.860}} \quad (1)$$

the parameters τ_{max} , \bar{s} are values of maximum shear stress in MPa and the slip corresponding to local shear stress in mm, respectively, were obtained as:

$$\tau_{max} = 3.5f_c'^{0.19} = 6.93 \text{ MPa} \quad (2)$$

$$\bar{s} = 0.051 \quad (3)$$

The bond - slip law is reported in Figure 3.15.

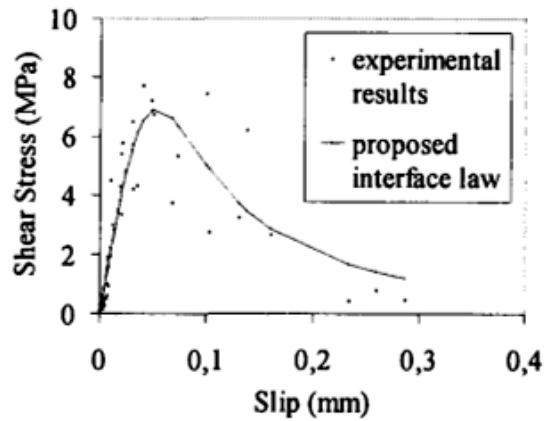


Figure 3.15. Bond-slip curve for FRP-concrete interface obtained from CFJT-Plate experimental data

5.2.7 Monti et al. (2003)

Monti et al. (2003) developed the following equations based on a parametric study using finite element analysis along with experimental data. The bond slip relationship is assumed to be bilinear (triangular) with the following expressions:

$$\tau = \tau_{max} (s/s_0) \quad \text{if } s \leq s_0 \quad (1)$$

$$\tau = \tau_{max} \frac{s_f - s}{s_f - s_0} \quad \text{if } s > s_0 \quad (2)$$

Then maximum bond stress can be expressed as with k_b being the same as that defined by Brosens and Van Gemert (1999).

$$\tau_{max} = 1.8k_b f_t \quad (3)$$

$$s_0 = 2.5\tau_{max} \left(\frac{t_a}{E_a} + \frac{50}{E_c} \right) \quad (4)$$

$$s_f = 0.33\beta_w \quad (5)$$

$$\beta_w = \sqrt{1.5 \frac{2-(b_p/b_c)}{1+(b_p/100)}} \quad (6)$$

5.2.8 Dai and Ueda (2003)

Dai and Ueda (2003) suggested bond-slip model, as expressed below.

$$\tau_{max} = \frac{-1.575\alpha k_a + \sqrt{2.481\alpha^2 k_a^2 + 6.3\alpha\beta^2 k_a G_f}}{2\beta} \quad (1)$$

$$s_0 = \tau_{max} / \alpha K_a \quad (2)$$

$$\tau = \tau_{max} \left(\frac{s}{s_0} \right)^{0.575} \quad \text{if } s \leq s_0 \quad (3)$$

$$\tau = \tau_{max} e^{-\beta(s-s_0)} \quad \text{if } s > s_0 \quad (4)$$

$$\text{where } \alpha = 0.028(E_p t_p / 1000)^{0.254}$$

$$\beta = 0.0035K_a(E_p t_p / 1000)^{0.34} \quad (5)$$

$$K_a = G_a / t_a$$

The fracture energy is given by Equation:

$$G_f = 7.554K_a^{-0.449} (f_c')^{0.343} \quad (6)$$

5.3 Finite Element Models

Many researchers investigated the bond–slip (τ - s) relationship performance of FRP on concrete by using Finite Element Method (FEM). Among them, Kang (1996), Niu and Wu (2001), Chen et al. (2001), Yang et al. (2003), Chen et al. (2003), Teng et al. (2002), Wu and Yin(2003), Yin and Wu(2003), Yan et al. (2004), Chen and Pan (2004), Niu and Wu(2005) Chen and Pan (2006), Lu et al (2005, 2006), and Zhao et al. (2007). Lu et al. (2005) suggested several models which are shown in Figure 3.16.

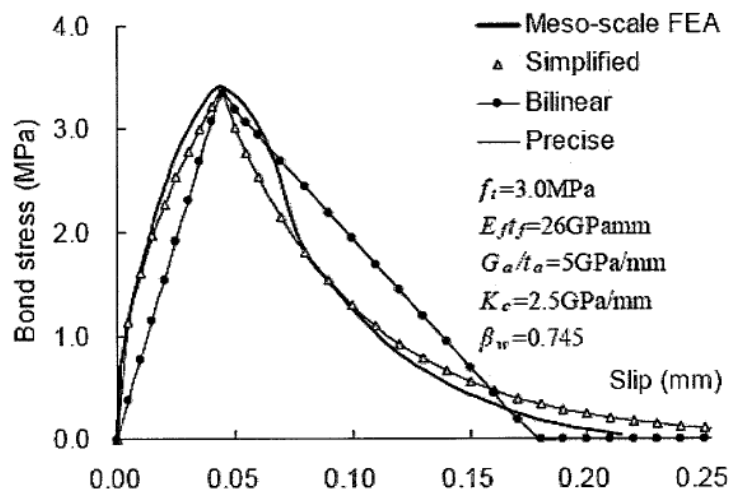


Figure 3.16. Bond slip models suggested by Lu et al. (2005)

Figure 3.16. shown that the precise model is accurate but somewhat complicated. Lu et al. (2005) conducted critical review of available bond strength models and shear stress-slip relationships. They compared the performance of the different models using an extensive experimental database of single and double shear tests, and suggested series of models based on empirical calibration of results from finite element simulations. The simplified version of their basic model, which requires fewer parameters to define it is given by:

$$\tau = \tau_{max} \sqrt{s/s_0} \quad \text{if } s \leq s_0 \quad (1)$$

$$\tau = \tau_{max} \exp[-\alpha(s/s_0 - 1)] \quad \text{if } s > s_0 \quad (2)$$

where

$$s_0 = 0.0195\beta_w f_t \quad (3)$$

$$\alpha = 1/[(G_f/\tau_{max}s_0)/(2/3)] \quad (4)$$

$$\tau_{max} = 1.5\beta_w f_t \quad (5)$$

$$s_f = 2 G_f/\tau_{max} \quad (6)$$

$$\beta_w = \sqrt{(2.25 - b_f/b_c)/(1.25 + b_f/b_c)} \quad (7)$$

The fracture energy is given by Equation:

$$G_f = 0.308\beta_w^2\sqrt{f_t} \quad (8)$$

$$P_u = b_b\sqrt{2E_p t_p G_f} \quad (9)$$

Lu et al. (2005) Based on the predictions of meso scale Finite element model were tested to control their models. They then compared several models and proposed modification on the models to propose precise and simplified models (Figure 3.17) and investigate the bilinear model.

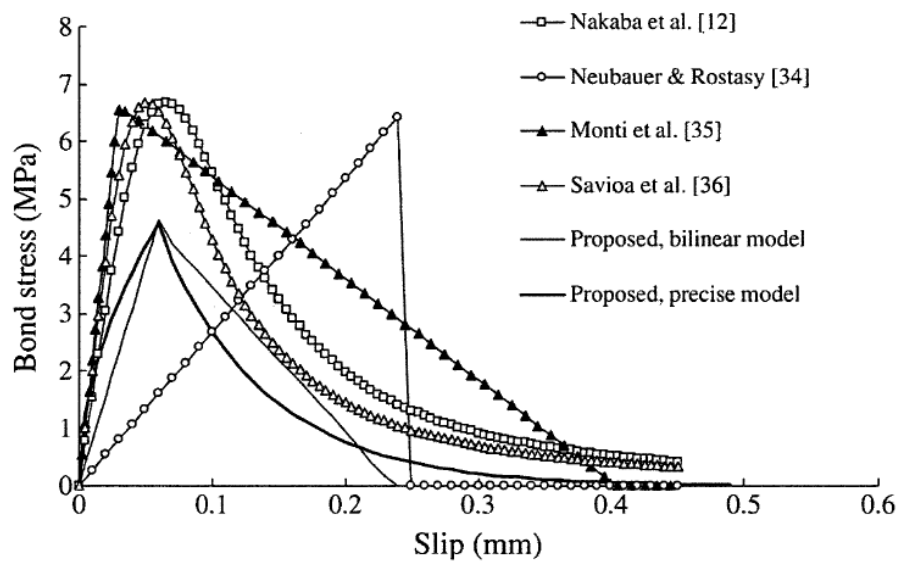
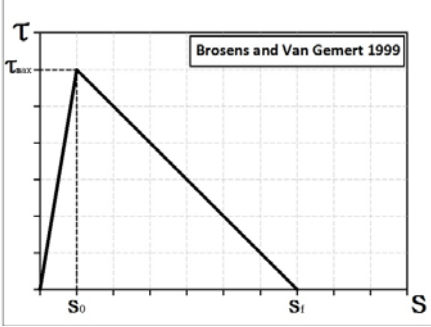
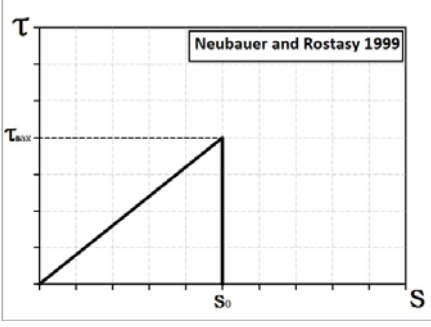
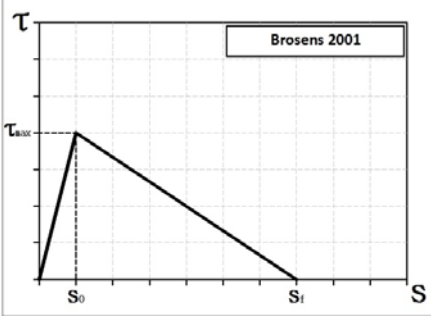
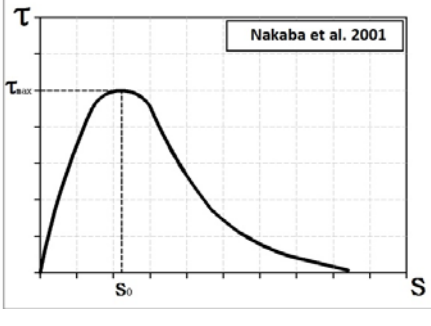


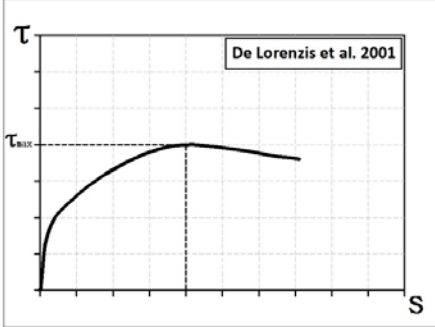
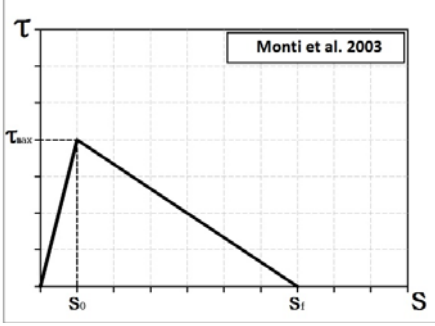
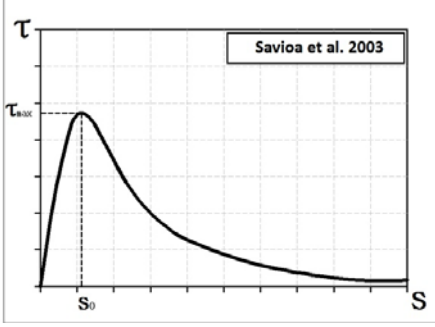
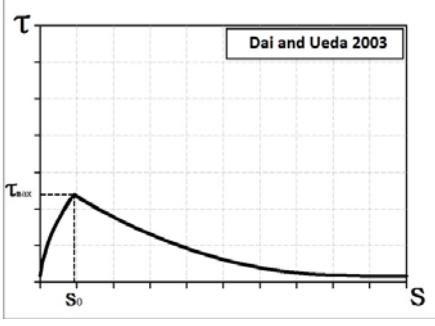
Figure 3.17. Bond-slip curves from existing bond-slip models (Lu et al. 2005)

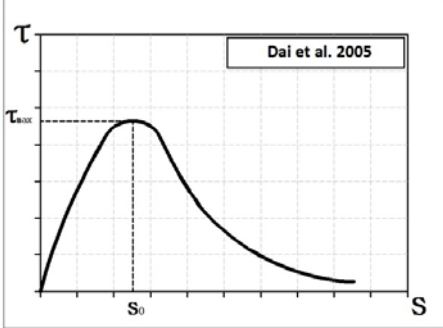
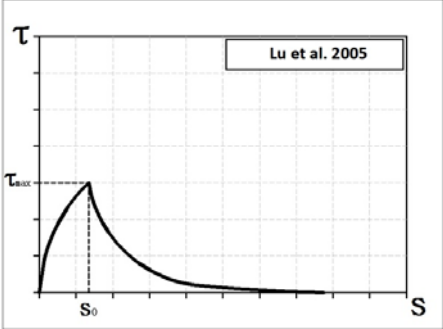
5.4 Conclusions of bond–slip models

- The model of Neubauer and Rostasy (1999), which is modified from Holzenkämpfer (1994), seems unrealistic because it does not consider slip after maximum bond stress.
- The models of Monti et al. (2003) and Lu et al. (2005) which are derived from Neubauer and Rostasy (1999) and Brosens and Van Gemert (1999), consider the maximum bond stress (τ_{max}) as function of concrete tensile strength (f_t) and width ratio factor (β_w), which is the size effect parameter considering the influence of the FRP bonded width relative to the concrete width Brosens and Van Gemert (1999).
- The slip s_0 (the slip when the bond stress reaches τ_{max}) in the models of Brosens et al. (2001) and Monti et al. (2003) consider characteristics of concrete and adhesive, while the slip s_0 in the model of Lu et al. (2005) is composed of a function of width ratio factor (β_w) and concrete tensile strength (f_t).
- The maximum slip s_f in the models of Brosens and Van Gemert (1999), Brosens et al. (2001) are similar to that of Lu et al. (2005) which as function of maximum bond stress (τ_{max}) in addition to the interfacial fracture energy (G_f), while only width ratio factor (β_w) is considered in the model of Monti et al. (2003).
- maximum bond stress (τ_{max}) in the model of Savoia et al. (2003) was obtained of that of Nakaba et al. (2001) with some minor modification which only considers concrete compressive strength (f_c) as parameter of maximum bond stress (τ_{max}), and the value of the slip s_0 changes.
- Only the models of Brosens and Van Gemert (1999), Brosens (2001), Monti et al. (2003) and Lu et al. (2005) give the three parameters τ_{max} , s_0 , and s_f , whereas only the model of De Lorenzis et al. (2001) considers maximum bond stress τ_{max} as a function of only FRP stiffness. The other models consider τ_{max} as a function of compressive or tensile strength of concrete, not depending on FRP stiffness.

Table 3.2. Bond stress-slip relationship

Authors	Investigations Type	τ -s Model	τ -s Shapes
Brosens and Van Gemert (1999)	Experimental Investigations	Bi-linear	 <p style="text-align: right; font-size: small;">Brosens and Van Gemert 1999</p>
Neubauer and Rostasy (1999)	Experimental Investigations	Linear ascending branch and a sudden drop (Elastic-brittle)	 <p style="text-align: right; font-size: small;">Neubauer and Rostasy 1999</p>
Brosens (2001)	Experimental Investigations	Bi-linear	 <p style="text-align: right; font-size: small;">Brosens 2001</p>
Nakaba et al. (2001)	Experimental Investigations	Single Curve	 <p style="text-align: right; font-size: small;">Nakaba et al. 2001</p>

Authors	Investigations Type	τ -s Model	τ -s Shapes
De Lorenzis et al. (2001)	Experimental Investigations	Elasto-plastic	 <p>De Lorenzis et al. 2001</p>
Monti et al. (2003)	Finite element analysis in conjunction with experiments	Bi-linear	 <p>Monti et al. 2003</p>
Savioa et al. (2003)	Analytical solutions derived from experimental test results	Single Curve	 <p>Savioa et al. 2003</p>
Dai and Ueda (2003)	Indirect analytical solutions derived from experimental test results	Nonlinear	 <p>Dai and Ueda 2003</p>

Authors	Investigations Type	τ -s Model	τ -s Shapes
Dai et al. (2005)	Indirect analytical solutions derived from experimental test results	Single Curve	 <p>The graph shows a single curve representing the relationship between shear stress (τ) and slip (s). The curve starts at the origin, rises to a peak value of τ_{max} at a slip value of s_0, and then gradually decays towards zero as slip increases further. The plot is labeled 'Dai et al. 2005'.</p>
Lu et al. (2005)	analytical Investigations "finite element Analyses" a database containing the results of 253 tests	Simplified	 <p>The graph shows a simplified curve representing the relationship between shear stress (τ) and slip (s). The curve starts at the origin, rises to a peak value of τ_{max} at a slip value of s_0, and then decays towards zero. The plot is labeled 'Lu et al. 2005'.</p>

6.0 Previous research (experimental test programs and variability)

Chajes et al. (1996) performed tests using single-lap shear tests (Figure 3.18) with constant bonded lengths with variations in adhesive type, surface preparation and concrete strengths. The concrete mix was varied by changing the water/cement ratio having compressive strengths ranging from 3500 to 6500 psi. The test specimen consisted of a 1-in.-wide composite plate bonded to a concrete block (6-in.-wide x 6-in.-high x 9-in.-long) with a 3-in. bond length. In the test setup, the concrete block was securely mounted to the bottom crosshead of a 30,000-lb capacity testing machine. Four different types of adhesives were used included two manufactured by the Sika Corp. (Sikadur 32, Hi-Mod and Sikadur 31, Hi-Mod gel), and two

manufactured by the Lord Corp. (Tyrite 7500 and Fusor 320/322). The surface preparations used were grinding with a stone wheel and mechanically abrading with a wire wheel. For all of the joints except those bonded with Tyrite. The results of the surface preparation tests showed that the failure was initiated due to the shearing of the concrete directly beneath the adhesive layer. To evaluate effects of adhesive type, the specimens that were bonded using Fusor and Tyrite were prepared by mechanical abrasion alone and mechanical abrasion combined with Chemglaze 9926 showed improved bond performance. Increased compressive strengths of concrete also showed increased values of failure loads. From these experiments it can be deduced that failure and bond performance is affected by adhesive/epoxy used, surface preparation and concrete compressive strength.

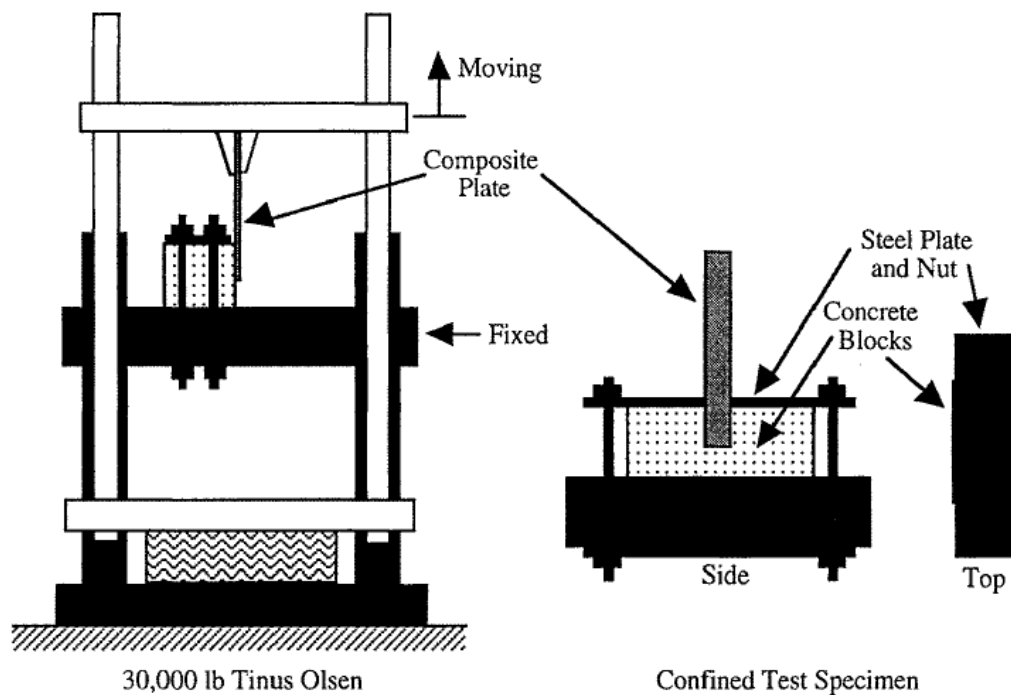


Figure 3.18. Single-lap shear bond test setup (Chajes et al. 1996)

Täljsten (1997) presented the result of single shear pullout tests (Figure 3.19) performed on concrete prisms onto which steel or CFRP plates have been bonded. The tests were divided into two groups, series S and series C. Mild steel was used in series S and CFRP plates in series C.

Four concrete prisms in series C were used in the tests (200mm-wide x 200mm-high x 1200mm-long). The thickness of the steel plates was kept constant during the test, but the anchor length were varied (100, 200, 300, 400 mm). The thickness of the adhesive layer was 2.0 mm. The anchor length was defined as the minimum length of FRP/steel plate that contributes to the load-bearing capacity which longer lengths do not contribute to the capacity. The test results show that there exists critical strain level in the concrete at failure. It has been found that this anchor length is approximately 300 mm for the steel plates. The results showed that there is a specific anchor length for each material used. It was shown that the strain in the concrete was the critical factor in determining the interfacial bond failure. The observed failure occurs directly in the thin concrete layer under the adhesive. The load response of the bond was determined and the debonding process was related to the strain distribution in the FRP.

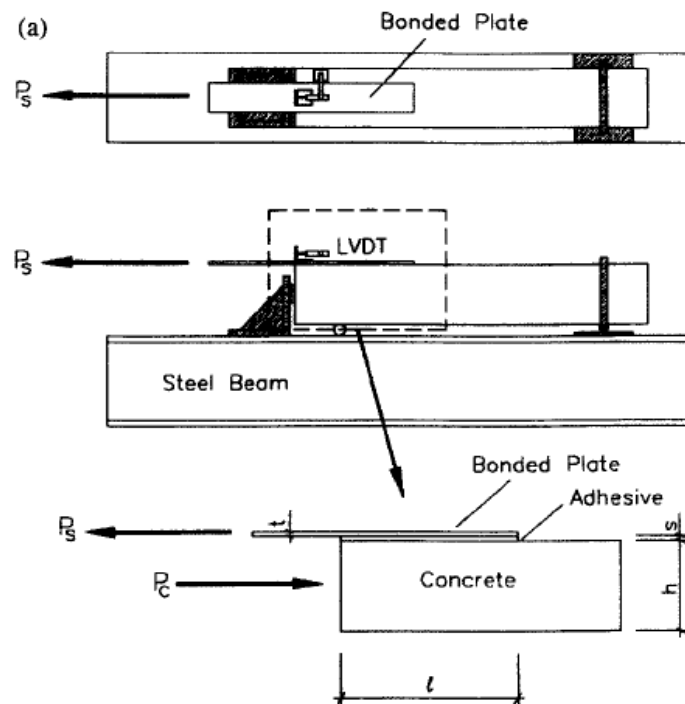


Figure 3.19. Sketch of the test equipment used in the tensile test series, (Täljsten et al. 1997)

Brosens and Van Gemert (1997) performed shear tests on two concrete prisms used was 150 x 150 x 300 mm and four bonded length, 150mm, 175mm, 200mm and 250 mm, of the CFRP laminates were adopted for test. The two concrete prisms connected by steel plates bonded on two opposite sides to apply the tensile force, while at other two opposite sides connected with 3 layers of CFRP laminates as shown in Figure 3.20. The results showed that increase in bonded length increases the fracture load, which is contrary to findings of other researchers, where they found that the critical bonded length is at least larger than 275 mm.

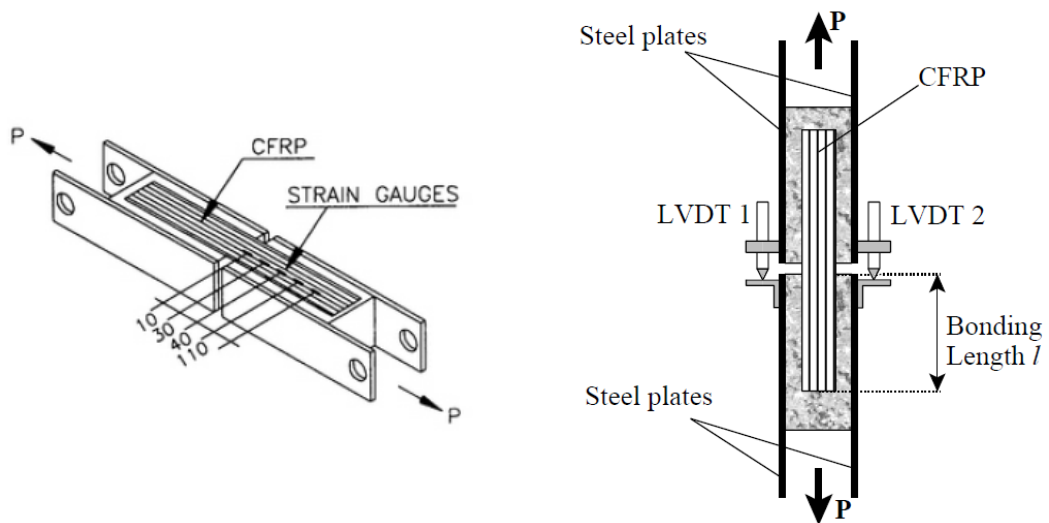


Figure 3.20. Shear test specimen (Brosens and Van Gemert 1997)

Maeda et al. (1997) performed experimental study on the bond mechanism of Carbon Fiber Sheets (CFS) using double-lap shear tests, where CFS loaded by pulling re-bars which are placed at center of the (100x100mm) concrete prism as seen in Figure 3.21.

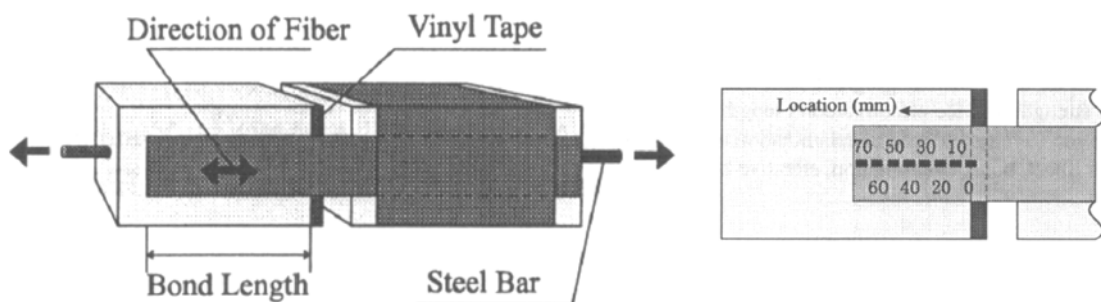


Figure 3.21. (a) Specimens, (b) Arrangement of strain gauges (Maeda et al. 1997)

The variables were the bonded length (75-700mm), stiffness of CFS (1 plie, 2 plies), and concrete strength (40.8-44.7MPa). Based on their experimental results showed that as the stiffness of FRP increases ultimate load also increases. At the early stage of loading, load is sustained in the vicinity of loading point; the active bonding area was shifted as delamination propagates completely. At any stage of loading, the area where CFS resists through bond stress is part of the effective bond length, as seen in Figure 3.22. The effective bond length decreases as the stiffness of CFS increases.

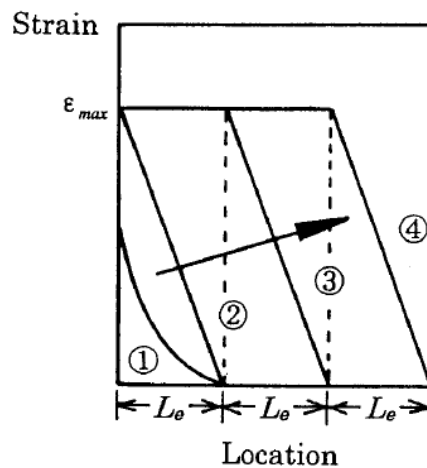


Figure 3.22. Schematic of strain distribution in CFS

Their experimental program attempted to simulate the strain distribution using FEM program WCOMR, in which smeared crack model and average stress-strain relationships were adopted, while the elastic modulus and the shear modulus in the bond element is 1.50MPa and 0.58MPa, respectively, and thickness of the bond elements representing the epoxy resin was 0.1 mm. The predicted strain distributions in CFS were found to be fairly accurate as long as the nonlinear behavior caused by concrete cracking was considered. The typical mesh used for the analysis is shown in Figure 3.23.

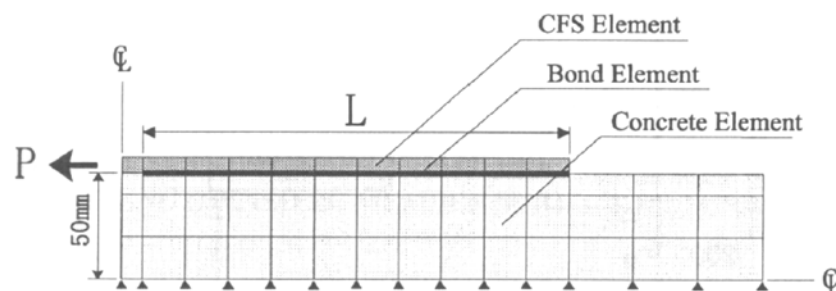


Figure 3.23. Finite element mesh

Bizindavyi and Neale (1999) conducted several experimental and analytical studies to investigate the load transition mechanism of composite laminates bonded to concrete. They performed single shear pull tests (Figure 3.24) were conducted for different types of laminates were (GFRP and CFRP), with different thicknesses (1, 2, and 3 plies) and also different types of concrete. The analytical results comparison to experimental results were seen to be in good agreement for loads less than the initial cracking load, especially for specimens with one 1-ply for both GFRP and CFRP laminates..

The observed modes of failure were shearing of the concrete beneath the glue line and rupture of the composite coupon.

Strain gauges were used to determine the strain distribution in the FRP at different load levels. From the strain data, the shear stress distribution along the bonded joint between FRP and concrete was determined. A uniform shear stress distribution along the bonded joint was assumed to determine the bond strength, which is the ultimate load divided by the bonded area. The values of the initial transfer lengths for GFRP-concrete and CFRP-concrete joints were estimated by defining the transfer length as the distance from the loaded end to the point on the joint where strain reaches zero.

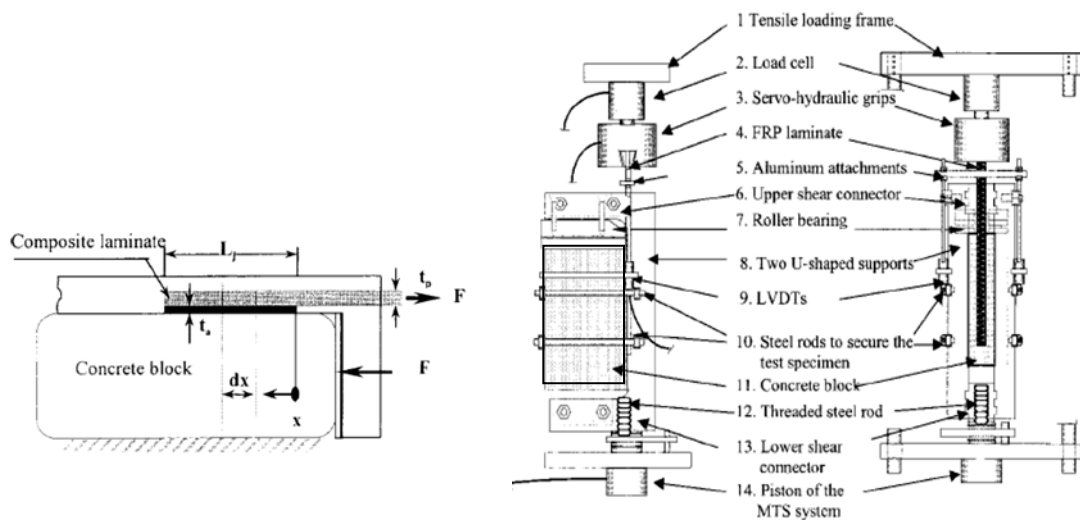


Figure 3.24. (a) Specimen configuration, (b) Test Rig, Side and front view
(Bizindavyi and Neale 1999)

De Lorenzis et al. (2001) studied the performance flexural tests as shown in Figure 3.25 to determine the effectiveness of the bonded length, FRP stiffness, strength and surface preparation of concrete. A total of 18 T-beams were tested in which of three series of specimens, each series consisted of six specimens with three different bonded lengths. Also the thickness of FRP and the concrete strength between each series were varied.

It was concluded, the FRP width does not affect the failure load, while the FRP stiffness influenced the ultimate load. Also, it was suggested that the surface preparation can significantly affect the average bond strength, where a roughened surface performs much better than a sand blasted surface. In addition, De Lorenzis et al. (2001) found that the concrete strength did not affect the bond strength. Finally, results showed that the bonded length does not have significant effect on the bond failure load. They reported that the bonded length L_e to be 93 mm.

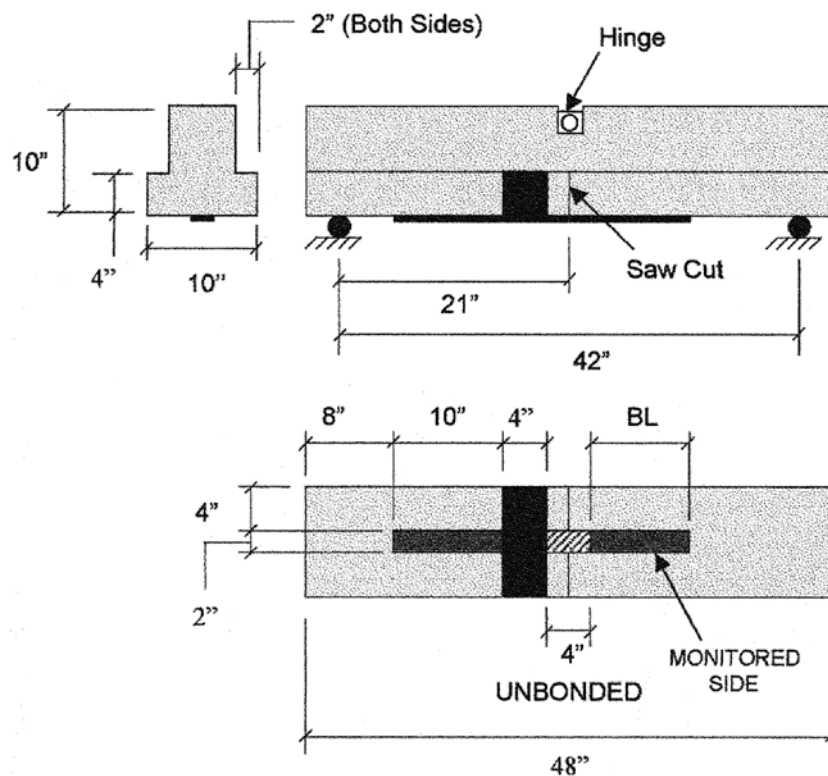


Figure 3.25. Test specimen. (Note: 1 in. = 25.4 mm.) (De Lorenzis et al. 2001)

Nakaba et al. (2001) performed double lap shear pull tests. The primary test variables of the FRP stiffness ($E_f t_f$), concrete strength, and putty thickness were studied to determine the influence of the strength of concrete and FRP. A theoretical analysis of the bonding behavior between FRP and concrete also performed to compare with experimental results. The concrete prism size was 100 x 100 x 600 mm, after reinforcing with FRP laminates the concrete prism was cracked at the center using a hammer on the notch. where FRP laminates loaded by pulling steel bars which are placed at the center of the cross-section of concrete prism 100x100mm as shown in Figure 3.26.

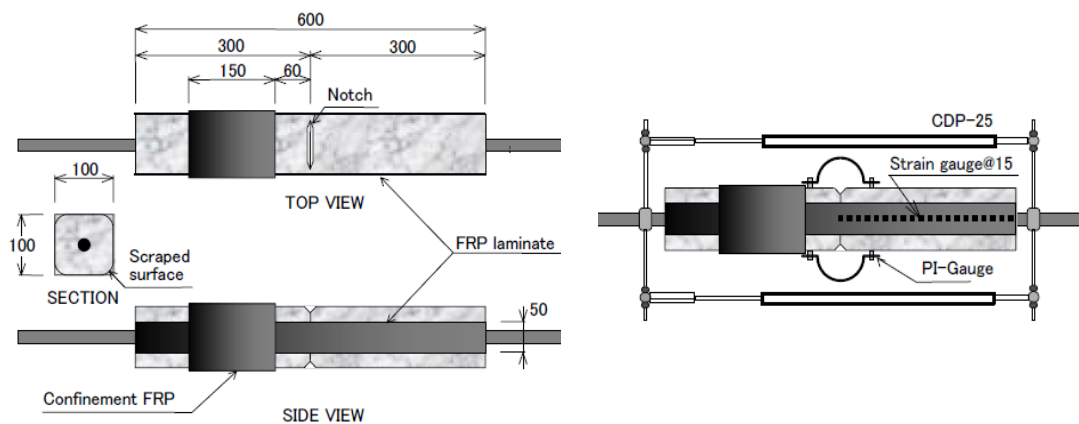


Figure 3.26. (a) Test specimen, (b) Data acquisition sketch (Nakaba et al. 2001)

There were three specimens in each combination of concrete (series C5 and series C2) and mortar and fiber (series M5). A total of 36 specimens were tested. The width and the bonding length of the FRP laminates were 50 mm and 300 mm, respectively. The LVDTs were used to measure the total displacement and crack width at the center. A total of 20 strain gages to obtain the strain distribution, the strain gages were installed on one face at an interval of 15 mm and one strain gage on the other side at the center of specimen.

It was concluded that the putty thickness has no effect on the maximum load while the maximum load increases as the stiffness of FRP increases. The local bond stress-slip is affected by concrete properties, where the increase of concrete strength increases the local bond stress, but the maximum local bond stress-slip is not affected by the FRP stiffness. The most of the specimens failed in bonding and some failed by FRP rupture.

Chen and Teng (2001) reviewed and assessed existing anchorage strength models of FRP and steel plates bonded to concrete with different bond lengths Hiroyuki and Wu (1997), Tanaka (1996), van Gemert (1980), Chaallal et al. (1998), Khalifa et al. (1998) and Neubauer and Rostásy (1997), they may be classified all the models into three categories: empirical models based directly on the regression of test data, models based on fracture mechanics, and models meant directly for design proposals that generally make use of some simple assumptions, by comparing them with experimental data a total of 55 specimens of single/double shear tests by Bizindavyi and Neale (1999), Chajes et al. (1996), Maeda et al. (1997), Täljsten (1997) and Swamy et al. (1986). This enabled the identification of the deficiencies of the existing models; they used a linearly ascending shear-slip model to describe the plate to concrete bond joints, as in Figure 3.27.

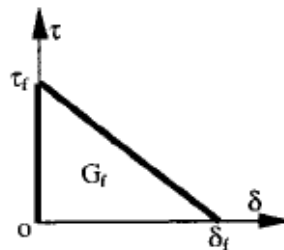


Figure 3.27. Shear-slip model for bonded concrete joints (Chen and Teng 2001).

For FRP-to-concrete bonded joints the typical values of the bond slip at maximum stress $\delta_l = 0.02$ and the ultimate bond slip $\delta_f = 0.2$ mm. Finally, results showed that an increase in the bonded length beyond the effective bond length cannot increase bond strength.

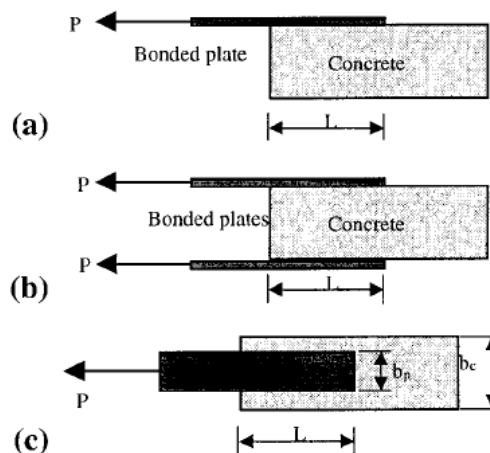


Figure 3.28. Single and double shear tests: (a) Single shear test, (b) Double shear test and (c) Plan

Dai et al. (2005) investigated the behavior of FRP sheet-concrete interface using single-lap pullout tests (Figure 3.29). The concrete prism size was 400 x 200 x 400 mm, the width of FRP laminate was kept the same width of all specimens at 100 mm, the bond length of 330 mm was applied. In their study four different adhesives and 3 different FRP sheets (Carbon, Aramid and Glass) were applied. The relative slip between FRP laminate and concrete were measure used two LVDT's at free end and loaded end of the bonded area. it is not necessary attaching many strain gauges on the FRP sheets to obtain local bond stress-slip (τ - s) relation, instead, they can be derived the local bond stress-slip relations from the relationship between pull-out forces and loaded end slips.

The experimental studies and analytical method to define nonlinear τ - s models of FRP sheet-concrete interface through pull-out tests was proposed. It was observed that the FRP stiffness and adhesives properties and the concrete compressive strength affect the fracture energy G_f , where all of these affecting factors were incorporated in the G_f formula. The shear stiffness of adhesive G_a affects G_f most, whereas the effect of concrete strength is much less than that of the adhesive but slightly greater than that of the FRP stiffness. It was also concluded that the G_f was shown to affect the ultimate interfacial load carrying capacity, Another parameter B which is the interfacial ductility index was shown to affect the configuration of the τ - s relationship.

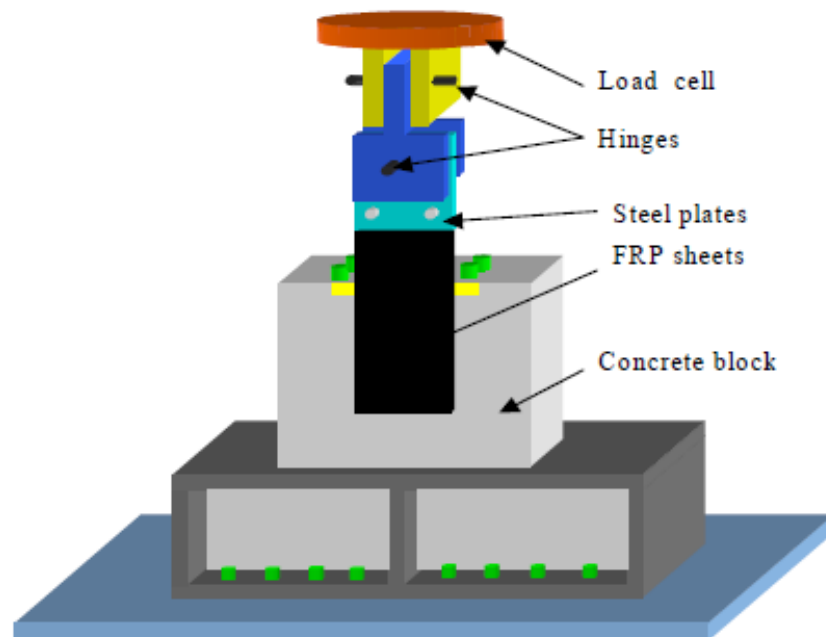


Figure 3.29. Pullout test setup (Dai et al. 2005)

Yao et al. (2005) carried out experimental study on the bond shear strength between FRP strip and concrete prism using the near end supported (NES) single lap shear test Figure 3.30. A total of 72 specimens in 7 series (I-1-16, II-1-6, III-1-8, IV-1-14, V-1-12, VI-1-8 and VII-1-8) conducted to investigate the effect of the bond length of FRP strip L_{frp} , height of concrete free edge and FRP strip to concrete prism width ratio b_{frp}/b_c . The results showed that the bonded length and ratio of width of FRP strip to concrete prism have been identified to have an effect on the bond strength, while the effects of concrete free edge on the bond strength is yet unclear. All of these test results were compared with the prediction from Chen and Teng's (2001) model. In general, the test results of Yao et al (2005) found to be quite good agreement with the predictions of Chen and Teng's (2001) bond strength model.

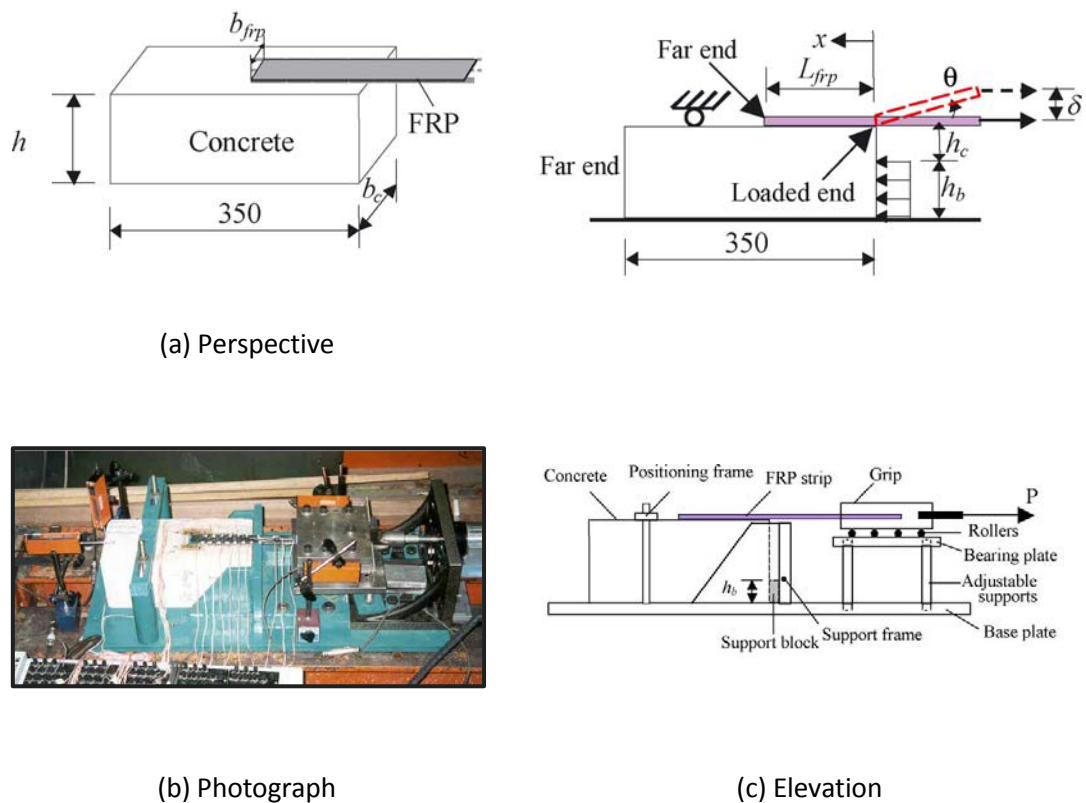


Figure 3.30. Test specimen (Yao et al. 2005)

(aggregate slightly exposed), the mechanical abrasion achieved the higher average interfacial bond strength. Yoshizawa et al. (1996) studied two concrete surface preparations: water jet and ordinary sander, they concluded that water jet on the concrete surface yielded the highest bonding strength. In their studies, Mitsu et al. (2000) used optical displacement meter to quantify concrete surface roughness. They used the resulting 3D profiles to assess the surface roughness through various indexes: maximum depth, superficial area, form factor and bearing ratio curve. They employed also various surface preparations such as sandpaper polishing, disk grinding, sand blasting and chipping. It was concluded that the sand blasting and chipping were the most effective methods of surface preparation to increase the bond strength.

7.3 Adhesive properties

Regression analysis of the test results performed by Dai et al. (2005) indicates that the interfacial fracture energy may be reduced by application of adhesives with higher shear modulus (G_{adh}/t_{adh}). In addition, the maximum bond stress increases with the shear stiffness of the adhesive layer. Since the available experimental data is limited the effects of the adhesive properties on the bond need to be investigated more.

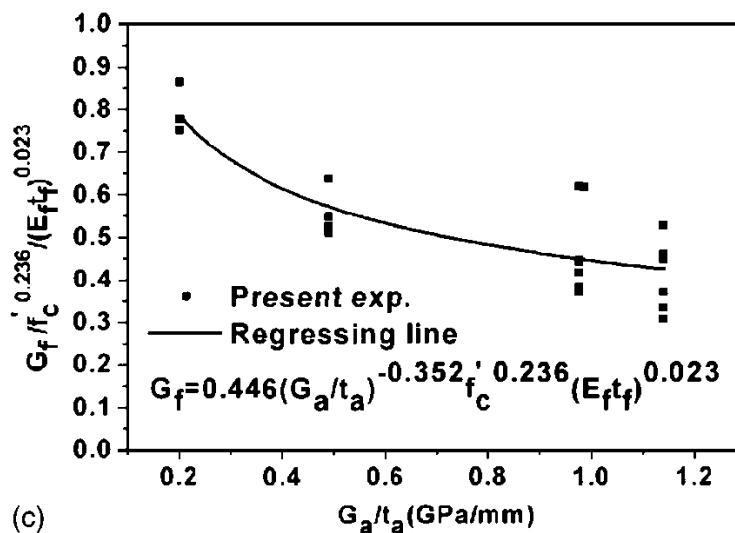


Figure 3.32. Effects of the adhesive properties on interfacial fracture energy of the bond (Dai et al. 2005)

7.4 Stiffness of FRP sheets

In their studies, Yoshizawa et al. (2000), Nakaba et al. (2001) and De Lorenzis et al. (2001) reported the effects of the stiffness of FRP sheets ($E_f t_f$) in which E_{frp} and t_{frp} are elastic modulus and thickness, respectively. The bond strength increases as the FRP stiffness increases. De Lorenzis et al. (2001) showed that with the increase in FRP stiffness the area under the shear vs slip curve remains the same therefore the local bond ductility decreases. They assumed that the maximum shear stress in the joint is proportional to $(E_{frp} t_{frp})^{0.5}$. The test results presented by Dai et al. (2005) shown that the fracture energy of the interface is hardly affected by the FRP stiffness with a relation of $(E_{frp} t_{frp})^{0.023}$

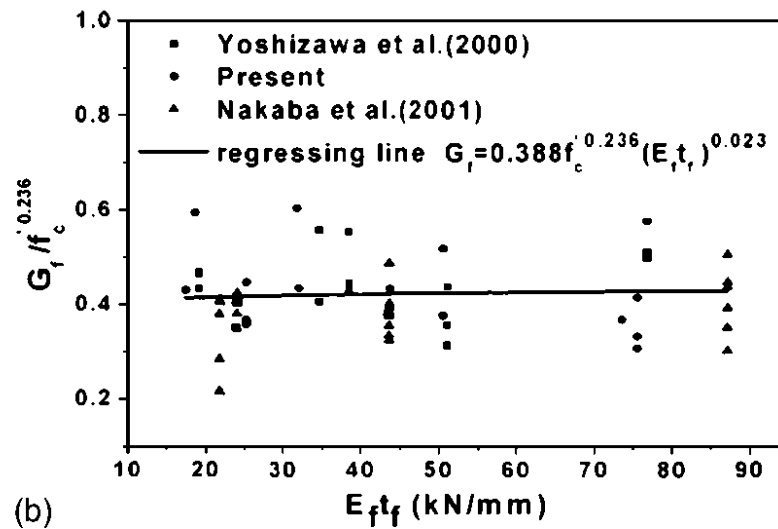


Figure 3.33. Effects of FRP stiffness on interfacial fracture energy of the bond (Dai et al. 2005)

7.5 Effective bond length

Many researchers have studied the effect of the FRP bond length. The previous studies have shown that there exists there exists an active bonding zone named called as the effective bond length L_e , along which most of the interfacial load is transferred between FRP sheets and concrete. When the bond length of FRP sheet-concrete interfaces exceeds the L_e , the bond strength will not increase significantly any longer.

Researchers have defined this length as the effective bond length, transfer length or critical anchor length Taljsten et al. (1997), Yao et al. (2005) and Cao et al. (2007). Generally, bond strength increases as the FRP bond length is increased. When the FRP bond length is increases beyond a certain extent, the bond length does not increase any further. Therefore, the average bond length decreases with the increase of sheet bond length.

Testing results given by Yao et al. (2005) showed that the effect of bond length on bond strength was not a significant. Furthermore, De Lorenzis et al. (2001) reported that the bond length did not affect the bond failure load. This result is more reasonable through the notion of existing effective bond length. In addition to the definition of effective bond length as previously described. Although extensive research has been conducted to investigate the bond behavior between FRP and concrete, there are no commonly acceptable analytical models to predict effective bond length. Yuan et al. (2004) deduced the effective bond length expression based on the relationship between fracture energy and shear stress-bond slip relationship.

In general, it was reported that the effective bond length increases with the stiffness of FRP sheets. However, due to the different materials used in various researches, the effective bond lengths can vary significantly such as 45 mm by Sato et al. (1997), 75 mm by Bizindavyi et al. (1999), 93 mm by De Lorenzis et al. (2001), 100 mm by Ueda et al. (1999) and 275 mm by Bronses et al. (1997).

7.6 Interfacial fracture energy

The Interfacial fracture energy G_f , which is defined as the area below the shear stress-bond slip curve, is important parameter for the bond characteristics. Based on different types of interfacial bond stress-slip relationships Yuan et al. (2001) proved that the maximum interfacial bond force can be expressed as function of the interfacial fracture energy G_f and FRP stiffness ($E_f t_f$). Interfacial fracture energy has been clearly defined by the theory of fracture mechanics and it can be used in the bond equations without any deviations. The effects of concrete strength, adhesive layer and stiffness of FRP sheets the on G_f have been hardly reported by Dai et al. (2005).

8.0 Conclusions based on previous research

As a result of the extensive literature review presented in this Chapter, the following conclusions can be drawn:

1. The test parameters that play significant roles in previous investigations can be summarized as:
 - the properties of base or substrate material (type, strength, and surface roughness),
 - FRP (type, mechanical properties, thickness, number of layers, width),
 - epoxy adhesive (strength, elongation, thickness),
 - the loading history and the environmental conditions (moisture, temperature, frost, pollution).

These variables have impact on the effective bond length, slip-bond curve, and rupture or fracture energy.

2. The test method can also play a significant role on test results. Both numerical and experimental studies have shown that the use of different test set-ups can lead to significantly different test results (Yao et al. 2005). Furthermore, it has been reported that small variations in test setups within a selected method, such as the height of the support or pushing block may also have an effect on test data (Yuan et al. 2004).
3. Previously suggested expressions for the effective FRP bond length were primarily a function of the thickness and elastic modulus of FRP. In recent years, the parameters affecting concrete strength and FRP strip width have also been incorporated into the expressions suggested for bond length.
4. Researchers have recently agreed that there exists an effective bond length beyond which the ultimate load capacity does not increase.
5. Various experimental and analytical investigations of the behaviour of bonded FRP-to-concrete joints have been carried out. Researchers have proposed bond stress-slip relationship models including the linear cut-off model, bilinear model, tri-linear model, and Popovics formula (Brosens et al 1999; Nakaba et al 2001; Ueda et al 1999)

9.0 References

- Arduini, M., and Nanni, A. (1997). "Behavior of Precracked RC Beams Strengthened with Carbon FRP Sheets, *Journal of Composites for Construction*, ASCE, Vol. 1, No.2, 63-69,.
- Bizindavyi, L., and Neale, K. W. (1997). "Experimental and Theoretical Investigation of Transfer Lengths for Composite Laminates Bonded to Concrete, Proceedings, Annual Conference of the Canadian Society for Civil Engineering, pp. 51-60.
- Bizindavyi L and Neale KW. (1999). "Transfer length and bond strength for composites bonded to concrete. *Journal of Composites for Construction (ASCE)* 1999: 3(4): 153–160.
- Bilotta, A., Di Ludovico, M., and Nigro, E. (2009). "FRP Debonding on Concrete Members: Experimental Investigation, Proceedings, 9th International RILEM Symposium on Non-Metallic (FRP) Reinforcement for Concrete Structures (FRPRCS-9), Sidney, Australia, 4 pp.
- Brosens, K., (2001). "Anchoring of Externally Bonded Steel Plates and CFRP Laminates for the Strengthening of Concrete Elements (Dissertation), Department of Civil Engineering, Katholieke University Leuven.
- Brosens, K. and Van Gemert, D. (1998). "Plate end shear design for external CFRP laminates." *Fracture Mechanics of Concrete Structures (FRAMCOS-3)*, Germany, 1793-804.
- Brosens, K. and Van Gemert, D.(1999). Anchorage design for externally bonded carbon fiber reinforced polymer laminates. *ACI, SP 188-56: 635–641*.
- Brosens, K. and Van Gemert, D.(1997). "Anchoring Stresses between Concrete and Carbon Fibre Reinforced Laminates," *Non-Metallic (FRP) Reinforcement for Concrete Structures*, Vol. 1, Japan Concrete Institute, Japan, pp. 271-278.
- Brosens, K. and D. V. Gemert. (1999). "Anchorage Design for Externally Bonded Carbon Fiber Polymer Laminates. *Proceeding of the Fourth International Symposium on FRP Reinforcement for Concrete Structures (FRPRCS-4)* , pp. 635-645.

- Buyukozturk, O., Gunes, O. and Karaca, E. (2004) Progress on Understanding Debonding Problems in Reinforced Concrete and Steel Members Strengthened using FRP Composites. *Construct. Build. Mater.* 18, 9-19.
- Casareto, M., Olivieri, A., Romelli, A. and Lagomarsino, S. (2003). "Bond behaviour of FRP laminates adhered to masonry", *Proceeding of the Advancing with Composites (Plast 2003)*, Milan, Italy.
- Cao S Y, Chen J F, Pan J W, Sun N. (2007). "ESPI measurement of bond-slip relationships of FRP-concrete interface [J]. *Journal of Composites for Construction*, ASCE, 11(2): 149–160.
- Chajes, M. J., Thomson, T. A., Januszka, T. F., and Finch, W. W. (1994). "Flexural Strengthening of Concrete Beams Using Externally Bonded Composite Materials." *Construction and Building Materials*, 8(3), 191-201.
- Chajes, M. J., Thomson, T. A. Jr, Farschman, C. A. (1995). "Durability of Concrete Beams Externally Reinforced With Composite Fabric". *Construction and Building Materials*, Vol. 9, No. 3, pp. 141-148.
- Chaallal, O., M.J. Nollet and D. Pematton, (1998). "Shear strength of RC by externally bonded side CFRP strips. *J. Composite Construct. ASCE*, 2: 111-113.
- Chen, J. F., Yang, Z. J., & Holt, G. D. (2001). "FRP or steel plate-to-concrete bonded joints: Effect of test methods on experimental bond strength. *Steel Compos Structures*, 1(2), 231–244.
- Chen JF, Teng JG. (2001). "Anchorage Strength Models for FRP and Steel Plates Bonded to Concrete. *Journal of Structural Engineering*, Vol. 127, No. 7, pp. 784-791.
- Chen, J.F. and Teng J.G. (2003). "Shear capacity of FRP strengthened RC beams: FRP debonding' *Construction and Building Materials*, 17(1), 27–41.
- Chen JF, Pan WK. (2004). "Stresses in simple shear test specimens for steel or FRP-to-concrete bond strength a 3D finite element study. In: *Proceedings of the advanced composites in construction; 20-22 April 2004, Surrey*, p. 473-82
- Chen JF, Pan WK. (2006). "Three dimensional stress distribution in FRP-to-concrete bond test specimens. *Constr Build Mater* 2006;20(1–2):46–58.

Chajes, M., J., Finch, Jr. W. W., Januszka, T. F., and Thomson, T. A., (1996). "Bond and Force Transfer of Composite Material Plates Bonded to Concrete, ACI Structural Journal, Vol. 93, No.2, 208-217.

Dai JG, Ueda T. (2003). "Local bond stress slip relations for FRP sheets concrete interfaces. In: Proc. of 6th international symposium on FRP reinforcement for concrete structures. Singapore: World Scientific Publications; p. 143–52.

Dai JG, Ueda T, Sato Y. (2005). "Development of the Nonlinear Bond Stress-Slip Model of Fiber Reinforced Plastics Sheet-Concrete Interfaces with A Simple Method. Journal of. Composite Construction, Vol. 9, No. 1, pp. 52-62.

De Lorenzis, L., Miller, B., and Nanni, A. (2001). "Bond of fiber reinforced polymer laminates to concrete." ACI Mater. J., 98(3), 256–264.

fib Bulletin 14 (2001). "Externally bonded FRP reinforcement for RC structures. Bulletin no. 14, fib.

Focacci F, Nanni A, Bakis CE. (2000). "Local bond-slip relationship for FRP reinforcement in concrete. J Compos for Constr;4(1):24–31.

Gunes, O., Lau, D., Tuakta, C. and Büyüköztürk, O. (2013). "Ductility of FRP-concrete systems: Investigations at different length scales." Construction and Building Materials, 49(915-25).

Guo, Z. G., Cao, S. Y., Sun, W. M., & Lin X. Y. (2005). "Experimental study on bond stresses-slip behaviour between FRP sheets and concrete. In Chen & Teng (Eds.), Proceedings of the International Symposium on Bond Behaviour of FRP in Structures, BBFS 2005 (pp. 77–83).

Hiroyuki, Y., & Wu, Z. (1997). "Analysis of debonding fracture properties of CFS strengthened member subject to tension. In Proceedings of 3rd international symposium on non-metallic (FRP) reinforcement for concrete structures (vol. 1, pp. 284–94).

Holzenkämpfer, O. (1994). "Ingenieurmodelle Des Verbundes Geklebter Bewehrung Für Detonbauteile (Dissertation). Technische Univ. Braunschweig. Braunschweig, Germany (in German), 1994.

Horiguchi, T., & Saeki, N. (1997). "Effect of test methods and quality of concrete on bond strength of CFRP sheet. In Proceedings of International Symposium on

Non-metallic (FRP) reinforcement for concrete structures, Sapporo, Japan, Japan Concrete Institute, Vol.1, pp. 265–270.

Kang, Q L.(1996). “Finite element analysis for reinforced concrete, Beijing, China Water Power Press, 120-126

Karbhari, V. M., Niu, H., and Sikorsky, C., (2006). “Review and Comparison of Fracture Mechanics-Based Bond Strength Models For FRP-Strengthened Structures, Journal of Reinforced Plastics and Composites, Vol. 25, No. 17, 1757-1738.

Khalifa, A., Gold, W. J., Nanni, A., & Aziz, A. (1998). “Contribution of externally bonded FRP to shear capacity of RC flexural members. Journal of Composites for Construction, ASCE, 2(4), 195–203.

Kobatake Y, Kimura K, Ktsumata H. (1993). “A retrofitting method for reinforced concrete structures using carbon fibre. In: Nanni A, editor. Fibre-reinforced-plastic (FRP) reinforcement for concrete structures: properties and applications. Amsterdam: Elsevier;, p. 435-50.

Lopez, G. J., Fernandez G. J. and Gonzalez, V. E. (2012). "Effect of Adhesive Thickness and Concrete Strength on FRP-Concrete Bonds." Journal of Composites for Construction, 16(6), 705-11.

Lu XZ, Teng JG, Ye JP, Jiang JJ. (2005). “Bond-Slip Models for FRP Sheets/Plates Bonded to Concrete. Engineering of Structure, Vol. 27, No. 6, pp. 920-937.

Lu X.Z. Jiang J.J. Teng J.G. Ye L.P., (2006). “Finite element simulation of debonding in FRP-to-concrete bonded joints, Construction and Building Materials 20 (2006) 412-424

Maalej, M., and Bian, Y. (2001). “Interfacial Shear Stress Concentration in FRP-Strengthened Beams. Composite Structures, 54, 417-26.

Maeda, T., Asano, Y., Sato, Y., Ueda, T., and Kakuta, Y., (1997). “A Study on Bond Mechanism of Carbon Fiber Sheet, Proceedings of the 3rd International Symposium on Non-Metallic (FRP) Reinforcement for Concrete Structures, Japan Concrete Institute, Sapporo, VoL 1, 279-285.

Malvar LJ. (1994). "Bond stress-slip characteristics of FRP rebars. California: Naval Facilities Engineering Service Center.

Mazzotti C, Savoia M, and Ferracuti B. (2008). "An experimental study on delamination of FRP plates bonded to concrete. *Construction and Building Materials*, 22(7):1409–1421.

Mitsui M, Fukuzawa K, Numao T, Fuda I. (2000). "Relations between Surface Roughness Indexes and Bond Strength between CFRP Sheets and Concrete," *Journal of the Society of Materials Science*, V. 49, No. 6. 2000, pp. 685-91.

McSweeney, B. M., and Lopez, M. M., (2005). "FRP-concrete Bond Behavior: A Parametric Study Through Pull-off Testing, *Proceedings of the Seventh International Symposium on FRP Reinforcement for Concrete Structures (FRPRCS- 7)*, 441-426.

Monti M, Renzelli M, Luciani P. (2003). "FRP Adhesion in Uncracked and Cracked Concrete Zones. *Proceedings of the Sixth International Symposium on FRP Reinforcement for Concrete Structures (FRPRCS-6)*, No.1, pp. 183-192.

Nakaba K, Kanakubo T, Furuta T, Yoshizawa H. (2001). "Bond Behavior Between Fiber-Reinforced Polymer Laminates and Concrete. *ACI Structural Journal*, Vol. 98, No. 3., pp. 359–367.

Niedermeier, R., (2006). "Stellungnahme zur richtlinie für das verkleben von betonbauteilen durch ankleben von stahllaschen-entwurf Miirzy Schreiben 1390 vom 30/10/1996 des lehrstuhls für Massivbau, Technische Univ. München, Munich, Germany (in German).

Neubauer, U. and F. S. Rostásy. (1997). "Design Aspects of Concrete Structures Strengthened with Externally Bonded CFRP Plates. *Proceedings of the Seventh International Conference on Structural Faults and Repairs*, No. 2, pp. 109-118.

Neubauer U, Rostasy FS. (1999). "Bond failure of concrete fiber reinforced polymer plates at inclined cracks-experiments and fracture mechanics model. In: *Proc. of 4th international symposium on fiber reinforced polymer reinforcement for reinforced concrete structures*, SP-188. Farmington Hills (MI): ACI. p. 369–82.

Niu H, and Wu Z, (2001). "Prediction of Debonding Failure Load due to Flexural Cracks of Concrete for FRP-Strengthened Structures," *Proceedings of the 5th*

International Conference on Fiber-Reinforced Plastics for Reinforced Concrete Structures, FRPRCS-5, V. 1. 2001, pp. 361-70.

Niu, H., and Wu, Z. (2005). "Numerical Analysis of Debonding Mechanisms in FRP-Strengthened RC Beams," *Computer-Aided Civil & Infrastructure Engineering*, Vol. 20, No. 5, pp. 354-368.

Pan, J. and Leung, C. K. Y. (2007). "Effect of Concrete Composition on FRP/Concrete Bond Capacity." *Journal of Composites for Construction*, 11(6), 611-8.

Perera, R., Recuero, A., Diego, A. D. and López, C. (2004). "Adherence analysis of fiber-reinforced polymer strengthened RC beams." *Computers & Structures*, 82(23–26), 1865-73.

Oehlers, D. J., Park, S. M. and Mohamed Ali, M. S. (2003). "A structural engineering approach to adhesive bonding longitudinal plates to RC beams and slabs." *Composites Part A: Applied Science and Manufacturing*, 34(9), 887-97.

Oehlers, DJ. and Seracino, R. (2004). "Design of FRP and steel plated RC structures, Adelaide, Australia, 2004, Elsevier, 22 8p.

Oehlers, D.J. (2005). "Generic Debonding Mechanisms in FRP Plated Beams and Slabs", *Proceedings of the International Symposium on Bond Behavior of FRP in Structures (BBFS)*, Hong Kong, International Institute for FRP in Construction, pp35-44.

Ritchie, P., Thomas, D., Lu, L. and Connelly, M. (1991). "External reinforcement of concrete beams using fiber reinforced plastics", *ACI Structural Journal*, 88(4), 490–500.

Saadatmanesh H., and Ehsani M.R. (1991). "RC beams strengthened with GFRP plates: experimental study", *Journal of Structural Engineering*, vol. 117, No. 11, 1991. pp.3417-343.

Sato, Y., Asano, Y., and Ueda, T. (2001). "Fundamental Study on Bond Mechanism of Carbon Fiber Sheet, *Concrete Library International, JSCE*, No.37, June 2001, 97-115.

Sandor Popovics (1973). "A numerical approach to the complete stress-strain curve of concrete. *Cement and concrete research*, 3(5):583–599.

- Sato, Y. (Yuichi), Kimura, K., and Kobatake, Y. (1997). "Bond behaviors between CFRP sheet and concrete." *J. Struct. Constr. Eng., AIJ*, No. 500, 75–82 (in Japanese).
- Savioa M, Farracuti B, Mazzotti D. (2003). "Non-linear bond–slip law for FRP concrete interface. In: Proc. of 6th international symposium on FRP reinforcement for concrete structures. Singapore: World Scientific Publications; p. 163–72.
- Sayed-Ahmed, E., Bakay, R. and Shrive, N. (2009). "Bond strength of FRP laminates to concrete: state-of-the-art review." *Electron Journal of Structural Engineering*, 9(1): 45-61.
- Shahawy, M.A., Beitelman, T., Arockiasamy, M. and Sowrirajan, R. (1996). "Experimental investigation on structural repair and strengthening of damaged prestressed concrete slabs utilizing externally bonded carbon laminates", *Composites: Part B*, Vol. 27B, pp217-224.
- Smith, S. T. and Teng, J. G. (2001). "Interfacial stresses in plated beams." *Engineering Structures*, 23(7), 857-71.
- Subramaniam, K. V., Carloni, C. and Nobile, L. (2007). "Width effect in the interface fracture during debonding of FRP from concrete. *Eng. Fract. Mech.* 74, 578–594.
- Swamy, R. N., Jones, R., and Charif, A. (1986). "Shear adhesion properties of epoxy resin adhesives." *Proc, Int. Symp. on Adhesion between Polymers and Concrete*, Chapman and Hall, London, 741-755.
- Tanaka, T. (1996). "Shear-Resisting Mechanism of Reinforced Concrete Beams with CFS as Shear Reinforcement. Graduation thesis, Hokkaido University, Japan.
- Täljsten B. (1994). "Plate bonding: strengthening of existing concrete structures with epoxy bonded plates of steel or fibre reinforced plastics [Doctoral]: Lulea University of Technology; 1994.
- Täljsten B. (1996). "Strengthening of Concrete Prisms Using the Plate Bonding Technique. *International Journal of Fracture*, No. 82, pp. 253-266.
- Täljsten B. (1997). "Defining Anchor Lengths of Steel and CFRP Plates Bonded to Concrete. *Int. J. Adhes. Adhes.* 17, 319–327.
- Teng, J. G. (2002). "FRP-Strengthened RC Structures. New York: Wiley, 2002.

Teng JG, Chen JF, Simth ST, Lam L. (2002). "FRP-strengthened RC structures. UK: John Wiley & Sons.

Teng, J.G., Chen, J.F., Smith S.T. and Lam, L. (2003). "Behaviour and strength of FRP strengthened RC structures: a state-of-the-art review", Proceedings of the Institution of Civil Engineers-Struct Build, pp51-62.

Teng, J. G., Lu, X. Z., Ye, L. P., & Jiang, J. J. (2004). "Recent Research on Intermediate Crack Induced Debonding in FRP Strengthened Beams. In Proceedings of the 4th International Conference on Advanced Composite Materials for Bridges and Structures, Calgary, AB, Canada.

Teng JG and Chen JF. (2007). "Debonding failures of RC beams strengthened with externally bonded FRP reinforcement: behaviour and modelling. In Proceedings of the First Asia-Pacific Conference on FRP in Structures (APFIS 2007), pages 12–14. The University of Hong Kong, Hong Kong, China.

Ueda, T., Sato, Y. and Asano, Y. (1999). "Experimental Study on Bond Strength of Continuous Carbon Fiber Sheets. Proc. Fourth Int. Symp. Fiber Reinforced Polym. Reinforced Concrete Struct., American Concrete Institute (SP-188), Detroit, MI, 407–416.

Ueda T, Dai J G. and Sato Y. (2003). "A Nonlinear Bond Stress–Slip Relationship for FRP Sheet–Concrete Interface. Proceedings of the International Symposium on Latest Achievement of Technology and Research on Retrofitting Concrete Structure, pp. 113–120.

Ueda, T., and Dai, J., (2005). "Interface Bond between FRP Sheets and Concrete Substrates: Properties, Numerical Modeling and Roles in Member Behavior, Progress in Structural Engineering and Materials, Vol. 7, Issue 1, 27-46.

Van Gemert, D. (1980). "Force transfer in epoxy-bonded steel–concrete joints. International Journal of Adhesion and Adhesives, 1, 67–72.

Van Gemert D., Ahmed O. and Brosens K. (1999). "Anchoring of externally bonded CFRP reinforcement, Extending Performance of Concrete structures, Proceedings of the International Seminar, 7 September 1999, Dundee, Scotland, pp. 81-92

- Vilnay O. (1988). "The analysis of reinforced concrete beams strengthened by epoxy bonded steel plates, *The International Journal of Cement Composites and Lightweight Concrete*, Number2 May.
- Wu, Z. S., Yuan, H. and Niu, H. (2002). "Stress transfer and fracture propagation in different kinds of adhesive joints', *Journal of Engineering Mechanics*, 128(5), 562–573
- Xia, S. H. and Teng, J. G. (2005). "Behaviour of FRP-to-concrete bonded joints." *Proceedings of the International Symposium on Bond Behaviour of FRP in Structures (BBFS 2005)*, Hong Kong, 411-8.
- Xiao, J., Li, J. and Zha, Q. (2004). "Experimental study on bond behavior between FRP and concrete." *Construction and Building Materials*, 18(10), 745-52.
- Yang, Z. J., Chen, J. F., and Proverbs, D. (2003). "Finite Element Modelling of Concrete Cover Separation Failure in FRP plated RC beams", *Construction and Building Materials*, Vol.17, pp3-13.
- Yang D, Hong S, Park S, (2007). "Experimental Observation on Bond-Slip Behavior between Concrete and CFRP Plate," *International Journal of Concrete Structures and Materials*, V. 1, No. 1. 2007, pp. 37-43.
- Yao, J., Teng, J.G., & Chen, J.F. (2005). *Experimental study on FRP-to-concrete bonded joints*, *Composites: Part B Engineering* (Vol.36, pp. 99–113) Elsevier.
- Yoshizawa, H., Myojo, T., Okoshi, M., Mizukoshi, M., and Kliger, H. S., (1996). "Effect of Sheet Bonding Condition on Concrete Members Having Externally Bonded Carbon Fiber Sheet," *Fourth Materials Engineering Conference, ASCE Annual Convention*, Washington D.C.
- Yoshizawa, H., Wu, Z., Yuan, H., and Kanakubo, T., (2000). "Study on FRP-concrete interface bond performance." *Trans. Jpn. Soc. Civ. Eng.*, 662(49), 105–119.
- Yuan H, Wu ZS. (1999). "Interfacial Fracture Theory in Structures Strengthened with Composite of Continuous Fiber. *Proceedings of Symposium of China and Japan: Science and Technology of the 21st Century*, pp. 142-155.
- Yuan, H., Wu, Z., and Yoshizawa, H., (2001). "Theoretical Solutions on Interfacial Stress Transfer of Externally Bonded Steel/Composite Plates, *Journal of Structural Mechanics and Earthquake Engineering, JSCE*, Vol. 18, No. 1, 27-39.

Yuan, H., Teng, J.G., Seracino, R., Wu, Z.S. and Yao, J. (2004), "Full-range behavior of FRP-to-concrete bonded joints", *Engineering Structures*, Vol. 26, No. 5, pp. 553-565.

Zhao, M., Dong, Y., Zhao, Y., Tennant, A. and Ansari, F. (2007). "Monitoring of Bond in FRP Retrofitted Concrete Structures." *Journal of Intelligent Material Systems and Structures*, 18(853-60).

Ziraba YN, Baluch MH, Basunbul AM, Azad AK, Al-Sulaimani GJ, Sharif IA. (1995). "Combined experimental-numerical approach to characterization of steel-glue-concrete interface. *Mater Struct*;28:5 18-25.

CHAPTER 4

THE UNSOLVED ISSUES IN THE DESIGN PROCESS OF FRP STRENGTHENED RC MEMBERS

1.0 Introduction

The direct calibration of the Cohesive Material Law (CML) or the interfacial τ - s relationship is one of the unsolved issues of the FRP-Concrete interfacial debonding phenomenon. Many researchers in the past tried to define a reliable method capable of describe the interaction between the FRP strip and the concrete substrate. In other words, they aimed to understand the quasi-brittle behavior of the bond between composites and concrete substrates via a constitutive law of a fictitious material (of zero thickness) that separates the two adherents. In this chapter, direct shear tests were used to calibrate the CML of the FRP-concrete debonding response obtained by Subramaniam et al. (2007).

2.0 Experimental Investigation

2.1. Experimental details and test setup

A test setup was designed to perform direct shear tests on FRP sheets bonded to concrete prisms. The experimental program was conducted by Subramaniam et al. (2007). In experimental tests, the loading apparatus was organized in order to apply a tensile load to the FRP strip, which was attached to the concrete block, while the concrete block was restrained against movement as shown in Figure 4.1. Details about the specimen geometry and the test configuration as provided by Subramaniam et al. 2007 are shown in Table 4.1.

Unidirectional carbon fiber reinforced polymer (CFRP) sheets were used, with a thickness t equal to 0.167 mm. The tensile strength and the Young's modulus of the FRP composite were equal to 3.83 GPa and 230 GPa, respectively. A length of the

FRP equal to 35 mm was left unbonded to provide an initial notch for the crack growth. Tests were performed using the global slip, g , as the control variable by increasing it at a constant rate equal to 0.00065 mm/s up to failure. Two LVDTs were mounted on the concrete prism near the loaded end of the composite to measure the global slip of the FRP as shown in Figure 4.1.

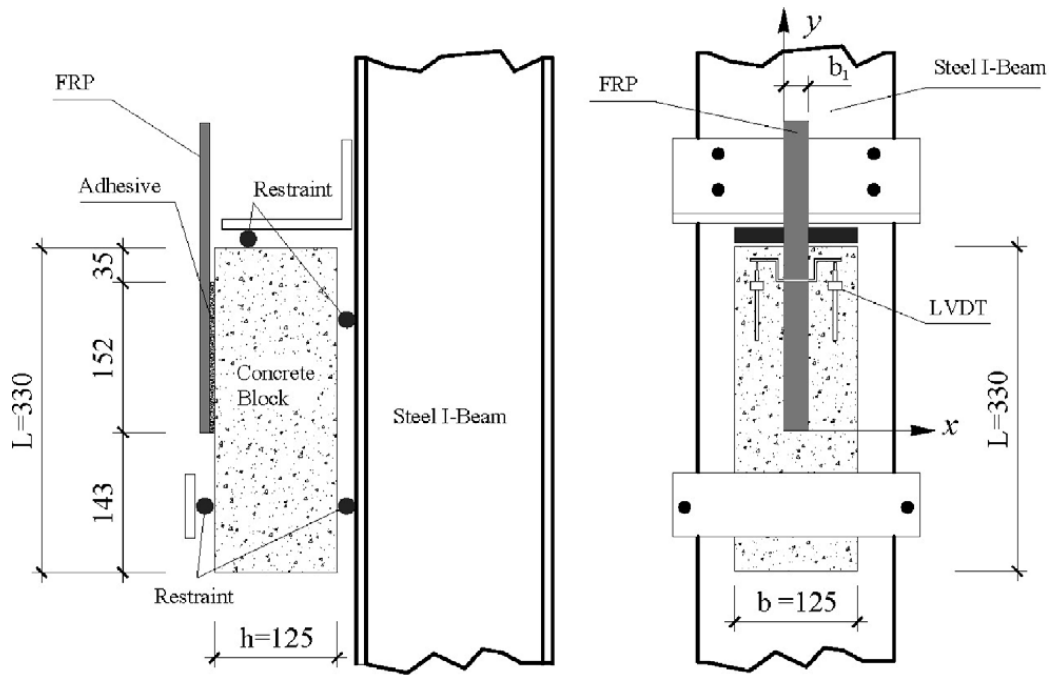


Figure 4.1: Specimen dimensions and loading arrangement

(Subramaniam et al. 2007)

Table 4.1: Details about the specimen geometry and the test configuration considered for the calibration of the CML's (Subramaniam et al. 2007).

Specimen Test	Concrete				CFRP		Direct shear results	
	f_c (MPa)	t_c (mm)	b_c (mm)	L_c (mm)	b_f (mm)	l_f (mm)	P_{crit} (KN)	$\sigma_u = P_{crit}/b_f*t_f$ (N/mm ²)
W_2	39	125	125	330	38	152	9.80	1544.83
W_3	39	125	125	330	38	152	10.02	1574.80
W_4	39	125	125	330	25	152	5.54	1326.66
W_5	39	125	125	330	25	152	5.44	1303.62
W_6	39	125	125	330	25	152	5.36	1284.26
W_8	39	125	125	330	19	152	4.27	1345.62
W_9	39	125	125	330	19	152	4.05	1275.79

2.2 Direct shear test results

Figure 4.2 shows a typical load response (the average of the two LVDTs is termed global slip, g , while the applied load is termed P) obtained for a 25 mm width strip tested by Subramaniam et al. (2007). All load-responses had a similar shape. Different widths were tested. The maximum load was obtained for the wider FRP sheet. The curves showed an initial linear ascending region followed by a non-linear response. The end of the non-linear part of the response was typically marked a by a load drop that indicated that the interfacial crack has formed. As the crack propagates, the load was nominally constant after the load drop and the value of the constant load is termed load- carrying capacity or bond strength and indicated as P_{crit} , which is determined as the mean value of the load when the global is within the range g_1 and g_2 (for specimen in Figure 4.2, $g_1=0.35$ mm, $g_2=0.75$ mm). The global slip range (g_1, g_2) varied for each test and was identified on the basis of the strain analysis results by Subramaniam et al. (2007).

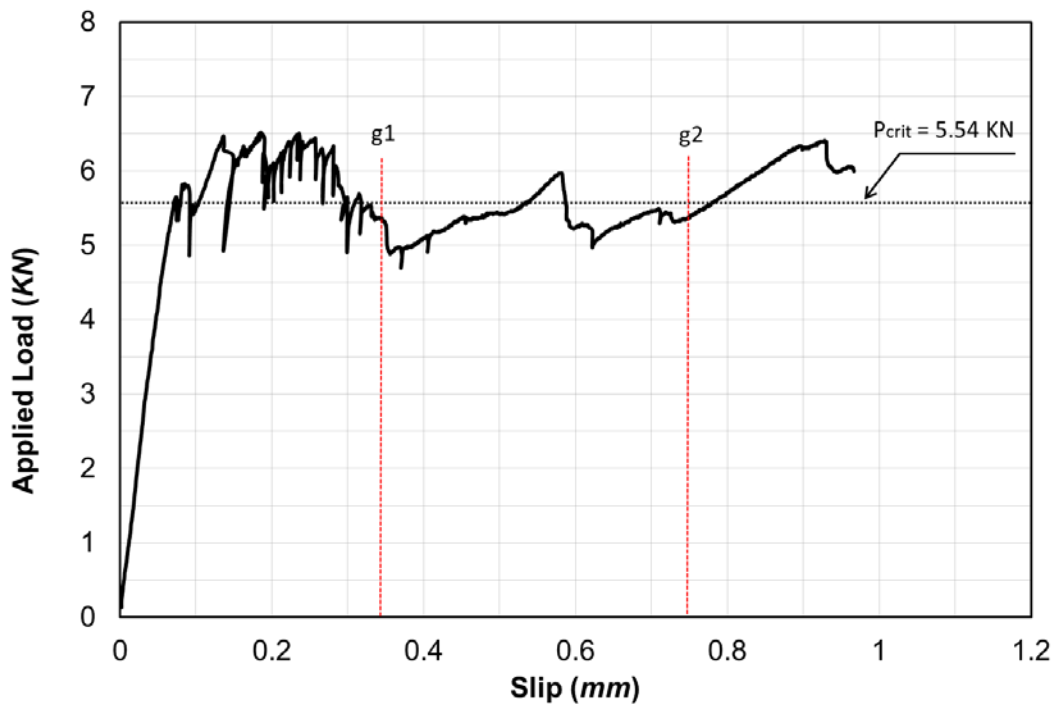


Figure 4.2: Typical load versus global slip response of the FRP bonded to concrete for test W_4 in Subramaniam et al. (2007)

3.0 Cohesive Material Law (CML)

As it is known, the analytical form of the bond-slip law is fundamental for a reliable structural analysis of concrete externally strengthened with FRP sheets. In other words, CML or the interfacial τ - s relationship is the most fundamental constitutive laws that characterize the bond of FRP sheet-concrete interfaces. The calibration of the cohesive material law can be derived from the analysis of the experimental load responses (applied load P and the corresponding slip at the loaded end s_{\max}).

The interfacial fracture energy, G_F , which corresponds to the area under the τ - s curve is obtained as:

$$G_F = \int_0^{s_f} \tau(s) ds \quad (1)$$

Several expressions of CML have been proposed in order to perform the indirect calibration. Each CML function contains several unknown parameters that were determined such that the adopted values minimized the difference between the experimental results and analytical predictions. CML functions considered in this work to fit the experimental load responses are: 1) D'Ambrisi et al. (2012) function, and 2) Dai et al. (2005) function.

3.1 CML based on load responses

3.1.1 D'Ambrisi et al. (2012)

The CML function influenced by the experimental results of PBO-FRCM materials used in the calibration to describe the cohesive material law, which is expressed D'Ambrisi et al. (2012) and is defined as:

$$\tau(s) = [\tau_o + A. (e^{-\alpha s} - e^{-\beta s})]. \left(1 - \frac{s}{s_f}\right) \quad 0 \leq s \leq s_f \quad (2)$$

where s = slip (relative displacement between fabric and matrix); s_f = final slip when value of bond stress is zero. The set of unknown parameters [A , α , β] (curve-fitting parameters); τ = bond stress; and τ_o = initial finite value of bond shear stress.

The bond-slip relation Eq. (2) represents a CML characterized by nonzero shear stress at $s = 0$ ($\tau(0) = \tau_o$). A typical $\tau(s)$ curve of FRP specimens is shown in Figure 4.3.

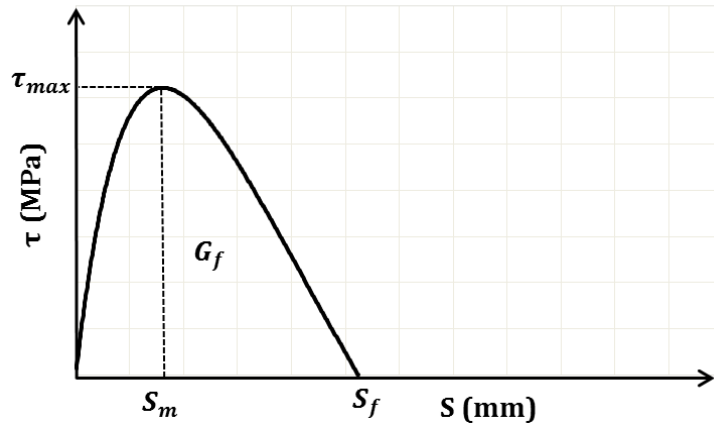


Figure 4.3: Typical CML (D'Ambrisi et al. 2012)

3.1.2 Dai et al. (2005)

The CML function was also fitted from the expression proposed by Dai et al. (2005). Eq. (3) provides the relationship of the shear stress (τ) and the relative slip (s) between the FRP sheet and concrete substrate, and is defined by:

$$\tau(s) = A. (e^{-\alpha s} - e^{-2\alpha s}) \quad 0 \leq s \leq s_f \quad (3)$$

The proposed $\tau(s)$ relationship has two unknown parameters (A , α). The $\tau(s)$ law given in Eq. (3) is influenced by the experimental results of FRP sheet used in the calibration. A typical $\tau(s)$ curve of FRP specimens is shown in Figure 4.4.

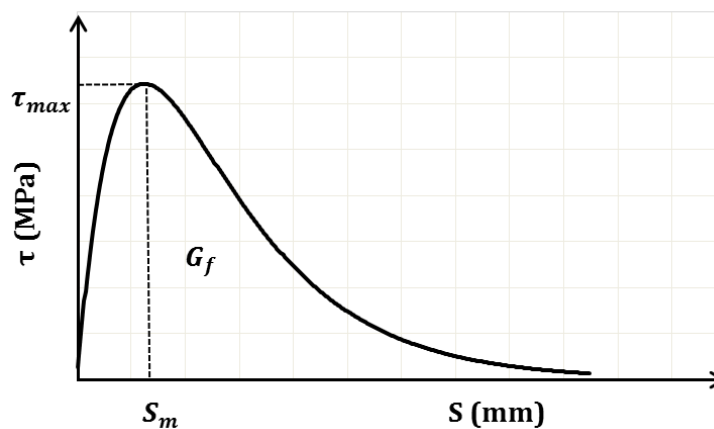


Figure 4.4: Typical CML (Dai et al. 2005)

3.2 Calibration method and construction of the analytical of the strain capacity (SC) response $\varepsilon_{\max}(\ell)$

In the following section, a method to calibrate parameters of a given cohesive material law (CML) is presented together with the analytical or numerical evaluation. The most widely adopted method for the calibration of CML named direct method, which is based on the experimental $\varepsilon_{\max}(\ell)$ curve (i.e., the $P_{\max}(\ell)$ curve divided by the axial stiffness $E_f A_f$ as follow.

$$\varepsilon_{\max}(\ell) = \frac{P_{\max}(\ell)}{E_f A_f} \quad (4)$$

where E_f is the elastic modulus of the fibers, and A_f is the cross-sectional area of the fibers.

Once the experimental $\varepsilon_{\max}(\ell)$ curve is selected, a best fitting procedure is used to calibrate the CML against the experimental data. This step requires that the $\varepsilon_{\max}(\ell)$ curve corresponding to a certain set \mathbf{p} of parameters is obtained by solving the fundamental differential equation that describes the Mode-II debonding phenomenon Focacci F, Carloni C (2015); Carloni C, Focacci F. (2016) and Malena et al. (2016). The best fitting procedure entails for the definition of a calibration criterion that is specific for the $\varepsilon_{\max}(\ell)$ curve. The calibration criterion should minimize the distance between the experimental and the analytical curves.

3.3 Construction of the analytical responses

The CML consents for the analytical or numerical evaluation of the strain profiles $\varepsilon(y)$, load response $P(g)$, joint capacity (JC) response $P_{\max}(\ell)$, and slip capacity (SLC) response $g_{\max}(\ell)$.

In particular, the term *analytical* will be used for the strain profile and the other responses obtained from the CML, even though numerical methods have been used for the solution of the differential equations and integrals herein presented. Figure 4.5 shows an idealized CML for an FRCC material and the associated relations $\varepsilon(y)$,

$P(g)$, $P_{\max}(\ell)$, and $g_{\max}(\ell)$ for a relatively long bonded length (Focacci F, Carloni C. (2015); Carloni C, Focacci F. (2016); and Focacci F, Carloni C (2015)).

The analytical responses associated with an assigned CML are determined by solving the differential equation (Focacci F, Carloni C (2015); Carloni C, Focacci F. (2016); Malena et al. (2016); and Focacci F, Carloni C (2015)).

$$\frac{d^2 s}{dy^2} = \frac{p_f}{E_f A_f} \tau(s) \quad (5)$$

where E_f is the fibers Young's modulus, A_f is the area of the fibers cross section and $s=s(y)$ is the slip at a distance y from the free end Figure 4.5. The boundary conditions must be enforced, for example, at the free end ($y=0$, Figure 4.5).

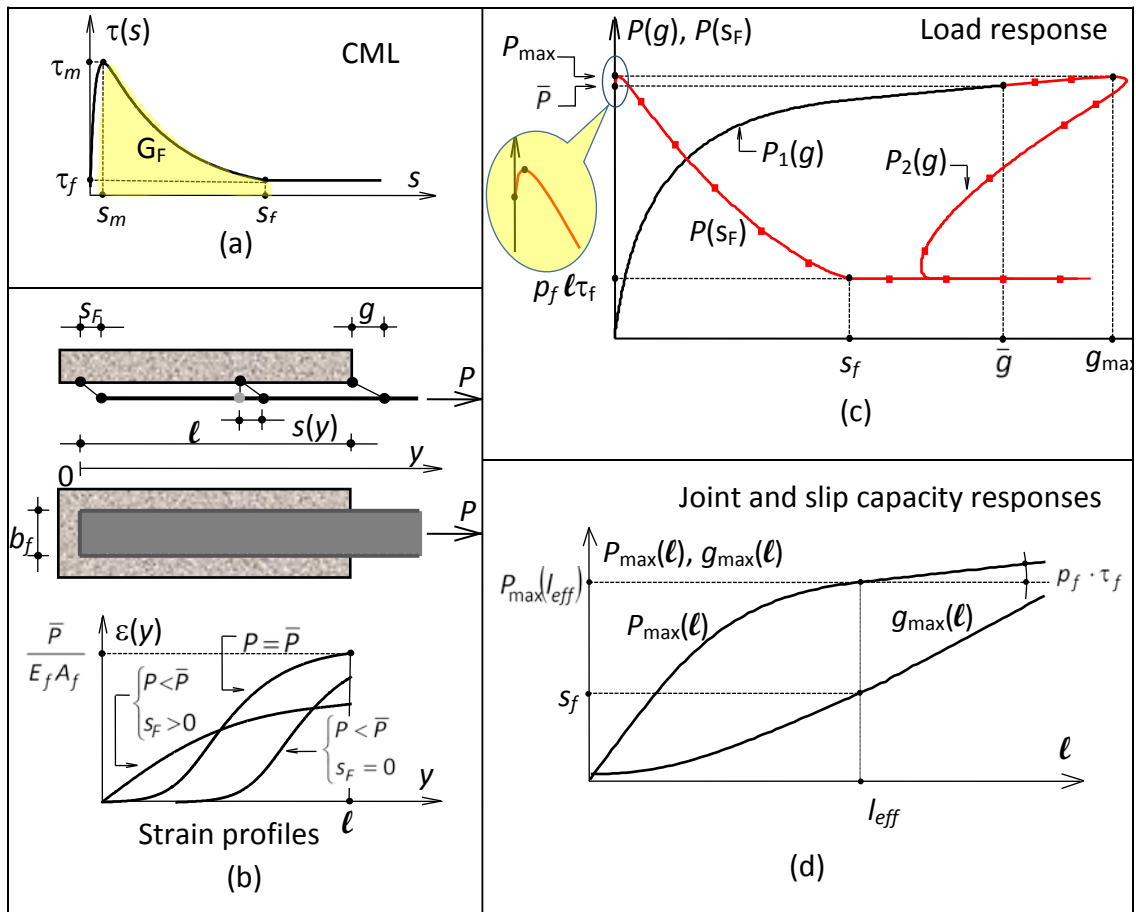


Figure 4.5 : (a) Typical CML for an FRCM composite. (b) Strain profiles consequent to the typical CML. (c) Load response corresponding to the typical CML. (d) Joint and slip capacity responses corresponding to the typical CML.

Construction of the strain profiles $\varepsilon(y)$

The strain profile $\varepsilon(y)$ associated with applied load P can be defined as:

$$\varepsilon(y) = \frac{d}{dy} s(y) \quad (6)$$

where $s(y)$ is a solution of differential Eq. (5) satisfying the condition (Figure 4.5b):

$$E_f A_f \left. \frac{ds}{dy} \right|_{y=l} = P \quad (7)$$

If the CML is followed by a constant shear stress τ_f ($s \geq s_f$, Figure 4.5a), when the loaded end slip g is greater than s_f a portion of the strain profile near the loaded end presents a constant slope:

$$\frac{d\varepsilon}{dy} = \tau_f \frac{\rho_f}{E_f A_f} \quad (8)$$

This is a peculiarity of some FRCM materials such as the one herein investigated D'Antino et al. (2014). For FRP composites, the shear stress is generally assumed equal to zero for slips greater than a certain slip s_f . Consequently, in the case of FRP composites, the strain profiles are constant at the loaded end for $g \geq s_f$.

Construction of the load responses $P(g)$

A procedure to construct the load response $P(g)$ was applied in Focacci et al. (2000) in order to characterize the bond properties of FRP rebars embedded to concrete, in D'Ambrisi et al. (2012) to characterize the bond properties of FRCM materials embedded to masonry, and D'Ambrisi et al. (2013) to characterize the bond properties of PBO-FRCM materials embedded to concrete.

A similar procedure is adopted herein and takes into account that the $P(g)$ response is comprised of two branches: in the first branch, named $P_1(g)$, corresponds to null slips s_F at the free end (Figure 4.5a,c). While in the second branch, named $P_2(g)$,

corresponds to nonzero slips s_F at the free end occur (Figure 4.5c). The procedure consists of the following steps.

Step 1: This step consists of determining the applied force \bar{P} and consequent loaded end slip \bar{g} at the onset of nonzero slip at the free end. These parameters can be determined by solving the differential Eq. (5) with the boundary conditions enforced at the free end ($y=0$, Figure 4.5):

$$\begin{cases} s(0)=0 \\ \varepsilon(0)=\left.\frac{ds}{dy}\right|_{y=0}=0 \end{cases} \quad (9a,b)$$

The force \bar{P} and the loaded end slip \bar{g} are then determined as:

$$\begin{aligned} \bar{g} &= \bar{s}(\ell) \\ \bar{P} &= E_f A_f \left.\frac{d\bar{s}}{dy}\right|_{y=\ell} \end{aligned} \quad (10a,b)$$

Where $\bar{s}(y)$ is the solution of differential Eq. (5) with the boundary conditions in Eq. (9a,b).

Step 2: This step consists of determining of the first branch $P_1(g)$ of the $P(g)$ response. $P_1(g)$ is obtained from Eq. (11) Focacci et al. (2000).

$$\begin{aligned} g &= s(\ell) \\ P_1(g) &= \sqrt{2p_f E_f A_f \int_0^g \tau(s) ds} \end{aligned} \quad (11a,b)$$

Step 3: This step consists of determining of the second branch $P_2(g)$ of the $P(g)$ response. $P_2(g)$ is determined by considering a set of values of the free end slip s_F and solving differential Eq. (5) with boundary conditions:

$$\begin{cases} s(0) = s_F \\ \varepsilon(0) = \left. \frac{ds}{dy} \right|_{y=0} = 0 \end{cases} \quad (12a,b)$$

The solutions $s(y) = s_{s_F}(y)$ of Eq. (5) with the boundary conditions in Eq. (12a,b) allows for associating the applied load P and loaded end slip g with each value of the free end slip s_F :

$$\begin{aligned} g(s_F) &= s_{s_F}(\ell) \\ P(s_F) &= E_f E_f \left. \frac{ds_{s_F}}{dy} \right|_{y=\ell} \end{aligned} \quad (13a,b)$$

The subscript s_F in Eq. (13a,b) indicates that the corresponding slip profile $s_{s_F}(y)$ is associated with a certain slip s_F at the free end. Hence, for each value of the parameter s_F the slip profile $s_{s_F}(y)$ is determined.

Therefore, for each value of s_F the loaded end slip $g(s_F)$ and the applied force $g(s_F)$ are computed. The second branch $P_2(g)$ of the $P(g)$ response is obtained by eliminating the parameter s_F between the functions $P(s_F)$ and $g(s_F)$.

Step 4: This step consists of determining of the $P(g)$ response. Finally, the entire $P(g)$ response is the union of branches $P_1(g)$ and $P_2(g)$, as shown in Figure 4.5c. It is worth noting that the existence of both branches $P_1(g)$ and $P_2(g)$ depends on the shape of the adopted CML: the first branch does not exist, i.e. $\bar{P}(0) = 0$, for a CML characterized by $\tau(0) = 0$ and finite derivative at $s = 0$, as observed in D'Ambrisi et al. (2013); Focacci F, Carloni C. (2015) and Carloni C, Focacci F (2016). Figure 4.5c shows the shape of the load response and also the relation $P(s_F)$ consequent to the typical CML represented in the same figure.

3.4 Direct calibration of CML best on strain profile

The most widespread technique to define the interfacial τ - s relationship consists in the direct calculation of local bond stress and slip from the variation of the strain measured by a series of strain gauges on the external face of a FRP sheet. This type

of procedure leads to an inaccurate evaluation of the bond stresses at the interface due to several causes, among which the highly nonlinearity nature of local fractures, the random distribution of discrete cracks and aggregates in the concrete and the irregularity in the adhesive layer and surface preparation. Part of these drawbacks is overcome by the use of DIC.

In recent years Dai et al. (2006) proposed a more reliable and accurate method in order to describe the behavior at the interface between the FRP strip and the concrete substrate considering the relationship among the strains of FRP sheets and the slips at the loaded end. This way appears to be more correct because the measurements of the load and slip at the loaded end in a pull-off test are much more stable than the strains obtained from strain gauges along the FRP strip. The main relationships considered by Dai et al. (2006) in the study of the debonding phenomenon, regarding shear stresses and slips along the FRP-concrete interface, are the followings:

$$\tau(y) = E_f t_f \frac{d\varepsilon}{dy} \quad (14)$$

$$s(y) = \int_0^y \varepsilon(t) dt \quad (15)$$

In their analysis Dai et al. (2006) used an exponential expression of the longitudinal strain to fit, through a nonlinear regression, the experimental strain-slip curve at the loaded end of the FRP strip. In this work, following a similar approach, an exponential function will be used to fit the trend of experimental strains along the FRP strip. However, it is important to highlight that the choice of the function is not unique and may be interesting to investigate the influence of this choice on the determination of the fracture parameters of the FRP-concrete interface.

The axial strain distribution along the FRP assumes a primary importance in the debonding phenomenon at the interface between FRP and concrete. If the detachment at the interface is already started and the bond length is long enough, this distribution is divided into three main regions: the stress-free zone (SFZ), the stress-transfer zone (STZ) and the fully-debonded zone (FDZ). The former is the portion of the FRP strip not yet interested by the debonding phenomenon in which both the strain and the shear stress are equal to zero. The STZ is the part of the FRP strip

where the transfer of shear stress takes place and it is usually characterized by a “S” shape of the strain profile. Eventually, in the FDZ the FRP strip is already detached from the concrete substrate: the strains are equal to their maximum value while the exchange for shear stress is no longer possible.

Ali-Ahmad et al. (2006) approximated the experimental nonlinear strain distribution along the bonded length using the following expression:

$$\varepsilon_{yy} = \varepsilon_0 + \frac{\alpha}{1 + \exp\left(-\frac{y - y_0}{\beta}\right)} \quad (16)$$

This expression is similar to the one proposed by Dai et al. (2006). One of the main problems in the choice of an exponential function to approximate strain data along the FRP strip is the impossibility to define a finite effective bond length (EBL), which is the minimum length needed to develop the maximum capacity of the interface. To overcome this problem, Dai et al. (2006) defined a conventional EBL corresponding to 96% of the ultimate load. In fact, the EBL can be obtained directly analyzing how the ultimate load changes compared to different values of the bond length. Above a certain value of the bond length, it's no possible to appreciate significant increases of the ultimate load; therefore this value corresponds to the EBL. As already mentioned, in Dai et al. (2006) method the load tends asymptotically to the maximum value, i.e. the ultimate load, so that is impossible to define a finite EBL without recurring to some approximation.

In this work other functions have been considered in order to highlight their influence on the determination of the fracture parameters of the FRP-concrete interface and to obtain a finite value for the effective bond length. The functions considered in this work to fit the strain distribution along the bonded length are:

- 1) Dai function;
- 2) Sine function;
- 3) Polynomial function;
- 4) “BI-function”, obtained considering a bilinear behavior of the interfacial τ -s relationship.

3.4.1 Dai et al. (2006) function

Dai et al. proposed the following function for the longitudinal strain:

$$\varepsilon(y) = \frac{A \exp(B(Ay + C))}{\exp(B(Ay + C)) + 1} \quad (17)$$

where A, B, and C are parameters evaluated through a non-linear regression.

The experimental strain at the interface were fitted through Eq. (17), while during the analysis it has been defined the shear stresses and the slips along the FRP-concrete interface through Eqs. (14) and (15). Inverting $s(y)$ and substituting the $y(s)$ expression in the $\tau(y)$ formula, it's possible to define the cohesive material law τ - s . Unfortunately, not all the $s(y)$ functions are reversible, so that is not always possible to define a $y(s)$ expression. In other cases, the integral of $\varepsilon(t)dt$ cannot be calculated and therefore the $s(y)$ function cannot be evaluated. Dai solved this integral using some mathematical tricks, not completely correct from an analytical point of view.

A more simple procedure to define the τ - s relationship is obtained combining the stresses and the slips aforementioned. Following this way, it is possible to plot the τ - s function and to determine on this graph the most important fracture parameters, such as τ_{\max} , slip_{\max} namely the slip corresponding to τ_{\max} , and G_F , the fracture energy, which is the area under the τ - s curve. The latter parameter was obtained using Dai formulations:

$$G = A^2 \frac{E_f t_f}{2} \quad (18)$$

3.4.2 Sine function

Another function that has been considered is a sine-type function that can be suitable to represent the S-shape trend of the experimental strain profile along the FRP strip:

$$\varepsilon(y) = \begin{cases} 0, & \text{if } \varepsilon_1(y)' > 0 \quad \& \quad \varepsilon_1(y)'' < 0 \\ \varepsilon_1(y), & \text{if } \varepsilon_1(y)' > 0 \\ 2D, & \text{if } \varepsilon_1(y)' < 0 \quad \& \quad \varepsilon_1(y)'' < 0 \end{cases} \quad (19)$$

Where $\varepsilon_1(y)$ is the following expression:

$$\varepsilon_1(y) = D \sin \left(\left(\frac{y-G}{E} \right)^F \pi - \frac{\pi}{2} \right) + D \quad (20)$$

and once again D, E, F, and G are parameters evaluated through a non-linear regression. y_A and y_B are the y coordinates along the FRP strip where the function changes from 0 to $\varepsilon_1(y)$ and from $\varepsilon_1(y)$ to 2D, respectively.

The function is composed of three parts and showed in Eq. (19). Considering a reference system that starts from the free end, y_A represents the position along the FRP strip where the transfer of shear stresses through the interface begins. Instead, y_B indicates the position from which the exchange in shear stresses is no longer possible due to the fact the FRP strip is completely detached from the concrete substrate. Analyzing the strains along the FRP strip, it can be noted that until $y \leq y_A$, they are equal to zero, while if $y_A < y < y_B$ they are represented by a sinusoidal function and finally if $y \geq y_B$ they are equal to 2D (ε_{\max}).

The value of y_B is obtained analyzing the first and the second derivative of the sinusoidal function in Eq. (19). When the second derivative of this expression is negative, the position in which the first derivate changes from a positive to a negative value corresponds to y_B . Eq. (19) was used to fit experimental strains while the shear stresses are calculated through Eq. (14). Unfortunately, it is no possible to evaluate the integral in Eq. (15) for the sine function; therefore the slips along the FRP strip were estimated computing the area under the $\varepsilon(y)$ curve for each range of experimental data. Proceeding in this way, the slips just evaluated corresponds to the central value between two consecutive positions along the FRP strip. Therefore, in order to combine correctly the slips and shear stresses, each slip was related with the mean value of the shear stress between the two corresponding experimental data.

The interfacial τ -s relationship was then plotted and the most important parameters were detected. It's important to highlight that the analytical expression of $\tau(s)$ cannot be obtained such as for Subramaniam et al. function because the integral in Eq. (15) cannot be solved. The fracture energy G_F was obtained computing the area under the τ -s curve.

3.4.3 Polynomial function

Fitting of the experimental strain profile was also attempted through a polynomial function:

$$\varepsilon(y) = \begin{cases} 0, & \text{if } \varepsilon_2(y)' > 0 \text{ \& } \varepsilon_2(y)'' < 0 \\ \varepsilon_2(y), & \text{if } \varepsilon_2(y)' > 0 \\ \varepsilon_2(y = y_D), & \text{if } \varepsilon_2(y)' < 0 \text{ \& } \varepsilon_2(y)'' < 0 \end{cases} \quad (21)$$

where $\varepsilon_2(y)$ is the following expression:

$$\varepsilon_2(y) = H(y - y_C)^3 + I(y - y_C)^2 + L(y - y_C) \quad (22)$$

where once again H, I, L, and y_C are parameters evaluated through a non-linear regression. y_C and y_D are the y coordinates along the FRP strip where the function changes from 0 to $\varepsilon_2(y)$ and from $\varepsilon_2(y)$ to $\varepsilon_2(y = y_D)$, respectively.

Such as for the sine function also for the polynomial one the function is composed of three parts and showed in Eq. (21). The positions y_C and y_D assume the same meaning of y_A and y_B for the sine function, respectively. Therefore, until $y \leq y_C$, the strains are equal to zero, if $y_C < y < y_D$ they are represented by a polynomial function while if $y \geq y_D$ they are equal to ε_{\max} . It can be observed that the polynomial expression results zero in $y = y_C$, where there should be no strains.

The value of y_D is obtained analyzing the first and the second derivative of the polynomial function in Eq. (21). When the second derivative of this expression is negative, the position in which the first derivative changes from a positive to a negative value corresponds to y_D . The value of ε_{\max} is obtained from Eq. (22).

The experimental strain at the interface were fitted through Eq. (21), while it's important to highlight that for the polynomial function is possible to define in an analytic way the interfacial τ -s relationship. In order to investigate the cohesive material law only the second expression in Eq. (21) may be considered. For simplicity, it is useful to change the reference system starting point in $y = y_0$ in order to obtain the following expression of the strains along the FRP strip:

$$\varepsilon(y) = Ay^3 + By^2 + Cy \quad (23)$$

The slips along the FRP strip are obtained by integration of Eq. (23) as follows:

$$s(y) = \frac{A}{4}y^4 + \frac{B}{3}y^3 + \frac{C}{2}y^2 \quad (24)$$

Therefore, the $y(s)$ relationship is obtained solving the following expression:

$$ay^4 + by^3 + cy^2 + e = 0 \quad (25)$$

where $a = A/4$, $b = B/3$, $c = C/2$, and $e = -s$.

Eq. (25) represents an expression of the fourth degree in y and can be solved referring to Cardano's formulas, obtaining two real solutions and two complex solutions. The procedure is summarized in the following equations:

$$\Delta_0 = c^2 + 12ae \quad (26)$$

$$\Delta_1 = 2c^3 + 27b^2e - 72ace \quad (27)$$

$$p = \frac{8ac - 3b^2}{8a^2} \quad (28)$$

$$q = \frac{b^3 - 4abc}{8a^3} \quad (29)$$

$$Q = \sqrt[3]{\frac{\Delta_1 + \sqrt{\Delta_1^2 - 4\Delta_0^3}}{2}} \quad (30)$$

$$S = \frac{1}{2} \sqrt{-\frac{2}{3}p + \frac{1}{3a} \left(Q + \frac{\Delta_0}{Q} \right)} \quad (31)$$

$$y_{1,2} = -\frac{b}{4a} - S \pm \frac{1}{2} \sqrt{-4S^2 - 2p + \frac{q}{S}} \quad (32)$$

$$y_{3,4} = -\frac{b}{4a} + S \pm \frac{1}{2} \sqrt{-4S^2 - 2p - \frac{q}{S}} \quad (33)$$

At the same time, the shear stresses along the FRP strip can be evaluated substituting Eq. (23) in Eq. (14), obtaining:

$$\tau(y) = E_f t_f (3Ax^2 + 2Bx + C) \quad (34)$$

Once that one of the two real solutions is obtained from Eqs. (32) or (33), it can be substituted in Eq. (34) in order to obtain finally the analytical expression of the cohesive material law τ - s at the interface between the FRP strip and the concrete substrate.

Another procedure to define the τ - s relationship is to combine directly the shear stresses and the slips calculated with Eqs. (14) and (15) in order to plot the τ - s function and to define the most important fracture parameters. The plot of the analytical function was compared with the plot obtained by combining the values of the stress and the slip corresponding to the same value of y . The two plots were identical. The fracture energy G_F was obtained computing the area under the τ - s curve.

3.4.4 Bilinear function

Several researchers have assumed a bilinear function to describe the cohesive material law, which is expressed as:

$$\tau_s(s) = \begin{cases} \tau_0 + \frac{\tau_m - \tau_0}{s_m} s & \text{if } 0 \leq s < s_m \\ \tau_{02} - \frac{\tau_{02}}{s_f} s & \text{if } s_m \leq s \leq s_f \end{cases} \quad (35)$$

Figure 4.6 shows the plot of the function and the parameters that are used in Eq. (35).

Defined the τ - s relationship at the interface between the FRP strip and the concrete surface, it is possible to calculate the slips and the strains along the FRP strip by integration of the fundamental differential equation that relate shear stresses and slips, expressed as:

$$\frac{d^2s(y)}{dy^2} - \frac{\tau(y)}{E_f t_f} = 0 \quad (36)$$

Solving Eq. (36), considering the bilinear cohesive law showed in Eq. (35), leads to the following expressions of the slips and the strains (as the derivative of the slips) along the FRP strip:

$$s(y) = \begin{cases} 0, & \text{if } 0 \leq y < y_0 \\ A(e^{\alpha(y-y_0)} + e^{-\alpha(y-y_0)} - 2), & \text{if } y_0 \leq y < (y_r + y_0) \\ C \cos(\beta(y-y_0)) + D \sin(\beta(y-y_0)) + \frac{\tau_{02}}{h_2}, & \text{if } (y_r + y_0) \leq y \leq (EBL + y_0) \\ s_f + ((y-y_0) - EBL)(-C\beta \sin(\beta EBL) + D\beta \cos(\beta EBL)), & \text{if } y > (EBL + y_0) \end{cases} \quad (37)$$

$$\varepsilon(y) = \begin{cases} 0, & \text{if } 0 \leq y < y_0 \\ \alpha A(e^{\alpha(y-y_0)} - e^{-\alpha(y-y_0)}), & \text{if } y_0 \leq y < (y_r + y_0) \\ -C\beta \sin(\beta(y-y_0)) + D\beta \cos(\beta(y-y_0)), & \text{if } (y_r + y_0) \leq y \leq (EBL + y_0) \\ -C\beta \sin(\beta EBL) + D\beta \cos(\beta EBL), & \text{if } y > (EBL + y_0) \end{cases} \quad (38)$$

where A, C, and D are integration constants, while α and β depends on the parameters that describes the bilinear function of Eq. (35).

Eq. (38) was used to fit experimental strains, therefore the parameters that characterize the bilinear function, i.e. τ_0 , τ_{\max} , s_0 , s_f , and the position along the FRP strip where the transfer of shear stresses through the interface begins, i.e. y_0 , are evaluated through a non-linear regression.

The function in Eq. (38) is composed of four parts. The length y_r and EBL are represented in Figure 4.6, and can be evaluated through an analytical way.

Some of the most important fracture parameters, such as τ_{\max} and s_m are defined directly through the non-linear regression of experimental strain.

The value of ε_{\max} is obtained in the fourth branch of Eq. (38).

The fracture energy G_F was obtained evaluating the area under the τ - s curve with the following expression:

$$G_f = \frac{(\tau_0 + \tau_{\max})s_m}{2} + \frac{(s_f - s_m)\tau_{\max}}{2} \quad (39)$$

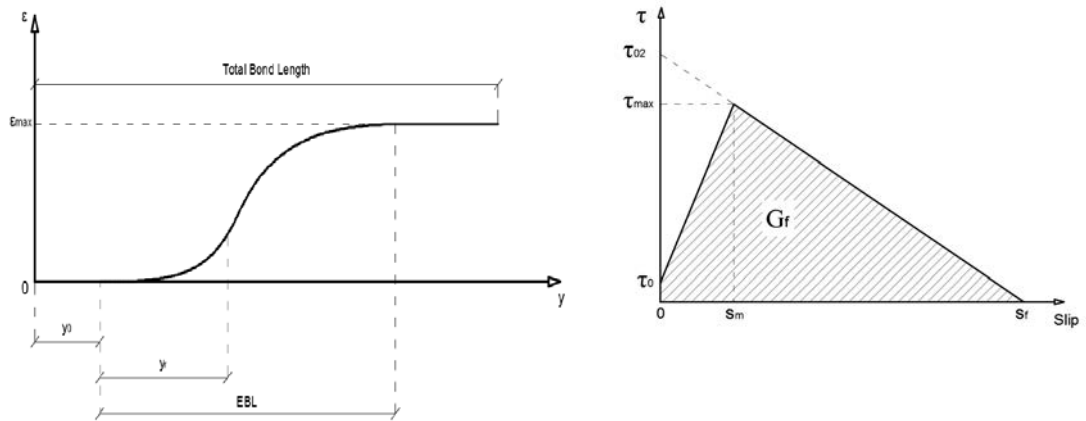


Figure 4.6: Typical CML (Bilinear function)

5.0 Beams

In case of the beam strengthened with FRP and subject to flexural deformation, the effect of the curvature should be taken into account as shown in Figure 4.7.

Interfacial crack-induced debonding between concrete and external FRP strips reinforcement (debonding initiating at flexural cracks along the beam) is the failure mode governing maximum FRP strain which can be adopted for flexural design.

Moreover, Fibers strain at debonding in tensile tests is lower than fibers strain at debonding in beams tests.

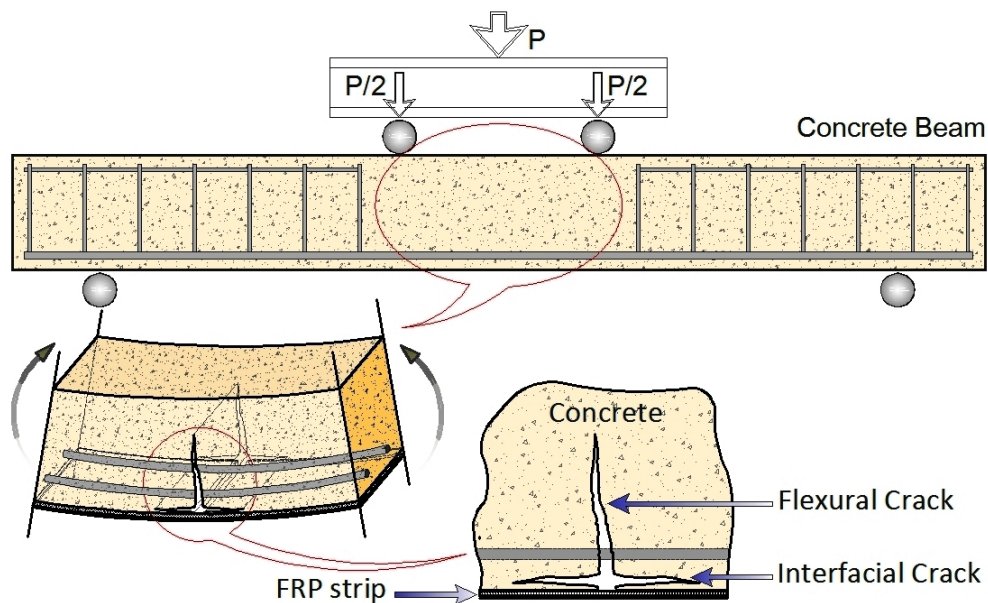


Figure 4.7: Interfacial crack in beam

6.0 Results and discussion

6.1 Calibrated CML functions for load responses

The procedure for obtaining the local bond stress-slip relationship is presented in the section 3. The best fitting curve of the load responses of specimen W_4 based on D'Ambrisi's et al. (2012) function is shown as in Figure 4.8.

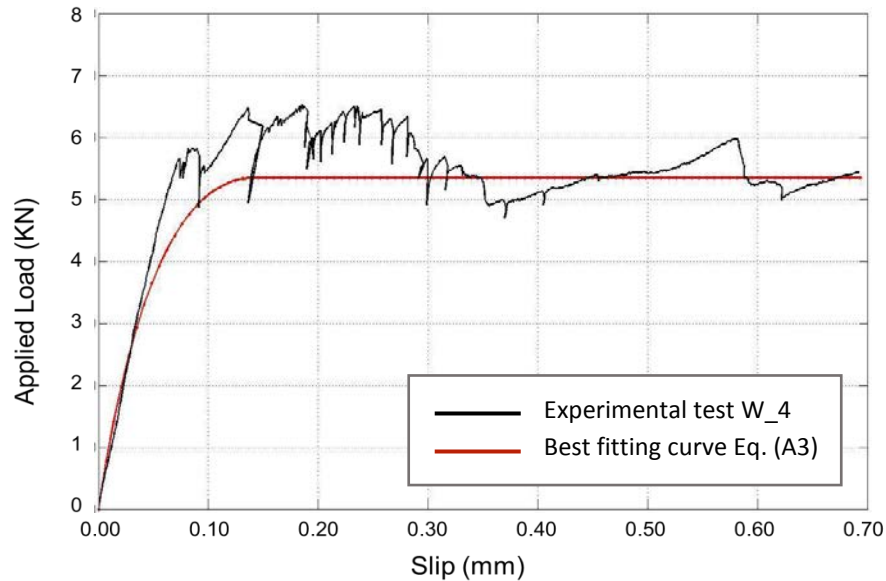


Figure 4.8: The best fitting curve of the load responses of specimen W_4

Based on the obtained best fitting curves of load responses using CML functions adopted by D'Ambrisi et al. (2012) and Dai et al. (2005), we can derive the relationship between the bond stress and the slip of the FRP and the concrete interface as shown in Figure 4.9.

Comparison between experimental τ - s diagrams for eight specimens, Figure 4.9a using D'Ambrisi et al. (2012) and Figure 4.9b using Dai et al. (2005). From these figures, the shape of the bond stress-slip curve in the case of D'Ambrisi et al. (2012) is similar to that of Dai et al. (2005). Generally, both curves are nonlinear and have two branches: a branch ascending until reaching the maximum value of the bond stress τ_{\max} , and a descending branch until the maximum value of the slip s_f at which bond stress falls to zero. Mover, In case of Eq. (2) a descending branch has a smaller slope compare to Eq. (3). Although the maximum local bond stress and fracture energy are almost smaller as shown in Figure 4.9 and Table 4.2.

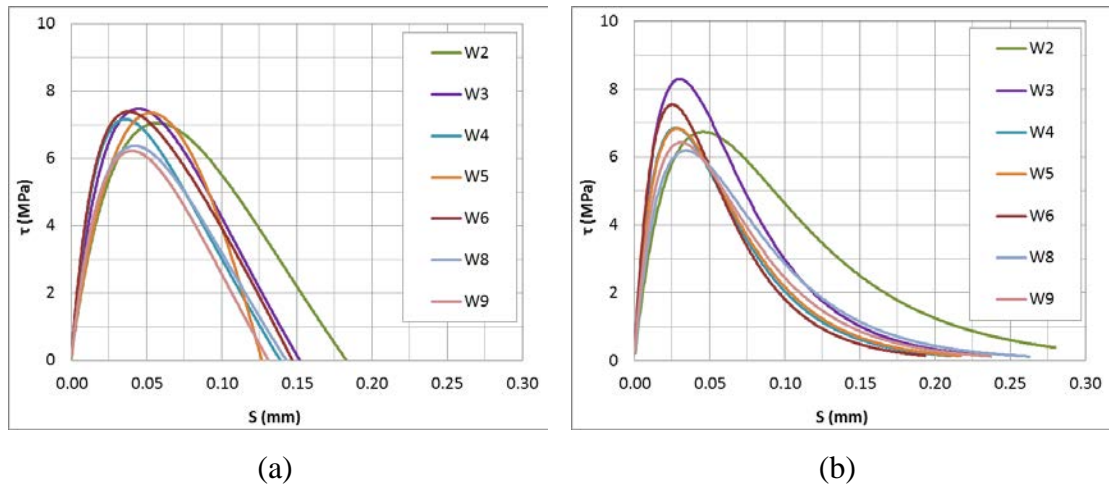


Figure 4.9: Bond stress-slip relationship between CFRP and concrete substrate:
 (a) all tested specimens Eq.(2) and (b) all tested specimens Eq.(3)

6.2 Comparison

CML results of specimen W_4 obtained from load responses using Eq. (2) and Eq. (3) are plotted together with CML results obtained from strain distribution using Eqs. of (Bilinear) (Polynomial) (Sinusoidal) and (Dai et al. 2006), for comparison. An example of the CML, which corresponds to test W_4 in Subramaniam et al. (2007), is depicted in Figure 4.10. From the Figure 4.10, it can be noted that using Dai et al. (2005) and D'Ambrisi et al. (2012) to fit load response, and Dai et al. (2006) to fit the strain profile (Figure 4.11) results are similar.

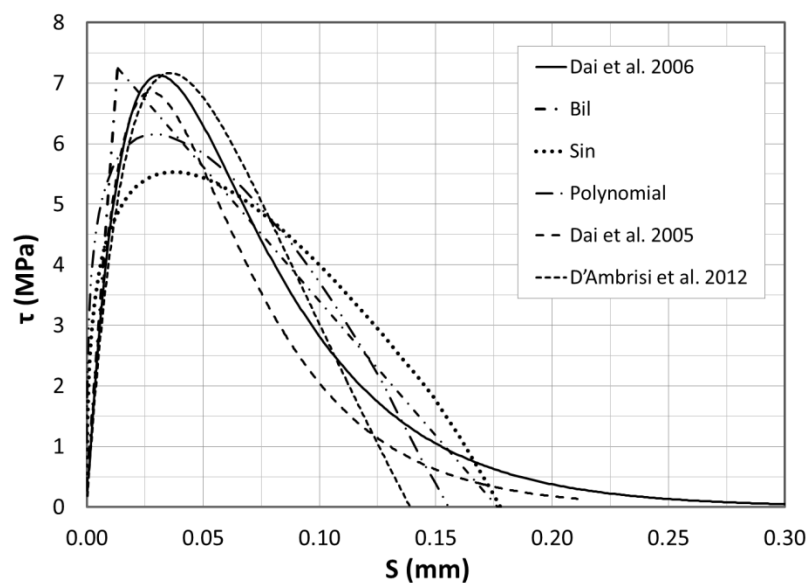


Figure 4.10: Cohesive material law τ - s for specimen W_4 obtained using six different functions to fit experimental data.

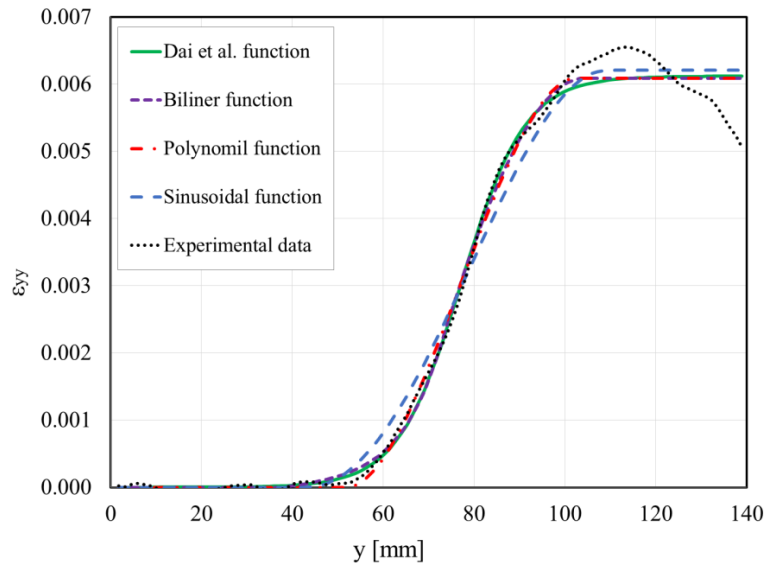


Figure 4.11: S-shape ε_{yy} profile for specimen W_4 using four different functions to fit experimental data.

The polynomial function, similarly to Dai function allows obtaining a good fitting of the experimental data. In fact, the function is able to follow the slope variations that are observed by analyzing the experimental epsilons and to adapt to their trend.

Additional considerations can be made considering the polynomial function. The method here considered starts from the analysis of experimental epsilon along the FRP strip. It is therefore an indirect measure, since the quantities that are actually measured during the debonding test are the slip between the FRP and the concrete substrate. We might consider proceeding starting from the fitting of slip along the FRP strip and obtaining the epsilons and the shear stresses respectively from the first and the second derivative. It was decided to apply the following expression:

$$s(x) = A * (x - D)^4 + B * (x - D)^3 + C * (x - D)^2$$

Where A, B, C and D are parameters evaluated through a linear regression. Two stretches were added to the polynomial function. The former refers to the portion of the FRP strip not yet affected by the exchange of shear stresses, where slip were imposed to zero. The latter refers to the portion of the FRP strip in which the detachment from the substrate has already occurred and slip is linear with a trend that shows a constant slope.

We can observe that using the latter method of fitting, similar results are obtained compared to those achieved starting from experimental epsilon, even if many pic within several tests cannot be analyzed with this procedure. It is therefore useful to

apply the method that starts from the analysis of the strains along the FRP strip. In general the polynomial function fits quite well to the “S” shape of the STZ (Stress Transfer Zone). In the τ -s graph there are no points of inflection, but the curve continues always with the same concavity. Almost all of the experimental data can be processed by using the polynomial function.

The bilinear function allows obtaining a good fitting of the experimental data. The sinusoidal function doesn't give a fitting close to the experimental data. This is because the function doesn't allow performing rapid changes in slope and therefore it adapts more slowly to the S shape of the STZ (Stress Transfer Zone). From all this it follows a lower slope (and therefore a lower first derivative) in the epsilon fitting which results in lower values of shear stresses exchange in the debonding process between the FRP strip and the concrete substrate. In the τ -s graph inflection points are not detected, but the curve continues always with the same concavity. Even in this case, almost all of the experimental data can be processed by using the sinusoidal function, which means that even if there are some irregularities in the results obtained, the function still managed to reproduce the overall behavior.

Table 4.2: Main parameters characterizing the CMLs

Specimen Test	Parameters	Bilin.	Polin.	Sin.	Dai	D'Ambris	Dai Eq. (A3)
W_2	τ_{max} (MPa)	6.35	6.41	4.47	7.67	7.053	6.740
	s_m (mm)	0.010	0.034	0.065	0.037	0.057	0.046
	G_F (MPa.mm)	0.82	0.79	0.87	0.80	0.798	0.867
W_3	τ_{max} (MPa)	8.63	8.47	4.79	9.95	7.478	8.297
	s_m (mm)	0.015	0.025	0.058	0.027	0.045	0.030
	G_F (MPa.mm)	0.67	0.74	0.81	0.75	0.694	0.713
W_4	τ_{max} (MPa)	7.21	6.00	5.59	7.18	7.165	6.857
	s_m (mm)	0.013	0.031	0.038	0.032	0.036	0.027
	G_F (MPa.mm)	0.65	0.65	0.68	0.65	0.594	0.541
W_5	τ_{max} (MPa)	7.97	6.65	4.24	7.95	7.356	6.842
	s_m (mm)	0.013	0.025	0.052	0.026	0.053	0.028
	G_F (MPa.mm)	0.59	0.58	0.65	0.58	0.616	0.555
W_6	τ_{max} (MPa)	8.39	6.68	4.41	8.44	7.393	7.545
	s_m (mm)	0.031	0.027	0.066	0.035	0.038	0.025
	G_F (MPa.mm)	0.88	0.85	0.88	0.85	0.674	0.544
W_8	τ_{max} (MPa)	7.62	6.77	4.84	8.06	6.378	6.191
	s_m (mm)	0.008	0.033	0.057	0.036	0.042	0.034
	G_F (MPa.mm)	0.80	0.80	0.84	0.84	0.557	0.609
W_9	τ_{max} (MPa)	7.10	6.21	4.12	7.63	6.225	6.429
	s_m (mm)	0.006	0.030	0.061	0.032	0.039	0.031
	G_F (MPa.mm)	0.74	0.71	0.77	0.71	0.504	0.570

7.0 Conclusions

In this work, available functions used to calibrate the cohesive material law (CML) of FRP-concrete joints, six CML were selected and calibrated. the experimental data conducted by Subramaniam et al. (2007).

Based on the results presented in Table 4.2, which corresponds to results obtained from fitting of experimental data with the functions previously described, comparing for each of the investigated parameters, the following conclusions can be drawn:

- Analyzing the fracture energy G_f , we can observe that also in this case there is a good affinity between all functions listed above, which it derives a value of G_f almost convergent.
- The maximum shear stress τ_{max} achieved from the sinusoidal function, is much lower than the ones obtained with Eq. (2), Eq. (3), Dai et al. (2006), and polynomial functions.
- Regarding the slip related to the maximum shear stress s_m , the values obtained with Eq. (3), Dai, and polynomial functions are almost convergent. At the same time Eq. (2) gives a value quite conservative, while the other functions differ enough from this result.

Ultimately we can assert that Eq. (3), Dai et al. (2006), and polynomial functions have a good affinity between them, leading to similar results and therefore quite reliable. Also the bilinear function leads to quite good results, even if the discrepancies in the definition of the s_m produce a cohesive material law τ - s slightly different.

8.0 References

Ali-Ahmad, M., Subramaniam, K.V., and Ghosn, M., 2006, "Experimental Investigation and Fracture Analysis of Debonding between Concrete and FRP," Journal of Engineering Mechanics, ASCE, V. 132, No. 9, pp: 914-923.

Carlioni C, Focacci F. FRP-masonry interfacial debonding: An energy balance approach to determine the influence of the mortar joints. European Journal of Mechanics A/Solids 2016;55:122-133.

D'Ambrisi A, Feo L, Focacci F. Bond-slip relations for PBO-FRCM materials externally bonded to concrete". *Compos Part B*, 2012;43(8):2938-2949.

D'Ambrisi A, Feo L, Focacci F. Experimental analysis on bond between PBO-FRCM strengthening materials and concrete. *Compos Part B* 2013;44(1):524–532.

Dai JG, Ueda T, Sato Y. Development of the nonlinear bond stress-slip model of fiber reinforced plastics sheet-concrete interfaces with a simple method. *J. Comp. Const.* 2005;9(1):52-62.

Dai JG, Ueda T, Sato Y. Unified analytical approaches for determining shear bond characteristics of FRP-concrete interfaces through pullout tests. *J. Adv. Concr. Technol.* 2006;4:133–45.

Focacci F, Nanni A, Bakis CE. Local bond-slip relationship for FRP reinforcement in concrete. *J Compos Constr* 2000;4(1):24-31.

Focacci F, Carloni C. A study of the fracture process at the FRP-masonry interface: The role of the periodic pattern of bricks and mortar joints. *Key Engineering Materials* 2015;624.

Malena M, Focacc F, Carloni C, De Felice G. The effect of the shape of the cohesive material law on the stress transfer at the FRP-masonry interface. *Compos Part B*; In press, Available online 9 November 2016, DOI: <http://dx.doi.org/10.1016/j.compositesb.2016.11.012>.

Subramaniam, K. V., C. Carloni, Nobile, L., 2007, "Width Effect in the Interface Fracture during Shear Debonding of FRP Sheets from Concrete." *Engineering Fracture Mechanics*, V. 74, No. 4, pp: 578-594.

CHAPTER 5

BOND BEHAVIOR OF STEEL-FIBER (SRP) COMPOSITES APPLIED ONTO A CONCRETE SUBSTRATE

1.0 Introduction

FRP (Fiber reinforced polymer) composites materials have experienced a continuous increase of use in structural strengthening and repair applications over the past decades. Among the several applications in which they are commonly involved, FRPs are widely used in the strengthening of reinforced concrete (RC) beams because they can increase significantly the flexural and shear strength of the element. Several issues related to the structural performances of FRPs applied to RC elements have been studied. Among them, the interfacial debonding mechanism between FRP composites and concrete substrate has gained an outstanding interest, since debonding is a brittle phenomenon and often occurs with no visible warning at a load level significantly lower than the flexural or shear capacity of the strengthened member corresponding to the rupture of the FRP reinforcement. The problem of bond between FRP and substrates was already investigated by different authors (Chajes et al. 1996, Taljsten 1997, Bizindavyi and Neale 1999, Focacci et al. 2000, Nakaba et al. 2001, De Lorenzis et al. 2001, Savoia et al. 2003, Dai and Ueda 2003, Lu et al. 2005, Leung and Tung 2006, Mazzotti et al. 2008). Recently, a new family of composite materials has been introduced as alternative to traditional FRP composites, to overcome their relatively high cost. Steel FRP gained a terrific interest, due to some advantages as the lower cost with respect to traditional FRP and good ductility performances (Casadei et al., 2005, Huang et al. 2005, Matana et al. 2005). SFRPs are currently considered for numerous applications in civil engineering such as strengthen and repair of reinforced concrete and masonry structures (Wobbe et al., 2004, Kim et al., 2005). They consist in high strength steel wires embedded in an epoxy matrix (steel reinforced polymer, SRP) or in a cementitious grout (steel reinforced grout, SRG).

Experimental investigations available in literature and related to SRP and SRG reinforcement systems have shown the potentialities of these new materials in improving the structural performance of concrete and masonry structures (Wobbe et al. 2004, Barton et al. 2005, Kim et al. 2005, Casadei et al. 2005, Huang et al. 2005, Pecce et al. 2006, Prota et al. 2006, Lopez et al. 2007, Saber et al. 2008, Mitolidis et al. 2012b, Balsamo et al. 2013, Menna et al. 2013, Bencardino & Condello 2014). On the other hand, some of these studies have also underlined differences with respect to FRPs, particularly in terms of bond behavior (Matana et al. 2005, Figeys et al. 2008, D'Ambrisi et al. 2013). This chapter presented the experimental results of concrete specimens subjected to two different test set-ups to investigate the debonding mechanism in SFRP-concrete joints. The interfacial cohesive material law for SFRP strips bonded to concrete is also investigated using digital image correlation (DIC).

2.0 Literature review

This literature review focuses only on research investigating the use and performance of SRP strips (high strength twisted steel wires impregnated with epoxy resin). In particular, regarding the bond behavior of SRP strips applied on concrete prisms, only few studies can be found in literature. Among these, the experimental studies performed by Matana et al. (2005), Figeys et al. (2005) and Mitolidis et al. (2008) are pointed out:

Matana et al. (2005) performed direct shear tests of 12 concrete blocks with dimensions (191 x 191 x 394 mm) (Figure 5.1). The SRP used in the experiments is 3X2 Hardwire embedded in polymeric resin, the properties of the fibers only reported in Table 5.1. The main test variables were the surface roughness and the bonded length. They were studied to investigate the bond behavior of SRP composite laminates. A summary of the test results is reported in Table 5.2, based on experimental results. Results showed that the surface roughness does not have significant effect on the bond failure load for SRP composite laminates. The failure of SRP specimens was shearing within the concrete substrate. It was reported that the bonded effective length for SRP and CFRP was about 127 mm and 102 mm, respectively.

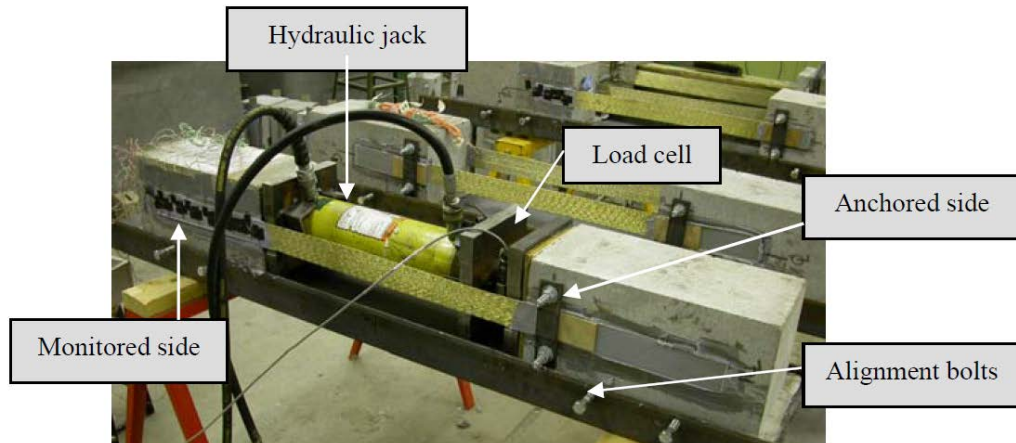


Figure 5.1: Direct shear test setup (Matana et. al, 2005)

Table 5.1: Material properties of SRP (Matana et. al, 2005)

Material property / Lamina type	SRP
Cord type	3X2
Cord area (in ²)	9.62×10 ⁻⁴
Sheet density (cords/in)	23
Average sheet thickness for 1 ply (in)	0.097
Tensile strength, f_{fu} (ksi)	327
Modulus of elasticity, e_f (ksi)	26000
Strain at failure, ϵ_{fu} (%)	1.63

Note: 1 in = 25.4 mm. 1 ksi = 6.89 MPa

Table 5.2: Test results (SRP, 1-23 cords/in density) (Matana et. al, 2005)

Specimen (1)	Ultimate load (kip) (2)	Ultimate strength (ksi) (3)	Ultimate strain - calculated (in/in) (4)	Ultimate strain - measured (in/in) (5)	Ratio (5)/(4) (%) (6)
P - 4 - 1	10.8	123	0.0047	N/A	N/A
P - 4 - 2	12.0	136	0.0052	0.0054	103
P - 4 - 3	11.6	131	0.0050	N/A	N/A
P - 4 - 4	8.1	91	0.0035	0.0031	87
P - 8 - 1	11.9	135	0.0052	N/A	N/A
P - 8 - 2	13.9	157	0.0060	N/A	N/A
P - 8 - 3	13.9	157	0.0060	0.0061	101
P - 8 - 4	11.5	130	0.0050	0.0041	83
P - 12 - 1	12.5	141	0.0054	N/A	N/A
P - 12 - 2	10.6	120	0.0046	N/A	N/A
P - 12 - 3	13.8	155	0.0060	N/A	N/A
P - 12 - 4	13.1	148	0.0057	0.0060	106

Note: N/A = Not available; 1 in = 25.4 mm, 1 kip = 4.45 kN, 1 ksi = 6.89 MPa

Figeys et al. (2005) studied the bond mechanism between SRP laminates and concrete prisms. Two concrete prisms are bonded together with SRP on two opposite sides (Figure 5.2) with bonded length (150 mm and 200 mm). The SRP used in the experiments is shown in Figure 5.3. One sheet (width: 950 mm) consists of 65 steel cords, 18 filaments are twisted in a cord. The filament in the middle has a diameter of 0.25 mm; the other 18 have a diameter of 0.22 mm. Test results were compared with CFRP laminates. It was reported that the specimens bonded with SRP laminates behaves stronger and stiffer than specimens strengthened with CFRP. All tests failed in the concrete substrate.

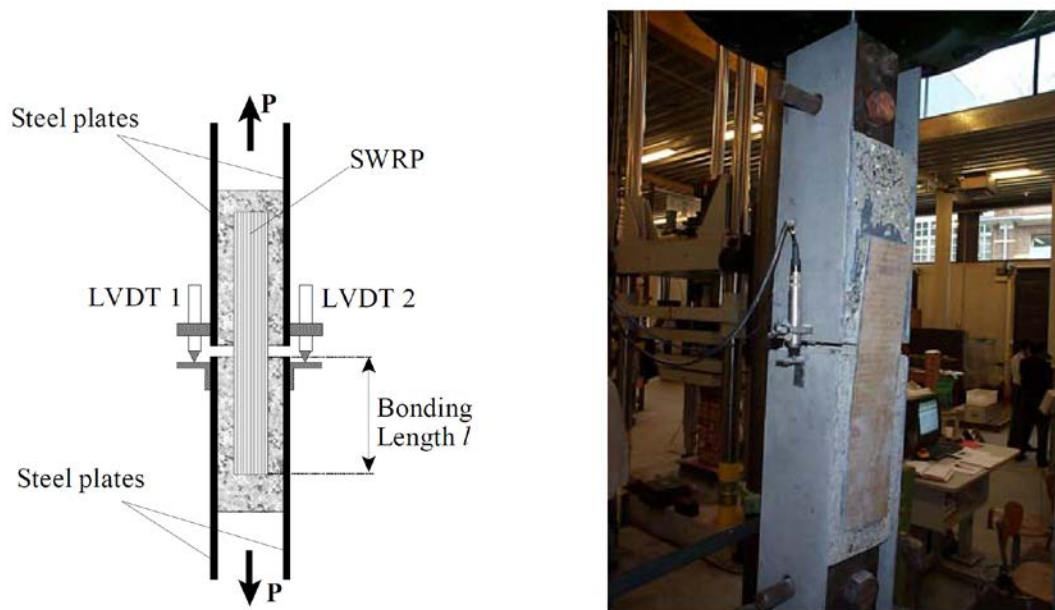


Figure 5.2: a) Scheme of shear test; b) photograph of test set sample (Figeys et al. 2005)

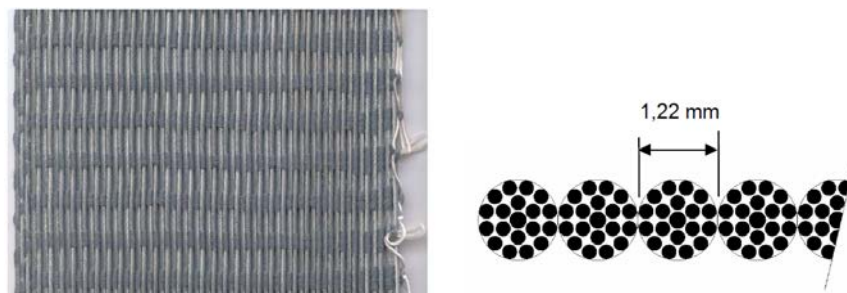


Figure 5.3: The SRP used in the experiments (Figeys et al. 2005)

Mitolidis et al. (2008) conducted an experimental study to investigate the bond strength of SRP strips bonded to concrete prisms. Shear tests were conducted using different types of composite materials (SRP and CFRP). SRP strips were of two types, SRP 3X2 cords (made by twisting 5 individual wires together) and SRP 12X cords (made by twisting three wires and nine wires together). In addition, the difference in the twisted wire cords used in each type, and also with different width of SRP strips (50 mm and 80 mm), and different bonded length of SRP strips (150 mm and 300 mm). The test set-up and configurations of representative specimens are shown in Figure 5.4, and the specimen data and key results from bond tests shown in Table 5.3.

The results showed that the bond strength of SRP strips is lower than CFRP strips, which is contrary to findings of other researchers, which is 76% lower than in the case that debonding strength of CFRP. In addition, the difference in width of SRP strips affect the debonding strength, i.e. an increase in the width of the SRP strips was found to increase the bond strength, while the different length of the strips, in each case to the upper anchorage length, seems not to influence the debonding strength. It was found that the effective bonded length is less than 150 mm.

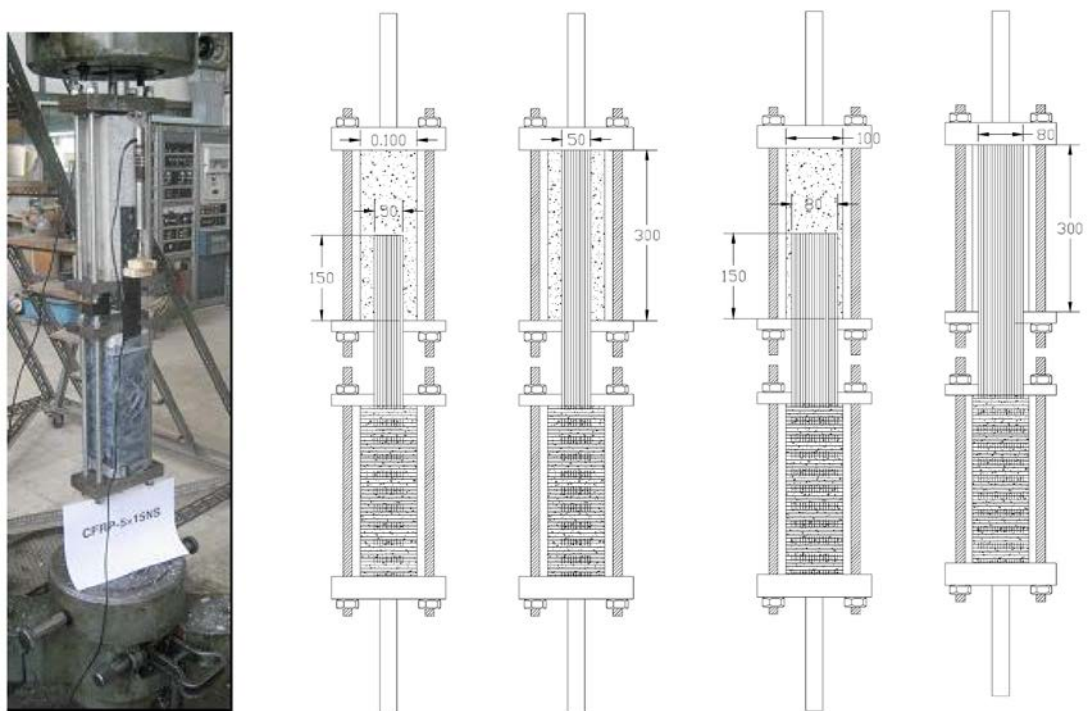


Figure 5.4: Experimental set-up and configurations of representative specimens (Mitolidis et al. 2008)

Table 5.3: Specimen data and key results from bond tests Mitolidis et al. (2008)

Specimen	Concrete grade	$t_f \times b_f \times L$	Type of sheet	$0.5P_{tot}$	$S_{tot}/S_{tot,u}$
		mm		kN	mm
CFRP-5X15NS	C20/25	1.20×50×150	CFRP	19.0	0.38/0.52
CFRP-5X30NS	C20/25	1.20×50×300	CFRP	18.5	0.50/0.70
SRP12-5X15NS	C20/25	1.23×50×150	SRP12X	13.7	1.09/1.25
SRP12-5X30NS	C20/25	1.23×50×300	SRP12X	13.5	0.55/1.11
SRP12-8X15NS	C20/25	1.23×80×150	SRP12X	19.0	0.55/ ---
SRP12-8X30NS	C20/25	1.23×80×300	SRP12X	21.0	0.58/0.99
SRP3X2-5X15NS	C20/25	1.23×50×150	SRP3X2	15.0	0.45/0.56
SRP3X2-5X30NS	C20/25	1.23×50×300	SRP3X2	14.0	--- /0.60
SRP3X2-8X15NS	C20/25	1.23×80×150	SRP3X2	20.3	0.37/0.79
SRP3X2-8X30NS	C20/25	1.23×80×300	SRP3X2	22.0	1.29/1.28

S_{tot} : Is the measured displacement between the outer points of the bond lengths.

Referring to available researches on bond between SRP and concrete prisms, can be included that a deeper investigation is required for further research to provide a fundamental understanding of their behaviour.

3.0 Experimental Program

3.1 Materials

3.1.1 Concrete:

All concrete prisms were cast from the same batch of concrete. The concrete was normalweight concrete with portland cement. The maximum aggregate size was 15 mm. Compressive strength of concrete was measured at 21, 28, 42, 56, 84, 112, 168, 224, and 420 days after casting using 150 mm side cubes and 150 mm × 300 mm cylinders tested according to EN12390-3 and EN12390-6, respectively. The average values of 3 tests for each day are plotted in Figure 5.5.

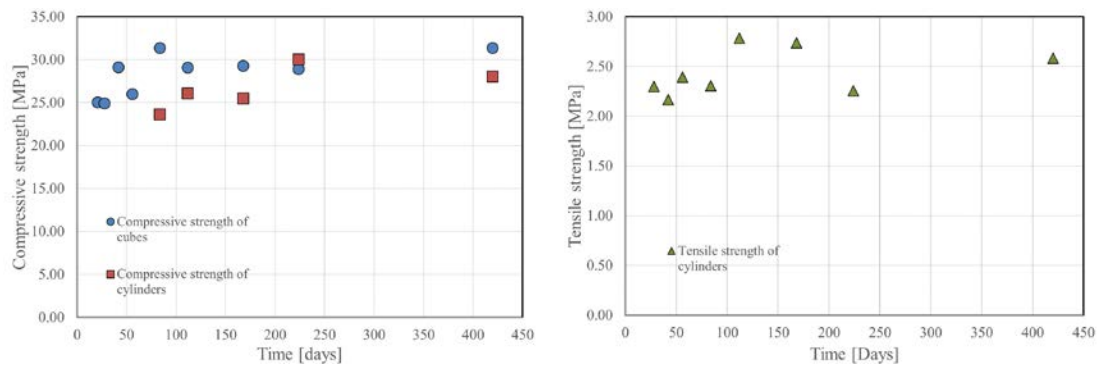


Figure 5.5: Strength development of cubic and cylindrical specimens over time

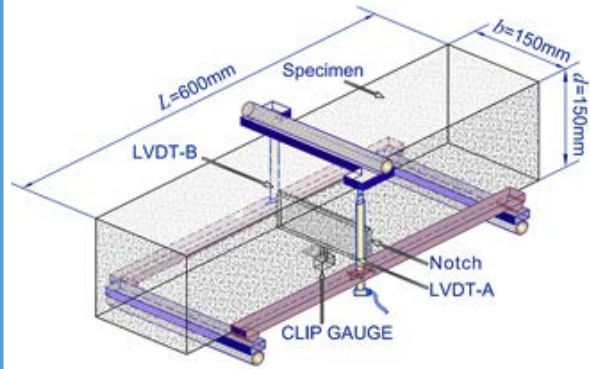
Three concrete prisms 600 mm length \times 150 mm width \times 150 mm depth and three concrete prisms 300 mm length \times 70 mm width \times 70 mm depth cast from the same concrete used for confined and control specimens were tested using a three point bending set-up (Figure 5.6) to evaluate the fracture energy of concrete. All concrete prisms had a central notch with a V-shaped tip. The notch length a_0 was equal to one third of the depth. The net span was equal to three times the depth of the specimen. The loading apparatus consisted of two cylindrical rollers that supported the prism base and a cylindrical roller at the top of the specimen, centered with respect to its length that was used to apply the load. Two steel plates were glued to the bottom face of the specimen and lay on the support rollers to avoid friction. An S-shaped steel plate was glued on the top face of the concrete prism with a central V-shaped section to ensure a good support for the loading cylindrical roller. From both sides of the concrete prism, a steel element, lying on the bottom supports, fastened an LVDT that reacted off of the S-shaped top plate. The two LVDTs measured the vertical deflection of the point of the prism where the load was applied. A clip-on gage, mounted near the edges of the central notch, measured the crack mouth opening displacement (CMOD) and was used to control the test. The rate of the test was equal to 0.001 mm/s.

The fracture energy, G_F , was evaluated as the area under the load-deflection response (Hoover and Bažant 2013, Elices et al. 1992, Hillerborg 1985).

The fracture energy obtained from three 600 mm \times 150 mm \times 150 mm prisms is equal to 0.105 N/mm (CoV = 0.048), while the fracture energy obtained from three 300 mm \times 70 mm \times 70 mm is equal to 0.111 N/mm (CoV = 0.117).

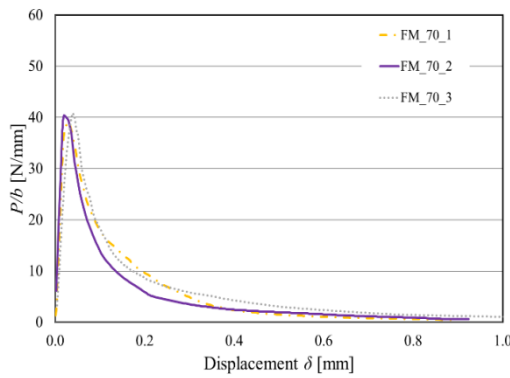


(a)

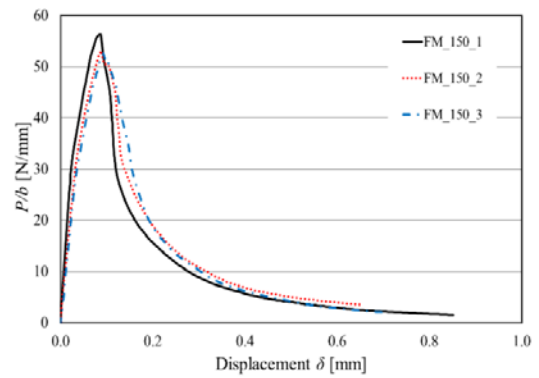


(b)

Figure 5.6: a) and b) Experimental set-up for fracture mechanics tests for 150 mm width specimens.



(a)



(b)

Figure 5.7: a) $P/b - \delta$ response for 70 mm width specimens.
b) $P/b - \delta$ response for 150 mm width specimens.

3.1.2 SRP Fiber

Steel fibers were in the form of a unidirectional sheet made of ultra-high strength galvanized steel micro-cords fixed to glass-fiber network which confers dimensional stability in the installation phases. Each fiber consists of five filaments. Three of the five filaments are straight, and the remaining two filaments are wrapped around the other three with a high torque angle (Figure 5.8). The cross-sectional area of the cord A_{cord} is 0.538 mm^2 .

Fiber sheets with three different densities (number of cords per millimeter of width) were investigated and are referred to in this investigation (Figure 5.9) as medium

density (MD), high density (HD) and ultra-high density (UHD). The MD steel fiber strips had 0.314 cords/mm, the HD steel fiber strips had 0.472 cords/mm, and the UHD steel fiber strips had 0.709 cords/mm. Table 5.4 summarized the mechanical properties of the SRP used in this work as reported by the manufacturer (Kerakoll 2016).

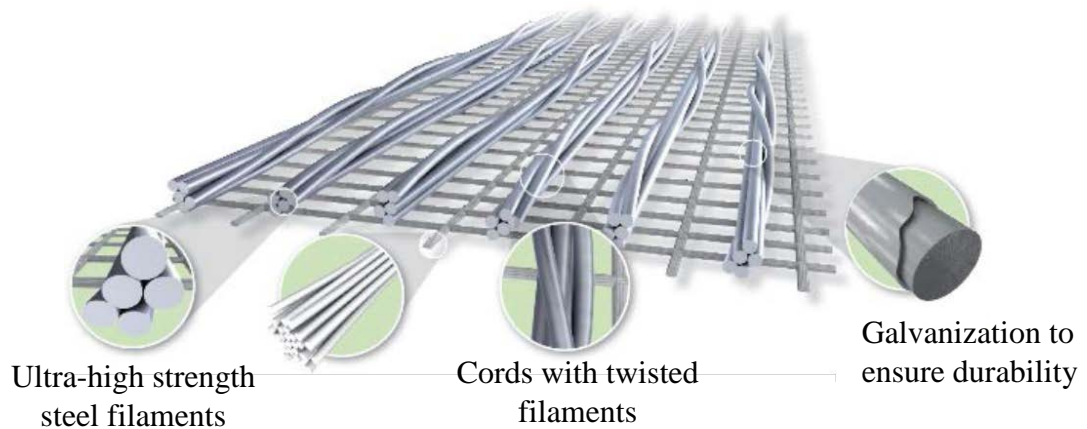


Figure 5.8: SRP Fiber (Kerakoll S.p.A.)

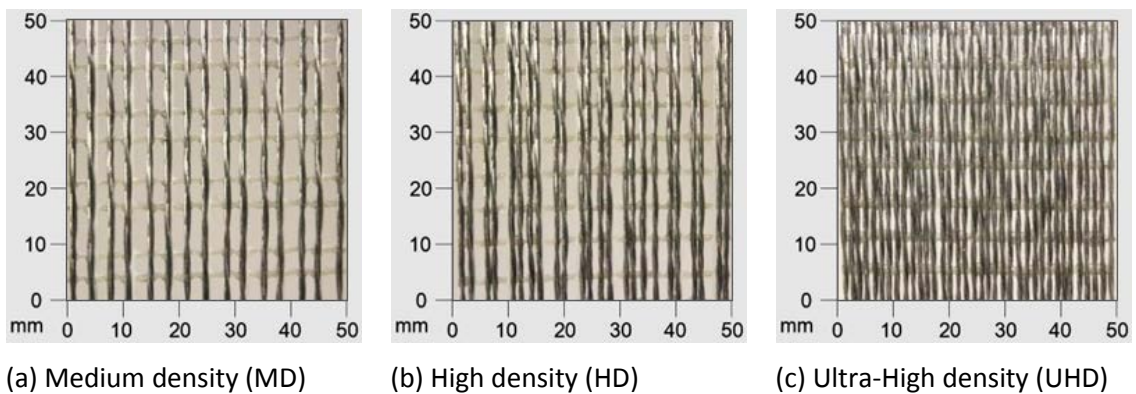


Figure 5.9: The SRP used in this work (Kerakoll S.p.A.)

Table 5.4. Properties of steel fibers provided by manufacturer (Kerakoll 2016)

Property	Medium Density	High Density	Ultra-High Density
Number of Cords/mm	0.314	0.472	0.709
Tensile Strength (MPa)	>3000	> 3000	> 3000
Elastic Modulus (GPa)	>190	> 190	> 190
Break Deformation (%)	>2	> 2	> 2
Equivalent Thickness (mm)	≈0.169	≈ 0.254	≈ 0.381

3.1.3 Adhesive

The epoxy matrix is a two-component epoxy thixotropic gel system (Figure 5.10), with high wettability for the impregnation of steel textiles. The mechanical properties of the matrix reported by the manufacturer (Kerakoll 2016) are provided in Table 5.5.



Figure 5.10: The epoxy resin used in this work (Kerakoll S.p.A.)

Table 5.5: Mechanical properties of matrix by provided by manufacturer (Kerakoll 2016)

Property	
Tensile Strength (MPa)	> 14
Flexural Elastic Modulus (GPa)	> 2.50
Elastic Modulus Under Compression (GPa)	> 5.30

3.2 Test set-up's and Methods

Nineteen concrete specimens were tested using the single-lap shear test set-up and six specimens were tested using a triple-point bending (TPB) set-up to analyze the debonding mechanism between the composite strips and the concrete surface and compare the results obtained using two different test methods. Prior to apply the reinforcement specimens were sandblasted with silica sand. Concrete prisms were reinforced following the manufacturer's recommendations, applying the steel-FRP strips using a wet layup process. Specimens were cured under ambient conditions for seven days after casting.

3.2.1 Single-lap shear test set-up (Method I)

Nineteen concrete prisms were tested using a direct single-lap shear test (Figure 5.11). FRP strips were externally bonded to one face of the concrete blocks. The classical push-pull configuration was adopted where fibers were pulled while the concrete prism was restrained. The dimensions of all concrete blocks were 150 mm width \times 150 mm depth \times 600 mm length. The epoxy resin was used to impregnate the fiber along the entire steel-FRP strip, also outside of the bonded area. The fibers were arranged across the width of the reinforcement in order to have approximately a distance between the external fibers of the grid and the edges of the matrix equal to half of the fiber spacing. The thickness of each layer of matrix was 2 mm, thus, the total thickness of the composite strip was equal to 4 mm. The bonded area started 70 mm from the top edge (loaded end of the strip) of the concrete prism to obtain an initial interfacial notch. The FRP strips were directly gripped by the machine head. The concrete prism was restrained against movement by two steel plates placed against the square faces of the prism. The bottom square plate was bolted to a cylindrical steel element that was gripped by the bottom wedges of the testing machine. The top plate was a C-shaped steel element designed to have the centroid as close as possible to the centroid of the bottom plate, in order to reduce the undesired effects of the inherent eccentricity of the single-lap shear tests. The top plate was connected to the bottom one through four steel bars bolted to the two plates. Three strain gages, aligned with the longitudinal axis of the bar, were mounted on each steel bar, and arranged 120° apart one another. The average of the three strain measurements on each bar gives an approximate estimate of the strain along the bar, which is used to analyze the initial pre-compression load applied to the specimen prior to starting the test and evaluate the stress on each bar during the test. Direct shear tests were conducted under displacement control using a close-loop servo-hydraulic universal testing machine. Two linear variable differential transducers (LVDT) were mounted on the concrete surface close to the top edge of the bonded region. The LVDTs (named LVDT a and b) reacted off of a thin aluminum Ω -shaped plate that was attached to the epoxy surface adjacent to the beginning of the bonded area. The average of LVDT a and b is defined as the global slip g in this paper. The global slip g was increased at a constant rate. All tests were conducted at a global slip rate equal to 0.00084 mm/s. Two additional LVDTs (named LVDT c and d) were

used to monitor the horizontal displacement of the concrete prism in the direction perpendicular to the face of the composite strip. Two LVDT holders were mounted onto the bottom plate using two magnets. The LVDT c and d were reacting off of the face of concrete block parallel to the one to which the composite was applied. The measuring point was approximately 300 mm from the bottom square face of the concrete block. The measurements of these two LVDTs were useful to monitor the amount of the rotation of the concrete prisms during the tests due to the eccentricity of the applied load. For some specimens, three-dimensional (3-D) digital image correlation (DIC) was used to analyze the displacement and strain fields on the FRP strip and on the portion of concrete close to the FRP strip. DIC is a non-contact measuring technique that allows for obtaining the surface displacement field. DIC mathematically correlates images of the specimens, taken during testing, that correspond to different applied load and displacement values. DIC recognizes and correlates points on the surface and computes their displacement with respect to the initial undeformed image. The surface strains are then determined as the gradients of the displacements after interpolating the displacement contours with a quintic B-spline collocation method. To enable the DIC measurements, the FRP strip surface and the adjacent concrete were covered uniformly with a white nonreflective paint prior to testing. Black paint was then sprayed on the white surface to create a speckle pattern, which is recognized and employed by the DIC software to obtain the displacement field. During testing the specimen was illuminated with normal white light to assure uniform light intensity on the composite surface. Images were taken at a frequency of 0.2 Hz.

Specimens were tested varying the density of steel fibers. For each density of steel fibers, the following set of parameters were considered as the standard ones: load rate equal to 0.00084 mm/s, bonded length equal to 300 mm and bonded width equal to 50 mm. Tests were conducted on different faces of the concrete prisms: the face opposite to the casting one was named bottom (B) side, the ones adjacent to the casting one were termed side (S) faces. Specimens were named following the notation DS-X-Y-A-B-C-Z, where X = bonded length (ℓ) in mm, Y = bonded width (b_f) in mm, A represents the steel fiber density (MD = medium density, HD = high density, UHD = ultra-high density); B indicates the use of DIC in the test (D = DIC, ND = no DIC); C denotes the side of the block on which test was performed (B = bottom, S = side), and Z = specimen number.

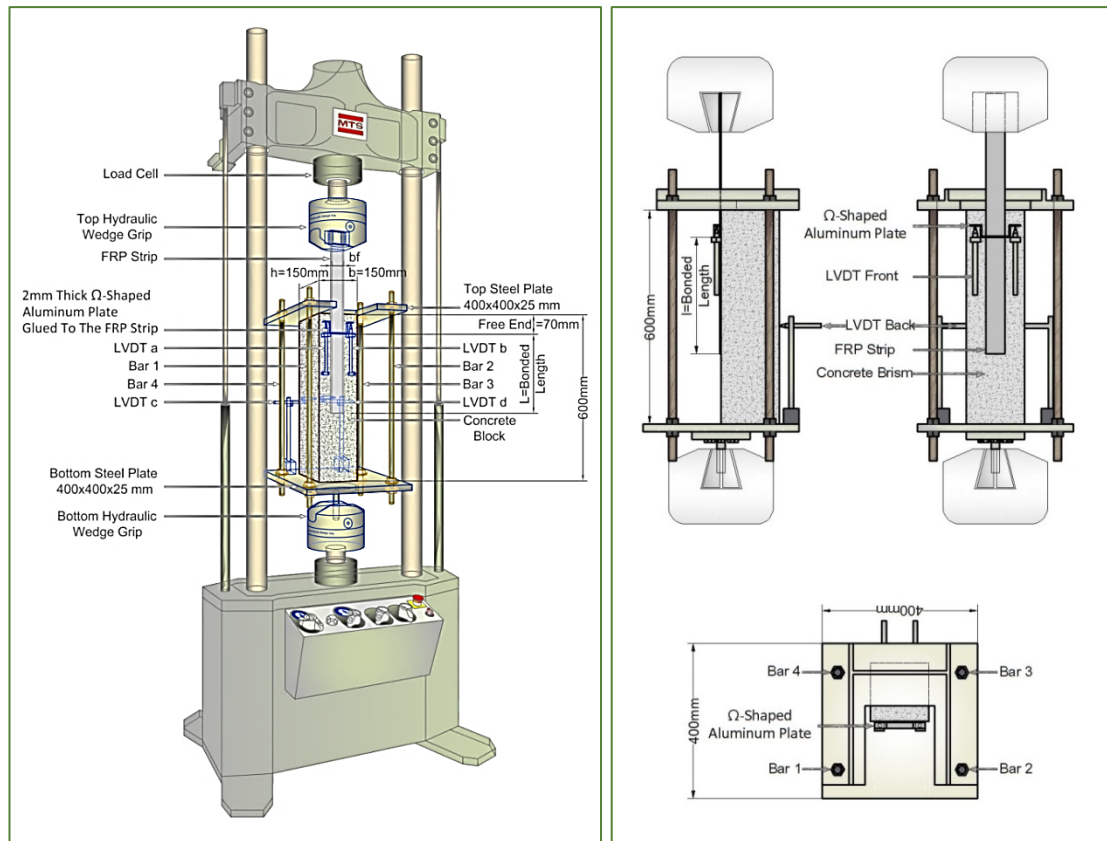


Figure 5.11: Direct-shear single lap test set-up

Table 5.6. Test specimen characteristics (Direct-shear single lap test set-up)

Specimen Name	Side	FRP strip			Fiber		DIC	Load rate [mm/s]
		Bonded width (mm)	Bonded length (mm)	Thick. (mm)	Density	N° fibers		
DS_300_50_HD_D_S_1	S	50	300	4	HD	24	✓	0.00084
DS_300_50_HD_D_S_2	S	50	300	4	HD	24	✓	0.00084
DS_300_50_HD_D_S_3	S	50	300	4	HD	24	✓	0.00084
DS_300_50_HD_D_S_4	S	50	300	4	HD	24	✓	0.00084
DS_300_50_HD_D_S_5	S	50	300	4	HD	24	✓	0.00084
DS_300_50_HD_ND_B_1	B	50	300	4	HD	24	✗	0.00084
DS_300_50_HD_D_B_2	B	50	300	4	HD	24	✓	0.00084
DS_300_50_HD_D_B_3	B	50	300	4	HD	24	✓	0.00084
DS_300_50_MD_ND_B_1	B	50	300	4	MD	15	✗	0.00084
DS_300_50_MD_ND_B_2	B	50	300	4	MD	15	✗	0.00084
DS_300_50_MD_ND_B_3	B	50	300	4	MD	15	✗	0.00084
DS_300_50_UHD_ND_S_1	S	50	300	4	VHD	35	✗	0.00084
DS_300_50_UHD_ND_S_2	S	50	300	4	VHD	35	✗	0.00084
DS_300_50_UHD_ND_S_3	S	50	300	4	VHD	35	✗	0.00084
DS_300_50_UHD_ND_B_1	B	50	300	4	VHD	35	✗	0.00084
DS_300_50_UHD_ND_B_2	B	50	300	4	VHD	35	✗	0.00084
DS_300_50_UHD_D_B_3	B	50	300	4	VHD	35	✓	0.00084
DS_300_50_UHD_D_B_4	B	50	300	4	VHD	35	✓	0.00084
DS_300_50_UHD_D_B_5	B	50	300	4	VHD	35	✓	0.00084

3.2.2 TPB test set-up (Method II)

Six concrete prisms 600 mm length \times 150 mm width \times 150 mm depth were tested using a triple point bending set-up (Figure 5.12). All specimens had a central notch with a U-shaped tip. The notch length a_0 was equal to half of the depth. The net span was equal to three times the depth of the specimen. For each prism the FRP strip was applied on the bottom face (B side) of the specimen, i.e. the same face where the prism was notched. The steel FRP strips were centered with respect to the bottom face of each block. The bonded width (b_f) and bonded length (ℓ) were equal to 50 mm and 400 mm respectively. Three specimens were strengthened with MD steel fibers while three specimens were reinforced with HD steel fibers. The test set-up is the same described in section (3.1.1) for the fracture mechanics tests except for the clip on gage that was not mounted on the specimen because of the presence of the FRP strip. The average of the two LVDTs measurements, that indicates the vertical deflection of the loading point, was used to control the test. The test rate was equal to 0.0005 mm/s.

Specimens were named following the notation TPB-X-Y-A-C-Z, where each symbol has the same meaning explained above for direct shear tests.

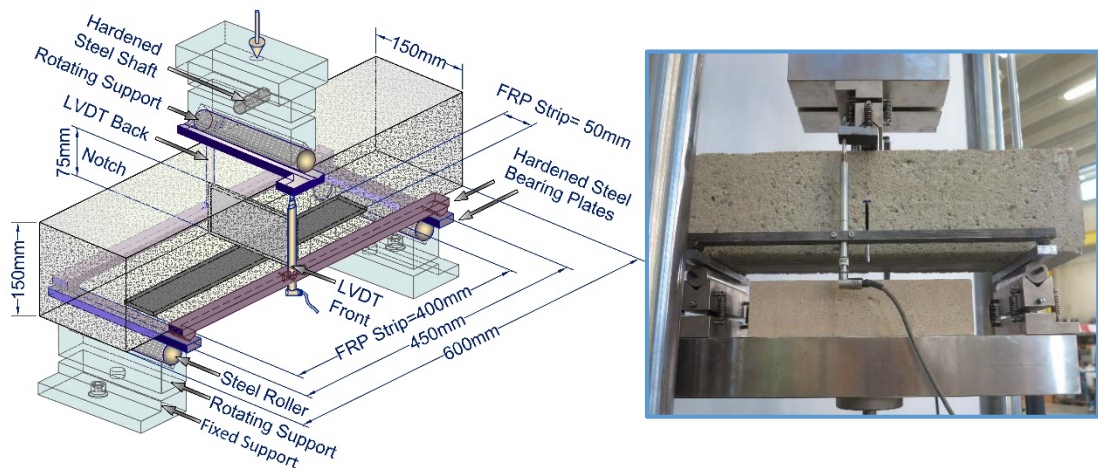


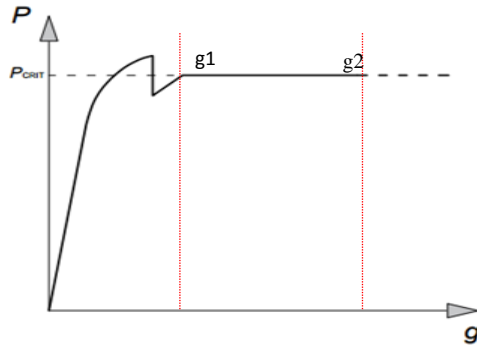
Figure 5.12: TPB test set-up

Table 5.7: Test Specimen Characteristics (TPB test set-up)

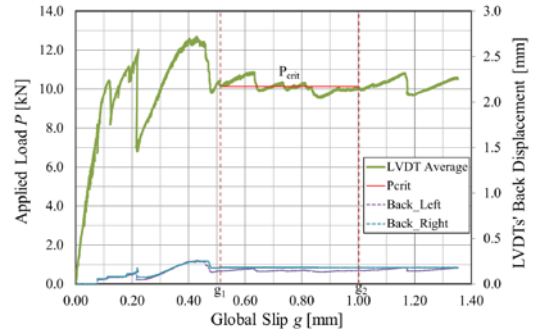
Specimen Name	Side	FRP strip			Fiber		Load rate [mm/s]
		Bonded width [mm]	Bonded length [mm]	Thickness [mm]	Density	N° fibers	
TPB_400_50_MD_B_1	B	50	400	4	MD	15	0.0005
TPB_400_50_MD_B_2	B	50	400	4	MD	15	0.0005
TPB_400_50_MD_B_3	B	50	400	4	MD	15	0.0005
TPB_400_50_HD_B_1	B	50	400	4	HD	35	0.0005
TPB_400_50_HD_B_2	B	50	400	4	HD	35	0.0005
TPB_400_50_HD_B_3	B	50	400	4	HD	35	0.0005

4.0 Results

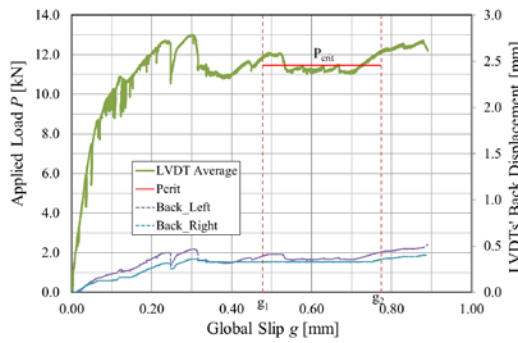
The load responses of direct shear tests are represented in Figure 5.13 for representative specimens, characterized by different fiber densities and different sides of application of the SFRP strips. The load responses of these specimens are similar in shape and appear to be analogous to the load-global slip response showed in Figure 5.13a. All load responses showed an initial linear portion, followed by a non-linear branch. A sudden drop in the load marked the onset of the interfacial crack propagation. As the crack propagated, the load remained nominally constant and its value P_{crit} was determined as the mean value of the load corresponding to the range of the global slip [g1-g2]. The global slip range [g1-g2] slightly varied for each test. This range was identified on the basis of the strain analysis results (presented in the next session) for specimens, in which DIC was employed, while it was identified directly on the load-global slip response for other specimens. The load P_{crit} is often termed load-carrying capacity or bond strength. Test results are summarized in Table 5.8. The rotations measured by LVDT-c and LVDT-d are reported as w_c and w_d , respectively. The failure mode always occurred in a thin mortar-rich layer of concrete, where the epoxy impregnates the substrate (Figure 5.14). For few specimens, cracks propagated also at the matrix-fiber interface.



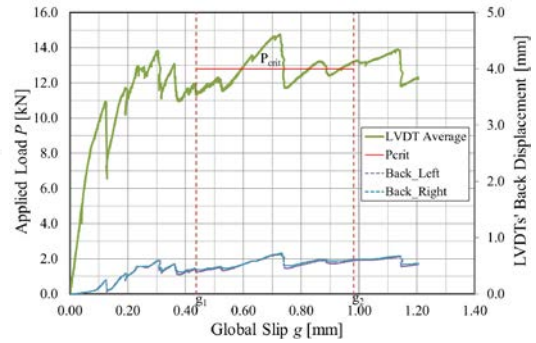
(a)



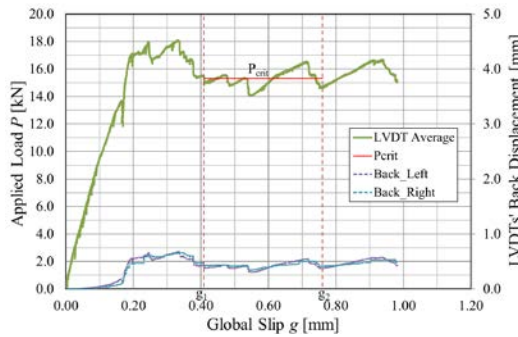
(b)



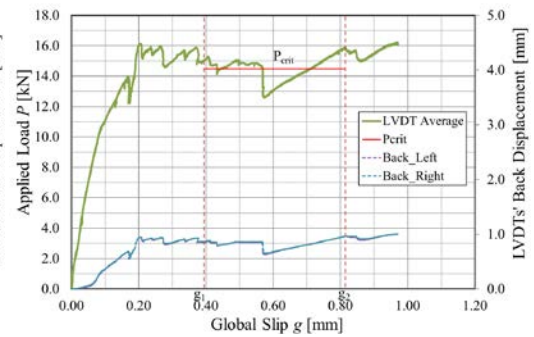
(c)



(d)



(e)



(f)

Figure 5.13. a) Typical load-global slip response for SFRP. b) Load response for specimen DS_300_50_MD_ND_B_2. c) Load response for specimen DS_300_50_HD_D_S_5. d) Load response for specimen DS_300_50_HD_ND_B_1. e) Load response for specimen DS_300_50_UHD_ND_S_3. f) Load response for specimen DS_300_50_UHD_D_B_5.

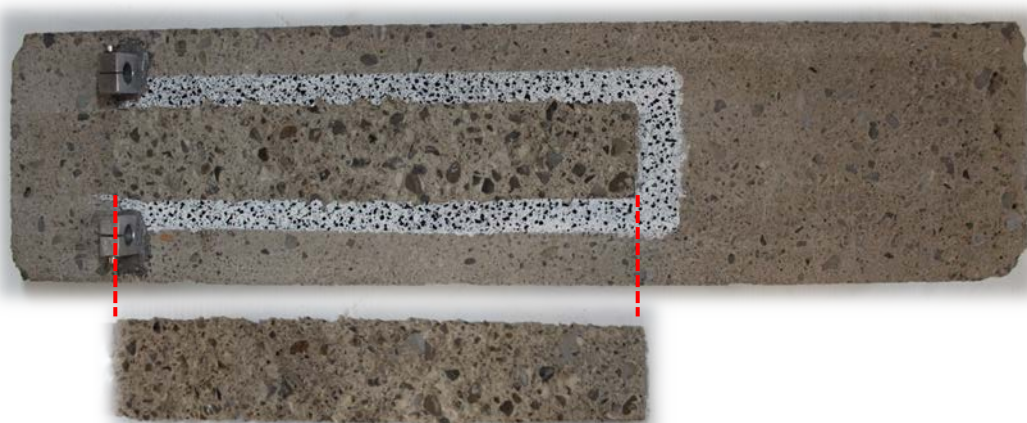


Figure 5.14. Failure mode for specimen DS_300_50_UHD_D_B_3.

Table 5.8: Test results (Direct-shear single lap test set-up)

Specimen Name	Actual width [mm]	g_1 [mm]	g_2 [mm]	P_{crit} [kN]	w_c	w_d
DS_300_50_HD_D_S_1	51.0	0.39	0.78	12.25	0.29	0.41
DS_300_50_HD_D_S_2	52.0	0.64	1.02	12.27	0.13	0.07
DS_300_50_HD_D_S_3	50.0	0.48	0.80	11.92	0.06	0.13
DS_300_50_HD_D_S_4	52.0	0.49	0.81	10.44	0.25	0.29
DS_300_50_HD_D_S_5	52.0	0.48	0.77	11.47	0.49	0.40
DS_300_50_HD_ND_B_1	52.0	0.44	0.98	12.78	0.70	0.72
DS_300_50_HD_D_B_2	52.0	0.47	0.96	12.64	0.54	0.48
DS_300_50_HD_D_B_3	52.5	0.43	0.85	12.28	0.34	0.47
DS_300_50_MD_ND_B_1	49.0	0.42	0.83	11.48	0.49	0.40
DS_300_50_MD_ND_B_2	48.0	0.52	1.00	10.14	0.26	0.25
DS_300_50_MD_ND_B_3	48.5	0.68	1.12	12.41	0.95	0.89
DS_300_50_UHD_ND_S_1	51.0	0.41	0.79	13.73	0.40	0.50
DS_300_50_UHD_ND_S_2	51.5	0.63	1.04	17.63	0.87	0.93
DS_300_50_UHD_ND_S_3	51.0	0.41	0.76	15.31	0.68	0.66
DS_300_50_UHD_ND_B_1	50.5	0.45	0.87	16.29	0.95	1.51
DS_300_50_UHD_ND_B_2	52.0	0.46	0.75	16.13	1.18	1.33
DS_300_50_UHD_D_B_3	50.0	0.46	0.80	16.07	0.96	0.94
DS_300_50_UHD_D_B_4	52.5	0.32	0.74	15.24	1.20	1.36
DS_300_50_UHD_D_B_5	50.0	0.39	0.81	14.49	1.00	1.01

The load responses of triple point bending tests performed on notched concrete specimens reinforced with MD steel fibers and HD steel fibers are presented in Figure 5.15a and 5.15b, respectively. The behavior of the load responses is similar to the one showed by direct-shear tests, a part for the constant plateau that in TPB tests appear to be shorter. Test results are summarized in Table 5.9. The failure usually consisted in debonding of the steel FRP strip from one side of the notched beam with the detachment of a concrete wedge from the bonded area near the notch (Figure 5.16). The concrete wedge can detach from one or both sides of the notch. The portion of the steel FRP strip debonded from the substrate has usually a thin layer of concrete attached.

Table 5.9: Test results (TPB test set-up)

Specimen Name	Actual width [mm]	g_1 [mm]	g_2 [mm]	P_{crit} [kN]	w_c	w_d
TPB_400_50_MD_B_1	52	/	/	14.98	/	/
TPB_400_50_MD_B_2	52.5	/	/	14.37	/	/
TPB_400_50_MD_B_3	51.5	/	/	17.23	/	/
TPB_400_50_HD_B_1	52.5	/	/	16.83	/	/
TPB_400_50_HD_B_2	51	/	/	16.49	/	/
TPB_400_50_HD_B_3	51.5	/	/	16.85	/	/

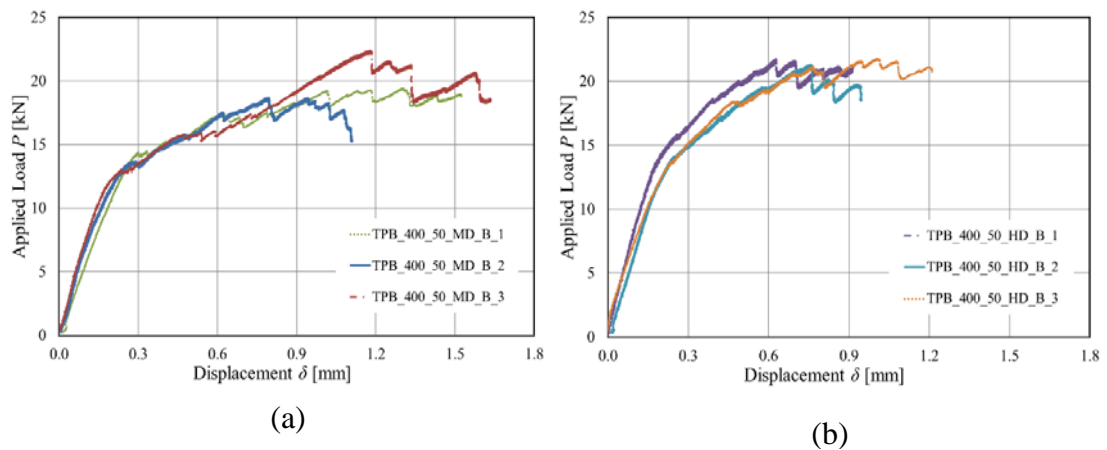


Figure 5.15: a) Load response for MD notched specimens tested in TPB. b) Load response for HD notched specimens tested in TPB.

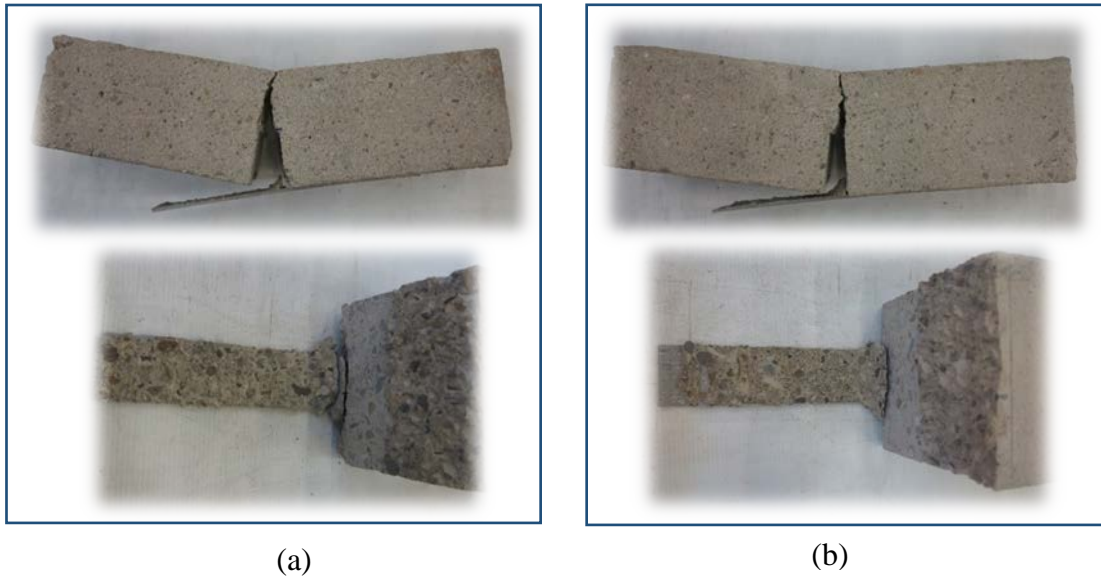


Figure 5.16: a) Failure mode for specimen TPB_400_50_MD_B_1. b) Failure mode for specimen TPB_400_50_HD_B_1.

4.1 Failure modes

The failure mode of all SFRP concrete specimens tested using a direct single-lap shear test set-up consists in debonding of the composite strip from the concrete substrate, as mentioned above. A thin layer of concrete remained attached to the epoxy matrix for all the length of the SFRP strip, a part for the free end of the composite strip where a quite-large concrete bulk remained glued to the strip. The detachment of the concrete bulk from the substrate determines an increase in the amount of energy needed to fully detach the reinforcement, causing an ascending branch in the last portion of almost all load-responses. Specimens DS_300_50_MD_ND_B_3 and DS_300_50_UHD_ND_S_2 showed a slightly different type of rupture, characterized by the propagation of the crack at the fiber-matrix interface in limited portions of the composite strip, as showed in Figure 5.17. This type of rupture affects both the global slip range and both the load bearing capacity, causing an increase of g_1 , g_2 and P_{crit} with respect to other specimens. Since results are highly affected by the propagation of the crack at the matrix-fiber interface, the aforementioned specimens will not be considered in the remainder of the work.

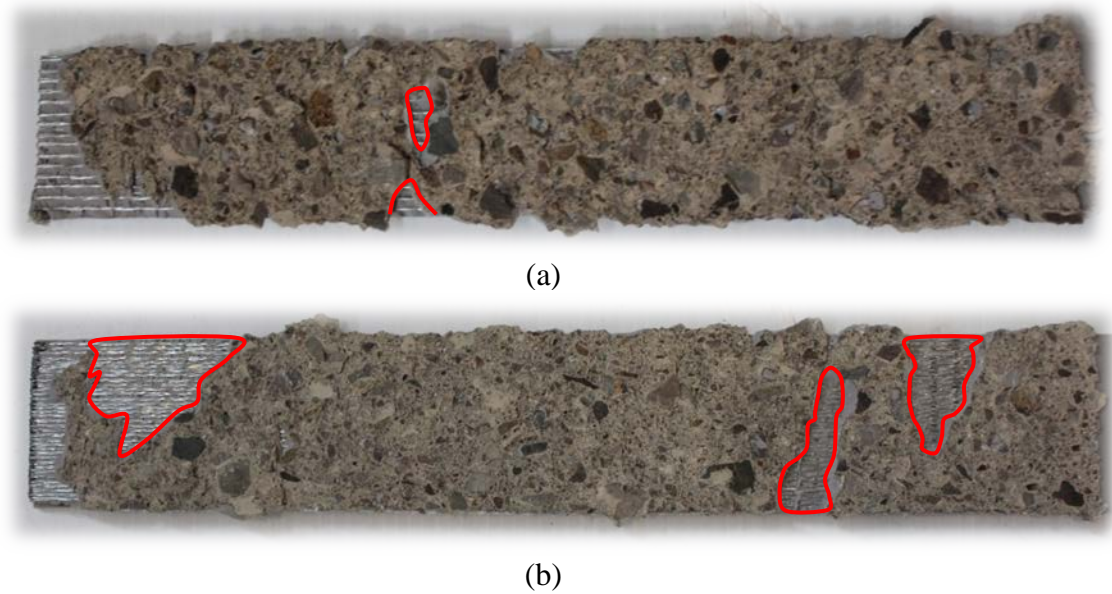


Figure 5.17 a) SFRP strip after debonding for specimen DS_300_50_MD_ND_B_3.
 b) SFRP strip after debonding for specimen DS_300_50_UHD_ND_S_2.

The failure mode of all SFRP concrete prisms tested using a triple point bending set-up consists in the detachment of the composite strip from one side of the specimen. It is worth to highlight that the debonding mechanism from the concrete substrate starts also in the opposite side of the prism. The debonded portion of the composite strip has usually a thin layer of concrete attached, a part for the portion near the initial notch, where a concrete wedge remains usually attached to the SFRP reinforcement. The concrete wedge can detach from one or both sides of the initial notch. Notwithstanding specimen TPB_400_50_MD_B_3 showed the same kind of rupture, the concrete wedges detached from one side of the prism appear to be greater with respect to other tests. This entails a higher amount of energy needed to fracture the concrete close to the initial notch and leads to an higher value of the maximum load and of P_{crit} , as showed in Figure 5.15a and Table 5.9, respectively. Figure 5.18 shows in red the large concrete wedge detached from the right side of the specimen with respect to the normal concrete wedge (green) detached from the left side. For these reasons specimen TPB_400_50_MD_B_3 will not be considered in the remainder of the work.

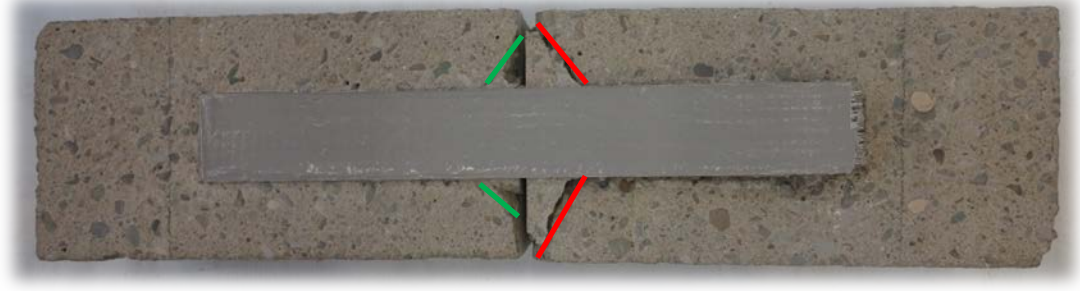


Figure 5.18: Failure mode for specimen TPB_400_50_MD_B_3

4.2 Strain analysis in direct-shear tests

In this work, DIC was used for some specimens to examine the strain field on the surface of the FRP strip in the axial direction. Displacements and strains were obtained for different square areas (subsets) for a 5 pixel step size, which provided points spaced at approximately 1.67 mm. Different subsets of 21, 31, and 41 pixels were used to study the influence of subset dimension on the results obtained. Results determined using different subsets are similar, therefore a subset size of 21 pixels (approximately 7 mm) edge was employed for the remainder of the specimens. The strain analysis reported in this section refers to the Cartesian system shown in Figure 5.19. The axial strain values were determined along the center line of the steel FRP strip by averaging the strain across a 15mm-wide strip for each value of y (Figure 5.22). Averaging the strain across a 15 mm width allow for taking into account the variation of the strain due to the presence of a non-homogeneous substrate and local material variations in the steel-FRP strip. A 15-mm strip was chosen based on the aggregate size. The experimental nonlinear strain distribution along the bonded length was approximated using three different equations:

$$- \quad \varepsilon(y) = \frac{A \exp(B(Ay + C))}{\exp(B(Ay + C)) + 1} \quad (1)$$

where A , B , and C are parameters evaluated through a non-linear regression analysis of the strains obtained from DIC.

$$- \quad \varepsilon(y) = \begin{cases} 0, & \text{if } \varepsilon_1(y)' > 0 \quad \& \quad \varepsilon_1(y)'' < 0 \\ \varepsilon_1(y), & \text{if } \varepsilon_1(y)' > 0 \\ 2D, & \text{if } \varepsilon_1(y)' < 0 \quad \& \quad \varepsilon_1(y)'' < 0 \end{cases} \quad (2)$$

Where $\varepsilon_1(y)$ is the following expression:

$$\varepsilon_1(y) = D \sin \left(\left(\frac{y-G}{E} \right)^F \pi - \frac{\pi}{2} \right) + D \quad (3)$$

and once again D, E, F, and G are parameters evaluated through a non-linear regression. y_A and y_B are the y coordinates along the FRP strip where function (2) changes from 0 to $\varepsilon_1(y)$ and from $\varepsilon_1(y)$ to 2D, respectively.

$$- \quad \varepsilon(y) = \begin{cases} 0, & \text{if } \varepsilon_2(y)' > 0 \quad \& \quad \varepsilon_2(y)'' < 0 \\ \varepsilon_2(y), & \text{if } \varepsilon_2(y)' > 0 \\ \varepsilon_2(y = y_D), & \text{if } \varepsilon_2(y)' < 0 \quad \& \quad \varepsilon_2(y)'' < 0 \end{cases} \quad (4)$$

Where $\varepsilon_2(y)$ is the following expression:

$$- \quad \varepsilon_2(y) = H(y - y_C)^3 + I(y - y_C)^2 + L(y - y_C) \quad (5)$$

where once again H, I, L, and y_C are parameters evaluated through a non-linear regression. y_C and y_D are the y coordinates along the FRP strip where function (4) changes from 0 to $\varepsilon_2(y)$ and from $\varepsilon_2(y)$ to $\varepsilon_2(y = y_D)$, respectively.

Equation (1) was introduced by Dai et al (2006), equation (2) is a polynomial equation while equation (4) is a sinusoidal equation.

For each equation, it's possible to define a set of parameters that best fits the experimental strain behavior, obtaining an analytical representation of the strain profile. The strain distribution during the debonding process can be divided into three main regions: (A) the stress-free zone (SFZ); (B) the stress-transfer zone (STZ); and (C) the fully-debonded zone (FDZ). The stress transfer occurs in the STZ, usually characterized by an "S" shape of the strain profile. In the FDZ the composite strip is completely debonded from the concrete substrate, i.e. no shear transfer is still

possible and the strains are essentially constant. The SFZ is localized in the portion of the SFRP strip near the free end and represents the part of the composite strip not yet affected by the shear transfer. While the global slip increase during the debonding mechanism, the “S” shape move gradually from the loaded end to the free end of the composite strip, and the strain in the FDZ appeared to be constant. This fact is consistent with the observation that the load remained constant (P_{crit}) after the debonding process propagated. Figure 5.20 represents the strain profiles of specimen DS_300_50_UHD_D_B_5 obtained at a fixed value of the global slip fitting the experimental values with the three different equations. Figure Y shows the distribution of the strain profile of the same specimen at 5 different values of the global slip between g_1 and g_2 using the equation from Dai et al (2006). It can be observed that a simple translation of the STZ further along the length of the SFRP strip occurred as the global slip increased while its shape remained constant.

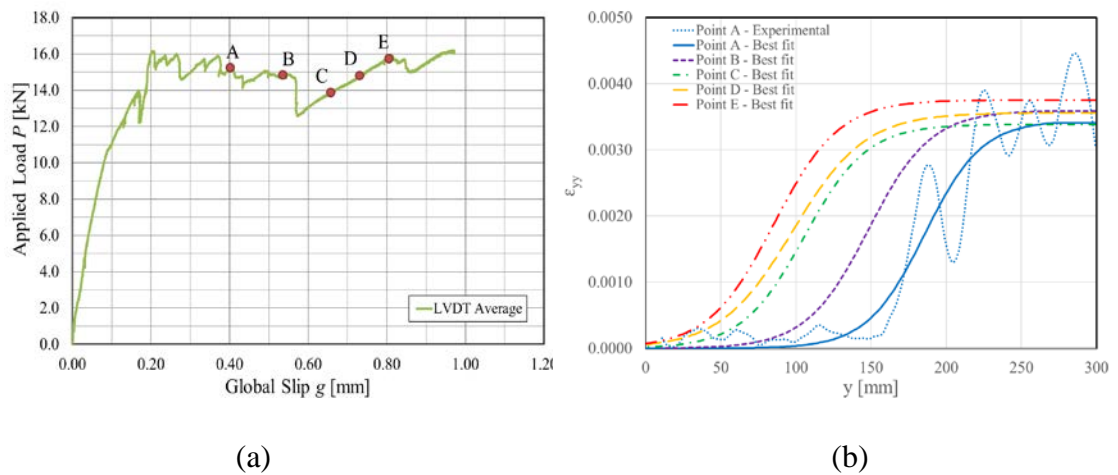


Figure 5.19: a) Load response for specimen DS_300_50_UHD_D_B_5. b) S-shape ϵ_{yy} profile for specimen DS_300_50_UHD_D_B_5.

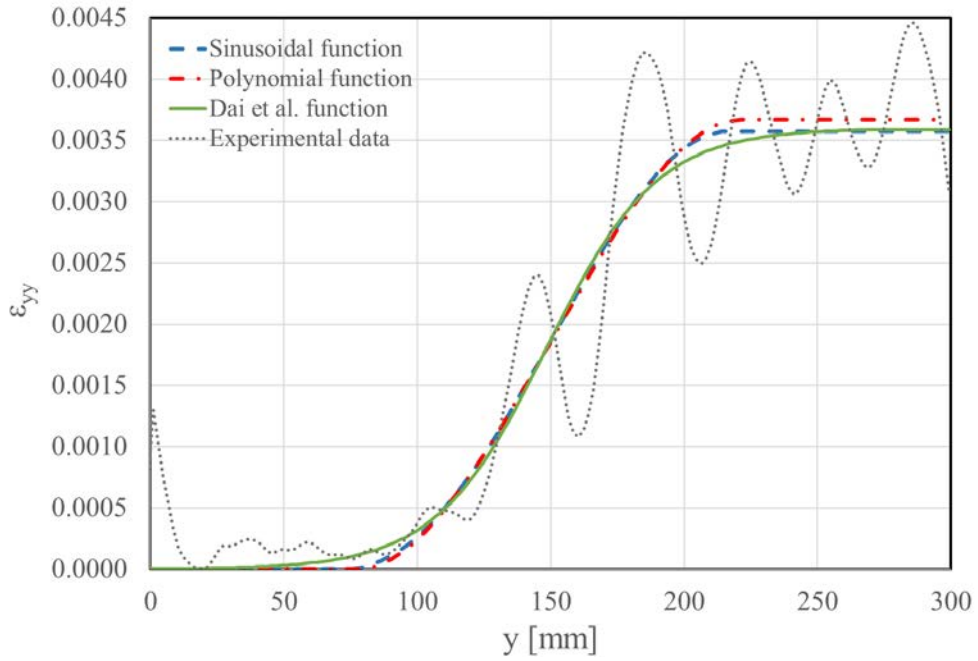


Figure 5.20: S-shape ε_{yy} profile for specimen DS_300_50_UHD_D_B_5 using three different functions to fit experimental data.

4.3 Interfacial cohesive material law

From the analytical equations representing the strain profile it's possible to define the value of the shear stress at any location of the composite strip, using the following relationship:

$$\tau_{zy}(y) = E_f t_f \frac{d\varepsilon_{yy}}{dy} \quad (6)$$

where E_f and t_f are respectively the elastic modulus and the thickness of the fibers.

At the same time, the slip between the SFRP strip and the concrete substrate at any location of the composite strip can be evaluated from the strain profile:

$$s(y) = \int_0^y \varepsilon_{yy} dy \quad (7)$$

Dai et al. (2006) showed that the bond stress-slip relationship can be obtained as follows:

$$\tau_{zy} = A^2 B E_f t_f \exp(-Bs)(1 - \exp(-Bs)) \quad (8)$$

The interfacial τ - s relationship can be expressed through an analytic formula also starting from the polynomial expression of the strains and using the solution

proposed by Cardano formula. The mathematical method to obtain the bond stress-slip relationship from the polynomial expression is showed in Appendix 1 for sake of brevity.

It is no possible to obtain an analytical formulation using the sinusoidal expression of the strains. Therefore, in this case, the τ - s relationship can be obtained only combining directly the shear stress and the respective slip at the same position (y) of the composite strip using Eq. (6) and (7), respectively.

The cohesive material law obtained for specimen DS_300_50_UHD_D_B_5 is represented in Figure 5.21. Three different equations were used to represent the strain profile.

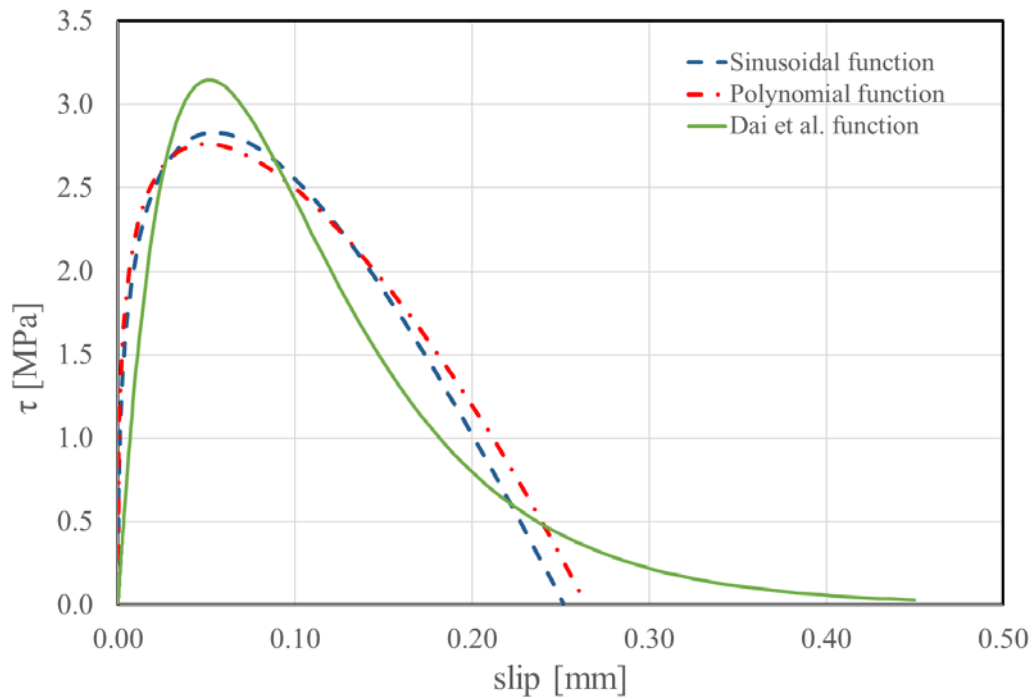


Figure 5.21: Cohesive material law τ - s for specimen DS_300_50_UHD_D_B_5 obtained using three different functions to fit experimental data.

The fracture energy G_F , i.e. the energy required to fully break the elementary unit area of the cohesive crack, corresponds to the area under the entire $\tau_{zy}(s)$ curve:

$$G_F = \int \tau_{zy}(s) ds \quad (9)$$

The effective bond length, L_{eff} , i.e. the active bonding zone along which the interfacial load is transferred between the SFRP strip and the concrete substrate, can be evaluated depending on the equation used to fit the experimental strain

$$L_{eff} = \frac{\sqrt{2E_f t_f}}{B\sqrt{G_f}} \ln\left(\frac{1+\alpha}{1-\alpha}\right) \quad (10)$$

$$L_{eff} = y_B - y_A \quad (11)$$

$$L_{eff} = y_D - y_C \quad (12)$$

Where α is assumed equal to 0.96.

Equation (10) was used by Dai et al. (2006), while equations (11) and (12) were used to evaluate the effective bond length, L_{eff} , for the sinusoidal and polynomial equation, respectively.

Table 5.10 summarize the mean value of the maximum strain along the SFRP strip, ϵ_{max} , the maximum shear stress, τ_{max} , the slip corresponding to the maximum shear stress, s_m , the effective bond length, L_{eff} , and the fracture energy, G_f , for each specimen tested employing DIC.

Table 5.10: Fracture mechanics parameters

Specimen Name	Function	ϵ_{max}	τ_{max} [MPa]	s_m [mm]	L_{eff} [mm]	G_f [N/mm]	P_{crit} [kN]	P_{theor} [kN]	P_{crit}/P_{theor} [%]
DS_300_50_HD_D_S_1	Dai	0.0044 (0.06)	2.86 (0.17)	0.056	147.5 (0.16)	0.47 (0.11)	12.25	10.81	88.3%
	Sin	0.0043 (0.04)	2.27 (0.12)	0.06 (0.15)	147.7 (0.12)	0.46 (0.08)	12.25	10.78	88.0%
	Pol	0.0042 (0.04)	2.69 (0.20)	0.048 (0.23)	119.5 (0.21)	0.44 (0.07)	12.25	10.46	85.4%
DS_300_50_HD_D_S_2	Dai	0.0042 (0.06)	3.17 (0.13)	0.046	125.4 (0.14)	0.42 (0.11)	12.27	10.47	85.3%
	Sin	0.0041 (0.04)	2.25 (0.13)	0.06 (0.11)	141.5 (0.12)	0.42 (0.08)	12.27	10.47	85.3%
	Pol	0.0041 (0.04)	2.73 (0.11)	0.042 (0.12)	109.6 (0.12)	0.40 (0.07)	12.27	10.26	83.6%
DS_300_50_HD_D_S_3	Dai	0.0042 (0.08)	2.43 (0.19)	0.061	165.1 (0.11)	0.43 (0.17)	11.92	10.16	85.2%
	Sin	0.0043 (0.11)	1.91 (0.18)	0.061 (0.34)	173.7 (0.1)	0.45 (0.23)	11.92	10.46	87.8%
	Pol	0.0042 (0.1)	2.48 (0.26)	0.051 (0.29)	133.0 (0.26)	0.44 (0.20)	11.92	10.27	86.2%
DS_300_50_HD_D_S_4	Dai	0.0035 (0.07)	2.29 (0.11)	0.045	144.9 (0.09)	0.30 (0.14)	10.44	8.83	84.6%
	Sin	0.0037 (0.1)	1.63 (0.11)	0.061 (0.19)	173.9 (0.06)	0.34 (0.2)	10.44	9.46	90.6%
	Pol	0.0036 (0.1)	2.09 (0.16)	0.043 (0.25)	128.7 (0.19)	0.32 (0.21)	10.44	9.07	86.9%

(cont.) Table 5.10: Fracture mechanics parameters

Specimen Name	Function	ϵ_{\max}	τ_{\max} [MPa]	s_m [mm]	L_{eff} [mm]	G_f [N/mm]	P_{crit} [kN]	P_{theor} [kN]	$P_{\text{crit}}/P_{\text{theor}}$ [%]
DS_300_50_HD_D_S_5	Dai	0.0038 (0.06)	3.25 (0.1)	0.038	111.6 (0.1)	0.36 (0.12)	11.47	9.64	84.0%
	Sin	0.0039 (0.05)	2.24 (0.12)	0.055 (0.07)	133.9 (0.09)	0.37 (0.1)	11.47	9.89	86.2%
	Pol	0.0038 (0.05)	2.84 (0.14)	0.034 (0.2)	99.6 (0.18)	0.35 (0.09)	11.47	9.55	83.3%
DS_300_50_HD_D_B_2	Dai	0.0041 (0.06)	3.37 (0.22)	0.043	120 (0.18)	0.42 (0.11)	12.64	10.43	82.5%
	Sin	0.0042 (0.06)	2.57 (0.25)	0.055 (0.26)	130.7 (0.20)	0.44 (0.12)	12.64	10.69	84.6%
	Pol	0.0042 (0.05)	3.04 (0.27)	0.042 (0.22)	106.1 (0.23)	0.43 (0.11)	12.64	10.54	83.3%
DS_300_50_HD_D_B_3	Dai	0.0042 (0.06)	2.89 (0.16)	0.05	138.4 (0.16)	0.42 (0.12)	12.28	10.46	85.2%
	Sin	0.0043 (0.09)	2.39 (0.11)	0.055 (0.15)	136.3 (0.15)	0.45 (0.17)	12.28	10.94	89.1%
	Pol	0.0043 (0.07)	2.60 (0.22)	0.049 (0.26)	124.7 (0.23)	0.44 (0.14)	12.28	10.85	88.4%
DS_300_50_UHD_D_B_3	Dai	0.0036 (0.05)	5.25 (0.29)	0.031	106.7 (0.32)	0.48 (0.10)	16.07	13.21	82.2%
	Sin	0.0042 (0.05)	2.56 (0.08)	0.056 (0.23)	186.9 (0.09)	0.63 (0.09)	16.07	15.11	94.0%
	Pol	0.0038 (0.06)	4.71 (0.29)	0.036 (0.46)	99.7 (0.42)	0.54 (0.11)	16.07	13.93	86.7%
DS_300_50_UHD_D_B_4	Dai	0.0041 (0.06)	3.50 (0.30)	0.059	178.1 (0.26)	0.62 (0.13)	15.24	15.68	102.9%
	Sin	0.0041 (0.05)	2.67 (0.12)	0.077 (0.18)	176.0 (0.13)	0.60 (0.1)	15.24	15.52	101.9%
	Pol	0.004 (0.07)	3.28 (0.28)	0.054 (0.35)	142.4 (0.30)	0.58 (0.14)	15.24	15.20	99.8%
DS_300_50_UHD_D_B_5	Dai	0.0035 (0.06)	3.25 (0.20)	0.045	156.1 (0.21)	0.43 (0.12)	14.49	12.54	86.5%
	Sin	0.0036 (0.06)	2.43 (0.15)	0.056 (0.12)	170.5 (0.12)	0.47 (0.11)	14.49	13.05	90.1%
	Pol	0.0035 (0.07)	3.12 (0.26)	0.043 (0.31)	130.1 (0.28)	0.44 (0.13)	14.49	12.64	87.2%

The theoretical load carrying capacity, P_{theor} , can be evaluated taking advantage of the expression proposed by Täljsten (1997) for FRPs bonded to a concrete surface:

$$P_{\text{theor}} = b_f \sqrt{2E_f t_f G_f} \quad (13)$$

Table 6 summarize the values of P_{theor} , for each test performed with DIC. In addition, the ratio $P_{\text{crit}}/P_{\text{theor}}$ (expressed as percentage) has been reported. The theoretical load carrying capacity, P_{theor} , appear to be slightly lower than the one evaluated from experimental tests (P_{crit}). The reason can be ascribed to the fact that the theoretical

formula proposed by Täljsten (1997) assume constant axial strain along all the width of the composite strip ignoring any possible interaction due to the concrete near the edges of the composite strip. In reality, strains are constant only in the central region of the SFRP strip (shear strains equal to zero) due to the *width effect* (Subramaniam et al. 2007). Therefore, the fracture mechanics Mode-II loading condition should be assumed only in the central region of the FRP strip. Neglecting the influence of the concrete near the edges, P_{theor} must result lower if compared with P_{crit} .

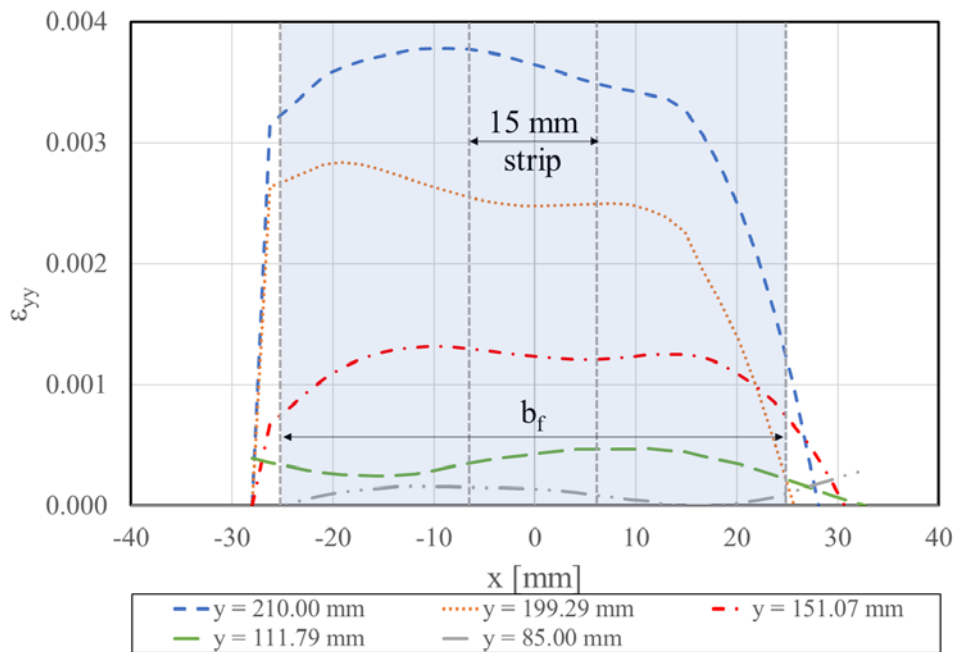


Figure 5.22: Typical variation of strain as a function of x , for different locations along the bond length for specimen DS_300_50_UHD_D_B_5

5.0 Discussion

5.1 Fracture mechanics parameters

In this section the fracture mechanics parameters obtained from the fitting of experimental results with three different functions are investigated. The analysis will consider only specimens tested with DIC and reported in Table 6.

In general, the three functions, i.e. Dai et al. (2006), sinusoidal and polynomial, show similar results for ϵ_{max} and G_f , while a large scatter can be observed considering L_{eff} , s_m and τ_{max} . Considering all the specimens, the value of L_{eff} obtained from the sinusoidal function is 32.7% and 14.9% higher with respect to the ones obtained

from the polynomial and Dai et al. (2006) functions, respectively. It appears clear that the sinusoidal fitting tends to overestimate the effective bond length. Differently from the polynomial and Dai et al. expressions, the sinusoidal function is not able to reproduce sharp changes in the slope of the epsilon behavior. This fact leads to an increase in the length of the S-shape profile causing higher values of L_{eff} . For this reason, the sinusoidal function will not be considered for the evaluation of the effective bond length, L_{eff} .

At the same way, the value of s_m and τ_{max} determined with the sinusoidal function appear to be different from the values defined with the polynomial and Dai et al. functions. As mentioned before, this aspect derived from the difficulty to reproduce sharp slopes with the sinusoidal fitting and lead to an overestimation of the s_m and to an underestimation of the τ_{max} . Therefore, the values of s_m and τ_{max} obtained from the sinusoidal function, could be not completely reliable.

Comparing concrete specimens reinforced with MD steel fibers on two different sides (S or B) it appears clear that the effective bond length, L_{eff} , is the same, while the fracture energy, G_f , seems to vary a little. The average value of L_{eff} for S-side specimens is equal to 118 mm (polynomial function) and 139 mm (Dai et al. function), while for B-side specimens is equal to 115 mm (polynomial function) and 129 mm. Therefore, the side on which the composite strip is applied doesn't affect the effective bond length. Contrarywise, the side of application of the strip influences the fracture energy. The average value of G_f for S-side specimens is equal to 0.39 N/mm (polynomial function), 0.41 N/mm (sinusoidal function) and 0.39 N/mm (Dai et al. function) and seems lower with respect to the average value obtained for B-side specimen that is equal to 0.43 N/mm (polynomial function), 0.44 N/mm (sinusoidal function) and 0.42 N/mm (Dai et al. function).

The UHD specimens tested on side B confirm the increase of the fracture energy when the bottom side is considered. The average value of G_f for these specimens is equal to 0.52 N/mm (polynomial function), 0.57 N/mm (sinusoidal function) and 0.51 N/mm (Dai et al. function). The reason of the increase of the fracture energy can be ascribed to the higher amount of aggregates on the bottom faces of the prisms with respect to the side faces. During casting, because of gravity, it is more probably to distribute a higher quantity of aggregates in the bottom part of the mold. Therefore, due to the higher amount of aggregates, it needs more energy to fracture the concrete surface on the bottom side with respect to the lateral one, as highlighted

from the experimental results. Specimen reinforced with UHD steel fibers show also an increase of L_{eff} that is equal to 124 mm and 147 mm for polynomial and Dai et al. function, respectively. It is reasonable to assume that an increase in the stiffness of the composite strip lead to an increase of the effective bond length.

5.2 FRP-SFRP analogy

Experimental results showed that the failure mode of concrete specimens tested using a single lap shear test set-up usually entails the fracture of a thin layer of concrete on the surface where the strip is bonded to prism. It is therefore reasonable to assume that the fracture energy, G_f , for specimens tested on the same side (S or B) should be approximately the same, independently from the stiffness of the composite strip. Using this assumption, it is possible to check if equation (13) is applicable also to SFRP. Referring to Table 5.8, the average value of P_{crit} for B-side specimens with MD, HD and UHD steel fibers is equal to 10.81 kN, 12.57 kN and 15.64 kN. The theoretical ratio between the critical load evaluated for MD steel fibers and HD steel fibers, P_{MD}/P_{HD} , and between the critical load evaluated for HD steel fibers and UHD steel fibers, P_{HD}/P_{UHD} should be equal to the following values, taking advantage of Täljsten formula:

$$P_{MD} / P_{HD} = \frac{b_f \sqrt{2E_f t_{f,MD} G_f}}{b_f \sqrt{2E_f t_{f,HD} G_f}} \sqrt{\frac{t_{f,MD}}{t_{f,HD}}} = \sqrt{\frac{0.169}{0.254}} = 0.816 \quad (14)$$

$$P_{HD} / P_{UHD} = \frac{b_f \sqrt{2E_f t_{f,HD} G_f}}{b_f \sqrt{2E_f t_{f,UHD} G_f}} = \sqrt{\frac{t_{f,HD}}{t_{f,UHD}}} = \sqrt{\frac{0.254}{0.381}} = 0.816 \quad (15)$$

The experimental ratio between the critical load evaluated for MD steel fibers and HD steel fibers, $P_{crit,MD}/P_{crit,HD}$ and between the critical load evaluated for HD steel fibers and UHD steel fibers, $P_{crit,HD}/P_{crit,UHD}$, is equal to 0.860 and 0.804, respectively. Similarly, comparing specimens with the composite strip applied on the S-side, the average value of P_{crit} is equal to 11.67 kN and 14.52 kN, for HD and UHD steel fibers, respectively. The experimental ratio $P_{crit,HD}/P_{crit,UHD}$, is equal to 0.804. In both cases the experimental results appear to be very close to the theoretical ones,

confirming the analogous behavior between FRP and SFRP composite strip bonded to concrete surfaces.

Comparing the average values of the critical load presented above, it's possible to appreciate the influence of the side of application of the composite strip on the experimental results. For HD steel fibers, the average value of P_{crit} evaluated on the B-side is 7.7% higher with respect to the one evaluated on the S-side. Similarly, for UHD steel fibers, the average value of P_{crit} evaluated on the B-side is 7.7% higher with respect to the one evaluated on the S-side. These results validate the considerations of section 6.2 confirming that it's needed a higher amount of energy to fracture the B-side surfaced due to the presence of a larger amount of aggregates.

5.3 Influence of the bond set-up

The influence of the bond set-up on the results can be analyzed considering tests conducted on specimens with MD and HD steel fibers, strengthened on side B. Referring to Table 5, it's possible to evaluate the average value of P_{crit} for different densities and different test-set-up. For specimens tested using a direct-shear test set-up, the average value of P_{crit} is equal to 10.81 kN and 12.57 kN for MD and HD steel fibers, respectively. For specimens tested using a TPB set-up, the average value of P_{crit} is equal to 14.68 kN and 16.72 kN. Results obtained from TPB set-up are 35.8 % greater than the one obtained from direct shear tests for MD steel fibers and 33.0 % greater for HD steel fibers. These results highlighted as the bond set-up as a great influence on bond results. In TPB set-up, the curvature of the specimen during the test enhance the bond between the composite strip and the concrete substrate, determining higher values of P_{crit} . It's possible to affirm that results obtained from the two different set-ups are not comparable each other.

6.0 Conclusions

This work presented the experimental results of concrete specimens subjected to two different test set-ups to investigate the debonding mechanism in SRP-concrete joints; single-lap shear test set-up and TPB set-up. Test variables included different test setup, fiber density, concrete surface treatment (side S or B). The interfacial cohesive material law for SRP strips bonded to concrete is also investigated using digital

image correlation (DIC). Based on the results of this work, The following conclusions can be drawn:

1. The behavior of the load responses of concrete specimens tested using TPB test set-up is similar to those using direct-shear test set-up, a part for the constant plateau that in TPB test appear to be shorter.
2. The failure mode of concrete specimens tested using a single lap shear test set-up usually entails the fracture of a thin layer of concrete on the surface where the strip is bonded to prism. While, the failure mode of all concrete specimens tested using a triple point bending set-up consists in the detachment of the composite strip from one side of the specimen
3. For HD steel fibers, the average value of P_{crit} evaluated on the B-side is higher with respect to the one evaluated on the S-side. Similarly, for UHD steel fibers, the average value of P_{crit} evaluated on the B-side is higher with respect to the one evaluated on the S-side.
4. The three functions Dai et al. (2006), sinusoidal and polynomial, show similar results for ε_{max} and G_f , while a large scatter can be observed considering L_{eff} , s_m and τ_{max} .
5. Results obtained from TPB set-up are 35.8 % greater than the one obtained from direct shear tests for MD steel fibers and 33.0 % greater for HD steel fibers.

7.0 References

Balsamo, A., Nardone, F., Iovinella, I., Ceroni, F., & Pecce, M. (2013). Flexural strengthening of concrete beams with EB-FRP, SRP and SRCM: Experimental investigation. *Composites Part B: Engineering*, 46, 91-101.

Barton, B., Wobbe, E., Dharani, L. R., Silva, P., Birman, V., Nanni, A., ... & Tunis, G. (2005). "Characterization of reinforced concrete beams strengthened by steel reinforced polymer and grout (SRP and SRG) composites." *Materials Science and Engineering: A*, 412(1), 129-136.

Bencardino, F., & Condello, A. (2014). "Structural behaviour of RC beams externally strengthened in flexure with SRG and SRP systems." *International Journal of Structural Engineering*, 5(4), 346-368.

Bizindavyi, L., & Neale, K. W. (1999). "Transfer lengths and bond strengths for composites bonded to concrete." *Journal of composites for construction*, 3(4), 153-160.

Casadei, P., Nanni, A., & Alkhrdaji, T. (2005). "Steel-reinforced polymer: An innovative and promising material for strengthening infrastructures." *Concrete Engineering International*, 9(1), 54-56.

CEN, EN 12390-3, 2009. Testing hardened concrete - Part 3: Compressive strength of test specimens. A1: 2011. Brussels: CEN.

CEN, EN 12390-6, 2009. Testing hardened concrete - Part 6: Tensile splitting strength of test specimens. Brussels: CEN.

Chajes, M. J., Finch, W. W., Januszka, T. F., & Thomson, T. A. (1996). "Bond and force transfer of composite material plates bonded to concrete." *ACI structural journal*, 93(2), 208-217.

Dai, J., Ueda, T., & Sato, Y. (2005). "Development of the nonlinear bond stress-slip model of fiber reinforced plastics sheet-concrete interfaces with a simple method." *Journal of Composites for Construction*, 9(1), 52-62.

Dai, J. G., & Ueda, T. (2003, July). "Local bond stress slip relations for FRP sheets-concrete interfaces." In *Proc. of 6th international symposium on FRP reinforcement for concrete structures* (pp. 143-152).

De Lorenzis, L., Miller, B., & Nanni, A. (2001). "Bond of fiber-reinforced polymer laminates to concrete." *ACI Materials Journal*, 98(3), 256-264.

Elices, M., Guinea, G. V., & Planas, J. (1992). "Measurement of the fracture energy using three-point bend tests: Part 3—influence of cutting the P- δ tail." *Materials and Structures*, 25(6), 327-334.

- Figeys, W., Schueremans, L., Van Gemert, D., & Brosens, K. (2008). "A new composite for external reinforcement: steel cord reinforced polymer." *Construction and Building Materials*, 22(9), 1929-1938.
- Focacci, F., Nanni, A., & Bakis, C. E. (2000). "Local bond-slip relationship for FRP reinforcement in concrete." *Journal of composites for construction*, 4(1), 24-31.
- Hoover, C. G., & Bažant, Z. P. (2013). "Comprehensive concrete fracture tests: size effects of types 1 & 2, crack length effect and postpeak." *Engineering Fracture Mechanics*, 110, 281-289.
- Hillerborg, A. (1985). "The theoretical basis of a method to determine the fracture energy G_F of concrete." *Materials and structures*, 18(4), 291-296.
- Huang, X., Birman, V., Nanni, A., & Tunis, G. (2005). Properties and potential for application of steel reinforced polymer and steel reinforced grout composites. *Composites Part B: Engineering*, 36(1), 73-82.
- Leung, C. K., & Tung, W. K. (2006). "Three-parameter model for debonding of FRP plate from concrete substrate." *Journal of engineering mechanics*, 132(5), 509-518.
- Lopez, A., Galati, N., Alkhrdaji, T., & Nanni, A. (2007). "Strengthening of a reinforced concrete bridge with externally bonded steel reinforced polymer (SRP)." *Composites Part B: Engineering*, 38(4), 429-436.
- Lu, X. Z., Teng, J. G., Ye, L. P., & Jiang, J. J. (2005). "Bond-slip models for FRP sheets/plates bonded to concrete." *Engineering structures*, 27(6), 920-937.
- Matana, M., Nanni, A., Dharani, L., Silva, P., & Tunis, G. (2005, December). Bond performance of steel reinforced polymer and steel reinforced grout. In *Proceedings of international symposium on bond behaviour of FRP in structures (BBFS 2005)*, Hong Kong (pp. 125-132).
- Mazzotti, C., Savoia, M., & Ferracuti, B. (2008). "An experimental study on delamination of FRP plates bonded to concrete." *Construction and Building Materials*, 22(7), 1409-1421.

- Menna, C., Asprone, D., Ferone, C., Colangelo, F., Balsamo, A., Prota, A., ... & Manfredi, G. (2013). "Use of geopolymers for composite external reinforcement of RC members." *Composites Part B: Engineering*, 45(1), 1667-1676.
- Mitolidis, G. J., Salonikios, T. N., & Kappos, A. J. (2012). "Tests on RC beams strengthened at the span with externally bonded polymers reinforced with carbon or steel fibers." *Journal of Composites for Construction*, 16(5), 551-562.
- Nakaba, K., Kanakubo, T., Furuta, T., & Yoshizawa, H. (2001). "Bond behavior between fiber-reinforced polymer laminates and concrete." *Structural Journal*, 98(3), 359-367.
- Pecce, M., Ceroni, F., Prota, A., & Manfredi, G. (2006). Response prediction of RC beams externally bonded with steel-reinforced polymers. *Journal of Composites for Construction*, 10(3), 195-203.
- Prota, A., Tan, K. Y., Nanni, A., Pecce, M., & Manfredi, G. (2006). Performance of shallow reinforced concrete beams with externally bonded steel-reinforced polymer. *ACI structural journal*, 103(2), 163.
- Saber, N., Hassan, T., Abdel-Fayad, A. S., & Gith, H. (2008, July). "Flexural behavior of concrete beams strengthened with steel reinforced polymers." In *Proceedings of the Fourth International Conference on FRP Composites in Civil Engineering, CICE*.
- Savoia, M., Ferracuti, B., & Mazzotti, C. (2003). "Nonlinear bond-slip law for FRP-concrete interface." In *Proc. of 6th international symposium on FRP reinforcement for concrete structures*. Singapore: World Scientific Publications (pp. 163-72).
- Täljsten, B. (1997). "Defining anchor lengths of steel and CFRP plates bonded to concrete." *International Journal of Adhesion and Adhesives*, 17(4), 319-327.
- Wobbe, E., Silva, P., Barton, B. L., Dharani, L. R., Birman, V., Nanni, A., ... & Tunis, T. (2004, May). "Flexural capacity of RC beams externally bonded with SRP and SRG." In *Proceedings of Society for the Advancement of material and Process Engineering 2004 Symposium* (pp. 16-20).

CHAPTER 6

A STUDY OF THE COMPRESSIVE BEHAVIOR OF CONCRETE COLUMNS CONFINED WITH STEEL-FRP JACKETS USING DIGITAL IMAGE ANALYSIS

6.0 Introduction

In recent decades, the use of innovative fiber reinforced composite materials has gained popularity in structural strengthening applications. Confinement of concentrically or eccentrically loaded columns has played a key role in strengthening existing structures given the more stringent code requirements and the beam-column hierarchical relationship in a frame subjected to seismic loading. Fiber reinforced polymer (FRP) composites offer some advantages when compared to traditional materials in confinement applications of structural elements. Features such as ease of installation, relatively short curing time, high strength-to-weight ratio, high corrosion resistance, and minimal change in dimension of the strengthened member make FRP composites an appealing alternative to other techniques such as concrete or steel jackets or external steel ties. The composite is typically wrapped around the column with fibers oriented perpendicular to the longitudinal axis of the column or with an angle if the sheets are continuously wrapped around it. The use of composite materials as a confinement system has been proven to be effective in terms of improving the load-bearing capacity and deformability of confined elements e.g., Saafi et al. (1999), Rochette and Labossière (2000).

A new type of FRP composite that is being explored for structural strengthening applications includes steel fiber sheets. The use of steel fibers was proposed as a lower-cost alternative to other fiber types, such as carbon or aramid. The resulting composites have been referred to in the recent literature by different names, such as steel reinforced polymer (SRP) composites, but are herein referred to as steel-FRP

composites. Different authors have studied the use of steel-FRP for flexural strengthening of RC beams Wobbe et al. (2004), Prota et al. (2004), Kim et al. (2005), Barton et al. (2005), Casadei et al. (2005), Prota et al. (2006), Pecce et al. (2006), Ceroni (2007), Balsamo et al. (2013), Hawileh et al. (2014) and RC slabs Napoli and Realfonzo (2015), and confinement of concrete columns El-Hacha and Mashrik (2012), Napoli and Realfonzo (2016).

In this study, the behavior of concrete compressive members confined by steel-FRP composite is investigated. An experimental study was carried out to understand the behavior of short concrete prisms with a square cross-section confined by steel fiber sheets embedded in an epoxy matrix. The effectiveness of the confinement is studied in terms of load-bearing capacity and ultimate strain with respect to unconfined (control) prisms. Test parameters considered in this study are the density of steel fibers, concrete corner condition, concrete surface treatment, FRP jacket length, and number of confinement layers. Digital image correlation (DIC) is used to study qualitatively and quantitatively the displacement and strain fields on one face of the composite during the test.

6.1 Background

Numerous experimental works have been carried out to study the behavior of the concrete columns confined by FRP composites. Different types of fibers such as carbon, glass, and aramid have been investigated, although studies on FRP composites with steel fibers are currently limited in the technical literature El-Hacha and Mashrik (2012), El-Hacha and Abdelrahman (2013), Napoli and Realfonzo, (2016). It has been observed that the type of fiber can affect the behavior of the confined concrete in terms of failure mode and enhancement of strength and ultimate strain Saafi et al.(1999), Rochette and Labossière (2000). Rochette and Labossière (2000) compared the results of FRP confined columns with different fiber types and found that the axial stiffness of the confining material influences the concrete cracking pattern and plays a key role in enhancing the ductility of the column.

The failure mode of most concrete specimens confined by FRP with carbon, glass, or aramid fibers is tensile fracture of the fibers. Failure has been observed to be sudden

and preceded by sounds attributed to micro cracking of the concrete and shifting of the aggregates, as well as changes in the appearance of the composite Mirmiran and Shahawy (1997). Failure of the fibers for FRP-confined columns with a cylindrical cross-section is generally reported to initiate near the mid-length of the specimen and extend towards the top and bottom surfaces, whereas for columns with a rectangular cross-section, rupture has occurred at one corner of the specimen Rochette and Labossière (2000). Premature failure of the confining composite, that is, rupture of the fibers at a strain level lower than the ultimate strain of fibers, has been observed in some studies De Lorenzis and Tepfers (2003).

Different axial stress-strain responses have been observed for different shapes of cross-sections confined by FRP, with circular cross-sections having a larger ultimate stress and strain than comparable square cross-sections Campione and Miraglia (2001). For rectangular cross-sections, a variable transverse strain distribution around the section has been observed Rochette and Labossière (2000). For non-circular sections, the confinement is not as effective as for circular sections due to arching action. It has been observed that for a given axial stress level, the transverse strains measured at the mid-width of the column face are higher than those close to the corners Rochette and Labossière (2000). This indicates that the confinement pressure at the mid-width of the column faces is lower than at the corners. Rounding the corners of the cross-section has been shown to enhance the ultimate strength and ultimate strain of carbon or aramid FRP-confined concrete relative to a similar cross-section with sharp corners Rochette and Labossière (2000).

Studies have also shown that inadequate length of the overlap at the end of wrapping may result in premature failure due to debonding of the overlapped region prior to tensile rupture of the fibers De Lorenzis and Tepfers (2003). If the length of the overlap is such that debonding does not occur, it should not influence the confining behavior De Lorenzis and Tepfers (2003). However, it should be noted that studies on the bond behavior of single or multi-layer steel-FRP composite bonded to a concrete substrate are currently limited in the technical literature.

6.2 Experimental program

6.2.1 Materials

All concrete prisms were cast from the same batch of concrete. The concrete was normalweight with portland cement and a maximum aggregate size of 15 mm. Compressive and tensile strength of concrete were measured at different ages. Compressive strength was measured using 150 mm cubes and 150 mm × 300 mm cylinders and tested according to EN 12390-3 (2009). Tensile strength was measured using 150 mm × 300 mm cylinders and tested according to EN 12390-6 (2009). The average values of three tests for each day are plotted in Figure 6.1. The range of days highlighted in Figure 6.1 within the dashed lines indicates the age of concrete at which the confinement tests were conducted.

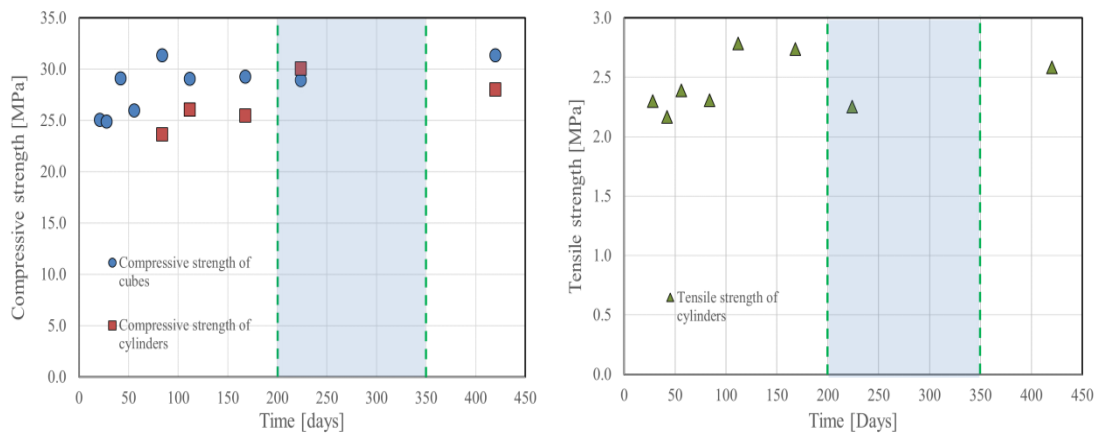


Figure 6.1. Concrete strength gain: (a) compressive strength; (b) tensile strength.

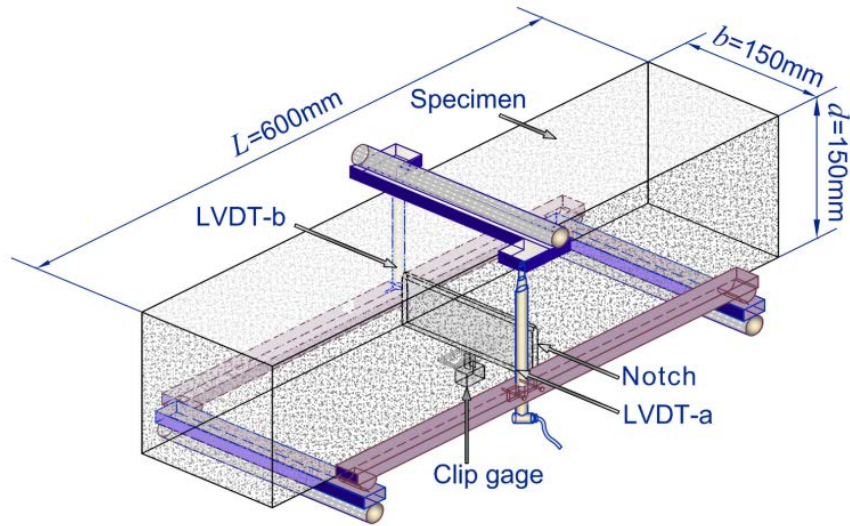
Three concrete prisms of width $b=150$ mm × depth $d=150$ mm × length $L=600$ mm and three concrete prisms of $b=70$ mm × $d=70$ mm × $L=300$ mm cast from the same concrete used for the confinement specimens were tested using a three point bending set-up to evaluate the fracture energy of concrete (Figure 6.2). All concrete prisms had a central notch with a V-shaped tip. The notch length a_0 was equal to one third of the prism depth. The net span was equal to three times the depth of the prism. The loading apparatus consisted of two steel cylinders that supported the prism base and a cylinder at the top of the prism, centered with respect to its length, that was used to apply the load. Two steel plates were glued to the bottom face of the prism and positioned on the support rollers to reduce friction. An S-shaped steel plate with a

central V-shaped section was glued on the top face of the prism to position the loading cylinder. On both sides of the concrete prism, a steel element, positioned on the bottom supports, fastened a linear variable displacement transducer (LVDT) that reacted off of the S-shaped top plate. The two LVDTs measured the vertical displacement δ of the prism where the load was applied. A clip-on gage, mounted near the edges of the central notch, measured the crack mouth opening displacement (CMOD) and was used to control the test. The rate of the test was equal to 0.001mm/s.

Figures 6.3 and 6.4, show the ratio of the applied load P normalized by the width b versus CMOD and δ responses of the 150 mm wide prisms and the 70 mm wide prisms, respectively. The fracture energy, G_F , was evaluated from the area under the load-deflection response Hillerborg (1985), Elices et al. (1992), Hoover and Bažant (2013). The average value of the fracture energy obtained from the three 150 mm \times 150 mm \times 600 mm prisms was 0.105 N/mm (CoV = 0.048), while the average value of the fracture energy obtained from the three 70 mm \times 70 mm \times 300 mm prisms was 0.111 N/mm (CoV = 0.117).

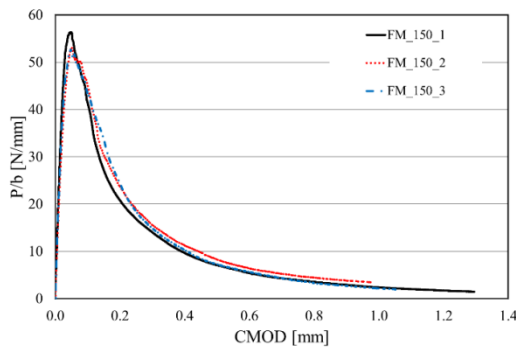


Figure 6.2. Experimental set-up for fracture mechanics tests for 150 mm width prisms (Photograph).

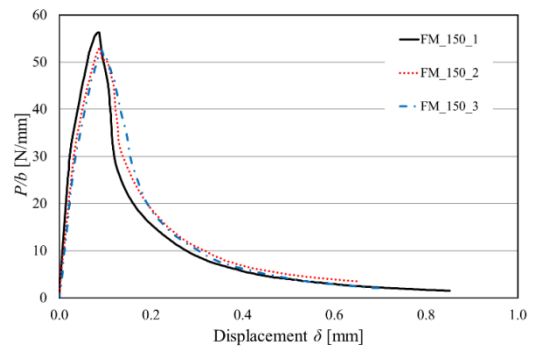


(b)

Figure 6.2. (cont.) Experimental set-up for fracture mechanics tests for 150 mm width prisms (Sketch)

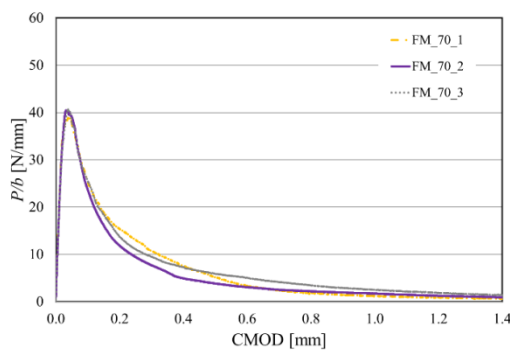


(a)

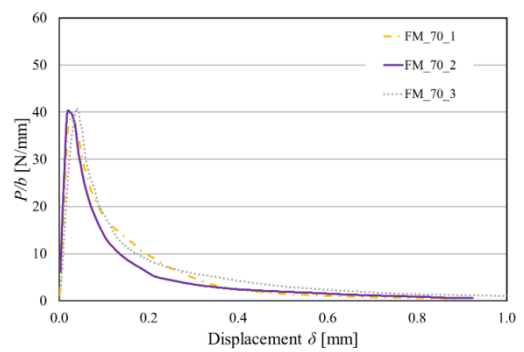


(b)

Figure 6.3. 150 mm width prisms: (a) $P/b - \text{CMOD}$ response; (b) $P/b - \delta$ response.



(a)



(b)

Figure 6.4. 70 mm width prisms: (a) $P/b - \text{CMOD}$ response; (b) $P/b - \delta$ response.

The composite material consisted of steel fiber sheets embedded in a polymeric matrix. Steel fibers were in the form of a unidirectional sheet made of ultra-high strength galvanized steel micro-cords fixed to a fiberglass micromesh to facilitate installation. Each micro-cord consists of five filaments. Three of the five filaments are straight, and the remaining two filaments are wrapped around the other three with a high torque angle. The cross-sectional area of the cord A_{cord} is 0.538 mm^2 . Fiber sheets with two different densities were investigated and are referred to in this paper as medium density (MD) and high density (HD). The MD steel fiber sheets had 0.314 cords/mm, and the HD steel fiber sheets had 0.472 cords/mm. Mechanical properties of the fibers reported by the manufacturer (Kerakoll 2016) are provided in Table 6.1.

The matrix was a two-component epoxy thixotropic gel system, with high wettability for the impregnation of steel textiles. The mechanical properties of the matrix reported by the manufacturer (Kerakoll 2016) are provided in Table 6.2.

Table 6.1. Properties of steel fibers provided by manufacturer (Kerakoll S.p.A.)

Property	Medium Density	High Density
Number of Cords/mm	0.314	0.472
Tensile Strength (MPa)	>3000	> 3000
Elastic Modulus (GPa)	>190	> 190
Ultimate Strain (%)	> 2	> 2
Equivalent Thickness (mm)	≈ 0.169	≈ 0.254

Table 6.2. Mechanical properties of matrix by provided by manufacturer (Kerakoll S.p.A.)

Property	Test Method
Tensile Strength (MPa)	> 14 EN 12188
Flexural Elastic Modulus (GPa)	> 2.50 EN ISO 178
Elastic Modulus Under Compression (GPa)	> 5.30 EN 13412

6.2.2 Methods

Twenty-five specimens were tested to investigate the influence of steel-FRP confinement on the behavior of concrete prisms subjected to a concentric compressive load. All prisms had a square cross-section. The nominal dimensions of the concrete prisms were $b=150 \text{ mm} \times d=150 \text{ mm} \times L=450 \text{ mm}$. All prisms were axially unreinforced, i.e., no internal reinforcement was provided since jacket-internal reinforcement interaction was outside the scope of this study.

Twenty confined specimens were classified in seven groups. Specimens from the same group were characterized by same parameters. Specimens were named following the notation SQ-X-A-B-C-D-Y-Z, where SQ indicates a square cross-section, X indicates the confined length (h_c) in mm, i.e. the portion of the prism length wrapped with the composite material; A indicates the fiber density (MD = medium density, HD = high density); B indicates the composite matrix (UC= unconfined, CE = confined epoxy-based matrix); C denotes the concrete surface treatment (T = treated with sand-blasting, UT = untreated); D indicates the concrete corner condition (R = rounded to a radius $r=17.5 \text{ mm}$, S = sharp), Y indicates the number of confinement layers (1L or 2L), and Z = specimen number. Five specimens were unconfined and used as control specimens. The unconfined specimens were named following the notation SQ-B-C-D-Z with the parameters B, C, D, and Z defined above. The details of the specimens and test parameters are summarized in Table 6.3.

The confined prisms were wrapped following the manufacturer's recommendations. The steel-FRP was applied using a wet layup process shown in Figure 6.5. Steel fibers sheets, with fibers oriented perpendicular to the longitudinal axis of the prism, were wrapped around the concrete prisms. Since the width of the fiber sheet was not the same as the length of the prism, the prisms were wrapped with two or three segments of the fiber sheet with no overlap of the different segments. The fiber sheets were bent before wrapping so that they were able to conform to the surface (Figure 6.5). An overlap length of 150 mm, corresponding to the width of one prism face, was provided for all specimens, forming a vertical seam at the corner. Specimens were cured under ambient conditions for seven days after casting.

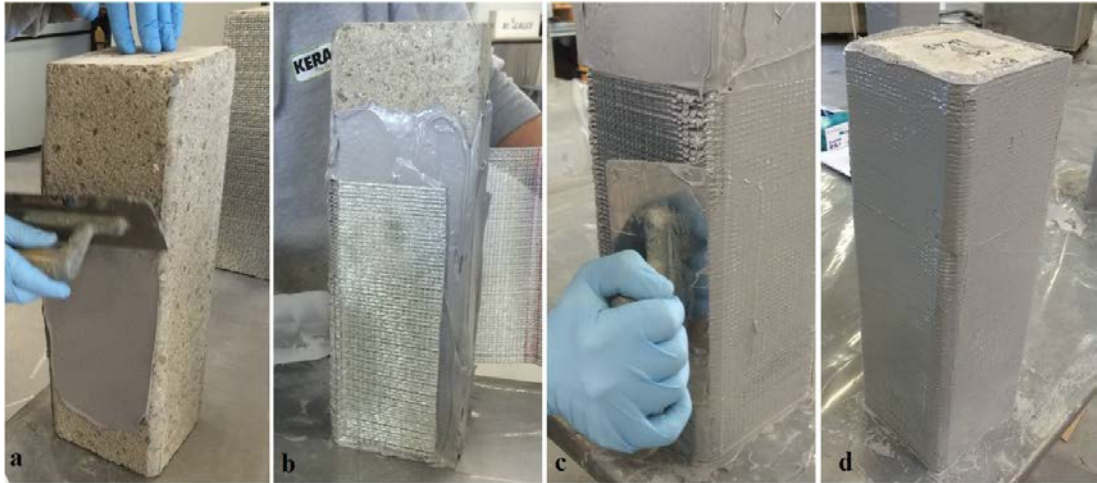


Figure 6.5. Specimen preparation: (a) application of matrix to concrete surface; (b) application of steel fiber sheet around the prism; (c) application of external layer of matrix; (d) finished specimen.

Prior to testing, both ends of each prism were capped with a 4 mm thick layer of high strength mortar to ensure that the ends were flat and parallel to one another. The compression tests were performed using a 4000 kN capacity compression testing machine. A photo of the test setup is shown in Figure 6.6(a). The specimens were tested under monotonically increasing displacement until failure. The distance between the two pressing plates was measured using two LVDTs named LVDT-a and LVDT-b mounted between the pressing plates see Figure 6.6(b). The displacement rate, determined by average value of the two LVDTs, was maintained at 0.2 mm/min by continuously monitoring and controlling the machine stroke. Testing was completed when a significant drop in load occurred in the post-peak response.

Axial strains were determined from the measurements from LVDT-a and LVDT-b. Certain specimens also included two additional LVDTs mounted directly to the specimen with bolts drilled into the concrete core (LVDT-c and LVDT-d in Figure 6.6(b)). LVDT-c and LVDT-d were oriented in the axial direction of the specimen and were located in the central third of the specimen length on opposite sides. Readings of applied load and displacement were acquired with a data acquisition system and stored on a personal computer.

For certain specimens, three-dimensional (3-D) digital image correlation (DIC) was used to analyze the displacement and strain fields on one face (front face) of the

confined prism. DIC is a non-contact measuring technique that allows for obtaining the surface displacement field. DIC mathematically correlates images of the specimen, taken during testing, that correspond to different applied load and displacement values. DIC recognizes and correlates points on the surface and computes their displacement with respect to the initial undeformed image. The surface strains are then determined as the gradients of the displacements after interpolating the displacement contours with a quintic B-spline collocation method Subramaniam et al. (2007). To enable the DIC measurements, the composite surface was covered uniformly with white nonreflective paint prior to testing. Black paint was then sprayed on the composite surface to create a speckle pattern (Figure 6.7a), which is recognized and employed by the DIC software to obtain the displacement field. During testing the specimen was illuminated with normal white light to assure uniform light intensity on the composite surface. Images were taken at a frequency of 0.1 Hz and were processed considering the origin of the Cartesian axes located at the top left edge of the specimen front face. Due to the potentially brittle nature of the failure, readings were recorded only until shortly after the peak load was achieved in order to protect the DIC equipment.

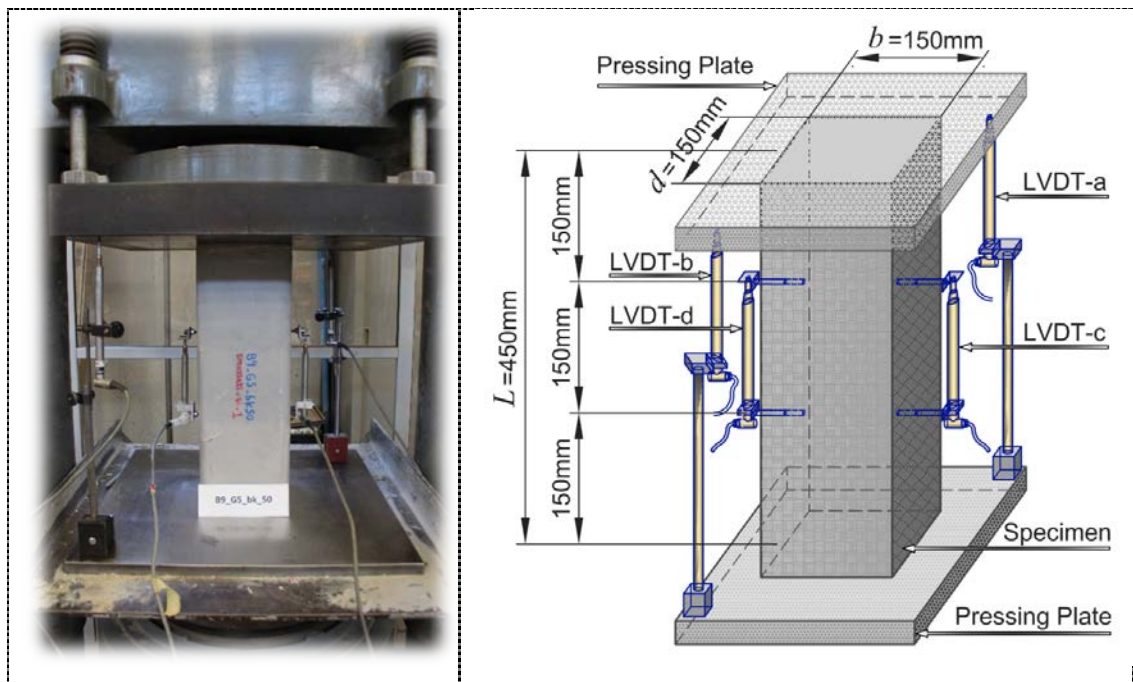


Figure 6.6. (a) Photo of specimen; (b) test setup.

Table 6.3. Test Specimen Characteristics

Group	Specimen Name	Jacket Length (mm)	Fiber Density	Surface Treatment	Corner		Instrumentation			
					Edge Type	Radius (mm)	LVDT-a and LVDT-b	LVDT-c and LVDT-d	DIC	
Control	SQ-UC-UT-S-1	-	-	None	Sharp	0	✓	✗	✗	
	SQ-UC-UT-S-2	-	-	None	Sharp	0	✓	✗	✗	
	SQ-UC-UT-S-3	-	-	None	Sharp	0	✓	✗	✗	
	SQ-UC-UT-S-4	-	-	None	Sharp	0	✓	✗	✗	
	SQ-UC-UT-S-5	-	-	None	Sharp	0	✓	✗	✗	
FRP-Confined	Group 1	SQ-450-HD-CE-UT-R-1L-1	450	High Density	None	Rounded	17.5	✓	✓	✓
		SQ-450-HD-CE-UT-R-1L-2	450	High Density	None	Rounded	17.5	✓	✓	✓
		SQ-450-HD-CE-UT-R-1L-3	450	High Density	None	Rounded	17.5	✓	✓	✓
	Group 2	SQ-450-HD-CE-UT-S-1L-1	450	High Density	None	Sharp	0	✓	✓	✓
		SQ-450-HD-CE-UT-S-1L-2	450	High Density	None	Sharp	0	✓	✓	✓
		SQ-450-HD-CE-UT-S-1L-3	450	High Density	None	Sharp	0	✓	✓	✓
		SQ-450-HD-CE-UT-S-1L-4	450	High Density	None	Sharp	0	✓	✗	✗
	Group 3	SQ-450-HD-CE-T-R-1L-1	450	High Density	Light Sand-Blasting	Rounded	17.5	✓	✓	✓
		SQ-450-HD-CE-T-R-1L-2	450	High Density	Light Sand-Blasting	Rounded	17.5	✓	✓	✓
		SQ-450-HD-CE-T-R-1L-3	450	High Density	Light Sand-Blasting	Rounded	17.5	✓	✓	✗
	Group 4	SQ-450-MD-CE-T-R-1L-1	450	Medium Density	Light Sand-Blasting	Rounded	17.5	✓	✓	✓
		SQ-450-MD-CE-T-R-1L-2	450	Medium Density	Light Sand-Blasting	Rounded	17.5	✓	✓	✓
		SQ-450-MD-CE-T-R-1L-3	450	Medium Density	Light Sand-Blasting	Rounded	17.5	✓	✓	✓
	Group 5	SQ-450-MD-CE-T-S-1L-1	450	Medium Density	Light Sand-Blasting	Sharp	0	✓	✓	✓
		SQ-450-MD-CE-T-S-1L-2	450	Medium Density	Light Sand-Blasting	Sharp	0	✓	✓	✓
		SQ-450-MD-CE-T-S-1L-3	450	Medium Density	Light Sand-Blasting	Sharp	0	✓	✓	✓
	Group 6	SQ-440-MD-CE-T-S-1L-1	440	Medium Density	Light Sand-Blasting	Sharp	0	✓	✓	✓
		SQ-440-MD-CE-T-S-1L-2	440	Medium Density	Light Sand-Blasting	Sharp	0	✓	✓	✓
	Group 7	SQ-450-MD-CE-T-S-2L-1	450	Medium Density	Light Sand-Blasting	Sharp	0	✓	✓	✓
		SQ-450-MD-CE-T-S-2L-2	450	Medium Density	Light Sand-Blasting	Sharp	0	✓	✓	✓

6.3 Results

6.3.1 Failure mode, Compressive strength, and Ultimate strain

The peak load of all unconfined and confined specimens was associated with crushing of concrete. After the peak load was achieved, the confined specimens continued to deform under decreasing applied load until failure occurred by separation of the FRP jacket at the vertical lap joint. For some confined specimens with MD steel fibers, namely specimens SQ-450-MD-CE-T-R-1L-1, SQ-450-MD-CE-T-S-1L-1 and SQ-450-MD-CE-T-S-1L-2, the opening of the FRP jacket was preceded by the rupture of some steel fibers near the corners. Failure was generally sudden but preceded by noises associated with cracking of the epoxy in the composite matrix. For most confined specimens, failure initiated near the middle third of the specimen length, and the FRP jacket was completely opened with transverse cracks (parallel to the fiber direction) that extended from the failed face to other faces of the specimen. Some of the transverse cracks were consistent with the locations where different steel fiber sheet segments abutted one another. Detachment of the overlapping layer of the jacket occurred along a limited portion of the specimen length. For several specimens, failure started in the layer of epoxy in between the two overlapping layers, and both layers of fibers opened with the internal layer having some concrete from the substrate attached. Photographs of a typical failed specimen are shown in Figure 6.7.

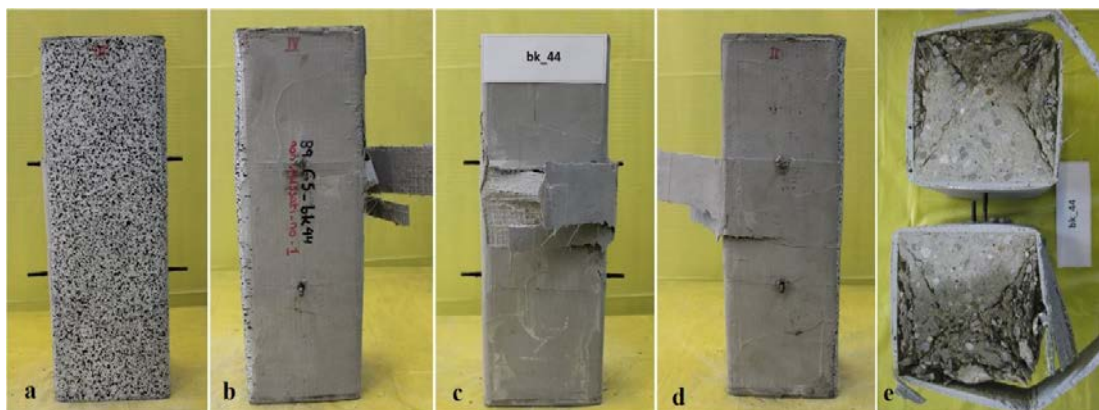


Figure 6.7. Failure mode of steel-FRP confined specimen (specimen SQ-450-HD-CE-UT-S-1L-1 shown): (a) front face; (b) right face; (c) back face; (d) left face; (e) cut section.

In some specimens, propagation of transverse cracks in the FRP jacket was observed near the bolts where LVDT-c and LVDT-d were mounted. Specimens SQ-450-HD-CE-UT-R-1L-1, SQ-450-HD-CE-UT-R-1L-3, and SQ-450-HD-CE-UT-S-1L-3 had LVDT-c and LVDT-d mounted on the face with the overlapping layer, and at failure the bolts were separated completely from specimens. Readings from LVDT-c and LVDT-d were also compromised for several specimens after the peak load was reached.

After testing, the conditions of the concrete core and jacket were documented. Crushed concrete was observed near the side surfaces of each specimen. For specimens with complete opening of the jacket, the steel-FRP sheets were observed to have pieces of concrete attached. Each specimen was sawcut near the midlength to observe the condition of the concrete cross-section. The typical conical shape of the cross-section was observed. Additional discussion on the crack patterns observed at the cross-section is presented in Section 6.4.3.

Table 6.4 summarizes the key experimental results obtained for each test specimen. Values provided for the unconfined specimens include the unconfined compressive strength (peak stress) f'_{co} , the unconfined ultimate compressive stress $f'_{co,u}$, and the corresponding values of strain ε_{co} and $\varepsilon_{co,u}$, respectively. Values provided for the confined specimens include the confined compressive strength (peak stress) f'_{cc} , the confined ultimate compressive stress $f'_{cc,u}$, and the corresponding values of strain ε_{cc} and $\varepsilon_{cc,u}$, respectively. Values of the ultimate stress and ultimate strain correspond to the stress and strain at which a significant drop in load occurred in the post-peak load response and are associated with specimen failure as discussed above. Values of stress were determined by dividing the force by the cross-sectional area of the prism (22,500 mm² and 22,237 mm² for specimens with sharp and rounded corners, respectively). Values of strain were determined by dividing the average of displacement readings from LVDT-a and LVDT-b by the initial distance between the pressing plates. Accordingly, the values of strain determined in this manner are considered to be *global* strain.

For reference, the control specimens had an average unconfined compressive strength $\overline{f'_{co}}$ of 26.0 MPa and an average compressive strain at peak load $\overline{\varepsilon_{co}}$ of

0.0030. Values of the ratios f'_{cc}/f'_{co} and $\varepsilon_{cc,u}/\varepsilon_{co}$ are provided in Table 4 for each confined specimen. Average values of the ratios f'_{cc}/f'_{co} and $\varepsilon_{cc,u}/\varepsilon_{co}$, along with the corresponding coefficient of variation (CoV), are also reported for each of the confined specimen groups. Results in Table 6.4 indicate that the steel-FRP confinement improves the strength and the ultimate strain of specimens relative to the unconfined condition. Group average values of f'_{cc}/f'_{co} ranged from 1.18 to 1.50, with the largest value obtained from specimens of Group 2, with prisms with sharp corners. Group average values of $\varepsilon_{cc,u}/\varepsilon_{co}$ ranged from 4.73 to 8.86, with the largest value obtained from specimens from Group 7, with two layers of confinement.

Table 6.4. Summary of Test Results

Group	Specimen	f'_{co} or f'_{cc}	$f'_{co,u}$ or f'_{ccu}	$\frac{f'_{cc}}{f'_{co}}$	Avg [CoV]	ϵ_{co} or ϵ_{cc}	$\epsilon_{co,u}$ or ϵ_{ccu}	$\frac{\epsilon_{cc,u}}{\epsilon_{co}}$	Avg [CoV]	A_{peak}	A_{total}	
	Name											(MPa)
Control	SQ-UC-UT-S-1	28.9	13.6	-	-	0.0034	0.0049	-	-	-	-	
	SQ-UC-UT-S-2	24.1	19.1	-		0.0032	0.0043	-		-	-	
	SQ-UC-UT-S-3	27.6	21.0	-		0.0029	0.0054	-		-	-	
	SQ-UC-UT-S-4	25.8	20.5	-		0.0028	0.0033	-		-	-	
	SQ-UC-UT-S-5	23.4	21.0	-		0.0027	0.0026	-		-	-	
Steel-FRP Confined	Group 1	SQ-450-HD-CE-UT-R-1L-1	34.9	31.0	1.35	1.39 [0.033]	0.0044	0.0111	3.72	4.73 [0.255]	0.103	0.324
		SQ-450-HD-CE-UT-R-1L-2	35.8	31.4	1.38		0.0048	0.0182	6.07		0.112	0.539
		SQ-450-HD-CE-UT-R-1L-3	37.3	31.1	1.44		0.0048	0.0132	4.42		0.121	0.409
	Group 2	SQ-450-HD-CE-UT-S-1L-1	38.2	34.0	1.47	1.50 [0.018]	0.0048	0.0113	3.77	5.13 [0.201]	0.134	0.365
		SQ-450-HD-CE-UT-S-1L-2	39.8	33.9	1.53		0.0055	0.0155	5.18		0.150	0.503
		SQ-450-HD-CE-UT-S-1L-3	38.6	33.1	1.49		0.0055	0.0188	6.26		0.163	0.614
		SQ-450-HD-CE-UT-S-1L-4	39.3	31.4	1.51		0.0056	0.0160	5.33		0.160	0.514
	Group 3	SQ-450-HD-CE-T-R-1L-1	37.4	30.3	1.44	1.46 [0.011]	0.0054	0.0135	4.50	4.88 [0.352]	0.150	0.408
		SQ-450-HD-CE-T-R-1L-2	37.8	32.1	1.46		0.0045	0.0203	6.76		0.135	0.626
		SQ-450-HD-CE-T-R-1L-3	38.3	33.3	1.47		0.0059	0.0102	3.39		0.155	0.314
	Group 4	SQ-450-MD-CE-T-R-1L-1	36.6	24.4	1.41	1.40 [0.018]	0.0053	0.0221	7.36	5.45 [0.302]	0.145	0.605
		SQ-450-MD-CE-T-R-1L-2	35.5	27.5	1.37		0.0046	0.0134	4.47		0.123	0.379
		SQ-450-MD-CE-T-R-1L-3	36.7	27.0	1.41		0.0058	0.0136	4.53		0.137	0.390
	Group 5	SQ-450-MD-CE-T-S-1L-1	33.4	22.5	1.29	1.31 [0.021]	0.0054	0.0202	6.73	5.53 [0.215]	0.135	0.522
		SQ-450-MD-CE-T-S-1L-2	34.8	24.0	1.34		0.0045	0.0130	4.35		0.116	0.358
SQ-450-MD-CE-T-S-1L-3		33.7	23.1	1.30	0.0052		0.0165	5.50	0.137		0.445	
Group 6	SQ-440-MD-CE-T-S-1L-1	31.0	22.3	1.19	1.18 [0.021]	0.0044	0.0210	7.00	6.68 [0.069]	0.115	0.491	
	SQ-440-MD-CE-T-S-1L-2	30.1	23.4	1.16		0.0055	0.0191	6.35		0.156	0.688	
Group 7	SQ-450-MD-CE-T-S-2L-1	38.3	37.6	1.48	1.45 [0.026]	0.0064	0.0246	8.22	8.86 [0.103]	0.185	0.862	
	SQ-450-MD-CE-T-S-2L-2	36.9	37.1	1.42		0.0062	0.0285	9.51		0.171	0.996	

6.3.2 Axial stress – Axial strain response

As mentioned in Section 6.2.2, LVDT-a and LVDT-b measured the displacement between the pressing plates, while LVDT-c and LVDT-d measured the axial displacement of the middle third of the specimen. Figure 6.8 shows the axial stress – axial strain response, determined by each individual LVDT, of representative specimens SQ-450-MD-CE-T-S-1L-2 (Figure 6.8a) and SQ-450-HD-CE-UT-S-1L-3 (Figure 6.8b). The graphs in Figure 6.8 show that the strain determined by the individual LVDTs was consistent until the peak stress was achieved, and then the strain determined by LVDT-c and LVDT-d differed from values determined by LVDT-a and LVDT-b. The difference was more significant for specimen SQ-450-HD-CE-UT-S-1L-3 (Figure 6.8b) than for specimen SQ-450-MD-CE-T-S-1L-2 (Figure 8a). This difference in strains determined by the different LVDT pairs is due to localized effects at the location of the LVDTs mounted directly to the specimen, which compromised the measurements after the peak stress was achieved. In the remainder of the axial stress – axial strain plots in this paper, readings from LVDT-a and LVDT-b are used to determine the axial strain from the average of the two readings.

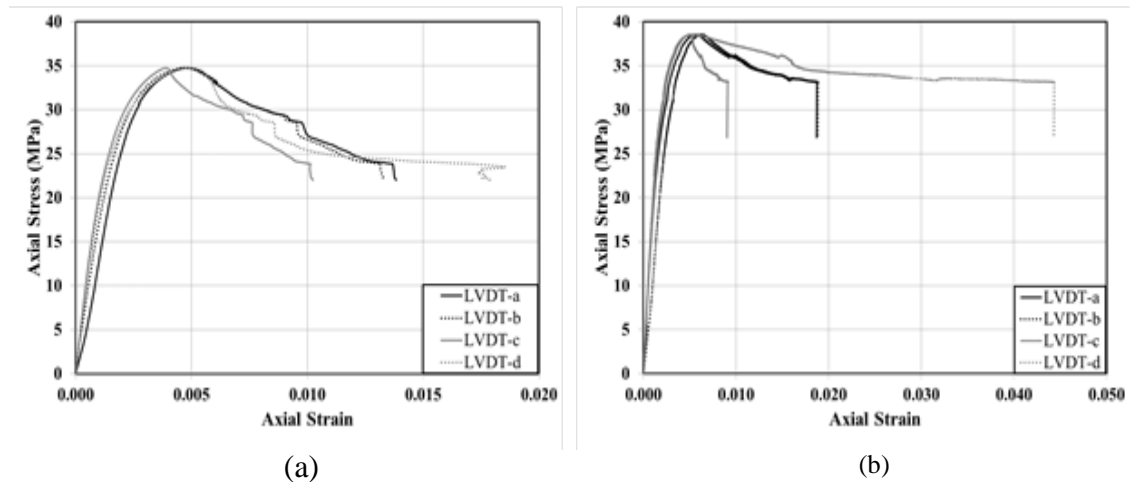
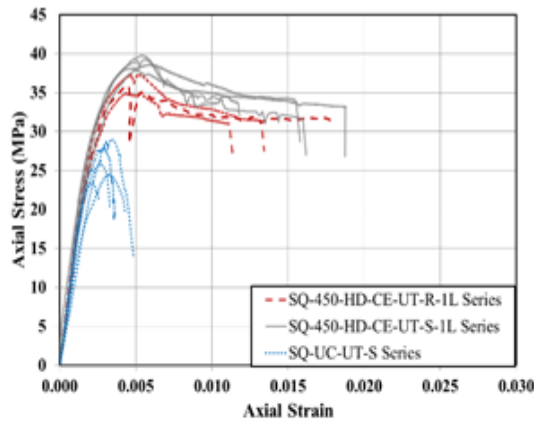
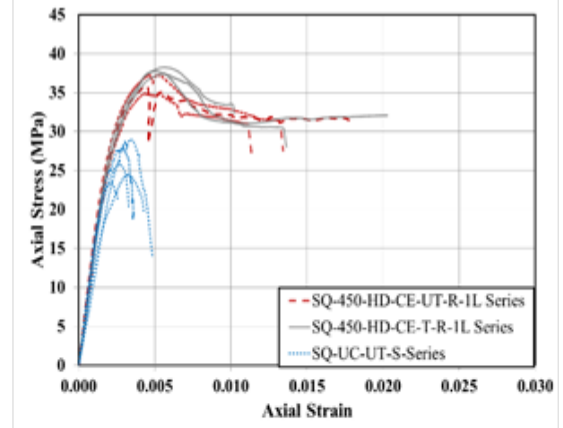


Figure 6.8. Axial stress - axial strain response determined by each LVDT for representative specimens: (a) SQ-450-MD-CE-T-S-1L-2; (b) SQ-450-HD-CE-UT-S-1L-3.

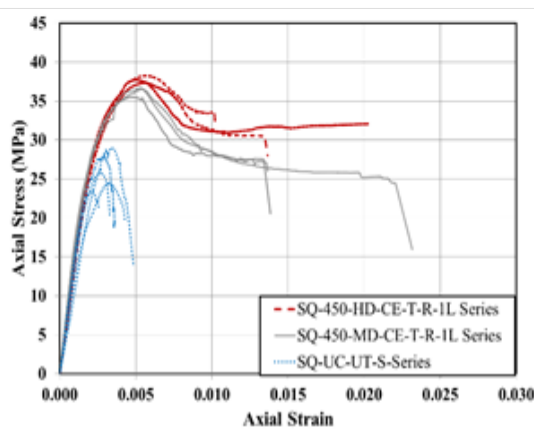
In Figure 6.9, the axial stress – axial strain responses of confined specimens from different groups are plotted and compared to illustrate the effect of a particular test parameter. The unconfined (control) specimens are also plotted in each graph for comparison. The general behavior of the steel-FRP confined specimens can be described as having an initial linear response that follows the unconfined behavior. After the unconfined strength is reached, the response of the steel-FRP specimens becomes non-linear, and the axial stress continues to increase until the peak stress is reached. Then for most specimens, a descending response is observed until failure occurs with a sudden drop in the axial stress, where failure is associated with jacket opening as discussed in Section 6.3.1. Influence of the test variables is further discussed in Section 6.4.1.



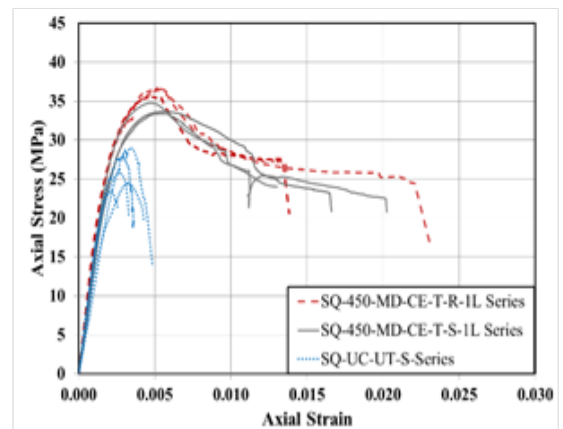
a. Groups 1 and 2



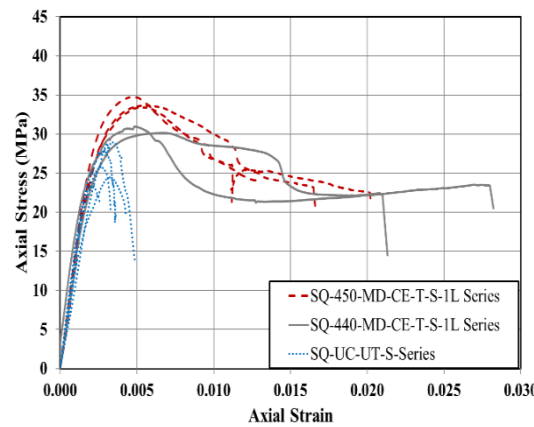
b. Groups 1 and 3



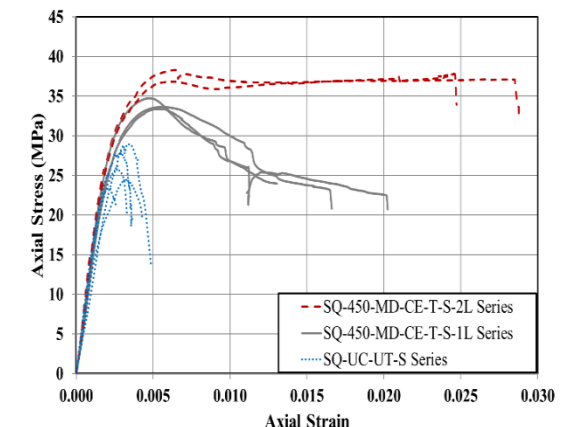
c. Groups 3 and 4



d. Groups 4 and 5



e. Groups 5 and 6



f. Groups 5 and 7

Figure 6.9. Axial stress – axial strain response for specimens in: a) Groups 1 and 2; b) Groups 1 and 3; c) Groups 3 and 4; d) Groups 4 and 5; e) Groups 5 and 6; f) Groups 5 and 7.

6.3.3 Steel-FRP jacket strains

Axial and hoop strains in the composite of confined concrete specimens can be highly variable due to the location and progression of concrete cracks. In this study, DIC was used to examine the strain field on the surface of the composite in the axial and hoop (fiber) directions. As discussed in Section 6.2.2, DIC readings were recorded only until shortly after the peak load was achieved, so the DIC results presented in this section do not include the post-peak response.

Displacements and strains were obtained for different square areas (subsets) for a 5 pixel step size, which provided points spaced at approximately 1.25 mm. Different subsets of 21, 31, and 41 pixels were used to study the influence of subset dimensions on the results obtained. Figure 6.10 shows the axial stress – axial strain response of specimen SQ-450-HD-CE-T-R-1L-1 in which axial strain was determined by DIC for the three subsets. Results determined using different subsets are similar, therefore a subset size of 31 pixels (approximately 3.40 mm) edge was employed for the remainder of the specimens.

In order to employ the DIC results, the strain values obtained by DIC and plotted in Figure 6.10 were determined considering strain values in eight squares in the central third of the specimen length. Each square had a side equal to 30 mm, and the horizontal and vertical spacing between adjacent squares was 30 mm and 10 mm, respectively, as shown in Figure 6.11. The strain determined by DIC was obtained by averaging the strains within these eight squares. Figure 10 also shows values of axial strain determined from measurements by LVDT-a and LVDT-b for comparison. Values of strain determined by DIC and the LVDTs are similar, with slight differences attributed to several factors. First, DIC and LVDT measurements were taken at different locations, i.e., DIC values were determined on the composite face, whereas LVDT measurements were taken outside the specimen on the pressing plates at opposite corners. Second, as explained above, values determined by DIC derive from an average of the strains in different locations of the specimen face.

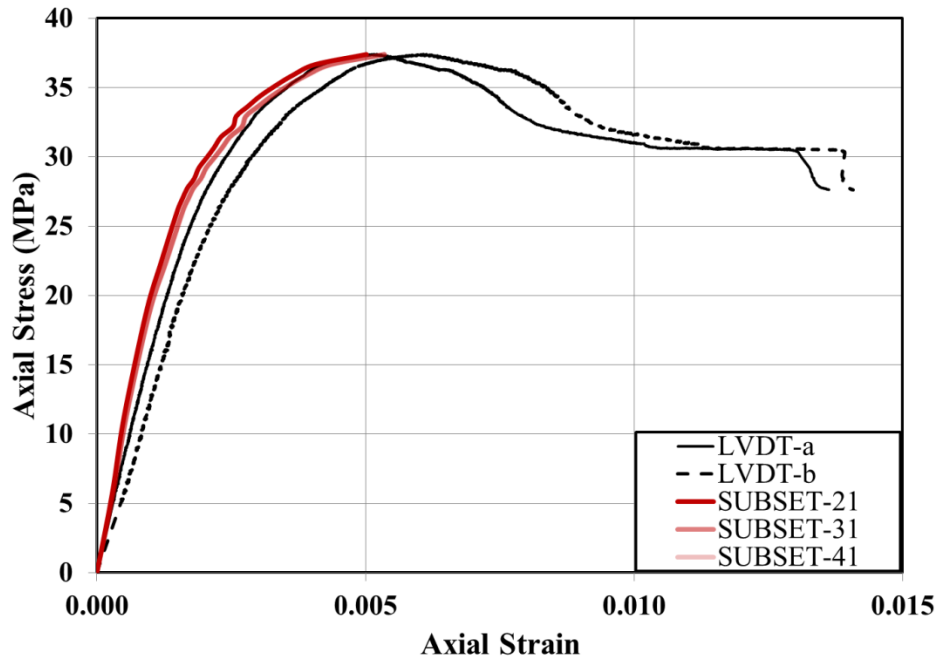


Figure 6.10: Comparison of axial stress – axial strain response determined by LVDTs and DIC (specimen SQ-450-HD-CE-T-R-1L-1).

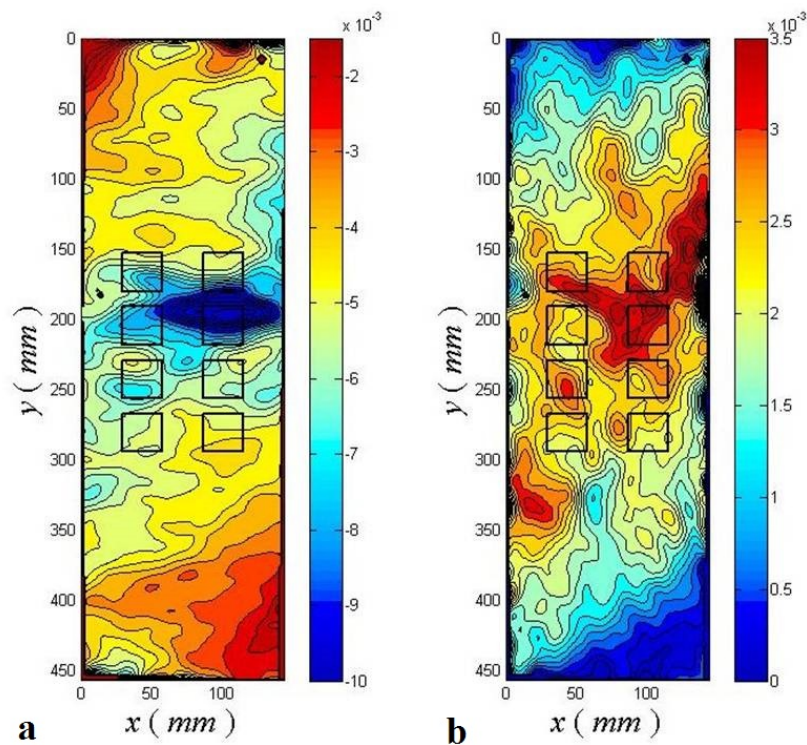


Figure 6.11. Representation of the eight squares used to calculate the values of the strain using DIC technique: (a) axial strain; (b) hoop strain.

Figure 6.12 shows the axial stress versus hoop and axial strain response of each confined specimen determined by DIC considering strain values in eight squares in the central third of the specimen length as described above. Specimens SQ-450-HD-CE-UT-S-1L-4 and SQ-450-HD-CE-T-R-1L-3 from Groups 2 and 3, respectively, are not shown in the graphs since DIC was not used for those specimens. Values of hoop strain at the peak stress were less than the fiber ultimate strain (0.02, Table 6.1) for all specimens.

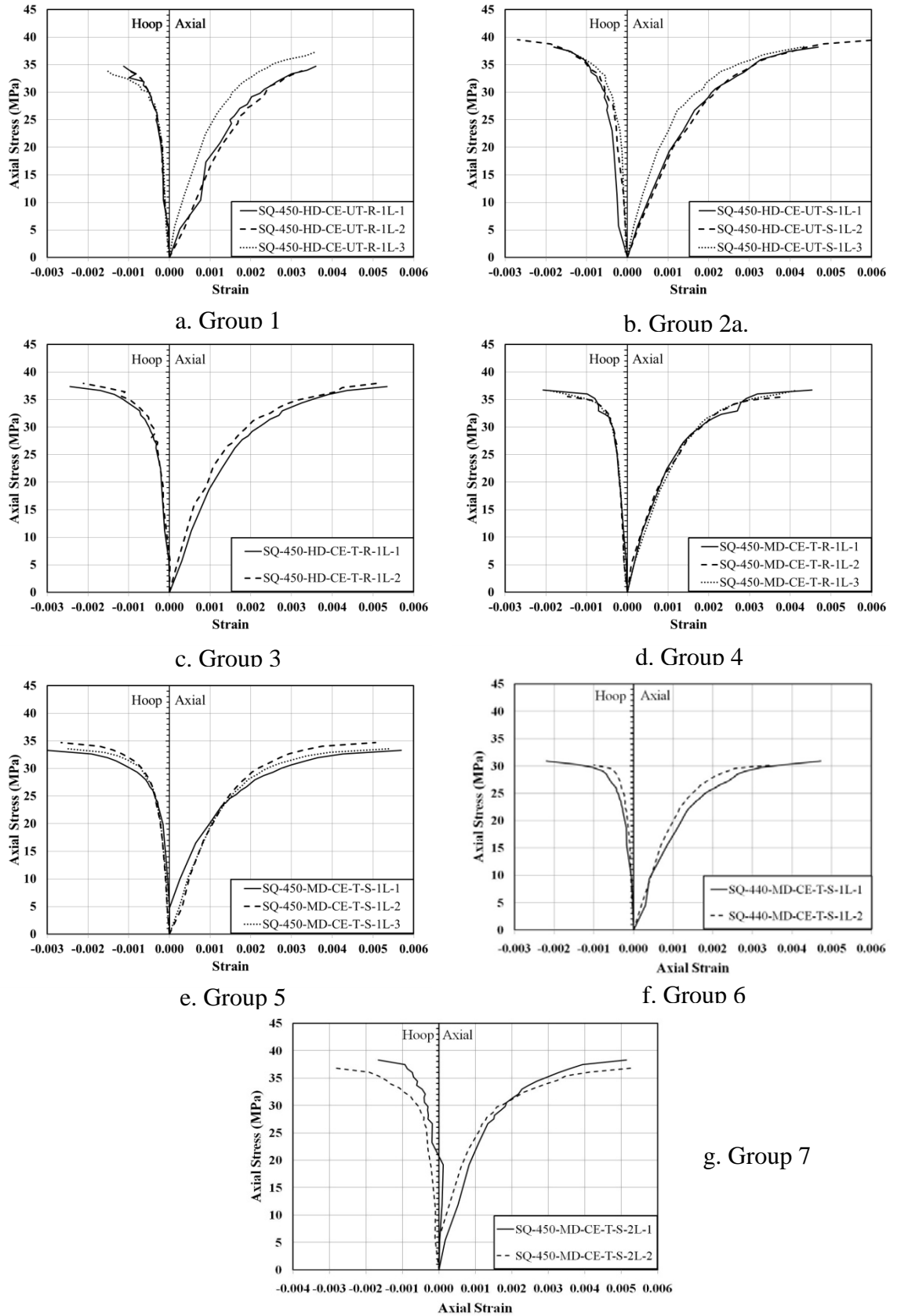


Figure 6.12. Axial stress – strain response determined by DIC for confined specimens: (a) Group 1; (b) Group 2; (c) Group 3; (d) Group 4; (e) Group 5; (f) Group 6; (g) Group 7.

6.4 Discussion

6.4.1 Influence of test variables

The influence of corner condition is examined by comparing the results of specimens in Groups 1 and 2, and specimens in Groups 4 and 5. The axial stress – axial strain response of specimens in Groups 1 and 2, which had high density fibers and an untreated surface but different corner conditions (rounded vs. sharp, Groups 1 and 2, respectively), is shown in Figure 6.9a. Specimens with sharp corners consistently had higher compressive strength f'_{cc} (average of 8%) and ultimate strain $\epsilon_{cc,u}$ (average of 8%) than those with corners rounded to a radius of 17.5 mm. Hoop strains at the peak load were also larger for specimens in Group 2 compared with those of Group 1, as shown in Figures 6.12a and 6.12b, which indicates a larger participation by the jacket. Further discussion on this test variable is included in Section 6.4.3.

Figure 6.9d compares the axial stress – axial strain response of specimens in Groups 4 and 5, which had medium density fibers and a treated surface but different corner conditions (rounded vs. sharp, Groups 4 and 5, respectively). Contrary to the results of Groups 1 and 2 with high density fibers, specimens with rounded corners had higher compressive strength than those with sharp corners. The different behavior can be partially explained considering the different types of failure obtained for specimen with medium density steel fibers, i.e., fiber rupture before jacket opening for specimens SQ-450-MD-CE-T-R-1L-1, SQ-450-MD-CE-T-S-1L-1 and SQ-450-MD-CE-T-S-1L-2 (Section 4.1). Values of compressive strength for Group 4 were approximately 7% larger than those of Group 5, whereas values of ultimate strain were approximately the same (Table 6.4). Hoop strains at peak load were lower for specimens in Group 4 compared with those of Group 5 (Figures 6.12d and 6.12e).

The influence of concrete surface treatment is examined by comparing the results of Groups 1 and 3. Figure 6.9b shows that Group 3 specimens with a sandblasted surface had higher compressive strength and ultimate strain than Group 1 specimens with no surface treatment. This increase can be attributed to better adhesion between

the composite material and the concrete substrate. Hoop strains at the peak load were also larger for specimens in Group 3 compared with those of Group 1, as shown in Figures 6.12c and 6.12a, which indicates a larger participation by the jacket for the sandblasted specimens.

The influence of fiber density is examined by comparing the results of Groups 3 and 4, with high and medium density fibers, respectively. Figure 6.9c shows that specimens reinforced with high density fibers (Group 3) had slightly higher compressive strength (average of 4%) than specimens reinforced with medium fibers (Group 4). On the other hand, the ultimate strain (Figure 6.9c) and the hoop strain at peak stress (Figures 6.12c and 6.12d) are approximately the same irrespective of fiber density. These results suggest that the increase in confined strength is not proportional to the fiber density.

The influence of jacket length is examined by comparing specimens in Groups 5 and 6. Figure 9e compares the response of specimens with a full length jacket ($h_c=450$ mm, Group 5) and those with a partial length jacket ($h_c=440$ mm, Group 6). As expected, Specimens in Group 5 had higher compressive strength than those in Group 6. Values of compressive strength for specimens in Group 5 were approximately 11% larger than those of Group 6. Hoop strains at the peak load were also larger for specimens in Group 5 compared with those of Group 6, as shown in Figures 6.12e and 6.12f. On the other hand, values of the ultimate strain for Group 5 specimens were approximately 17% lower than those of Group 6 (Table 6.4). It is possible that the increased ultimate strain for specimens with a partial length jacket is due to localized deformation of the unconfined concrete outside the jacket at the specimen ends. As noted in Section 6.3.1, values of axial strain are global values considering the entire specimen length.

The influence of the number of jacket layers is examined by comparing the results of specimens in Groups 5 and 7, with one and two layers, respectively. Specimens in Group 7 had compressive strengths higher than those in Group 5. Values of compressive strength for specimens in Group 7, with two layers of confinement, were approximately 11% larger than those of Group 5, with one layer of confinement. Similarly, values of ultimate strain for the Group 7 specimens were

approximately 60% larger than those of Group 5 (Table 4). Hoop strains at the peak load were similar for specimens in Group 7 compared with those of Group 5, as shown in Figures 12g and 12e. These results suggest that increasing the number of jacket layers increases both the axial strength and the deformability, however the increase in axial strength is not proportional to the number of jacket layers. Additional discussion is provided in Section 6.4.2.

6.4.2 Ductility

Ductility can be characterized by the area under the axial stress – axial strain curve Rochette and Labossiere (2000). As mentioned in Section 6.3.1, failure of the confined specimens in this study was mostly associated with opening of the jacket. Accordingly, the post-peak response and the corresponding area under the axial stress-axial strain curve in the post-peak region are related both to the strain in the concrete and debonding of the composite. Since the jacket overlap length was the same for all specimens, it is reasonable to assume that the bond behavior of specimens with the same fiber density should be similar and comparable.

Although the post-peak response of the confined specimens was a softening behavior, the post-peak axial deformability is compared in this section. In this study, the total area under the curve A_{total} up to the ultimate strain and corresponding stress was compared to the area under the curve A_{peak} up to the peak stress and corresponding strain. Values of A_{peak} and A_{total} are reported in Table 6.4 for each confined specimen.

The ratio A_{total}/A_{peak} provides information on the strain reserve after the peak stress is reached. Figure 6.13 compares the average value of A_{total}/A_{peak} for each group. Specimens in Groups 1 through 5 had average values of A_{total}/A_{peak} in the range of 3.0-4.0. The average value for specimens in Group 6 was slightly larger (between 4.0 and 4.5), even though the steel-FRP jacket was not full length. This may be due to the additional deformability of the unconfined regions at the specimen ends, as noted in Section 6.4.1. Specimens in Group 7, which was the only group with two layers of fibers, had an average value that exceeded 5.0. This shows that the ductility increases

with increasing composite stiffness, as noted by Rochette and Labossiere (2000). Thus, although two layers of fiber sheets did not significantly improve the strength of the specimen, it did improve the deformability.

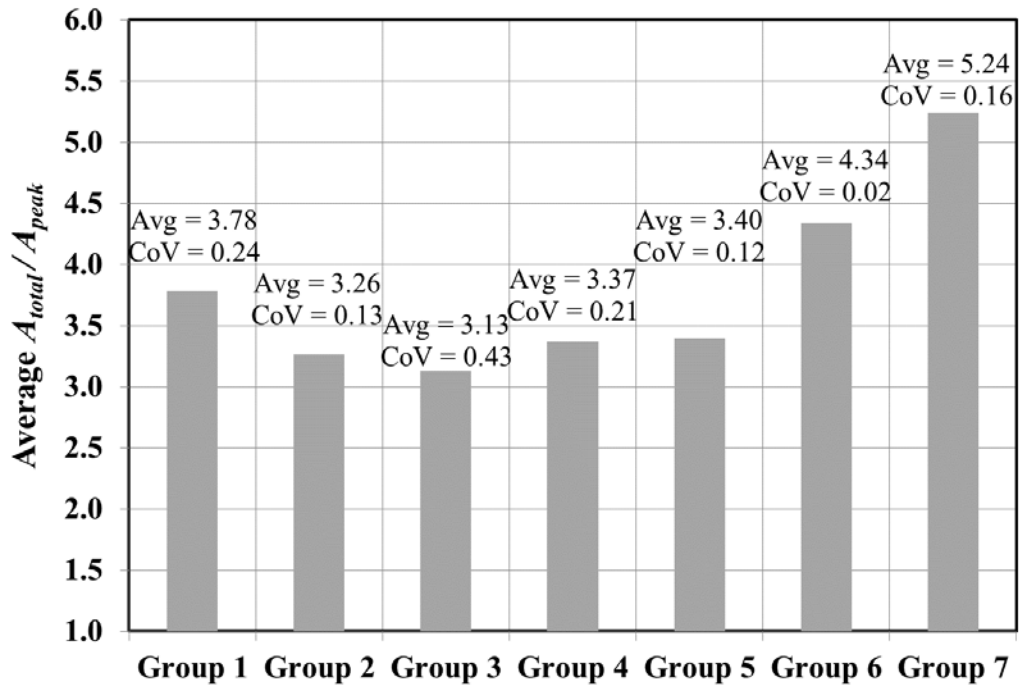


Figure 6.13. Average A_{total}/A_{peak} for each group.

6.4.3 Fracture surface of cross-section

As mentioned in Section 6.3.1, the specimens were sawcut in the plane of the cross-section near the specimen midlength after testing to study the condition of the concrete. In general, the concrete was observed to be crushed near the confinement layer, and the arching effect could be observed by the formation of parabolic zones of crushing that formed along the four side faces of the specimen. Figure 6.14 shows the cut section of specimen SQ-450-HD-CE-UT-S-1L-1, with sharp corners, and specimen SQ-450-HD-CE-UT-R-1L-3, with corners rounded to a radius of 17.5 mm. For each cross-section, the height of the parabola was measured at each of the four sides, and the average height was determined for each specimen. For specimens with the same cross-sectional dimensions, an increase in parabola height corresponds to an increase in parabola length. It was observed that the average height (and therefore

length) of the parabola was larger for specimens with sharp corners than those with rounded corners. The significance of this observation can be examined from a fracture mechanics point of view. The profile of the parabola reflects the crack propagation, therefore a longer profile of this crack corresponds to a larger amount of energy needed to open it. Hence, higher values of the compressive strength for confined prisms are related to longer profiles of the parabola in the cross-section areas, as confirmed by the experimental results.

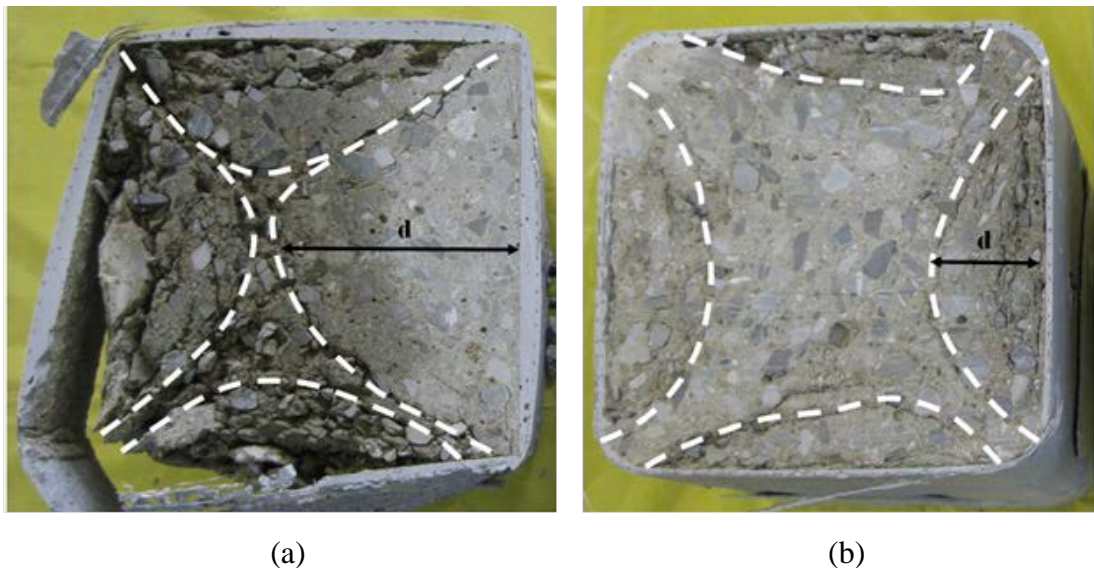
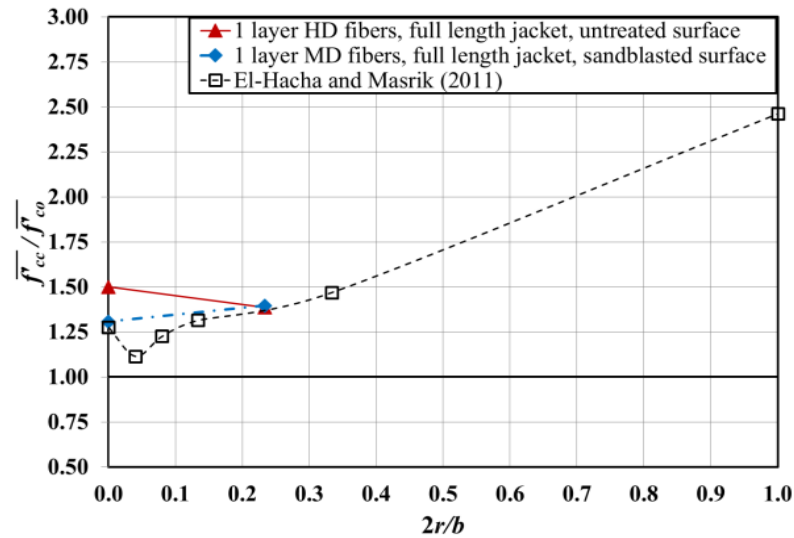


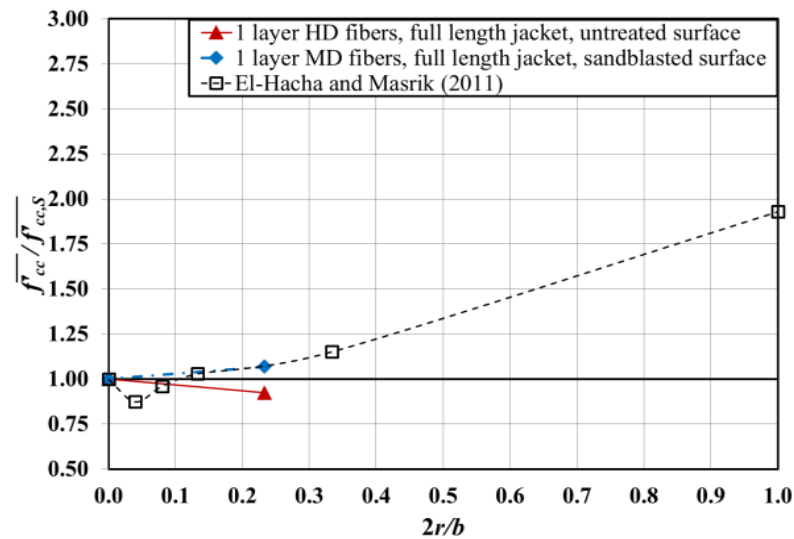
Figure 6.14. Photos of cut cross-sections after failure:
 (a) SQ-450-HD-CE-UT-S-1L-1; (b) SQ-450-HD-CE-UT-R-1L-3.

In the study by El-Hacha and Mashrik (2012), steel-FRP confined concrete prisms with a square cross-section were tested with different corner radii, with specimens ranging from $r=0$ (sharp) to $r=b/2$ (corresponding to a circular cross-section). Figure 6.15 compares the results of the Groups 1 and 2 specimens from the present study with those from the El-Hacha and Maskrik study in terms of the corner radius ratio, $2r/b$. Figure 6.15a plots the results in terms of the ratio of the average confined strength to the average unconfined strength, $\overline{f'_{cc}}/f'_{co}$, whereas Figure 6.15b plots the results in terms of the ratio of the average confined strength relative to the average confined strength of the confined specimen with sharp corners, $\overline{f'_{cc}}/f'_{cc,S}$. Test

results from both studies show that particular values of the ratio $2r/b$ correspond to compressive strengths that are lower than those of specimens with a sharp corner condition (i.e., $2r/b=0$). The authors postulate that this is the result of the arching effect described above, and that the range of corner radius ratio values for which this effect is observed may be a function of the stiffness of the fiber investigated. More work is needed to study this issue.



(a)



(b)

Figure 6.15. Variation of the ratio: a) $\overline{f'_{cc}}/f'_{co}$; and b) $f'_{cc}/f'_{cc,S}$

with respect to corner radius ratio $2r/b$

6.5 Conclusions

This work presented the experimental results of short concrete prisms confined with steel-FRP composite. Test variables included fiber density, concrete surface treatment, corner condition, jacket length, and number of jacket layers. Digital image correlation (DIC) is used to study qualitatively and quantitatively the displacement and strain fields on one face of the composite. Based on the results of this study, the following conclusions can be made:

1. The peak load of all unconfined and confined specimens was associated with crushing of concrete. After the peak load was achieved, the confined specimens continued to deform under decreasing applied load until failure occurred by separation of the FRP jacket at the vertical lap joint.
2. Steel-FRP confinement improved the strength and the ultimate strain of specimens relative to the unconfined condition. Group average values of f'_{cc}/f'_{co} ranged from 1.18 to 1.50, with the largest value obtained from specimens of Group 2, with prisms with sharp corners. Group average values of $\epsilon_{cc,u}/\epsilon_{co}$ ranged from 4.73 to 8.86, with the largest value obtained from specimens of Group 7, with two layers of confinement.
3. Concrete surface treatment increased the confined compressive strength.
4. Increases in fiber density were not proportional to increases in confined compressive strength.
5. Full-length jackets were more effective in increasing the confined compressive strength than partial length jackets.
6. Increasing the number of jacket layers from one to two did not increase the confined concrete strength significantly, but it did increase the deformability.
7. Specimens confined with high density fibers and having a sharp corner condition had a larger confined compressive strength than those with a rounded corner condition. This was attributed to the arching effect observed by the formation of parabolic zones of crushing that formed along the four side faces of the specimens. Values of corner radius ratio $2r/b$ for which this effect is observed may be a function of the stiffness of the fiber investigated. More work is needed to study this issue.

6.6 References

- Barton B., Wobbe E., Dharani L.R., Silva P., Birman V., Nanni A., et al. (2005). "Characterization of reinforced concrete beams strengthened by steel reinforced polymer and grout (SRP and SRG) composites." *Mater Sci Eng A*; 412(1–2):129–36.
- Campione, G., Miraglia, N. (2001). "Strength and Strain Capacities of Concrete Compression Members Reinforced with FRP." *Cement and Concrete Composites*, 25(1), 31-41.
- Casadei P., Nanni A., Alkhrdaji T., Thomas J. (2005). "Performance of double-t prestressed concrete beams strengthened with steel reinforced polymer." *Adv Struct Eng*; 8(4):427–42.
- Ceroni F, Pecce M. (2007). "Cracking behaviour of RC beams externally strengthened with emerging materials." *Constr Build Mater*; 21:736–45.
- De Lorenzis, L., Tepfers, R. (2003). "Comparative Study of Models on Confinement of Concrete Cylinders with Fiber-Reinforced Polymer Composites." *J. Compos. Constr.*, 7(3), 219-237.
- EN 12390-3. (2009). "Testing hardened concrete – Part 3: Compressive strength of test specimens", European Committee for Standardization, Brussels, Belgium.
- EN 12390-5. (2009). "Testing hardened concrete – Part 5: Flexural strength of test specimens", European Committee for Standardization, Brussels, Belgium.
- El-Hacha, R., Mashrik, M.A. (2012). "Effect of SFRP Confinement on Circular and Square Concrete Columns." *Eng Struct*, 36, 379-393.
- Elices, M., Guinea, G. V., Planas, J. (1992). "Measurement of the fracture energy using three-point bend tests: Part 3—influence of cutting the P- δ tail." *Materials and Structures*, 25(6), 327-334.
- Hawileh R., Abdalla J., Nawaz W., Alzeer A., Muwafi R., Faridi A. (2014). "Strengthening reinforced concrete beams in flexure using hardwire steel fiber sheets." In: *Proc. of CICE*. Vancouver, Canada, August 20–22; p. 22.
- Hoover, C. G., Bažant, Z. P. (2013). "Comprehensive concrete fracture tests: size effects of types 1 & 2, crack length effect and postpeak." *Eng Fract Mech*, 110, 281-289.

Hillerborg, A. (1985). "The theoretical basis of a method to determine the fracture energy G_F of concrete." *Materials and structures*, 18(4), 291-296.

Kerakoll S.p.A. – web site: <www.kerakoll.com> [accessed Aug 2016]

Kim J.Y., Fam A., Kong A., El-Hacha R. (2005). "Flexural strengthening of RC beams using steel reinforced polymer (SRP) composites." In: Proc. of the 7th int. symp. FRP reinforcement for concrete structures, ACI SP-230, 1, Paper #93; 2005. p. 1647–64.

Mirmiran, A., Shahawy, M. (1997). "Behavior of Concrete Columns Confined by Fiber Composites." *J. Struct. Eng.*, 123(5), 583-590.

Napoli, A., Realfonzo, R. (2015). "Reinforced concrete beams strengthened with SRP/SRG systems: experimental investigation." *Const Build Mat*; 93:654:677.

Napoli, A., Realfonzo, R. (2016). "Compressive Behavior of Concrete Confined by SRP Wraps." *Const Build Mat*; <http://dx.doi.org/10.1016/j.conbuildmat.2016.01.055>

Pecce M., Ceroni F., Prota A., Manfredi G. (2006). "Response prediction of R/C beams externally bonded with steel reinforced polymers." *J Compos Constr*; 103(2):195–203.

Prota A., Manfredi G., Nanni, A., Cosenza E., Pecce M. (2004). "Flexural strengthening of R/C beams using emerging materials: ultimate behavior." In: Proc. of CICE. Adelaide, Australia; p. 163–70.

Prota A., Tan K.Y., Nanni A., Pecce M., Manfredi G. (2006). "Performance of shallow R/C beams with externally bonded steel-reinforced polymer." *ACI Struct J*, 103(2):163–70.

Rochette, P., Labossière, P. (2000). "Axial Testing of Rectangular Column Models Confined with Composites." *J. Compos. Constr.*, 4(3), 129-136.

Saafi, M., Toutanji, H., Li, Z. (1999). "Behavior of Concrete Columns Confined with Fiber Reinforced Polymer Tubes." *ACI Mat J*, 96(4), 500-509.

Subramaniam KV, Carloni C, Nobile L. (2007). "Width effect in the interface fracture during shear debonding of FRP sheets from concrete." *Eng Fract Mech*, 74 (4):578–94.

Wobbe E., Silva P., Barton B.L., Dharani L.R., Birman V., Nanni A., Alkhrdaji T.,

Thomas J., Tunis T. (2004). "Flexural capacity of R/C beams externally bonded with SRP and SRG." In: Proc. of society for the advancement of material and process engineering symp. Long Beach, CA, USA; p. 20–7.

Wu, Y.F., and Wang, L. (2009). "Unified Strength Model for Square and Circular Concrete Columns Confined by External Jacket." ASCE J. Struct. Eng. 135(3), 253–61.

APPENDIX I

Photographs of the Failure Mode and Crack Patterns (Chapter 2)



Figure I.1: Crack patterns of beam BGH-A1-01



Figure I.2: Crack patterns of beam BGH-A1-02



Figure I.3: Crack patterns of beam BGN-A2-01



Figure I.4: Crack patterns of beam BGN-A2-02



Figure I.5: Crack patterns of beam BSN-A2-03

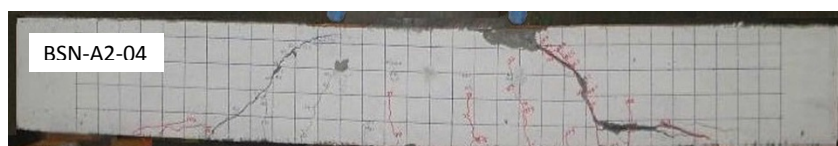


Figure I.6: Crack patterns of beam BSN-A2-04

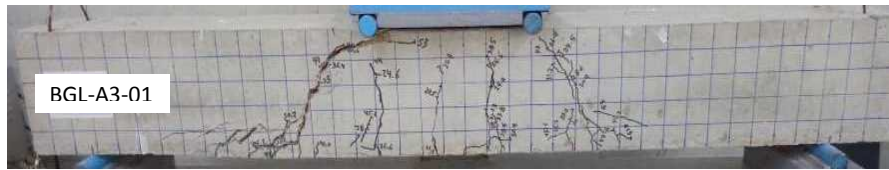


Figure I.7: Crack patterns of beam BGL-A3-01

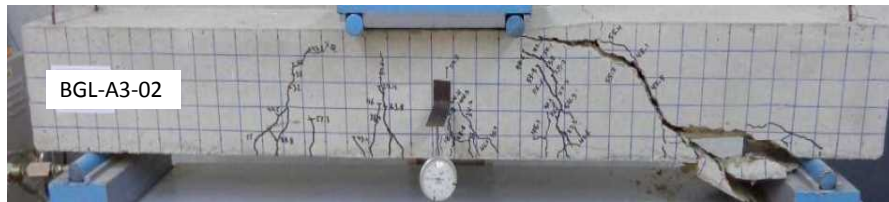


Figure I.8: Crack patterns of beam BGL-A3-02



Figure I.9: Crack patterns of beam BGH-A3-03



Figure I.10: Crack patterns of beam BGH-A3-04

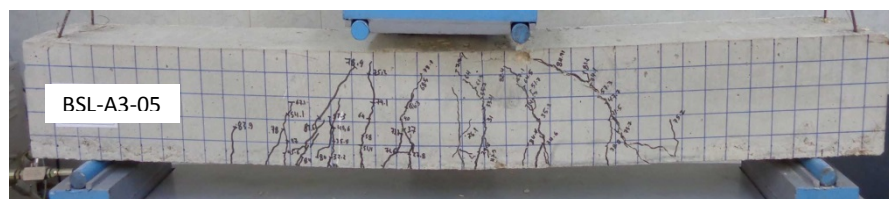


Figure I.11: Crack patterns of beam BSL-A3-05



Figure I.12: Crack patterns of beam BSL-A3-06

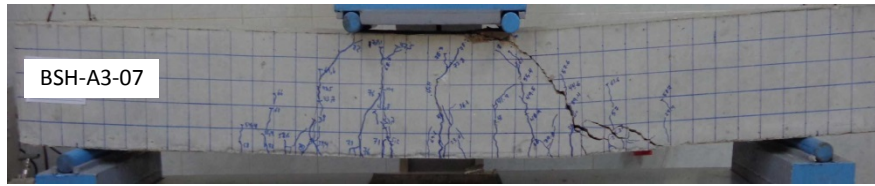


Figure I.13: Crack patterns of beam BSH-A3-07

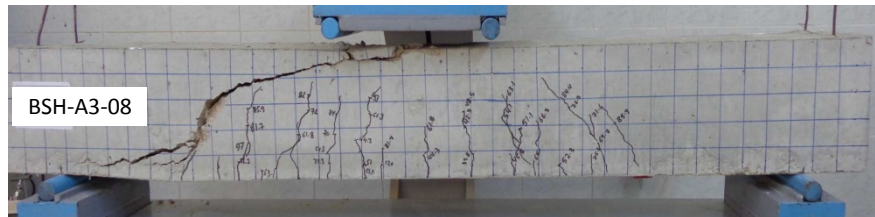


Figure I.14: Crack patterns of beam BSH-A3-08

APPENDIX II

Photographs of the experimental program of debonding investigation (Chapter 5)

